V. 121, NO. 1
JANUARY 2024

ACI MATERIALS JOURNAL

A JOURNAL OF THE AMERICAN CONCRETE INSTITUTE

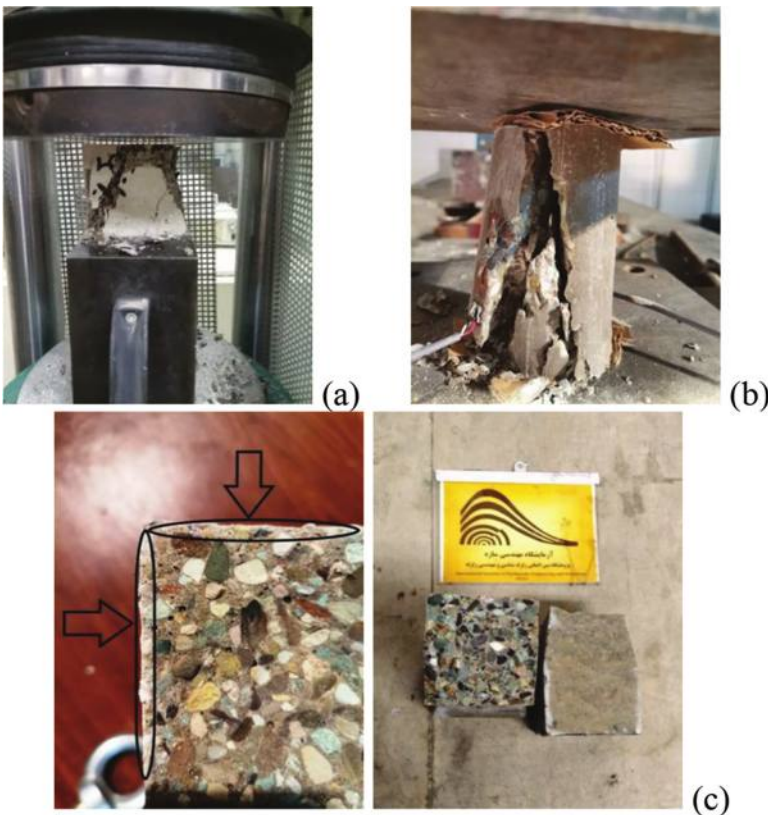

American Concrete Institute

CONTENTS

ACI Materials Journal

January 2024, V. 121, No. 1

A JOURNAL OF THE AMERICAN CONCRETE INSTITUTE
AN INTERNATIONAL TECHNICAL SOCIETY

Discussion is welcomed for all materials published in this issue and will appear ten months from this journal's date if the discussion is received within four months of the paper's print publication. Discussion of material received after specified dates will be considered individually for publication or private response. ACI Standards published in ACI Journals for public comment have discussion due dates printed with the Standard.

The *ACI Materials Journal* (ISSN 0889-325x) is published bimonthly by the American Concrete Institute. Publication office: 38800 Country Club Drive, Farmington Hills, MI 48331. Periodicals postage paid at Farmington, MI, and at additional mailing offices. Subscription rates: $199 per year, payable in advance. POSTMASTER: Send address changes to: *ACI Materials Journal*, 38800 Country Club Drive, Farmington Hills, MI 48331.

Canadian GST: R 1226213149.

Direct correspondence to 38800 Country Club Drive, Farmington Hills, MI 48331. Telephone: +1.248.848.3700.
Website: http://www.concrete.org.

PRINTED WITH SOY INK

MEETINGS

FEBRUARY 2024

24-25—Advanced Materials for Sustainable Infrastructure Development - Exploring Emerging Technologies for Reducing Carbon Emissions, Ventura, CA, www.grc.org/advanced-materials-for-sustainable-infrastructure-development-grs-conference/2024

FEBRUARY-MARCH 2024

25-1—Accelerating Sustainable Concrete Construction: A Holistic View, Ventura, CA, www.grc.org/advanced-materials-for-sustainable-infrastructure-development-conference/2024

MARCH 2024

3-5—ASA Shotcrete Convention and Technology Conference, Austin, TX, https://shotcrete.org/2024-asa-shotcrete-convention-and-technology-conference-online

6-8—6th Symposium on Ultra-High Performance Concrete and High Performance Building Materials for Sustainable Construction (HiPerMat 2024), Kassel, Germany, www.uni-kassel.de/fb14bau/en/institute/institut-fuerkonstruktiven-ingenieurbau-iki/hipermat-2024

7—Condition Assessment and Structural Health Monitoring for Concrete Structures, Tripoli, Lebanon, https://acts-int.com/conferences

14-15—2024 Decorative Concrete Expo, Canton, OH, www.deco-cretesupply.com/expo

18-21—NRMCA 2024 Annual Convention, Tampa, FL, www.nrmca.org/conferences-events

APRIL 2024

4-6—2024 APA UHPC Workshop, Tacoma, WA, www.archprecast.org/2024-spring-workshop

7-12—RILEM Spring Convention 2024, Milan, Italy, https://rilem.cte-eventi.com

10-26—The Masonry Society's 2024 Spring Meeting, Virtual, https://masonrysociety.org/event/2024-spring-meeting-virtual

14-17—PTI Post-Tensioning Convention, Indianapolis, IN, www.post-tensioning.org/events/conventions.aspx

15-18—CRSI 2024 Spring Business & Technical Meeting, Anaheim, CA, www.crsi.org/event/2024-spring-business-technical-meeting

ACI CONCRETE CONVENTION: FUTURE DATES

2024—March 24-28, Hyatt Regency New Orleans, New Orleans, LA
2024—November 3-7, Philadelphia Marriott Downtown, Philadelphia, PA
2025—Mar. 30-Apr. 3, Sheraton Centre Toronto Hotel, Toronto, ON, Canada
2025—October 26-30, Hilton Baltimore & Baltimore Marriott Inner Harbor, Baltimore, MD

For additional information, contact:
Event Services, ACI
38800 Country Club Drive
Farmington Hills, MI 48331
Telephone: +1.248.848.3795
email: conventions@concrete.org

ON FRONT COVER: 121-M07, p. 89, Fig. 11—Failure modes of: (a) cubic specimens in compression; (b) cylindrical specimens in compression; and (c) dumbbell-shaped specimens in tension.

Contributions to *ACI Materials Journal*

The *ACI Materials Journal* is an open forum on concrete technology and papers related to this field are always welcome. All material submitted for possible publication must meet the requirements of the "American Concrete Institute Publication Policy" and "Author Guidelines and Submission Procedures." Prospective authors should request a copy of the Policy and Guidelines from ACI or visit ACI's website at **www.concrete.org** prior to submitting contributions.

Papers reporting research must include a statement indicating the significance of the research.

The Institute reserves the right to return, without review, contributions not meeting the requirements of the Publication Policy.

All materials conforming to the Policy requirements will be reviewed for editorial quality and technical content, and every effort will be made to put all acceptable papers into the information channel. However, potentially good papers may be returned to authors when it is not possible to publish them in a reasonable time.

Discussion

All technical material appearing in the *ACI Materials Journal* may be discussed. If the deadline indicated on the contents page is observed, discussion can appear in the designated issue. Discussion should be complete and ready for publication, including finished, reproducible illustrations. Discussion must be confined to the scope of the paper and meet the ACI Publication Policy.

Follow the style of the current issue. Be brief—1800 words of double spaced, typewritten copy, including illustrations and tables, is maximum. Count illustrations and tables as 300 words each and submit them on individual sheets. As an approximation, 1 page of text is about 300 words. Submit one original typescript on 8-1/2 x 11 plain white paper, use 1 in. margins, and include two good quality copies of the entire discussion. References should be complete. Do not repeat references cited in original paper; cite them by original number. Closures responding to a single discussion should not exceed 1800-word equivalents in length, and to multiple discussions, approximately one half of the combined lengths of all discussions. Closures are published together with the discussions.

Discuss the paper, not some new or outside work on the same subject. Use references wherever possible instead of repeating available information.

Discussion offered for publication should offer some benefit to the general reader. Discussion which does not meet this requirement will be returned or referred to the author for private reply.

Send manuscripts to:
http://mc.manuscriptcentral.com/aci

Send discussions to:
Journals.manuscripts@concrete.org

LETTER FROM THE EDITORS-IN-CHIEF

As 2024 begins, we are fortunate to look back at a successful 2023 and look forward to an exciting new year. First and foremost, we thank all authors for their excellent contributions to the *ACI Structural Journal* and *ACI Materials Journal*. In 2017, ACI began a transition in journal management by appointing editorial boards. On behalf of the editorial boards, we thank the reviewers for their commitment to providing timely, high-quality reviews. We have been fortunate to have a great community of reviewers who have stepped up to provide these reviews while remaining dedicated to the high quality and success of the journals.

It is important to recognize that ACI has a phenomenal search engine that members can use to identify resources that have appeared in ACI publications (**https://www.concrete.org/publications/internationalconcreteabstractsportal.aspx**). The ACI journals are a great resource for ACI committees, ACI members, and students. Students are able to access these resources and more through their free membership (**https://www.concrete.org/membership/becomeamember.aspx**). This search engine also includes a large number of International Partners. ACI has worked to inform readers of the contents of the journal when new issues of the journal are made available online, and this service reaches over 27,000 members.

The editorial board has worked closely with ACI staff to institute new policies and practices for the journal. The dual-unit requirement has been eliminated to encourage the solicitation and publication of more international papers. The board has also permitted papers that are slightly longer, moving the word limit from 10,000 to 12,000 words per paper. Special issues were introduced in 2019 to provide focus on timely topics and emerging areas. Specifically, the *ACI Materials Journal* hosted special issues on pozzolans and chlorides in 2019, computational modeling in 2020, rheology and additive manufacturing in 2021, and sustainability and resilience in 2023 (**https://www.concrete.org/publications/acistructuraljournal/specialissues.aspx**).

The board and staff have worked diligently to reduce the time to publication, reducing the average time from submission to publication from 11.2 to 8.0 months for the *ACI Structural Journal* and from 9.0 to 6.7 months for the *ACI Materials Journal*. It can also be noted that from 2014 to 2022, the impact score increased from 1.22 to 1.83 for the *ACI Materials Journal* and from 1.24 to 1.88 for the *ACI Structural Journal*.

While it is important to reflect on measures taken and their impact, it is also important to look toward the future. The editorial board is committed to continual improvement. During 2022 and 2023, the editorial team made several recommendations that will be implemented in 2024. First, the journals will institute associate editors for the first time. The associate editors will aid in recruiting high-quality manuscripts, providing strategic suggestions to the editorial board for journal development, and coordinating the manuscript review process. Second, ACI articles will be more prominently shared through SmartBrief.

Finally, the inaugural Editors-in-Chief, Robert Frosch for the *ACI Structural Journal* and Jason Weiss for the *ACI Materials Journal*, will complete their terms of appointment in 2023 and 2024, respectively. We want to personally thank all the authors, reviewers, editorial board members, and ACI staff for all their help throughout the last 6+ years. We are pleased to announce that Mike Kreger has been named Editor-in-Chief of the *ACI Structural Journal* and Shiho Kawashima has been named Editor-in-Chief of the *ACI Materials Journal*.

The ACI journals continue to strive to publish papers on high-quality research pertaining to civil engineering materials and structures. Specifically, ACI focuses on papers that impact practice using hypothesis-driven, high-level scientific research.

Sincerely,
Mike Kreger,
Editor-in-Chief, *ACI Structural Journal*

Jason Weiss,
Editor-in-Chief, *ACI Materials Journal*

REGISTER TODAY

TECHNOLOGY FORUM

MAY 14-16, 2024, SANTA FE, NM, USA

Hilton Santa Fe - Historic Plaza, 100 Sandoval Street

The **Technology Forum** is an innovation-focused educational and networking event for concrete professionals **powered by the ACI Foundation's Concrete Innovation Council**.

Whether you are an emerging professional or a seasoned veteran, the ACI Foundation Technology Forum is the place to learn about **current trends, emerging technologies, and discoveries within the concrete industry**.

Join us for an exciting and insightful event featuring thought leaders and technology innovators to discuss the future of the concrete industry.

aci Foundation
Building the Future

acifoundation.org

ACI MATERIALS JOURNAL TECHNICAL PAPER

Title No. 121-M01

Chlorides in Concrete: Science-Based Exposure Classifications and Allowable Limits

by David Trejo and Gokul Dev Vasudevan

Inconsistencies in standards and codes result in confusion, increased costs, and do not promote the efficient use of concrete. In addition to inconsistencies, the lack of science-based approaches and data used for defining criteria in these standards and codes can limit the reliability and trust of these requirements. A review of industry documents indicates that inconsistencies and lack of science-based approaches exist across many documents, both throughout the industry and within ACI, relating to the corrosion of steel reinforcement embedded in concrete. This paper proposes to address five key issues to promote science-based standardization of requirements necessary for reinforced concrete systems exposed to corrosive conditions. These five issues include the need for: 1) standardization of chloride testing methods and requirements; 2) standardization of chloride reporting units; 3) standardization of terminology for specifying chlorides in cementitious systems; 4) standardization of exposure classifications for corrosive conditions; and 5) standardization of allowable chloride limits.

This paper presents current inconsistencies in guide documents and codes for each of the items listed previously and then proposes an approach to standardize each using either available data and/or a scientifically based approach. Recommendations for testing, reporting, definition of exposure classifications, and allowable chloride limits are then proposed. It is hoped that the systematic approach used herein will lead to standardization and consistency, less confusion, and will promote the efficient use of durable and economical concrete.

Keywords: admixed chloride; allowable chloride concentration; corrosion; critical chloride concentration; exposure classification; limit state design; probability of corrosion.

INTRODUCTION AND BACKGROUND

Chlorides in concrete can result in corrosion of the embedded steel reinforcement. Chlorides are introduced into the concrete either from the constituent materials or from the surrounding environment. Chlorides introduced into the concrete from the constituent materials (for example, water, cement, and aggregates) are referred to as admixed chlorides, C_{admix}. Small amounts of admixed chlorides in new concrete typically do not result in corrosion activity. However, to minimize the risk of reinforcement corrosion when the concrete constituent materials contain chlorides, many specifying documents, including documents published by the American Concrete Institute (ACI), limit the number of chlorides that can be present in new concrete. These limits are referred to as the allowable chloride limits, C_{limit}, and these limits require that $C_{admix} \leq C_{limit}$.

ACI documents have a long history of publishing C_{limit} values. However, the information in different ACI documents varies significantly, and justifying and defending these chloride limits has been challenging. One reason for this is because current ACI documents contain no data on how allowable chloride limits have been determined. A methodology that can justify these values and can provide consistent requirements across all ACI documents is needed.

In addition to chlorides being introduced into the concrete from the constituent materials, chlorides can also be introduced to the concrete from the environment in which the reinforced concrete is constructed. The rate at which these chlorides penetrate the concrete and reduce the service life of the structure depends on the concentration of the chloride in the exposure solution and the transport mechanisms in which the chlorides are transported into the concrete. Current ACI documents define several exposure conditions for corrosive environments. However, several exposure conditions are not included in the published exposure conditions and a systematic, science-based approach to define these exposure conditions has not yet been developed. In addition to the need for a science-based approach to define allowable chlorides in concrete, a systematic methodology based on fundamental principles of corrosion is needed to standardize corrosion exposure conditions for reinforced concrete systems.

In addition to the need for both standardized and consistent C_{limit} values and exposure classifications, it is important that other requirements be standardized for consistency. The following sections address existing challenges and needs associated with: 1) chloride testing; 2) chloride reporting; 3) terminology used for specifying chlorides; 4) definition of exposure classifications for reinforced concrete (RC) structures exposed to corrosive conditions; and 5) quantification of allowable chloride limits in concrete. Because solutions for items 1 through 3 are straightforward, recommendations on standardizing consistent requirements for these items are proposed in the following sections. Recommended methodologies for defining corrosive exposure classifications and allowable chloride limits will require a more detailed and comprehensive approach and these proposed methodologies will be presented in the "Results" section of this paper.

ACI Materials Journal, V. 121, No. 1, January 2024.

MS No. M-2022-133.R5, doi: 10.14359/51739198, received February 20, 2023, and reviewed under Institute publication policies.

Table 1—Chloride testing criteria in ACI documents

Document/ guide	Table No. in document	Required chloride testing description	Normalized units	Relevant details provided in footnotes
ACI 201.2R-16	Table 9.5.2.1.2	1. Acid soluble (ASTM C1152/C1152M) 2. Water soluble (ASTM C1218/C1218M)	% by mass of cementitious materials	All chloride contents expressed as percent Cl^- by mass of cement.
ACI 222-19	Table 4.2.3	1. Acid soluble (ASTM C1152/C1152M) 2. Water soluble (ASTM C1218/C1218M)	% by mass of cementitious materials	1. Portland cement-based systems only. Total cementitious material includes portland cement and SCM; however, for determining allowable admixed chloride level, the SCM content cannot exceed the portland cement content. 2. Typically interior concrete protected from moisture, high humidity, or both.
ACI 301-20	Table 4.2.2.6(e)	Maximum water-soluble chloride ion (Cl^-) content in concrete (no test standard defined)	% by mass of cementitious materials	The maximum cementitious materials content used in determining chloride content shall not exceed two times the mass of portland cement.
ACI 318-19	Table 19.3.2.1	Maximum water-soluble chloride ion (Cl^-) content in concrete (no test standard defined)	% by mass of cementitious materials	The mass of supplementary cementitious materials used in determining the chloride content shall not exceed the mass of the portland cement.
ACI 329R-14	Table 6.2.2.2	Maximum water-soluble chloride ion content in concrete (ASTM C1218)	% by weight of cement	Water-soluble chloride ion content that is contributed from the ingredients including water, aggregates, cementitious materials, and admixtures shall be determined on the concrete mixture by ASTM C1218 at age between 28 and 42 days.
ACI 350-20	Table 4.3(c)	Maximum water-soluble chloride ion content in concrete (no test standard defined)	% by weight of total cementitious materials	Water-soluble chloride ion content that is contributed from the ingredients including water, aggregates, cementitious materials, and admixtures shall be determined on the concrete mixture by ASTM C1218 at age between 28 and 42 days.

Testing requirements for chlorides in concrete: current practice and new recommendations

Test methods used to quantify chlorides are important in understanding the potential risk of corrosion. Table 1 shows the criteria for chloride testing in several ACI documents. Note that both ASTM C1152/C1152M-20 (2020) and ASTM C1218/C1218M-20 (2020) are allowed for quantifying chlorides in new concrete in some ACI documents. Also note that ACI 222R-19 and ACI 318-19 allow ASTM C1524/C1524M-20 (2020) to quantify chlorides in new concrete. This is generally used when aggregates contain bound chlorides that are not released over the life of the structure.

Trejo et al. (2019) reported that the ratio of the water-soluble (ASTM C1218) to acid-soluble (ASTM C1152) chlorides (w/a) can vary from 0.08 and 0.77 for systems containing ordinary portland cement (OPC) only, OPC and Type C fly ash, OPC and Type F fly ash, OPC and slag, and OPC and silica fume. The authors reported that the w/a is significantly different for these different systems and because of this, both water-soluble and acid-soluble testing for C_{limit} quantities should not be allowed. The authors also recommended that C_{limit} values should be based on ASTM C1218 testing only or C1152 testing only, but not both. However, Ahmed and Trejo (2023) later reported that water-soluble testing following ASTM C1218 is sufficiently conservative to account for chlorides that may be released because of carbonation. The authors then recommended that only ASTM C1218 be required to quantify C_{admix} when assessing if $C_{admix} \leq C_{limit}$. Because there is little correlation between water-soluble (ASTM C1218) and acid-soluble (ASTM C1152) chloride testing and because water-soluble chloride testing has been reported to be sufficiently conservative, it is recommended that all ACI documents require only ASTM C1218 testing to assess chlorides in new concrete, with one exception.

The sole exception to requiring ASTM C1218 testing should be when coarse aggregate contains chlorides and crushing these coarse aggregates as required in the C1218 test would release chlorides that would likely never be released in service. Under these conditions, ASTM C1524 should be allowed for quantifying chlorides in the aggregates and ASTM C1218 should be required for quantifying chlorides in the other combined constituent materials, excluding the coarse aggregates. The C_{admix} for this case would be the sum of the results from the ASTM C1218 and ASTM C1524 test methods.

Normalization of chlorides in concrete: current reporting and new recommendations

The literature commonly reports chloride concentrations as: 1) a percentage by mass of concrete; 2) a percentage by mass of cement; and 3) a percentage by mass of cementitious materials. ACI documents refer to chloride concentrations as a percentage based on cement or cementitious materials mass. However, ACI 201.2R-16 and ACI 329R-14 require chloride content calculations be determined by mass of cement only. ACI 350.5-12 bases the determination of chloride concentration based on mass of total cementitious materials (OPC and supplementary cementitious materials [SCMs]), with no reported limits on how much SCM can be used in the calculations. The ACI 222 and 318-19 documents also allow the inclusion of SCM content when determining the percent chlorides, but limit the amount of SCMs that can

Table 2—Exposure classifications reported in ACI documents

Document/guide	Category	Class	Condition	Severity
ACI 222-19 and ACI 201.2R-16	RC in wet conditions	NA	NA	NA
	RC in dry or protected conditions	NA	NA	NA
ACI 318-19 and ACI 301-20	Corrosion protection of reinforcement	C0	Concrete dry or protected from moisture	NA
		C1	Concrete exposed to moisture but not to an external source of chlorides	NA
		C2	Concrete exposed to moisture and an external source of chlorides from deicing chemicals, salt, brackish water, seawater, or spray from these sources	NA
ACI 329R-14	Corrosion protection of reinforcement	C0	Concrete dry or protected from moisture	NA
		C1	Concrete exposed to moisture but not to an external source of chlorides	Moderate
		C2	Concrete exposed to moisture and an external source of chlorides from deicing chemicals, salt, brackish water, seawater, or spray from these sources	Severe
ACI 350-20	Corrosion protection of metals	EC0	Concrete that will be dry or protected from moisture in service	Negligible
		EC1	Concrete that will be exposed to moisture but to no more than 500 ppm of chloride from external source	Moderate
		EC2	Concrete that will be exposed to moisture and an external source of chlorides in service—from deicing chemicals, salt, seawater, or spray from these sources	Severe
		EC3	Concrete that will be exposed to chemicals including gases that are more corrosive than those described in EC2	Very severe

be used in the calculation to no more than the mass of the OPC. ACI SPEC-301 limits the SCM content when determining chloride content to no more than two times the mass of the OPC. Table 1 shows a summary of these cases.

Should the normalization of the chloride concentration be a function of OPC content, OPC+SCM content, or OPC+SCM with some SCM limit? Azad and Isgor (2016) reported that the addition of SCMs, up to approximately 50% replacement, can provide similar resistance to chloride-induced corrosion and therefore suggest limiting the amount of SCMs when determining percent chlorides to no more than the OPC content. Having different requirements for normalizing the chloride content in the ACI documents results in confusion. Because data are available from Azad and Isgor (2016), it is recommended that calculations for determining chlorides in concrete now be based on the mass of OPC and SCM, where the SCM content for calculation purposes shall not exceed the OPC mass. Updates can be made if new information becomes available.

Terminology for specifying C_{limit} values: current practice and recommendations

ACI 301, 318, and 350.5 all limit the C_{limit} by specifying the "maximum water-soluble chloride-ion (Cl^-) content in concrete, percent by mass of cementitious materials." ACI 329 has the same text with the exception of requiring only by mass of cement. ACI 201.2 simply states that the C_{limit} values are "limits to chlorides in newly constructed concrete," and ACI 222 specifies "chloride limit for new construction (percent by mass of cementitious material)." Although all seem similar, these differences cause confusion and consistent standardization across all documents would be beneficial.

In addition to standardizing the terminology in ACI documents, the documents provide no guidance on how many tests should be performed to quantify C_{admix} (where C_{admix} must be equal to or less than C_{limit}). Is one test sufficient to quantify C_{admix} as long as it does not exceed the C_{limit}? Because this paper will later introduce a probabilistic approach to define C_{limit} values, the authors recommend requiring more than one test for quantifying C_{admix}. The following text for the requirement of C_{limit} is recommended for all ACI documents:

"Maximum mean water-soluble chloride content, percent by mass of cementitious materials[1,2,3]"

with the following footnotes:

1. Testing to be performed on concrete of ages between 28 and 42 days following ASTM C1218 requirements with a minimum of three test samples required;

2. When determining percent by mass of cementitious materials, mass of SCM cannot exceed mass of OPC; and

3. Applicable for conventional black reinforcement only.

The importance of requiring a "mean" value will be discussed later.

Exposure classifications: current practice and needs

Corrosion of steel in concrete is an electrochemical process requiring well-defined conditions. Exposure classification should be dependent on conditions that cause this corrosion. However, this is currently not the case. Table 2 shows the current exposure classifications from six different ACI guides, codes, or specifications. In general, these documents specify environmental exposures as dry, exposed to moisture but not external chlorides, and exposed to moisture with external chlorides. Note that ACI 350-20 includes a very severe classification, *EC*3, where concrete is exposed to chemicals including gases that cause more corrosion than a severe condition. It is important to note herein that corrosion of metals requires at least two conditions in addition to the presence of the metal: moisture and oxygen. However, due to the high pH of concrete pore solution, conventional reinforcement is generally protected from corrosion. But if

admixed chlorides are sufficiently high or if chlorides are transported into the concrete and reach a critical concentration at the steel reinforcement surface, corrosion will initiate and propagate.

Therefore, three environmental conditions, not two, will influence the corrosion initiation and propagation of the conventional steel reinforcement embedded in non-carbonated concrete; these include: 1) the presence of moisture; 2) the presence of oxygen (at the cathode); and 3) the amount of chlorides present in the new concrete and/or surrounding environment. When chlorides are present in the constituent materials, the probability of active corrosion increases with increasing chloride concentrations. This is why ACI and other organizations limit chlorides in new concrete.

When an RC structure is exposed to an environment that contains chlorides, the chloride concentration and the manner in which the chlorides are transported into the concrete can influence the time to corrosion and service life. For example, when an RC structure is exposed to a solution containing chlorides and the exposure condition includes wetting and drying of the concrete (for example, in splash or tidal zones), the main mechanism of chloride transport into the concrete is through absorption. Alternatively, when RC is exposed to a solution containing chloride and the exposure is continuous, the main mechanism of chloride transport is diffusion (and possibly permeation). In general, the transport of chlorides through absorption is much faster than diffusion-only transport. Therefore, the type of chloride exposure is important.

In addition, if a structure is exposed to wetting-and-drying cycles but is only intermittently exposed to wet cycles containing chlorides (for example, application of anti-icers or deicers), the number of chloride applications will also influence the time to corrosion. So, in addition to the type of exposure, the number of chloride applications will also be an influencing factor for defining exposure classifications. How these will be included in the definition of exposure classifications is presented later.

C_{limit} values: existing specified limits and needs

In addition to the various chloride testing methods being allowed with little correlation between these test methods and varying normalization methods for reporting chloride concentrations, many of the published C_{limit} values vary throughout ACI documents. Table 3 shows the C_{limit} values published in the ACI documents. One reason for these variations in C_{limit} values is the lack of C_{crit} data necessary to justify these limits. It is important to note that if C_{limit} values are published to minimize the probability of corrosion, it must be known how much chlorides cause corrosion. Chopperla et al. (2022) provided a comprehensive assessment of challenges and inconsistencies associated with ACI documents and C_{limit} values. If the amount of chlorides that result in active corrosion of steel reinforcement embedded in concrete is not defined, how can a justifiable limit on C_{admix} be defined? Having C_{crit} data will allow for a limit state design (LSD) approach to define C_{limit} values based on some probability in which the admixed chlorides would result in active corrosion of the reinforcement. Fortunately, C_{crit} data are now becoming available, and significantly more data will be available in the near future from on-going research. These data will provide for more comprehensive, justifiable, and defendable C_{limit} values. An LSD approach to define C_{limit} values is presented later.

Table 3—C_{limit} values specified in ACI documents

Document/ guide	Category	Class	Acid soluble (ASTM C1152/ C1152M)*	Water soluble (ASTM C1218/ C1218M)*
ACI 201.2R-16	RC in dry or protected conditions	NA	0.20	0.15
	RC in wet conditions	NA	0.10	0.08
ACI 222-19	RC in dry or protected conditions	NA	0.30	0.25
	RC in wet conditions	NA	0.20	0.15
ACI 318-19 and ACI 301-20	Corrosion protection of reinforcement (C)	C0	NA	1.00
		C1		0.30
		C2		0.15
ACI 329R-14	C Corrosion protection of reinforcement	C0	NA	1.00
		C1		0.30
		C2		0.15
ACI 350-20	Corrosion protection of metals	EC0	NA	0.10
		EC1		0.10
		EC2		0.10
		EC3		0.10

*For exact terminology, please refer to Table 1.

RESEARCH SIGNIFICANCE

Criteria necessary for designing corrosion-resistant RC structures varies significantly throughout the concrete industry. Standardization and consistency are needed. In addition to standardizing testing requirements, reporting methods, and terminology used for testing and reporting, standardization of exposure conditions and allowable chlorides for new concrete is sorely needed. Unfortunately, allowable chloride limits specified by many organizations, including ACI, are subjective, deterministic, and lack a scientific foundation. A systematic framework that specifies C_{limit} values based on C_{crit} data and some acceptable risk of corrosion (that is, probability of failure, P_f) could lead to standardized requirements. However, because C_{limit} values are dependent on exposure conditions, exposure classifications must also be standardized. In this work, exposure classifications, based on electrochemical fundamentals, are proposed. Following this, a systematic probabilistic framework that specifies C_{limit} values is developed based on LSD principles. The benefits offered by this framework include providing a systematic and scientific approach to specify C_{limit} values, allowing specifiers to modify C_{limit} values when

different materials are used, and allowing different C_{limit} values for different acceptable risks.

RESULTS AND DISCUSSION

In the earlier sections of this paper, it was noted that ACI documents have various requirements for specifying and quantifying chlorides in new concrete, and these same documents report various C_{limit} values. In addition, the documents have no standardized exposure classifications, and the methodology for defining these exposure classifications seems to be subjective and non-scientific. These issues cause confusion in our industry and can lead to inefficiencies and increased costs for RC systems. The previous sections identified five issues within the ACI documents and provided recommendations for three of these issues: 1) standardization of a required testing method for quantifying C_{admix} in concrete; 2) standardization of the normalization of chloride concentrations; and 3) standardization of the terminology used to specify C_{limit} values. The two additional issues require a more comprehensive discussion and assessment.

The first additional issue includes the development of a systematic and science-based approach for defining exposure classes. This approach should be based on electrochemical principles of steel embedded in concrete. The second additional issue is the development of a probabilistic, risk-based approach to quantifying C_{limit} values; these are presented next.

SCIENCE-BASED APPROACH TO DEFINING CORROSIVE EXPOSURE CONDITIONS

In general, ACI documents report C_{limit} values for three general exposure conditions: 1) dry exposure conditions; 2) wet exposure conditions containing no external chlorides; and 3) wet exposure conditions containing chlorides. These exposure conditions indicate that moisture and chlorides are the only contributing factors for corrosion initiation and propagation, which is not correct. The basic electrochemical mechanism of steel exposed to moisture includes both anodic (Eq. (1)) and cathodic reactions (Eq. (2)), as follows

$$Fe \rightarrow Fe^{2+} + 2e^{-} \quad (1)$$

$$O_2 + 2H_2O + 4e^{-} \rightarrow 4OH^{-} \quad (2)$$

Note that for this case, only iron, oxygen, and water need to be present for corrosion to occur. As already noted, the high pH of the pore solution protects the steel reinforcement from corrosion except when chlorides are present. Chlorides are believed to react with the iron near the anode as follows

$$Fe^{2+} + 2Cl^{-} \rightarrow FeCl_2 \quad (3)$$

The ferrous chloride that is formed in the reaction between iron and chlorides is soluble, thereby exposing the reinforcement to continued chlorides and the potential for continued corrosion. Although ACI documents imply that only moisture and chlorides are necessary for corrosion, oxygen is also required. This should be included in exposure classifications.

In addition to the presence of water and oxygen, it should be noted that it is not just the presence of chlorides that influence the durability of the RC system. The rate at which chlorides are transported into the concrete towards the steel reinforcement will significantly influence the time to corrosion and severity of the exposure condition. The rate of chloride transport is dependent on three exposure conditions: the concentration of the exposure solution, the mechanism of transport of the chlorides into the concrete, and the duration or number of chloride exposures.

The concentration of the chlorides in the exposure solution influences the rate at which chlorides are transported into the concrete; higher exposure solution concentrations will result in faster ingress. As such, chloride concentration should be considered when developing exposure classifications. In addition to the chloride concentration, it is well established that the mechanism of exposure influences the transport rate into the concrete: diffusion-only-based chloride transport (for example, continuous exposure) is significantly slower than absorption-based transport (for example, cyclic or wetting and drying exposure). Therefore, the mechanism of exposure should also be accounted for when developing exposure classifications. Lastly, the duration of the exposure (or number of exposures) will influence the time to corrosion; a structure exposed to a few chloride exposures will be much less likely to exhibit corrosion of the embedded reinforcement than a structure that is regularly exposed to the same chloride solution. Therefore, the availability of oxygen and moisture, the concentration of the chloride exposure solution, the mechanism of transport into the concrete, and the duration or number of chloride exposures for wetting and drying applications are significant factors that should be considered when establishing exposure classifications.

If it is assumed there could be two moisture states (moist and dry), two oxygen states (present or not present), three chloride levels (none to very low, moderate, and high), and two exposure types (continuous and cyclic), a full factorial design would require 24 exposure classifications. Also, when both oxygen and moisture are present and the chloride concentration is moderate or high, exposure conditions should be further separated for duration of chloride exposure. As duration of anticipated exposure conditions could be difficult to quantify for actual structures, the number of chloride exposures may be a more definable term and will be used herein. Therefore, another two exposure conditions should be included, making for a total of 26 potential exposure conditions.

Table 4 shows the factorial design of the 26 exposure conditions considering the influencing variables presented. Table 4 also shows the potential for corrosion under these conditions. Note herein that CS indicates corrosion from salts. Corrosion from carbonation (CC) is not addressed in this publication. The NA in the table indicates "not applicable" and that these conditions likely would not occur under typical exposure conditions. For example, the condition when there is no moisture present in the concrete or surrounding environment and the chloride level is high would likely not occur because chlorides are generally

Table 4—Factorial design of factors potentially resulting in corrosion

Oxygen	Moisture	Chloride concentration	Type of moisture and/or chloride exposure	Potential for corrosion	Exposure classification
Not present	Not present	None	Continuous	NA	NA
			Cyclic	NA	NA
		Moderate	Continuous	NA	NA
			Cyclic	NA	NA
		High	Continuous	NA	NA
			Cyclic	NA	NA
	Present	None	Continuous	None/very low	CS0
			Cyclic	NA	NA
		Moderate	Continuous	None/very low	CS0
			Cyclic	NA	NA
		High	Continuous	None/very low	CS0
			Cyclic	NA	NA
Present	Not present	None	Continuous	None/very low	C0
			Cyclic	NA	NA
		Moderate	Continuous	NA	NA
			Cyclic	NA	NA
		High	Continuous	NA	NA
			Cyclic	NA	NA
	Present	None	Continuous	Low	CS1
			Cyclic	Low	CS1
		Moderate	Continuous	Low/moderate	CS2
			Cyclic-low*	Moderate	CS3
			Cyclic-high†	High	CS4
		High	Continuous	Moderate	CS3
			Cyclic-low*	High	CS4
			Cyclic-high†	Very high	CS5

*Corresponds to less than or equal to 10 chloride applications per annum.

†Corresponds to more than 10 chloride applications per annum.

associated with being present in an exposure solution and thus, the concrete.

From Table 4, it can be seen that there are six exposure conditions for RC systems, from an exposure condition that would result in very low or no likelihood of corrosion to an exposure condition that could result in a very high potential for corrosion. The authors should note that an attempt has been made to distinguish these different exposure classifications based on likelihood of future corrosion. These classifications are based on the authors' best knowledge, and others may recommend a different number of exposure classifications. The contribution herein is not the number of classifications but the systematic approach that includes the fundamental requirements needed for active corrosion in generating these classifications.

The condition where the potential for corrosion is none or very low, proposed exposure classification CS0, indicates that the basic conditions required for corrosion are not present under these exposure conditions. When oxygen and moisture are present, the potential for corrosion depends on the concentration of chlorides in the exposure solution, the exposure type (continuous or cyclic), and the number of chloride solution applications. The exposure classification increases with increasing exposure severity. Table 5 summarizes the proposed exposure classifications from CS0 to CS5.

LIMIT STATE DESIGN APPROACH TO DEFINING C_{limit} VALUES

LSD, also known as load and resistance factor design (LRFD), refers to a design method commonly used in structural engineering. A limit state is a condition state that no longer fulfills some relevant criteria. For example, in structural design, one limit state could be when the load exceeds the capacity of the member, thereby resulting in failure of the member (this is often referred to as the ultimate limit state). For this work, the limit state criteria relate to the state of corrosion of the steel reinforcement embedded in the concrete. The limit state herein is defined as the corrosion initiation of the steel reinforcement, where active corrosion is assumed to be failure. This limit state condition is commonly

Table 5—Summary of proposed exposure classifications

Oxygen	Moisture	Chloride concentration	Type of moisture and/or chloride exposure	Potential for corrosion	Exposure classification
Not present	Present	Any (none to high)	Continuous	None/very low	CS0
Present	Not present	None	None	None/very low	CS0
	Present	None	Continuous	Low	CS1
			Cyclic	Low	CS1
		Moderate	Continuous	Low/Moderate	CS2
			Cyclic-low number of applications*	Moderate	CS3
			Cyclic-high number of applications†	High	CS4
		High	Continuous	Moderate	CS3
			Cyclic-low number of applications*	Moderate/high	CS4
			Cyclic-high number of applications†	Very high	CS5

*Corresponds to less than or equal to 10 chloride applications per annum.

†Corresponds to more than 10 chloride applications per annum.

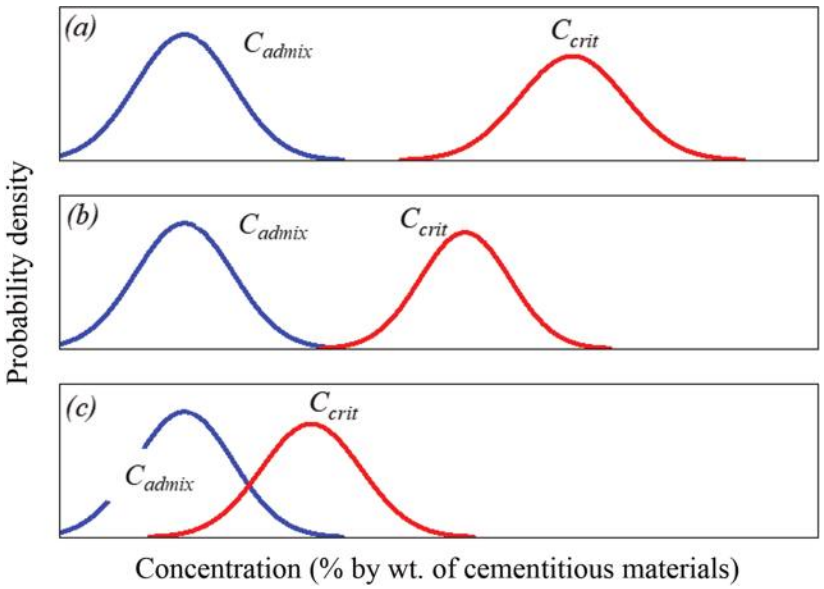

Fig. 1—Examples of different probabilities of corrosion based on overlap of C_{admix} *and* C_{crit}.

referred to as a serviceability limit state. In general, a limit state separates a desired state from the adverse state (failure) and a system designed using LSD should resist "failure" during its life, with some appropriate level of reliability (or probability of failure).

In this paper, the authors use an LSD approach to quantify C_{limit} values for new concrete based on the distribution of C_{admix} and C_{crit} values and an acceptable probability of failure (P_f). This approach evaluates the probability of corrosion resulting from admixed chlorides, C_{admix}, for conventional steel reinforcement embedded in concrete exposed to a wet environment containing no chlorides. The probability of corrosion is determined for various C_{admix} distributions with different mean values. Using these probabilities, a value for $C_{limit+wet}$ can then be determined based on some acceptable probability of corrosion. Following this, the C_{limit} for the exposure condition where moisture and chlorides are present, $C_{limit-wet+cl}$, can be estimated knowing that $C_{limit-wet+cl}$ should be less than $C_{limit-wet}$. Note herein that the authors recommend that $C_{limit-dry}$ be defined as the C_{crit}, which will result in $C_{limit-wet+cl} \leq C_{limit-wet} \leq C_{limit-dry}$. Current specifications use this logic.

To better understand the approach used herein, Fig. 1 shows some hypothetical scenarios involving the probability curves of C_{admix} and C_{crit}. Figure 1(a) shows the case in which the probability curves of C_{admix} and C_{crit} have very little overlap. This signifies that there is very low probability of active corrosion. Figure 1(b) shows the case where the distribution curves exhibit some small overlap. This signifies there is limited, but some probability of active corrosion. Figure 1(c) shows the case where the curves exhibit significant overlap. The greater the overlap, the higher the probability of active corrosion.

The probability of failure, P_f, involving two normal distributions can be determined by first identifying the reliability index, β, determined as follows

$$\beta = \frac{\mu_{admix} - \mu_{crit}}{\sqrt{(\sigma_{admix})^2 + (\sigma_{crit})^2}} \quad (4)$$

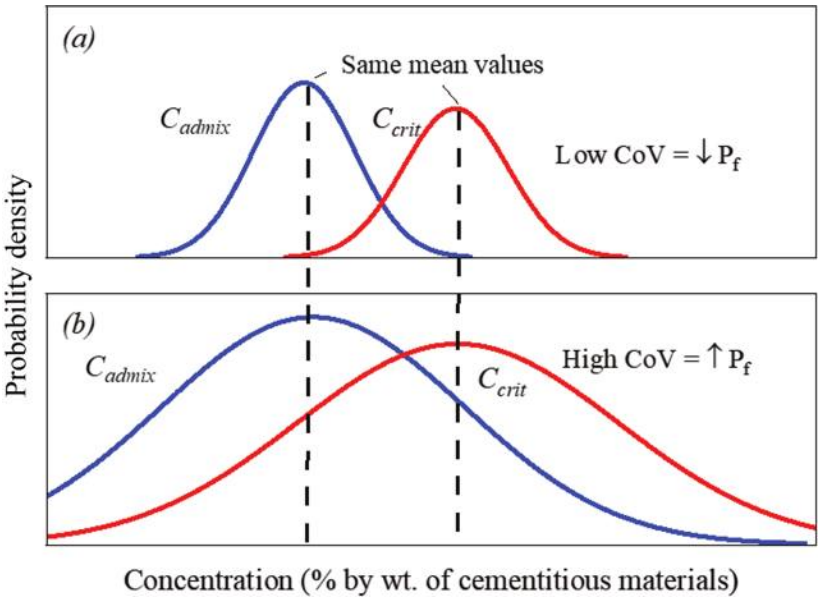

Fig. 2— Example of effect of CoV on P_f.

where μ_{admix} and μ_{crit} are the mean values of C_{admix} and C_{crit}; and σ_{admix} and σ_{crit} are the standard deviations of C_{admix} and C_{crit}, respectively. The σ_{admix} and σ_{crit} values can be defined as a percentage of their respective mean values using their respective coefficients of variance (CoV) as follows

$$\sigma_{admix} = \text{CoV}_{admix} \times \mu_{admix} \quad (5)$$

$$\sigma_{crit} = \text{CoV}_{crit} \times \mu_{crit} \quad (6)$$

Note that the CoV is a critical factor in quantifying P_f. Figure 2 shows the difference in P_f when two data sets have the same mean, but different CoV values. As CoV increases, the overlap between C_{admix} and C_{crit} also increases, resulting in a higher probability of active corrosion and failure, P_f.

The equation to determine β (Eq. (4)) is valid only for normal distributions and does not hold true if the assumptions of normality are violated. Once β is determined, P_f can be estimated as follows

$$P_f = \Phi(-\beta) \quad (7)$$

where Φ is the inverse cumulative normal function. To implement the LSD principle, the CoV of both the C_{admix} and C_{crit} distributions are required. The C_{admix} and C_{crit} data and distributions and the subsequent analysis to determine the CoV and P_f are presented next.

C_{admix} and C_{crit} data

In this study, C_{crit} values were determined using data from the critical chloride testing procedure developed by Trejo et al. (2021) and reported by Halmen and Adil (2020). These data included results from the ASTM C1152 (acid-soluble) test method. Because water-soluble chloride testing is recommended for the ACI document requirements, the acid-soluble chloride results will be converted to water-soluble chloride values using the factor shown in Fig. 3 (Vaddey et al. 2020). Note that this conversion is only applicable for systems containing only OPC (that is, no SCMs).

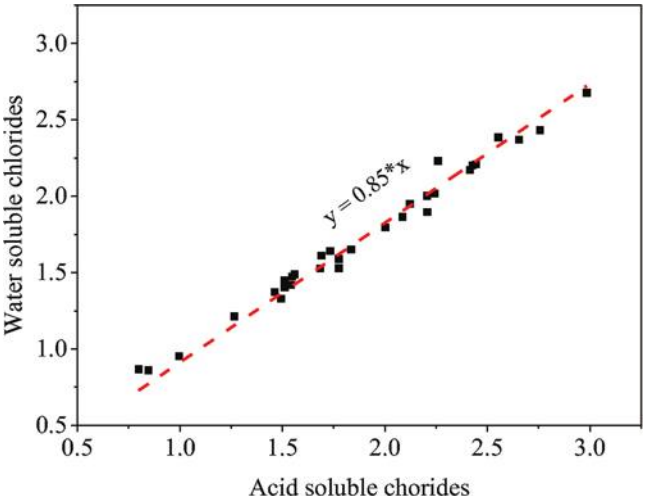

Fig. 3—Correlation between acid- and water-soluble chlorides for OPC-only systems.

Distributions of C_{admix} and C_{crit}

The P_f depends on the CoV of the C_{admix} and C_{crit} data sets. The eventual C_{limit} values determined herein are determined from quantifying the admixed chlorides, C_{admix}, from a set of 81 concrete specimens. C_{crit} data are obtained from testing 54 concrete specimens (Halmen and Adil 2020). Using these data sets for C_{admix} and C_{crit}, C_{limit} values can be determined for different risk preferences—that is, different P_f values. In this analysis, the authors retain the same distribution and CoV for C_{admix} and then vary the mean values (μ_{admix}) to identify an acceptable probability of failure, P_f, to define the C_{limit} for concrete exposed to moisture containing no chlorides (that is, $C_{limit\text{-}wet}$). To determine the CoV, data sets of both C_{admix} and C_{crit} concentrations are required. The distributions of the C_{admix} and C_{crit} data can be assessed by constructing histograms. Figure 4 shows the distributions of C_{admix} and C_{crit}. It

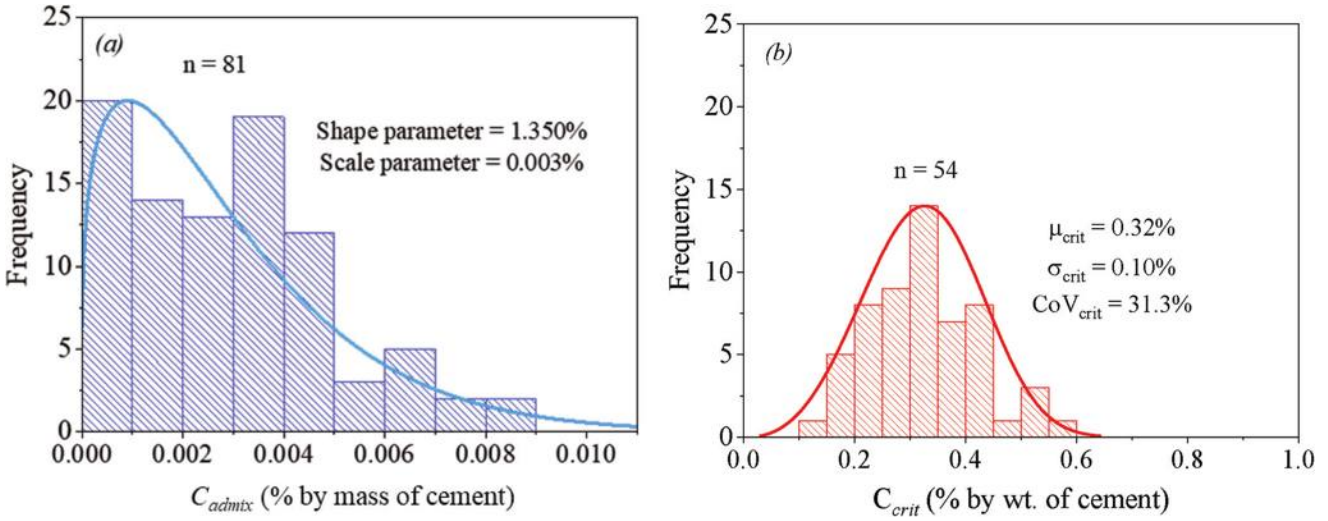

Fig. 4—C_{admix} *and* C_{crit} *distributions for OPC systems.*

can be clearly seen that the distribution of C_{admix} is skewed to the left, indicating that it is a non-normal distribution. This was confirmed using the Kolmogorov-Smirnov (KS) test. Unlike the C_{admix} data, the distribution for C_{crit} appears normal and this was affirmed using the KS test for normality. The CoV_{crit} is estimated to be 31.3%, as shown in Fig. 4(b).

As noted earlier, the LSD approach is valid only if both underlying distributions are normal. CoV_{admis} cannot be estimated from the data set shown in Fig. 4(a). Therefore, the C_{admix} data set needs to be transformed to mimic a normal distribution using the Box-Cox transformation approach. This is presented next.

Normal approximation of data sets

The LSD approach presented is valid only if the underlying distributions (that is, C_{admix} and C_{crit}) are normally distributed. Although central limit theorem states that data in sufficiently large numbers (that is, greater than 1000) are normally distributed, such large data sets are seldom available. Normality is an important assumption for many statistical parametric tests (including determining the reliability index and failure). Therefore, because the C_{admix} distribution is skewed (that is, not normal), the results obtained from Eq. (4) and hence, Eq. (7) will be inaccurate if these data are used as-is.

One technique to transform the non-normal C_{admix} distribution to a normal distribution is to use the Box-Cox transformation. This transformation technique involves applying a factor, λ, to transform the data so that it mimics a normal distribution. The value of λ corresponding to a non-normal dataset can be determined using the following equation

$$y(\lambda) = \begin{cases} \dfrac{y^{\lambda} - 1}{\lambda} & \lambda \neq 0 \\ \log(y) & \lambda = 0 \end{cases} \quad (8)$$

where y is the data set to be transformed. Based on the factor λ, the Box-Cox approach specifies the most appropriate transformation for the data set. The value of λ can range between –3 and 3 and each value corresponds to a specific transformation.

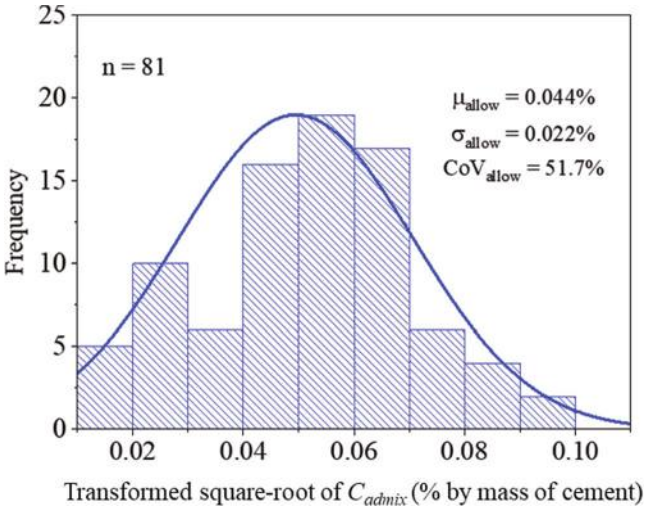

Fig. 5—Transformed C_{admix} *distribution for OPC system.*

Using Eq. (8), λ was determined to be 0.51 for the C_{admix} dataset. For a λ value of approximately 0.5, a square root transformation is recommended. The transformed C_{admix} dataset is shown in Fig. 5. It can be seen that this new distribution is not skewed. The normality of the transformed distribution was assessed using the KS test and the p-value associated with the test indicates the transformed distribution is normal. The CoV_{admix} is estimated to be 51.7% as shown in Fig. 5. Q-Q plots confirmed the normality of the transformed data set.

Probability of failure using LSD approach

The LSD approach can be used to calculate the P_f associated with a range of mean C_{admix} and mean C_{crit} values. Table 6 shows the P_f values for select mean C_{crit} and C_{admix} values. Note that only a fraction of the P_f data are shown in Table 6 and this table can be expanded along both dimensions. As discussed, the ranges of C_{admix} and C_{crit} are dependent on many factors. Also, to determine P_f in Table 6, a CoV_{admix} value of 51.7% and a CoV_{crit} value of 31.3% are used, as determined earlier. Note that this table is applicable for these conditions only. This table can be used in two ways:

Table 6—Probability of corrosion corresponding to mean C_{admix} and mean C_{crit} values

Admixed chlorides (C_{admix}, % by wt. of cementitious materials)	Critical chloride threshold (C_{crit}, % by wt. of cementitious materials)										
	0.26	0.27	0.28	0.29	0.3	0.31	0.32	0.33	0.34	0.35	0.36
0.068	0.0152	0.0137	0.0124	0.0113	0.0103	0.0095	0.0088	0.0082	0.0076	0.0071	0.0067
0.07	0.0164	0.0148	0.0134	0.0122	0.0111	0.0102	0.0094	0.0088	0.0082	0.0076	0.0071
0.072	0.0178	0.0160	0.0145	0.0131	0.0120	0.0110	0.0101	0.0094	0.0087	0.0081	0.0076
0.074	0.0193	0.0173	0.0156	0.0142	0.0129	0.0118	0.0109	0.0101	0.0093	0.0087	0.0081
0.076	0.0209	0.0187	0.0168	0.0152	0.0139	0.0127	0.0117	0.0108	0.0100	0.0093	0.0087
0.078	0.0225	0.0202	0.0181	0.0164	0.0149	0.0136	0.0125	0.0115	0.0107	0.0099	0.0092
0.08	0.0243	0.0217	0.0195	0.0176	0.0160	0.0146	0.0134	0.0123	0.0114	0.0106	0.0098
0.082	0.0262	0.0234	0.0210	0.0189	0.0172	0.0156	0.0143	0.0132	0.0122	0.0113	0.0105
0.084	0.0282	0.0251	0.0225	0.0203	0.0184	0.0168	0.0153	0.0141	0.0130	0.0120	0.0111
0.086	0.0303	0.0270	0.0242	0.0218	0.0197	0.0179	0.0164	0.0150	0.0138	0.0128	0.0118
0.088	0.0325	0.0290	0.0259	0.0233	0.0211	0.0192	0.0175	0.0160	0.0147	0.0136	0.0126
0.09	0.0349	0.0310	0.0278	0.0249	0.0225	0.0205	0.0186	0.0171	0.0157	0.0145	0.0134
0.092	0.0373	0.0332	0.0297	0.0267	0.0241	0.0218	0.0199	0.0182	0.0167	0.0154	0.0142
0.094	0.0399	0.0355	0.0317	0.0285	0.0257	0.0233	0.0212	0.0193	0.0177	0.0163	0.0151
0.096	0.0427	0.0379	0.0339	0.0304	0.0274	0.0248	0.0225	0.0206	0.0189	0.0173	0.0160
0.098	0.0455	0.0404	0.0361	0.0324	0.0292	0.0264	0.0240	0.0219	0.0200	0.0184	0.0170
0.1	0.0485	0.0431	0.0384	0.0345	0.0310	0.0281	0.0255	0.0232	0.0213	0.0195	0.0180
0.102	0.0516	0.0458	0.0409	0.0367	0.0330	0.0298	0.0271	0.0246	0.0225	0.0207	0.0190
0.104	0.0549	0.0487	0.0435	0.0389	0.0350	0.0317	0.0287	0.0261	0.0239	0.0219	0.0202
0.106	0.0582	0.0517	0.0461	0.0413	0.0372	0.0336	0.0304	0.0277	0.0253	0.0232	0.0213
0.108	0.0618	0.0549	0.0489	0.0438	0.0394	0.0356	0.0322	0.0293	0.0268	0.0245	0.0225
0.11	0.0654	0.0581	0.0518	0.0464	0.0417	0.0377	0.0341	0.0310	0.0283	0.0259	0.0238
0.112	0.0692	0.0615	0.0549	0.0491	0.0442	0.0399	0.0361	0.0328	0.0299	0.0274	0.0251
0.114	0.0731	0.0650	0.0580	0.0519	0.0467	0.0421	0.0381	0.0347	0.0316	0.0289	0.0265

1% P_f line

2% P_f line

2.5% P_f line

5% P_f line

4% P_f line

3% P_f line

1. To specify C_{limit} values based on C_{admix} and C_{crit} values and an acceptable P_f; or

2. To determine P_f associated with certain C_{admix} and C_{crit} values.

The authors show additional "step" lines in Table 6 to identify the 1, 2, 3, 4, and 5% P_f values. It should be noted that this probability of corrosion is the probability of corrosion resulting from the admixed chlorides when both moisture and oxygen are available and therefore, the C_{limit} value determined is associated with the $C_{limit\text{-}wet}$ condition.

The first step line in Table 6 indicates acceptable $C_{limit\text{-}wet}$ values for a P_f of 1%. From Table 6, for a C_{crit} value of 0.32% by mass of cement (as reported by Halmen and Adil [2020]), the mean $C_{limit\text{-}wet}$ value must be less than 0.07% to not exceed a P_f of 1%. For the same C_{crit} value, the mean $C_{limit\text{-}wet}$ value must be less than 0.128% to not exceed a P_f of 5%. To limit the risk of active corrosion within 2.5%, it is recommended to specify $C_{limit\text{-}wet}$ values to within the shaded grey region.

Note that the values of $C_{limit\text{-}wet}$ and C_{crit} are mean values, and these mean values are significantly different than the "maximum" values currently required in the ACI documents. For example, a mean maximum value of 0.10 with a CoV of 50% would have an 83rd percentile value of 0.15 and a maximum value of a bit more than this.

Table 6 can also be used to determine the probability of failure associated with different mean C_{admix} and mean C_{crit} values. For example, for a C_{crit} value of 0.36% and a C_{admix} value of 0.10%, the associated probability of failure is 1.80%. It can be clearly seen from the table that the probability of failure increases when the mean values of C_{admix} and C_{crit} become closer in proximity to each other.

The probabilities of failure associated with the C_{limit} values specified in some of the ACI documents are shown in Fig. 6. In this figure, the ACI documents are either marked with a "*w*," which denotes water-soluble chlorides, or an "*a*," which denotes acid-soluble chlorides. For dry conditions shown in Fig. 6(b), the P_f is associated with the RC structure being exposed to moisture at some point during its service life. As noted earlier, there is a lack of consensus among the ACI documents regarding C_{limit} values; therefore, the P_f associated with each value differs. It can be seen in Fig. 6 that P_f values range between 1.34 and 100% depending on the limits specified for RC in wet and dry conditions with no external chlorides (but with some intermittent exposure to moisture) in the ACI documents. To overcome these

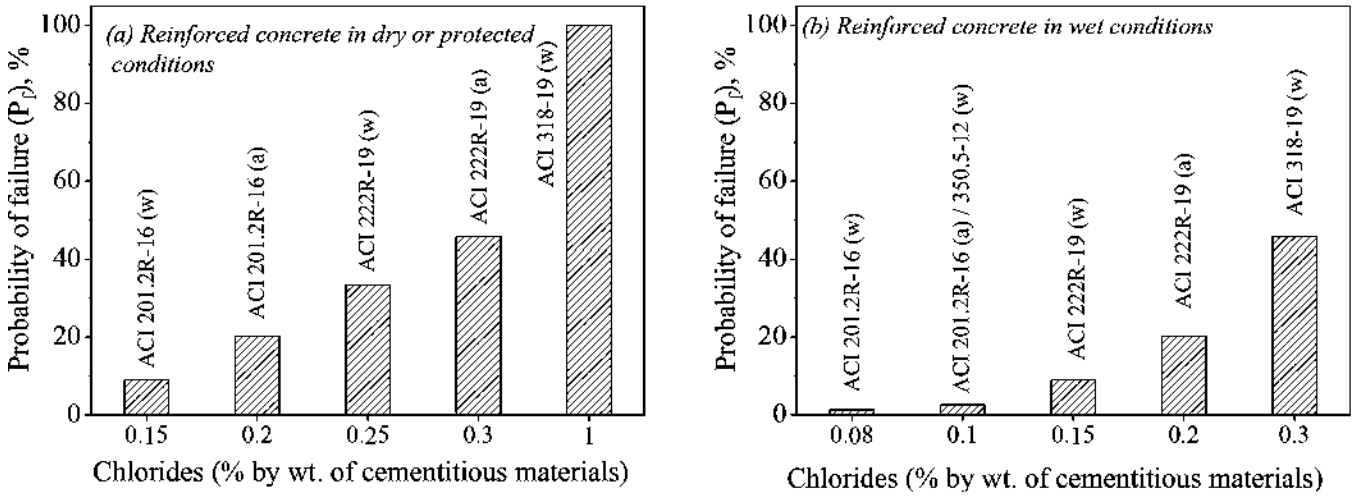

Fig. 6—Probabilities of failures for C_{limit} *specified in some ACI documents (assuming* C_{crit} *of 0.32% and OPC-based systems).*

Table 7—Proposed exposure classifications and C_{limit} values for OPC-based systems containing conventional reinforcement

Exposure classification	Reason for exposure classification	Some typical conditions	Maximum mean water-soluble chlorides*,†, C_{limit}
CS0	No O_2	RC well below water surface	0.30
	No H_2O	Interior RC that will never have sufficient moisture to result in corrosion	
CS1	No chlorides present, but O_2 and H_2O present	RC below freshwater surface but close to surface such that water contains O_2; RC in fresh water splash zone	0.10
CS2	O_2, H_2O, and moderate Cl^- present, slow Cl transport	RC below brackish water surface but close to surface such that water contains O_2; coastal atmospheric conditions (that is, airborne chlorides)	0.08
CS3	O_2, H_2O, and moderate to high Cl^- present, slow to fast Cl^- transport	RC in brackish water splash zone; RC below seawater surface but close to surface such that water contains O_2	0.08
CS4	O_2, H_2O, and high Cl^- present, fast Cl transport	RC in seawater splash zone; RC structures exposed to less than 10 applications of anti-icers or deicers per annum	0.08
CS5	O_2, H_2O, and high Cl^- present, fast Cl transport	RC structures exposed to more than 10 applications of anti-icers or deicers per annum	0.06

*Denoted in percent by mass of cementitious materials; for calculation of normalized chloride concentration, mass of SCM cannot exceed mass of cement.

†Testing to be performed on concrete of ages between 28 and 42 days as per ASTM C1218, minimum of three samples is required.

inconsistencies in the ACI documents, a unified, systematic, probabilistic framework is developed to quantify and specify chloride limits in concrete. Standardization of exposure classifications, C_{limit} values, testing methods, normalization of chloride concentration, and terminology is essential. Deem-to-satisfy requirements, such as maximum water-cementitious materials ratio, should be developed by appropriate committees for these exposure classifications.

Recommendations provided by the authors for C_{limit} limits are shown in Table 7. In the first scenario (no oxygen present) and the second scenario (no moisture present), a C_{limit} value of 0.30% is recommended; this value is slightly lower than the C_{crit} (0.32%) as determined by Halmen and Adil (2020). Although corrosion will generally not occur under these dry scenarios, there is a likelihood that these conditions could change during the service life of the structure. Therefore, to minimize the risk of active corrosion, it is recommended to specify a C_{limit} that is slightly lower than the C_{crit}. For the next two scenarios, where oxygen and moisture are present, but no external chlorides are present, a C_{limit} of 0.10% is recommended. Note that this corresponds to an approximate P_f of 2.5%. Other P_f values could be selected, and discussion among ACI committees is needed to identify an acceptable P_f. For other scenarios, where oxygen, moisture, and external chlorides are present, C_{limit} values are specified based on the logic that $C_{limit\text{-}wet+cl} \le C_{limit\text{-}wet} \le C_{limit\text{-}dry}$. A summary of this work and recommendations are presented in the next section.

SUMMARY AND RECOMMENDATIONS

Current ACI documents provide a wide range of allowable chloride limits (C_{limit}) for new concrete. Not only do these limits vary, but the exposure classifications, the tests required to quantify the chlorides, the normalization of chloride contents, and the terminology used in the documents vary. In addition, no information is provided on the number of samples that need to be tested to verify whether C_{admix} is less than C_{limit}. Because C_{limit} values should be based on exposure conditions, ACI documents should standardize consistent exposure classifications across all documents. These exposure classifications should be based on

fundamental requirements of the electrochemical process. This paper presented standardized exposure classifications based on electrochemical fundamentals and identified six exposure classifications.

This paper also presented a limit state design (LSD) approach to defining C_{limit} values. This approach identified the risk of corrosion resulting from admixed chlorides in concrete exposed to wet conditions containing no chlorides. This paper recommends that the C_{limit} for dry conditions, $C_{limit\text{-}dry}$, not exceed the C_{crit} value as the designer or builder can seldom ensure that the concrete at some point in its service life will not be exposed to moisture. Lastly, this paper recommends that $C_{limit\text{-}wet+cl}$ be less than $C_{limit\text{-}wet}$. Using these three criteria, C_{limit} values are recommended for each of the six exposure classifications.

This research also identified other discrepancies in the ACI documents, and the authors recommend standardizing the method used to quantify chlorides in concrete, standardizing the normalization procedure of the chloride concentration, standardizing the number of samples to be tested, and unifying the terminology used to define the C_{limit} values. The authors recommend standardizing these throughout all ACI documents.

Based on the information presented in this paper, the following recommendations are proposed:

1. Standardize exposure classifications throughout all ACI documents based on the proposed electrochemistry-based criteria;

2. Specify uniform C_{limit} values in all ACI documents using the proposed LSD approach;

3. Require that chloride testing in all ACI documents use the water-soluble chloride test method (ASTM C1218) when chlorides are not present in the coarse aggregate; when chlorides are present in the coarse aggregate, allow the use of ASTM C1218 and C1524;

4. Standardize how the chloride concentration is determined throughout all ACI documents; the chloride content should be normalized as a percentage by mass of total cementitious materials and for calculation purposes, the mass of the supplementary cementitious materials (SCMs) in the cementitious materials should not exceed the mass of the ordinary portland cement (OPC), and;

5. Use consistent terminology throughout all ACI documents when referring to maximum allowable chlorides in new concrete; the term "maximum ***mean*** water-soluble chlorides" should be used to specify C_{limit} values.

It is hoped that the systematic and science-based approaches used herein to define exposure conditions and allowable chloride limits will provide a sound foundation for achieving consensus within the ACI documents. As with all research, as new data become available, new analyses should be performed.

AUTHOR BIOS

David Trejo, *FACI, is Professor and Hal D. Pritchett Endowed Chair in the School of Civil and Construction Engineering at Oregon State University, Corvallis, OR. He is a past Chair and past member of ACI Committee 222, Corrosion of Metals in Concrete, and a member of ACI Committees 201, Durability of Concrete, and 236, Material Science of Concrete. His research interests include corrosion of steel in cementitious materials, service-life analyses, innovative concrete materials and systems for improved construction and performance, and modeling deterioration mechanisms.*

Gokul Dev Vasudevan *is a Graduate Faculty Lecturer in the School of Environmental, Civil, Agricultural, and Mechanical Engineering at the College of Engineering at the University of Georgia, Athens, GA. His research interests include cement and concrete decarbonization, pathways to carbon neutrality of cement and concrete industry, and civil engineering pedagogy.*

REFERENCES

ACI Committee 201, 2016, "Guide to Durable Concrete (ACI 201.2R-16)," American Concrete Institute, Farmington Hills, MI, 84 pp.

ACI Committee 222, 2019, "Guide to Protection of Reinforcing Steel in Concrete Against Corrosion (ACI 222R-19)," American Concrete Institute, Farmington Hills, MI, 60 pp.

ACI Committee 301, 2020, "Specifications for Concrete Construction (ACI SPEC-301-20)," American Concrete Institute, Farmington Hills, MI, 69 pp.

ACI Committee 318, 2019, "Building Code Requirements for Structural Concrete (ACI 318-19) and Commentary (ACI 318R-19) (Reapproved 2022)," American Concrete Institute, Farmington Hills, MI, 624 pp.

ACI Committee 329, 2014, "Report on Performance-Based Requirements for Concrete (ACI 329R-14)," American Concrete Institute, Farmington Hills, MI, 46 pp.

ACI Committee 350, 2020, "Code Requirements for Environmental Engineering Concrete Structures (ACI 350-20) and Commentary (ACI 350R-20)," American Concrete Institute, Farmington Hills, MI. 553 pp.

ACI Committee 350, 2012, "Specifications for Environmental Concrete Structures (ACI SPEC-350.5-12)," American Concrete Institute, Farmington Hills, MI, 60 pp.

Ahmed, A., and Trejo, D., 2023, "Quantifying the Conservativeness of Water-Soluble Chloride Testing," *ACI Materials Journal*, V. 120, No. 2, Mar., pp. 13-24

ASTM C1152/C1152M-20, 2020, "Standard Test Method for Acid-Soluble Chloride in Mortar and Concrete," ASTM International, West Conshohocken, PA, 4 pp.

ASTM C1218/C1218M-20, 2020, "Standard Test Method for Water-Soluble Chloride in Mortar and Concrete," ASTM International, West Conshohocken, PA, 3 pp.

ASTM C1524/C1524M-20, 2020, "Standard Test Method for Water-Extractable Chloride in Aggregate (Soxhlet Method)," ASTM International, West Conshohocken, PA, 5 pp.

Azad, V. J., and Isgor, O. B., 2016. "A Thermodynamic Perspective on Admixed Chloride Limits of Concrete Produced with SCMs," *Chloride Thresholds and Limits for New Construction*, SP-308, American Concrete Institute, Farmington Hills, MI, pp. 1-18.

Chopperla, K. S. T.; Smith, S.; Drimalas, T.; Vaddey, N. P.; Bentivegna, A.; Kurtis, K. E.; Thomas, M. D. A.; and Ideker, J. H., 2022, "Unified Durability Guidance in ACI Committee Documents," *ACI Materials Journal*, V. 119, No. 2, Mar., pp. 29-41.

Halmen, C., and Adil, P., 2021, "A Collaborative Study for the Development of a Standard Critical Chloride Threshold Test Method," Concrete Research Council, ACI Foundation, Farmington Hills, MI, 183 pp.

Trejo, D.; Vaddey, N. P.; and Shakouri, M., 2019, "Factors Influencing Chloride Test Results of Different Cementitious Systems," *ACI Materials Journal*, V. 116, No. 1, Jan., pp. 135-145. doi: 10.14359/51712240

Trejo, D.; Vaddey, N. P.; and Halmen, C., 2021, "Standardizing Test to Quantify Chloride Threshold of Steel in Concrete," *ACI Materials Journal*, V. 118, No. 1, Jan., pp. 177-187.

Vaddey, N. P.; Trejo, D.; and Shakouri, M., 2020, "Predicting Chloride Testing Outcome of Different Cementitious Systems," *ACI Materials Journal*, V. 117, No. 1, Jan., pp. 139-151. doi: 10.14359/51719149

ACI MATERIALS JOURNAL TECHNICAL PAPER

Title No. 121-M02

Performance of Quality-Controlled Recycled Concrete Aggregates

by Amit Kumar, Gyani Jail Singh, Priyanshu Raj, and Rajesh Kumar

This research examines the performance of quality-controlled recycled concrete aggregates (QRAs) with fly-ash-based cement. Compared to concrete made from untreated recycled concrete aggregates (URC), quality-controlled recycled aggregate concrete (QRC) has superior physical, mechanical, and durability properties. Except for sorptivity, the physical, mechanical, and durability properties of QRC are almost identical to those of natural aggregate concrete (NC). The compressive strength, splitting tensile strength, flexural strength, fracture energy, and modulus of elasticity of QRC are higher than those of URC by 18.0%, 16.8%, 60.0%, 27.17%, and 43.46%, respectively. The abrasion resistance of QRC is approximately 60% higher than URC. Scanning electron microscope (SEM) image and energy-dispersive X-ray (EDX) analysis prove that quality control produces denser old interfacial transition zones (OITZ) with fewer microvoids. The QRA improves not only the pore structure but also the weak mortar structure attached to the aggregate. There is also a strong correlation between the compressive strength and splitting tensile strength, flexural strength, fracture energy, and modulus of elasticity of QRC. QRA can be used to compute the mixture proportions for concrete (certainly up to medium-strength concrete) according to either the Indian standard or the international standard. It is challenging to improve the sorptivity of recycled concrete aggregates closer to NC. In addition, QRC has an initial sorptivity of two times (initial) and a final sorptivity of 1.8 times higher than NC, whereas URC has an initial sorptivity of 3.5 times (initial) and a final sorptivity of 2.35 times higher than NC.

Keywords: durability; mechanical properties; mechanical treatment; performance; physical properties; quality control; recycled concrete aggregate (RA).

INTRODUCTION

The quality of recycled concrete aggregate (RA) affects the mechanical and durability properties of recycled aggregate concrete (RC).[1] With low-quality RA and increasing replacement level, RC performance deteriorates.[2,3] Due to the degraded quality of RA by the mortar attached to it, its use is limited to 25% replacement of natural aggregate (NA) in concrete of strength below 35 MPa (5075 psi), as mentioned in different international standards.[4] In general, the physical and mechanical properties of aggregates are critical quality parameters when used in civil engineering.[5] Because there are no specific criteria in the literature regarding RA quality,[4] NA may be considered as a reference. To achieve optimal RA performance, its physical and mechanical properties may be improved in the same range as specified for NA.

Removal of mortar by mechanical treatment is one of the methods to improve the physical and mechanical properties of RA.[1,6-11] Purushothaman et al.[7] considered RA abrasion values as a quality criterion for mechanical treatment. By using the mechanical treatment method, researchers have obtained only crushing and abrasion values that are closer to NA. Thus, even RCs with treated RAs have inferior compressive strength and modulus of elasticity (MOE). Moreover, this method was extended to 300 drum revolutions with 12 charges by Pandurangan et al.[8] The bond strength of RC is observed to be significantly lower than natural aggregate concrete (NC), despite its compressive strength being close to that of NC. According to the literature, some researchers randomly selected 12 charges and 500 drum revolutions for the mechanical treatment of RA without specifying any criteria.[9] The authors achieved only up to a 40% replacement of NA with treated RA without varying concrete tensile and compressive strength.

Alqarni et al.[10] used 150, 300, and 450 drum revolutions for eight charges with a diameter of 60 mm (2.36 in.) for mechanical treatment and assumed RA grading as a quality parameter. Considering this, the authors could not reach the target strength of the concrete mixtures at a replacement level of more than 33% by RA. In addition, an unreasonable quality parameter of reducing the water absorption of RA to less than 1% was suggested by Dilbas et al.[11] Controlled water absorption of RA is crucial to RC's workability, mechanical properties, water-cement ratio (w/c), and durability properties.[12] Meanwhile, international standards specify a 0.5 to 4% water absorption range for NA.[13] Therefore, RA need not have a water absorption below 1% to achieve the desired strength and durability properties. When RA is mechanically treated to lower its water absorption below 1%, its other properties, particularly its crushing and impact properties, may be severely affected. Additionally, lowering the water absorption below 1% by mechanical treatment cannot be applied to all types of RA, mainly those containing parent aggregates that are relatively weak in impact and crushing.

In another way, lowering the mortar-covered and mortar-only aggregate parts makes it possible to bring the water absorption of RA below 1%. The process will undoubtedly reduce the productivity of RA, which will increase production costs. To achieve the desired physical, mechanical, and durability properties of an NC, the physical and mechanical properties of NA meet some specific criteria set

ACI Materials Journal, V. 121, No. 1, January 2024.

MS No. M-2022-260.R4, doi: 10.14359/51740259, received July 1, 2023, and reviewed under Institute publication policies.

by different national and international standards. Therefore, a quality control process must include water absorption, specific gravity, crushing values, impact values, abrasion values, flakiness index (shape), and elongation index (size) as quality parameters. Therefore, Dilbas et al.'s[11] approach may not be considered a universal quality control method. This approach replaced only 60% of the NA with the treated RA in the concrete without degrading its properties. Consequently, a random selection of some physical or mechanical properties of RA as quality parameters or drum revolutions and charges in mechanical treatment results in a limited number of other properties within NA's limits. Thus, the inferior quality of RA produces RC with mechanical and durability properties lower than NC.

According to some authors, the high water absorption of RA significantly impacts the workability, mechanical properties, *w*/*c*, and durability of RC.[11,12,14,15] Water absorption of more than 3% may be considered high water absorption, and up to or below 3% may be considered controlled water absorption of RA.[4] The water absorption capacity of RA changes when exposed to cement paste.[16] Despite additional water added, the oven-dried RA may never have reached the saturated surface-dry (SSD) condition, and the excess amount of water may not be completely absorbed by it.[15] As a result, the effective *w*/*c* increases in the concrete.[12] The 80% SSD state of RA results in the best compressive strengths in the concrete compared to SSD, and then the oven-dried condition.[15] According to Mefteh et al.,[17] RA with controlled water absorption and air-dry state produced the most effective concrete strength.

Thus, the controlled water absorption of RA is necessary to achieve its highest performance because it reduces the total amount of water (which is to be absorbed) by a significant extent. According to Poon et al.,[18] when recycled aggregate is used in a dry state (air-dried) as a replacement for NA, the workability of fresh concrete and the compressive strength of hardened concrete are almost unchanged compared to NC. Additionally, a two-stage mixing approach (TSMA) with partially saturated recycled aggregate is recommended to solve the higher water absorption setbacks of RA.[15] Furthermore, fly-ash-based cement improved RC's physical, mechanical, and durability properties.[19,20] Bhasya and Bharatkumar[21] also investigated the mechanical and durability properties of RC made from 100% treated RA. However, the authors could not achieve NC-like durability or mechanical properties for RC. These properties have been improved by increasing the binder content and reducing the water-binder ratio (*w*/*b*) in the concrete. Therefore, by improving RA quality, RC may achieve NC-like properties with fly-ash-based cement. The specific objective of the current research is as follows.

- Identification of the physical and mechanical properties of concrete composed of untreated recycled concrete aggregate (URC).
- Quality control of mechanically treated recycled concrete aggregate (TRA).
- Developing an RC consisting of TRA (quality-controlled) at a 100% replacement level with fly-ash-based cement.
- Determine the performance of concrete composed of quality-controlled TRA compared to URC and NC.

RESEARCH SIGNIFICANCE

Despite repeated attempts, most studies have failed to obtain either the mixture proportions' target strength or the desired mechanical and durability properties of concrete using RAs as effectively as in the case of NA concrete. Different national and international standards specify certain minimum quality criteria for NAs to estimate the mixture proportions of concrete. The present research is intended to identify whether the quality control of RA meets the code mixture proportions criteria. Furthermore, according to the present research, if the physical and mechanical properties of RAs are within the range provided by the codes for NA, RC will have comparable performance to NA concrete, except for sorptivity. Sorptivity is a major concern for RC. Besides the microcracks and porosity found in adhered mortar, RC's sorptivity is influenced to a great extent by the chemical composition of the adhered mortar. To improve RC's sorptivity, additional treatments may be required for RA.

RESEARCH METHODOLOGY

Quality control by mechanical treatment

The RA is constructed from concrete cubes cast at different but fixed locations (construction sites) and brought to the National Institute of Technology Patna's laboratory in India. In a laboratory jaw crusher, concrete cubes are crushed to a maximum size of 22 mm (0.78 in.). In this case, the RA is referred to as untreated recycled concrete aggregate (URA). Crushed samples have a strength of 30 to 55 MPa (4351 to 7977 psi) and have been aged between 2 and 3 years. Mechanical treatment is performed by ball milling (Los Angeles) involving different charges and drum revolutions. The aggregate is sieved using sieves conforming to Indian standards of 4.75 and 20 mm (0.18 and 0.78 in.) after treatment. After mechanical treatment, the characteristics of TRA are shown in Table 1 for 28 combinations of charges and drum revolutions. The TRA*ij* denotes the aggregate treated at a certain combination of charges and drum revolutions at 5 kg (11 lb) URA feeding, where i (= 0, 3, 5, 7, 9, 10, 11) is the number of charges and j ($2 \leq j \leq 5$) denotes the number of drum revolutions in hundreds.

A multi-criteria decision-making technique, such as the Technique for Order of Preference by Similarity to Ideal Solution (TOPSIS) (Fig. 1), is employed to ensure consistency of quality control during mechanical treatment.[22] The TRA*ij* quality determining factors include water absorption, specific gravity, crushing value, impact value, flakiness index, elongation index, and machine performance (mortar removed) for each combination of charges and drum revolutions (Table 1). Various combinations of charges and drum revolutions are examined as alternatives, and TRA*ij* quality-determining parameters are considered as responses. A decision matrix is formed considering alternatives as rows and responses as column elements. Each of these properties is given a weight (W_j) of 0.20, 0.25, 0.25, 0.15, 0.05, 0.05, and 0.05, respectively, to assess the mathematical impact of the responses on the performance index (PI) of each alternative.

Table 1—Physical and mechanical properties of recycled concrete aggregate after mechanical treatment, and machine performance

	Physical properties				Mechanical properties		Machine performance
TRA*ij*	Specific gravity	Water absorption, %	Flakiness index, %	Elongation index, %	Crushing value, %	Impact value, %	% removed mortar
URA	2.56	4.24	9.92	29.10	31.21	26.51	—
TRA02	2.56	3.10	14.77	21.00	24.62	20.59	14.34
TRA03	2.57	3.03	12.39	30.59	24.49	19.59	14.47
TRA04	2.57	3.13	17.45	25.78	23.34	18.82	17.78
RA05	2.59	2.50	11.75	22.52	22.76	18.28	21.86
TRA32	2.65	3.00	8.39	19.20	24.81	20.47	18.03
TRA33	2.55	3.15	8.34	22.04	21.56	20.41	26.18
TRA34	2.57	2.98	10.47	19.20	21.41	19.52	28.87
TRA35	2.64	2.31	12.25	16.30	21.81	18.63	31.13
TRA52	2.63	2.73	10.86	25.88	23.45	18.49	25.86
TRA53	2.65	1.84	13.45	18.81	20.04	16.67	31.92
TRA54	2.69	1.95	10.44	17.81	20.11	16.01	36.99
TRA55	2.73	1.91	12.28	18.51	20.35	13.22	41.50
TRA72	2.59	2.05	12.18	26.67	22.02	15.56	29.20
TRA73	2.71	2.34	11.45	28.89	19.80	12.64	35.89
TRA74	2.63	1.95	9.68	15.60	19.26	13.89	39.93
TRA75	2.79	1.00	14.25	18.31	18.63	12.05	52.99
TRA92	2.71	2.47	7.50	29.41	21.22	16.28	31.52
TRA93	2.67	2.84	9.24	23.30	21.15	14.20	37.43
TRA94	2.71	1.25	18.09	27.93	19.14	9.80	52.64
TRA95	2.75	1.02	12.89	19.62	17.44	11.42	56.23
TRA102	2.60	2.98	7.03	14.83	20.83	16.67	27.15
TRA103	2.63	3.18	9.05	22.08	21.53	17.09	45.67
TRA104	2.74	1.78	7.31	20.18	19.78	13.66	49.53
TRA105	2.77	1.91	8.33	9.53	17.67	13.36	50.56
TRA112	2.63	2.58	8.28	22.54	23.22	16.76	31.27
TRA113	2.70	2.58	8.73	14.38	20.15	12.77	42.14
TRA114	2.66	2.41	4.18	17.72	19.22	15.42	48.37
TRA115	2.71	1.84	5.47	10.50	17.98	13.69	53.36

Note: TRA*ij* is combination of balls and drum revolutions in mechanical treatment, where *i* denotes number of balls ($i = 0, 3, 5, 7, 9, 10, 11$) and *j* denotes number of revolutions in hundreds ($2 \le j \le 5$).

After multiplying the normalized decision matrix with the assigned weight coefficient, a weighted decision matrix is obtained. Then, the most ideal and least ideal solutions are found from the weighted normalized matrix for every response. The PI—that is, the relative closeness coefficient for each alternative—is evaluated based on the most optimal and least ideal solution of the responses.

Based on the performance of the responses corresponding to each alternative, the multi-criteria decision-making technique provided ranking to a TRA*ij*, as shown in Fig. 2. The PI is strongly correlated with TRA*ij* quality parameters. An alternative consisting of a higher PI may represent the most effective combination of charges and drum revolutions for the mechanical treatment. As coarse aggregates, the ranks one, two, and three of TRA*ij* may be assumed to be the most effective quality-controlled recycled concrete aggregate (QRA). The QRA consisting of ranks one, two, and three is abbreviated as QRA1, QRA2, and QRA3 in the following.

Experimental program

In the subsequent paragraphs, the mixture proportions composed of NA, URA, QRA1, QRA2, and QRA3 will be abbreviated as NC, URC, QRC1, QRC2, and QRC3. The particle-size distributions of NA, URA, QRA1, QRA2, and QRA3 are shown in Fig. 3(a). Before preparing the concrete, the abrasion values (hardness) of NA, URA, QRA1, QRA2, and QRA3 are verified (Table 2). The values are 15.4%, 37.32%, 18.54%, 22.36%, and 20.80%, respectively.

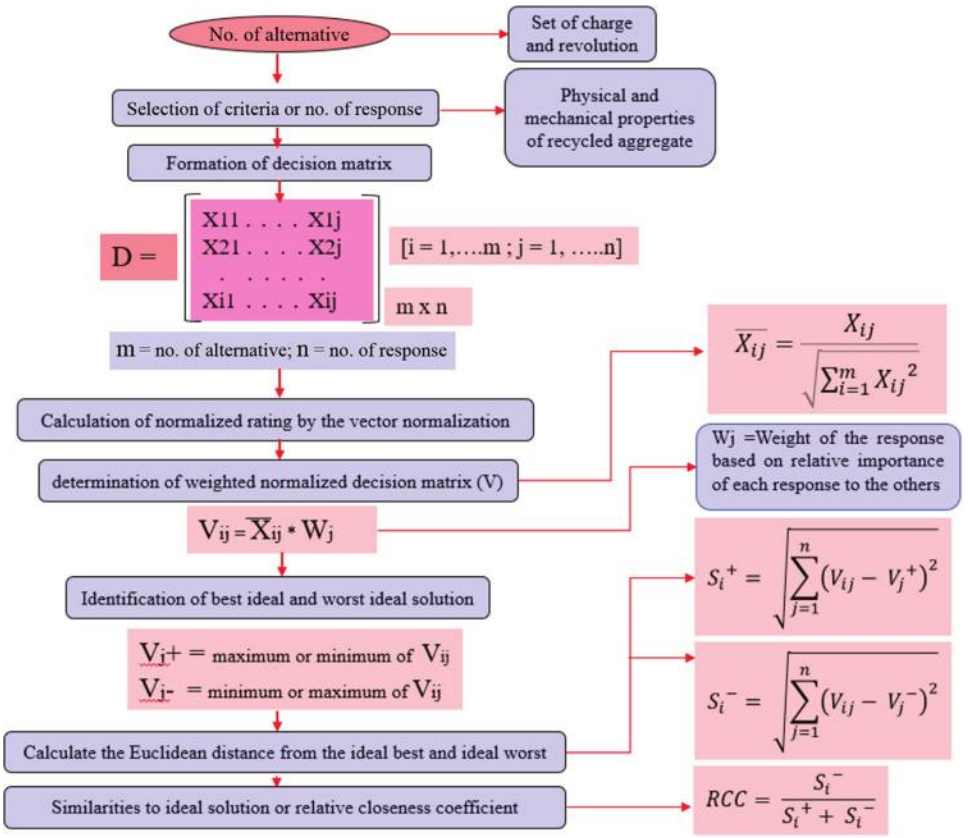

Fig. 1—Detailed formulation of statistical tool TOPSIS.

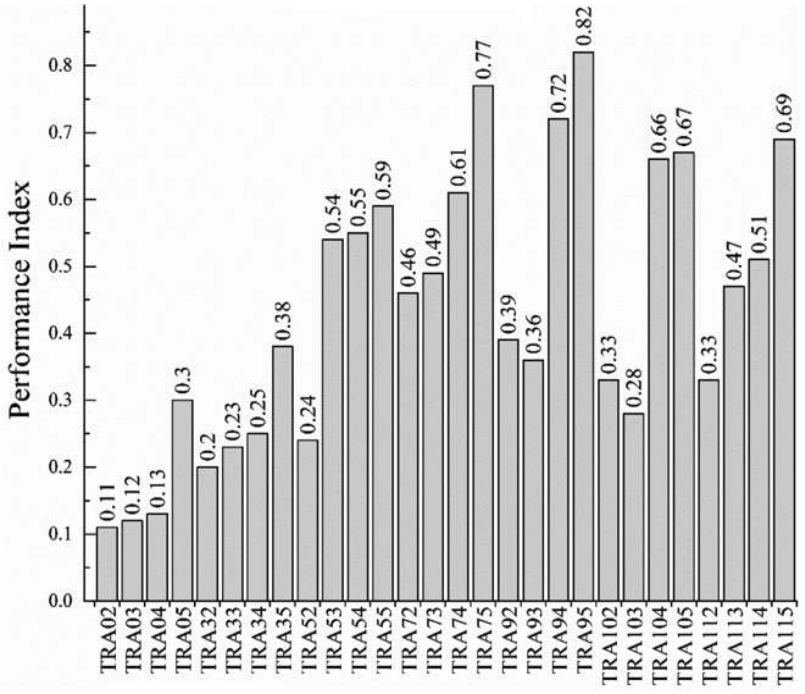

Fig. 2—Performance index of mechanically treated RA.

Therefore, QRA1, QRA2, and QRA3 have abrasion values under the range specified for NA.[23] River sand (as a fine aggregate), potable water, a high-range water-reducing admixture (HRWRA), and portland pozzolana cement (PPC) (Table 3) are used to prepare the mixture proportions.

The mixture proportions for Grade M45 concrete are prepared using IS 10262:2019[24] with a target strength of 53.25 MPa (7723 psi), a *w/c* of 0.35, and slump of 75 mm (2.95 in.) (Table 4). Several trials are conducted for a slump range of 100 to 125 mm (3.94 to 4.92 in.) to determine the dose of HRWRA because, most of the time, aggregate in

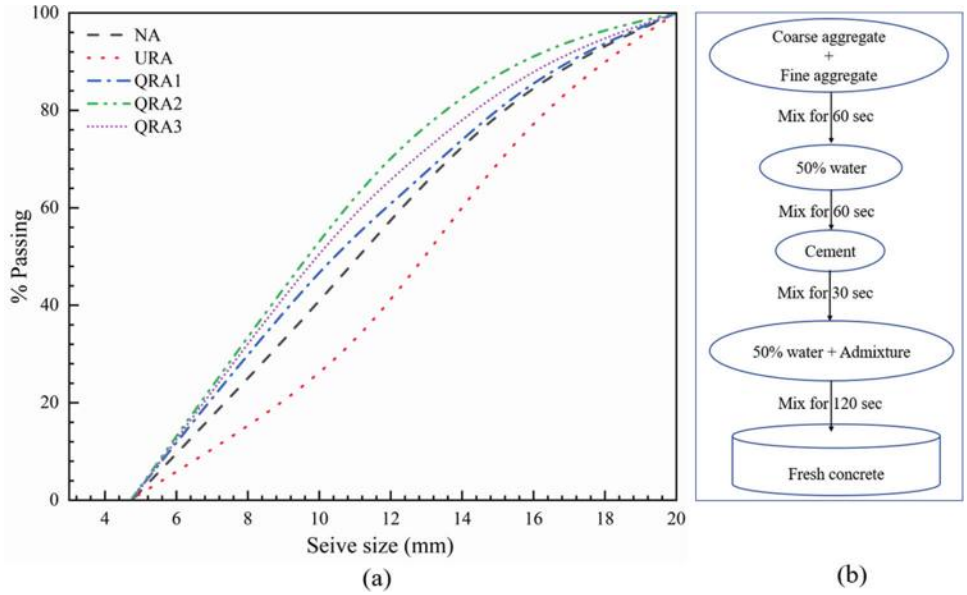

Fig. 3—(a) Gradation curve of NA, URA, QRA1, QRA2, and QRA3; and (b) flowchart of two-stage mixing approach.

Table 2—Physical and mechanical properties of coarse aggregate and physical properties of fine aggregate

Physical properties	Natural aggregate	Recycled aggregate				Fine aggregate (river sand) Zone III
		URA	QRA1	QRA2	QRA3	
Water absorption, %	0.70	4.24	1.02	1.0	1.25	0.4
Specific gravity	2.82	2.56	2.75	2.79	2.71	2.65
Impact value, %	9.44	26.51	11.42	12.05	9.80	—
Crushing value, %	17.21	31.21	17.44	18.63	19.14	—
Abrasion value, %	15.40	37.32	18.54	22.36	20.80	—
Rodded bulk density, kg/m^3 (lb/ft^3)	1536.00 (95.89)	1321.33 (82.48)	1583.33 (98.84)	1556.00 (97.14)	1546.32 (96.53)	—
Void content, %	44.53	48.39	42.43	43.52	42.95	—
Flakiness, %	27.20	9.92	12.89	14.25	18.09	—
Elongation, %	41.19	29.1	19.62	18.31	27.93	—
Fineness modulus	—	—	—	—	—	2

Table 3—Physical properties and strength of PPC

Physical properties and strength	Value/unit
Unit weight	1430 kg/m^3 (89.27 lb/ft^3)
Specific gravity	2.73
Standard consistency	33%
Initial setting time (IST)	2 hours
Final setting time (FST)	4 hours
Soundness (Le Chatelier)	1 mm (0.0394 in.)
Fineness (air permeability)	385 m^2/kg (270,682 in.^{2}/lb)
7-day compressive strength	24.66 MPa (3576 psi)
28-day compressive strength	35.39 MPa (5132 psi)

a dry state is used during construction. Hence, this study focuses on the air-dry state of aggregates during concrete preparation, rather than saturated surface dryness. To maintain the effective *w*/*c*, a water correction is applied for each mixture proportion prepared in an SSD condition. According to Principallo,[12] Mefteh et al.,[17] and Poon et al.,[18] RA in an air-dry state performs better rather than in SSD state. However, to maintain the fresh properties of concrete, the present study closely follows the TSMA proposed by Mi et al.[25] (Fig. 3(b)).

In addition, a motorized rotatory drum is used to produce concrete using a TSMA.[25] Vibrating tables are used to compact samples in molds. Samples are immersed in water for 28 days and cured after being removed from the mold after 24 hours. For each mixture proportion, sample preparation is shown in Table 5. For the experiments, 195 samples were prepared. The average data from three specimens are reported.

Table 4—Mixture proportions of concrete (in SSD condition)

Constituent materials	Weight, kg/m^3 (lb/ft^3)				
	NC	URC	QRC1	QRC2	QRC3
Cement	432.42 (26.99)	432.42 (26.69)	432.42 (26.99)	432.42 (26.99)	432.42 (26.99)
Water	151.35 (9.45)	151.35 (9.45)	151.35 (9.45)	151.35 (9.45)	151.35 (9.45)
Coarse aggregate	1170.02 (73.04)	1062.45 (66.32)	1140.32 (71.18)	1156.91 (72.22)	1123.74 (70.15)
Fine aggregate	693.98 (43.32)	694.18 (43.33)	693.59 (43.29)	693.59 (43.29)	693.59 (43.29)
HRWRA	3.89 (0.24)	3.68 (0.23)	4.32 (0.27)	4.32 (0.27)	4.32 (0.27)

Table 5—Description of specimens and test conducted

Experiments	Test method	Specimen size, mm (in.)	Testing age, days	No. of specimens
Compressive strength	IS 516 (Part 1/Sec 1):2021[26]	Cube, 150 (5.91)	7, 28, 91	9
Splitting tensile strength	ASTM C496/C496M-04[27]	Cylinder, 150 x 300 (5.91 x 11.81)	28	3
Flexural strength	ASTM C78/C78M-18[28]	Prism, 100 x 100 x 500 (3.94 x 3.94 x 19.68)	28	3
Modulus of elasticity, Poisson's ratio, peak strain	ASTM C469-02[29]	Cylinder, 150 x 300 (5.91 x 11.81)	30 to 32	6
Fracture energy (notched beam)	RILEM[30]	Prism, 100 x 100 x 500 (3.94 x 3.94 x 19.68)	28	3
Water absorption, density	ASTM C642-97[31]	Cube, 100 (3.94)	28	3
Sorptivity	ASTM C1585-04[32]	Disc, 100 x 50 (3.94 x 1.97)	29 to 38	3
UPV	IS 516 (Part 5):2018[33]	Cube, 150 (5.91)	28	—
RCPT	ASTM C1202-19[34]	Disc, 100 x 50 (3.94 x 1.97)	28 to 30	3
Drying test	Purushothaman et al.[7]	Cube, 100 (3.94)	28	3
Abrasion test	IS 15658:2006[35]	Cube, 70.6 (2.78)	28 to 29	3
Alkalinity test	Purushothaman et al.[7]	—	28	—

RESULTS AND DISCUSSION

The following section discusses how QRA1, QRA2, and QRA3 perform in concrete. These sections discuss in detail the physical, mechanical, and durability properties of NC, URC, QRC1, QRC2, and QRC3.

Physical properties

Table 2 shows the physical properties of NA, URA, QRA1, QRA2, and QRA3. The rodded bulk density of these aggregates is determined following IS 2386, Part III-1963.[36] The rodded bulk density of URA is significantly lower than NA due to its low specific gravity and high mortar content. In contrast to previous studies,[22] it is clear from the rodded bulk density of QRA1, QRA2, and QRA3 that the mortar attached to the aggregates was removed efficiently, and the residual mortar compacted over the aggregates (Table 2). The lower abrasion value of QRA indicates better mortar removal and compaction of residual mortar. Other physical and mechanical properties of QRA1, QRA2, and QRA3 are within the range specified for NA (Table 2). These observations are consistent with the performance-based quality control approach used in this study. The physical properties of all mixtures are determined according to ASTM C642-97[31] and presented in Table 6. The percent water absorption for NC, URC, QRC1, QRC2, and QRC3 is 4.30, 7.51, 4.29, 4.69, and 4.48%. The water absorption of URC is approximately 1.75 times higher than that of NC and the quality-controlled recycled aggregate concrete (QRC). The QRC samples have water absorption closer to NC with insignificant deviation.

NC, URC, QRC1, QRC2, and QRC3 have a percent void content of 9.96, 16.13, 11.04, 11.03, and 10.53. The bulk density of this concrete is 2304.84, 2161.32, 2311.09, 2281.35, and 2297.53 kg/m^3 (143.88, 134.93, 144.28, 142.42, and 143.43 lb/ft^3), respectively. The bulk density of QRC1, QRC2, and QRC3 is closer to NC; however, the bulk density of URC is significantly lower than that of NC. According to these observations, URC has approximately 62% higher void content than NC. Despite this, QRC has only 6 to 11% more voids than NC. A quality control treatment may improve void content by 51 to 56% in QRC compared to URC by removing weak adhered mortar and refining pore structures in RA. In addition, Bhasya and Bharatkumar[21] obtained 37% lower void content in concrete composed of thermomechanically treated RA than URA. Thus, the quality improvement demonstrated in the present study produces significantly improved bulk density and reduced void content in concrete.

The ultrasonic pulse velocity (UPV) and dynamic MOE are determined following ASTM C597-09[37] and IS 516 (Part 5):2018.[33] The UPV values of the NC, URC, QRC1, QRC2, and QRC3 mixtures are 5.2, 4.7, 5.1, 5.0, and 5.1 km/s (204,724, 185,039, 200,787, 196,850, and 200,787 in./s), respectively (Fig. 4(a)). All these mixtures can be classified as an excellent class as the UPV values of the samples are higher than 4.4 km/s (173,228 in./s). Based on the UPV

Table 6—Physical properties, pH value, and abrasion resistance of concrete

Mixture proportions	Bulk density, kg/m^3 (lb/ft^3)	Water absorption, %	Void content, %	Drying test, % weight loss	pH	Abrasion resistance	
						Volume loss, m^3 (ft^3)	% volume loss
NC	2304.84 (143.88)	4.30	9.96	3.51	12.89	6.07×10^{-6} (214.3×10^{-6})	1.77
URC	2161.32 (134.93)	7.51	16.13	6.65	12.91	9.15×10^{-6} (323.13×10^{-6})	3.94
QRC1	2311.09 (144.28)	4.29	11.04	4.40	12.98	7.22×10^{-6} (254.94×10^{-6})	2.63
QRC2	2281.35 (142.42)	4.69	11.03	3.80	12.87	7.15×10^{-6} (252.49×10^{-6})	2.53
QRC3	2297.53 (143.43)	4.48	10.53	3.87	12.99	5.65×10^{-6} (199.52×10^{-6})	1.56

Table 7—Mechanical properties of concrete

Mixture proportions	Modulus of elasticity, MPa	Poisson's ratio	Peak stress (cylinder), MPa	Peak strain	Dynamic modulus, GPa	Fracture energy, N/m (lb/in.)
NC	37,673	0.120	42.72	0.0023	59.24	381.33 (2.18)
URC	25,653	0.123	36.38	0.0027	46.88	301.67 (1.72)
QRC1	34,963	0.134	40.67	0.0024	56.65	362.26 (2.07)
QRC2	36,802	0.130	41.60	0.0022	55.60	379.13 (2.16)
QRC3	36,842	0.125	43.56	0.0025	56.13	383.64 (2.19)

Note: 1 MPa = 145 psi; 1 GPa = 145 ksi.

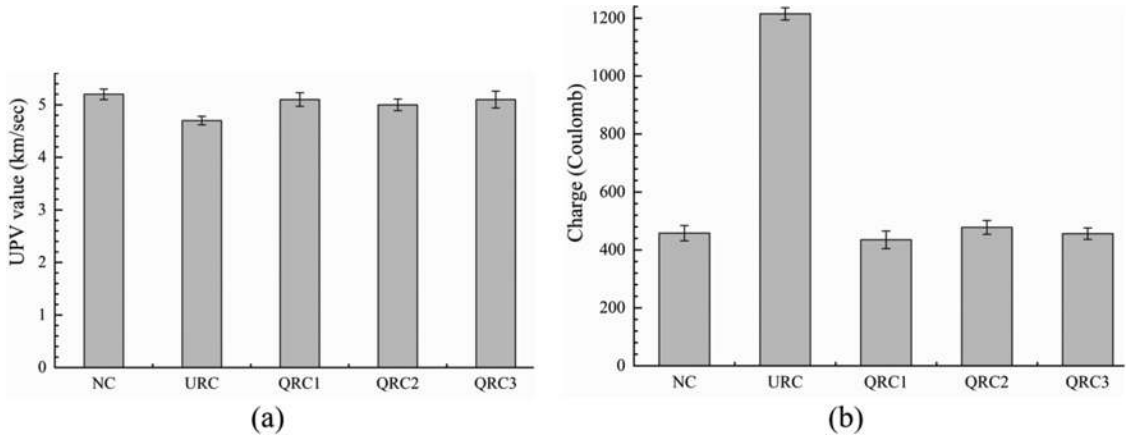

Fig. 4—(a) UPV values; and (b) RCPT values of NC, URC, QRC1, QRC2, and QRC3.

results, these concretes' dynamic MOE are 59.24, 46.88, 56.65, 55.60, and 56.13 GPa (8592.04, 6799.37, 8216.39, 8064.1, and 8140.97 ksi), respectively (Table 7). The URC, QRC1, QRC2, and QRC3 samples have dynamic MOE in the factions of NC of 0.79, 0.96, 0.94, and 0.95, respectively. Thus, the dynamic MOE of QRC1, QRC2, and QRC3 is only 4 to 6% less than NC. However, URC has a 21% lower dynamic modulus compared to NC.

In summary, the improved quality of RA produces bulk density, water absorption, void content, and structural integrity in QRC like NC. QRC has comparable dynamic moduli to NC, which predicts similar internal compactness, interfacial characteristics, and microcracks. The UPV value of URC indicates it is relatively less dense and has high porosity, cracks, and voids compared to NC. URC has a significantly lower dynamic modulus, indicating low internal compactness, inferior interfacial characteristics, and higher microcracks than NC.

Compressive strength

The compressive strength test is conducted following IS 516 (Part 1/Sec 1):2021[26] and depicted in Fig. 5. NC, URC, QRC1, QRC2, and QRC3 have 28-day compressive strengths of 53.27, 45.19, 50.94, 51.53, and 53.35 MPa (7726, 6554, 7388, 7473, and 7737 psi), respectively. QRC1 and QRC2 have marginally lower compressive strengths than NC at 28 days. However, QRC3 achieves a target mean strength similar to NC. The 28-day compressive strength of the URC mixture is 15.14% (approximately 8.06 MPa [1169 psi]) lower than the target strength. At 91 days, QRC1 and QRC2 have compressive strengths similar to NC, and QRC3 has approximately 7.0% more than NC. URC has a

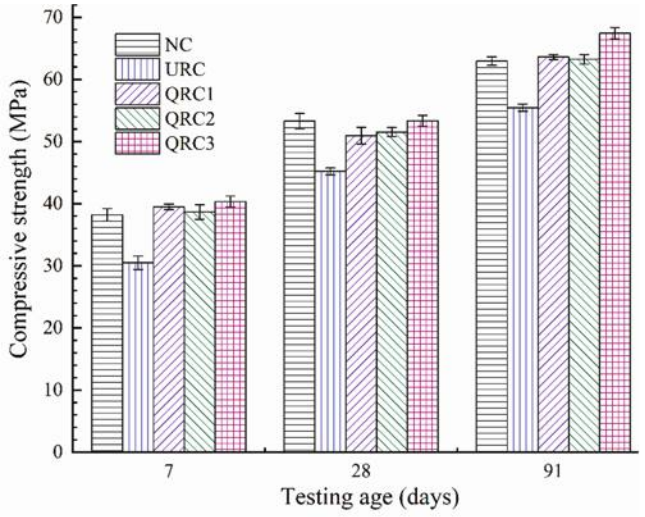

Fig. 5—Compressive strength of NC, URC, QRC1, QRC2, and QRC3. (Note: 1 MPa = 145 psi.)

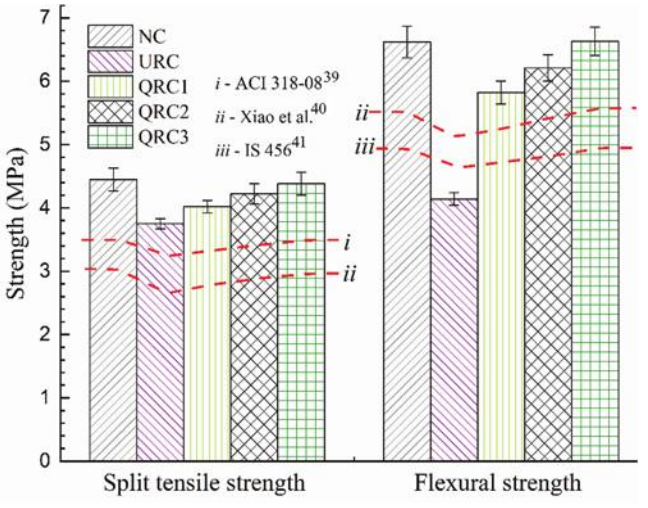

Fig. 6—Splitting tensile strength and flexural strength of NC, URC, QRC1, QRC2, and QRC3. (Note: 1 MPa = 145 psi.)

significantly lower 91-day compressive strength (approximately 12%) than NC.

Performance-based quality control ensures QRC3 has the same compressive strength as NC or the target strength. According to Kim,[1] bulk density and water absorption of RA are major strength-determining parameters. The bulk density of QRA1, QRA2, and QRA3 is approximately similar to that of NA, with a deviation of less than 3%. However, the compressive strength of QRC1 and QRC2 is approximately 5% lower than that of NC at 28 days due to the relative quality difference in QRA1, QRA2, and QRA3. On the other hand, QRA1, QRA2, and QRA3 absorb 1.02, 1.00, and 1.25% water, respectively. The water absorption of QRA3 is 23 to 25% more than that of QRA1 and QRA2. As a result of the higher but controlled water absorption in QRA, QRC1, QRC2, and QRC3 exhibit the same or higher compressive strength as NC at 91 days.

According to Rashid et al.,[22] the RA has a higher water-retention capacity than the NA, and it was demonstrated by Singh et al.[38] that the presence of internal moisture improves concrete's 28- and 91-day compressive strengths. A substantial amount of water is retained by QRA3 compared to QRA1 or QRA2 based on the water absorption of the material. Consequently, a stronger calcium-silicate-hydrate (C-S-H) is produced, strengthening the old interfacial transition zone (OITZ). Additionally, the bulk density of URA is significantly lower than that of NA, and water absorption is out of the limit set for NA in different national and international standards.[13] Therefore, the URC could not achieve its target strength.

Splitting tensile strength and flexural strength

The splitting tensile test is conducted following ASTM C496/C496M-04[27] and IS 516 (Part 1),[26] and the flexural strength (modulus of rupture) test is conducted following ASTM C78/C78M-18.[28] Figure 6 shows that NC, URC, QRC1, QRC2, and QRC3 have average splitting tensile strengths of 4.45, 3.75, 4.02, 4.22, and 4.38 MPa (645, 543, 583, 612, and 635 psi), respectively. QRC1 and QRC2 have 10% and 5% lower splitting tensile strength than NC. QRC3, however, has a splitting tensile strength closer to NC. The difference in splitting tensile strength between URC and NC is 16%. These splitting tensile strengths are further compared with the predicted value using Eq. (1) as per ACI 318-08[39] for NC and Eq. (2) as proposed by Xiao et al.[40] for RC, as shown in Fig. 6.

$$f_t = 0.49 \times f_c^{0.50} \quad (1)$$

$$f_t = 0.24 \times f_c^{0.65} \quad (2)$$

At present, the correlation between compressive strength and splitting tensile strength differs from the preceding correlations reported in the literature (Fig. 7(a)). It is evident from Fig. 7(a) that QRA produces QRC with a higher splitting tensile strength than previous studies because of its superior quality (Zhou and Chen[42]). As a result of the excellent angularity maintained in the crushing process, URC has slightly higher splitting tensile strength than the previous study. It is evident from Fig. 6 that ACI 318-08[39] and Xiao et al.[40] underestimate the splitting tensile strengths of URC, QRC1, QRC2, and QRC3 compared to the experimental results.

Figure 6 shows NC, URC, QRC1, QRC2, and QRC3 have flexural strengths of 6.62, 4.14, 5.82, 6.21, and 6.63 MPa (960, 600, 844, 900, and 961 psi), respectively. Even though QRC1 and QRC2 have 12.1 and 6.2% lower flexural strength than NC, QRC3 has the same flexural strength as NC. The URC mixture has a 37.45% lower flexural strength than NC. The relation between compressive strength and flexural strength given by Xiao et al.[40] (Eq. (3)) for RC, and for NC as proposed in IS 456:2000[41] (Eq. (4)), underestimates the flexural strength compared to the experimental value for NC and QRC (Fig. 6). A strong correlation exists between compressive and flexural strength (Fig. 7(b)). Due to the poor quality of the URA, the flexural strength of URC is lower than predicted by IS 456[41] and Xiao et al.[40] However, the improved QRA quality produces a flexural strength of QRC higher than estimated by IS 456[41] and Xiao et al.[40] Overall, the improved quality of QRA in terms of surface

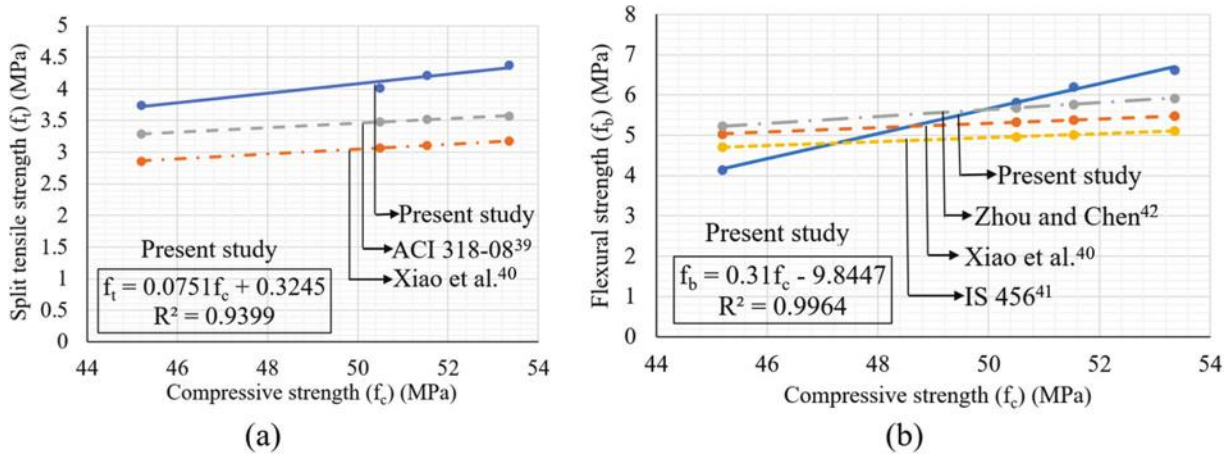

Fig. 7—(a) Correlation between compressive strength and splitting tensile strength; and (b) correlation between compressive strength and flexural strength of URC, QRC1, QRC2, and QRC3. (Note: 1 MPa = 145 psi.)

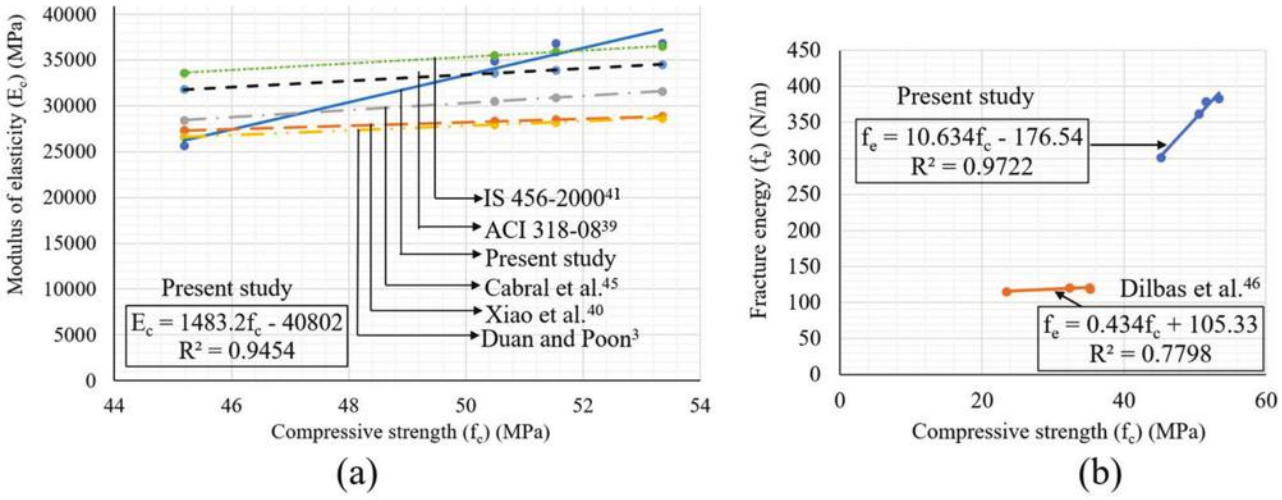

Fig. 8—(a) Correlation between compressive strength and MOE; and (b) correlation between compressive strength and fracture energy of URC, QRC1, QRC2, and QRC3. (Note: 1 MPa = 145 psi; 1 N/m = 0.0057 lb/in.)

characteristics (texture), shape (angularity), abrasion values (hardness), crushing values (strength), and elastic properties of aggregates (stiffness) improves the tensile strength or fracture toughness of these QRCs.[43,44]

$$f_b = 0.75 \times \sqrt{f_c} \quad (3)$$

$$f_b = 0.70 \times \sqrt{f_c} \quad (4)$$

Modulus of elasticity, Poisson's ratio, peak strain, and peak stress

The MOE and Poisson's ratio are determined following ASTM C469-02.[29] Table 7 shows the MOE, Poisson's ratio, peak strain, and peak stress of NC, URC, QRC1, QRC2, and QRC3. NC, URC, QRC1, QRC2, and QRC3 have MOE of 37,673, 25,653, 34,963, 36,802, and 36,842 MPa (5,464,006.7, 3,720,653.1, 5,070,954.42, 5,337,678.82, and 5,343,480.33 psi), respectively. According to the results, the MOE for QRC are comparable to those for NC. Furthermore, URC has a significantly lower MOE than NC and differs by 32%. NC, URC, QRC1, QRC2, and QRC3 have Poisson's ratios of 0.120, 0.123, 0.134, 0.130, and 0.125, respectively. In this study, the Poisson's ratios are between 0.1 and 0.2, similar to those reported for plain concrete.[39] NC, URC, QRC1, QRC2, and QRC3 have peak strains of 0.0023, 0.0027, 0.0024, 0.0022, and 0.0025, respectively. The peak stress of these samples is 42.72, 36.38, 40.67, 41.6, and 43.56 MPa (6196, 5276, 5898, 6033, and 6317 psi), respectively. The peak stress and corresponding peak strain of QRC1, QRC2, and QRC3 agree with NC and the literature.[21] URC has a significantly higher peak strain and lower peak stress value.

Furthermore, Fig. 8(a) shows a strong correlation between compressive strength and MOE for RC. As a result of the low quality of the treated aggregates, most previous studies overestimate the MOE of URC and underestimate the MOE of RC (Fig. 8(a)).[45] RA quality control produces RC with equivalent MOE to NC. The MOE of QRC, calculated by IS 456,[41] an Indian Standard Code for NC, agrees with the experiments. According to the relation, the MOE of QRC increases with its compressive strength. There is a direct correlation between peak strain and the MOE of concrete or aggregates. Therefore, peak strains for QRC1, QRC2, and QRC3 are similar to NC. Compressive strength and

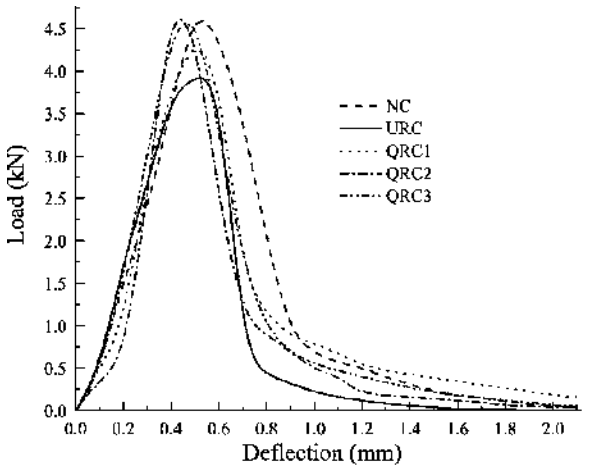

Fig. 9—Load-deflection curve of notched beams for fracture energy of NC, URC, QRC1, QRC2, and QRC3. (Note: 1 kN = 224.81 lb; 1 mm = 0.0394 in.)

peak stress are correlated in concrete. Additionally, QRC1, QRC2, and QRC3 have similar Poisson's ratios to NC based on their unit weights and compressive strengths.[47]

Fracture energy

According to the International Union of Laboratories and Experts in Construction Materials, Systems and Structures (RILEM),[30] fracture energy is determined using a notched beam with a U-shaped notch of 8 mm (0.315 in.) width and 30 mm (1.18 in.) depth. With the universal testing machine, a three-point bending test was performed. The loading rate remained constant during this test, so the maximum loading on a specimen was reached within 30 to 60 seconds. Figure 9 shows the load-deflection curve of NC, URC, QRC1, QRC2, and QRC3 notched beams. Additionally, Table 7 shows fracture energies for NC, URC, QRC1, QRC2, and QRC3, which are 381.33, 301.67, 362.26, 379.13, and 383.64 N/m (2.18, 1.72, 2.07, 2.16, and 2.19 lb/in.), respectively. As a result, QRC3 has fracture energy similar to NC. The URC has lower fracture energy than the NC by approximately 21%.

Based on the experimental results of Dilbas and Çakır,[46] the correlation coefficient among compressive strength and fracture energy for RC is found to be 0.78 (Fig. 8(b)). However, the same correlation coefficient for NC is found to be 0.96. Such difference in correlation coefficients might be due to the low quality of treated RA. In the present study, the correlation coefficient is 0.97 for QRC due to the superior quality control of RA. Thus, controlling RA quality significantly improved the correlation between compressive and fracture energy.

Rapid chloride-ion penetrability testing and electrical resistivity

A rapid chloride-ion penetrability test (RCPT) is conducted according to ASTM C1202-19.[34] NC, URC, QRC1, QRC2, and QRC3 have chloride-ion penetrations of 458, 1215, 435, 478, and 456 coulombs, respectively (Fig. 4(b)). The QRC1, QRC2, and QRC3 mixtures possess similar chloride-ion penetrability to NC and are classified under the very low permeability class (Table 8). In contrast to these mixtures, URC has a medium permeability class. Additionally, Table 8 shows the electrical resistivity of NC, QRC1, QRC2, and QRC3 higher than 200 Ω·m (7874.02 Ω·in.), which are classified under the very low permeability class.[34,48] At the same time, the URC has an electrical resistivity of 196.25 Ω·m (7726.38 Ω·in.) and falls under the medium permeability class. The surface texture shows a strong new interfacial transition zone (NITZ) and strengthening OITZ in QRA. According to the bulk density, UPV values, and dynamic modulus, the QRC1, QRC2, and QRC3 mixtures are uniform and closely packed. QRC1, QRC2, and QRC3 have a denser matrix formation based on their compressive strength. Consequently, these properties indicate a reduced pore size and shape and a lowered ingress path, indicating improved impermeability.

Sorptivity

The sorptivity of NC, URC, QRC1, QRC2, and QRC3 is measured according to ASTM C1585-04.[32] Figure 10(a) shows that NC, URC, QRC1, QRC2, and QRC3 have different sorptivity values. The NC, URC, QRC1, QRC2, and QRC3 samples have maximum initial absorptions of 0.69, 2.41, 1.97, 1.38, and 1.73 mm (0.03, 0.09, 0.07, 0.05, and 0.06 in.), respectively. These samples also have secondary absorptions of 1.60, 3.77, 3.37, 3.14, and 2.88 mm (0.06, 0.15, 0.13, 0.12, and 0.11 in.). The initial and secondary absorptions of QRC1, QRC2, and QRC3 are much lower than those of URC. A porous interface between old mortar and parent aggregate and microcracks in the mortar produces high sorptivity in QRC mixtures.[49] Controlled quality of TRA, especially attached mortar and the OITZ, reduced the sorptivity of QRC mixtures more than in previous studies. According to this study, QRC has a lower maximum initial absorption (1.97 mm [0.07 in.]) than Bhasya and Bharatkumar[21] (3.50 mm [0.14 in.]). The secondary absorptions of these QRCs are also lower than those reported in the literature.[6]

The present research demonstrates that two factors govern the QRC's sorptivity. First, there is the availability of mortar-attached, mortar-covered, and mortar-only aggregates in QRA. These aggregate types have high porosity and microcracks; therefore, QRC's sorptivity cannot be reduced to NC. Removing the amount of adhered mortar optimally improves QRC's sorptivity (Fig. 10(a)). The second is the chemical composition of the mortar that is attached to QRA (Fig. 10(b)). According to Liu et al.,[50] calcium hydroxide in residual mortar may lower the pH in the pore solution. This results in the decomposition of C-S-H and their leaching into fresh concrete. Concrete may become more porous, and its impermeability may decrease. Therefore, some other treatment is needed to remove calcium hydroxide present in residual mortar to make QRC comparable with NC in terms of sorptivity.

Drying test, alkalinity test, and abrasion resistance

A drying test is conducted to determine the weight loss of the concrete specimen following Purushothaman et al.[7] For NC, URC, QRC1, QRC2, and QRC3, the weight loss

Table 8—RCPT results of concrete (ASTM C1202)

Specimen	Initial current, mA	Resistivity, Ω·m	Total passing charge, coulombs	Chloride-ion penetrability level	Corrosion protection level
NC	31.7	296.73	458.00	Very low	High
URC	48.0	196.25	1215.00	Low	Medium
QRC1	35.2	267.52	435.00	Very low	High
QRC2	38.6	243.35	478.00	Very low	High
QRC3	25.5	368.95	456.00	Very low	High

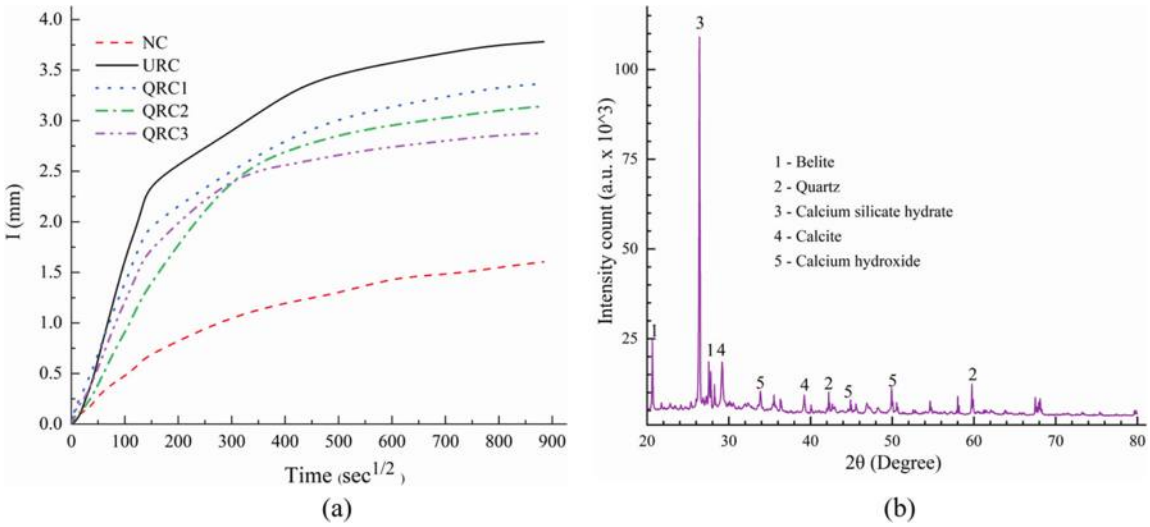

Fig. 10—(a) Sorptivity test results of NC, URC, QRC1, QRC2, and QRC3; and (b) X-ray diffraction (XRD) analysis for minerals composition of attached mortar. (Note: 1 mm = 0.0394 in.)

during drying tests is 3.51, 6.65, 4.40, 3.80, and 3.87% (Table 6). Thus, URC shows approximately 1.9 times greater weight loss in the drying test than NC. QRC1 has weight loss approximately 25% higher than NC, whereas QRC2 and QRC3 weight losses are only 8 to 10% higher than NC. The pH of these concrete samples is measured according to Purushothaman et al.[7] and is higher than 12 and lower than 13 (Table 6), which is well within the acceptable range. In the abrasion tests, following IS 15658:2006,[35] NC, URC, QRC1, QRC2, and QRC3 show volume losses of 1.77%, 3.94%, 2.63%, 2.53%, and 1.56%, respectively (Table 6). Volume loss of URC, QRC1, and QRC2 is approximately 123, 49, and 43% greater than NC. Meanwhile, QRC3 showed a 12% reduction in volume losses compared to NC. The concrete matrix, coarse aggregate quality, and the bond between the matrix and aggregate significantly impacted the concrete's abrasion resistance.[6,51,52] However, there is a higher PI for QRA1 and QRA2 than for QRA3. Compared to QRC1, QRC2, and NC, QRC3 has a significantly lower volume loss. This may be possible because higher drum revolutions may affect the OITZ negatively. However, future studies are required.

Microstructures

A microstructure analysis is conducted to observe the effect of quality-controlled RA on interfacial transition zone (ITZ) modification in concrete. Figure 11(a) shows scanning electron microscope (SEM) images of the polished fresh-cut surfaces of NC, and Fig. 12 shows URC, QRC1, QRC2, and QRC3. Due to the porous nature of the mortar attached to URA, the OITZ in URC is highly porous (less dense), discontinuous, and has macrovoids (Fig. 12(a)). There is poor adhesion between the OITZ and URC. A similar observation was also made by Dilbas et al.[11] Thus, reducing the attached mortar optimally produces denser OITZs with fewer microvoids (Fig. 12(b) to (d)). Quality control of RA improves not only the pore structure but also the weak mortar structure attached to the aggregate.[11]

However, in the OITZ of QRC1, a microcrack and a slightly loose structure are clearly visible. The increase of 400 revolutions to 500 revolutions reduces the strength of the OITZ by widening the microcracks, which may further widen during shrinkage of cement paste (Fig. 12(b) to (d)). The SEM image of NC has similar cracks between the interface of cement paste and NA (Fig. 11(a)). This type of crack generally appears in NC due to the plastic shrinkage in the concrete matrix. In this way, QRA3 has relatively lower material properties than QRA1, despite QRC3 having superior physical and mechanical properties compared to QRC1. As for increasing charges in mechanical treatment, these also have some detrimental effects on the OITZ, but they are not as severe as increasing the number of drum revolutions. Therefore, QRC2 has some material properties, such as compressive strength, that are higher than QRC1.

In QRC, the reduced intensity of Al, S, and Ca is associated with a reduction in the formation of ettringite (Fig. 13). Furthermore, gypsum and brucite are less abundant in the ITZ of QRC, which is confirmed by lower Ca, S, and Mg

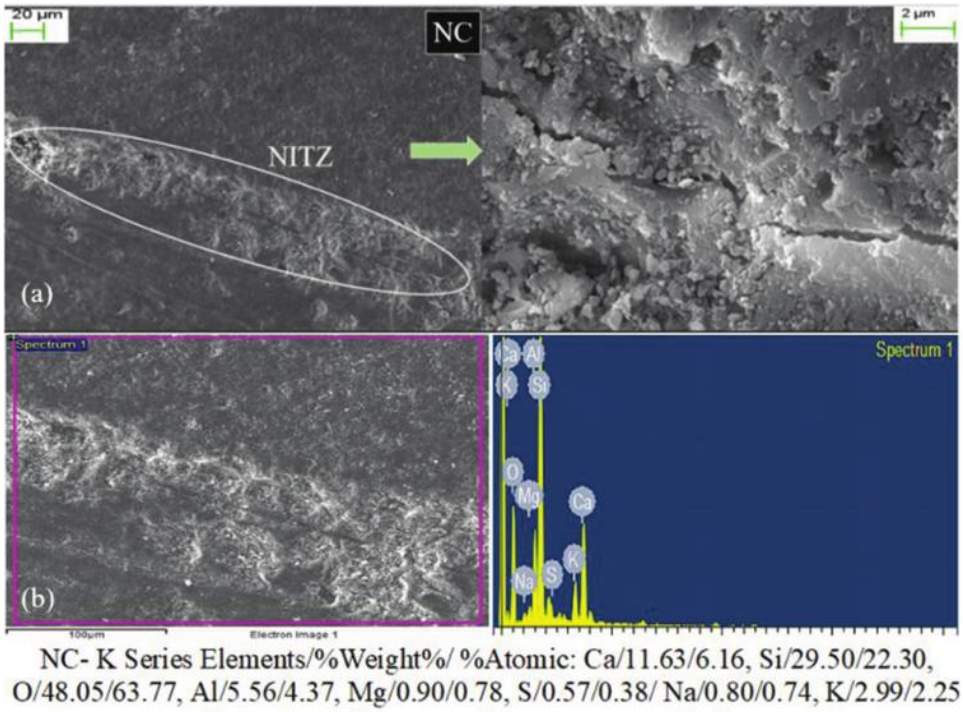

Fig. 11—(a) SEM images for microstructural examination of NC at ITZ; and (b) EDX analysis for elemental composition of NC at ITZ.

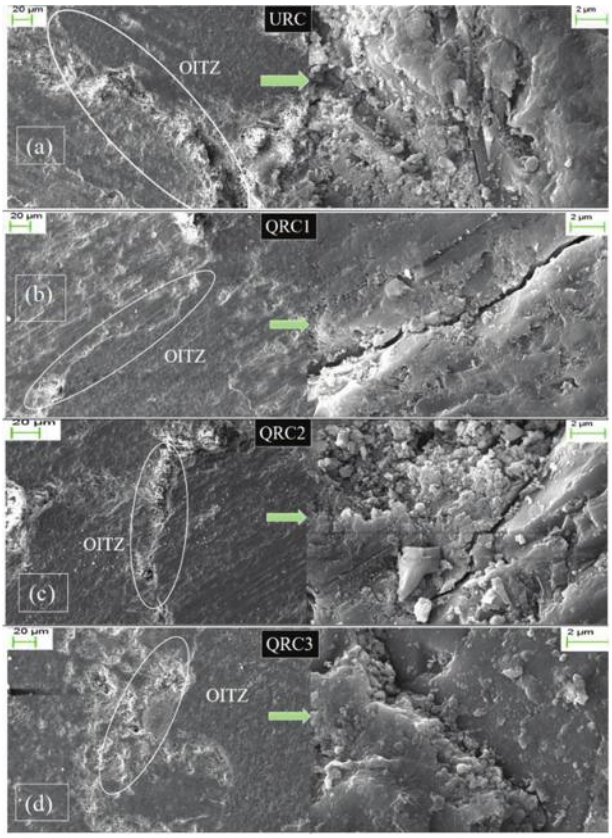

Fig. 12—SEM images for microstructural examination of URC, QRC1, QRC2, and QRC3 at OITZ.

levels and indicates densified pores.[53] Figure 13 illustrates that calcium and its oxides, which are responsible for concrete strength, are more readily available in QRC than in URC. Furthermore, Si-rich C-S-H may be responsible for increasing the strength of the OITZ in QRC.[54] QRC has a lower Ca/Si ratio than URC in the present study. Thus, the OITZ is improved by maximum CH use in QRC and the formation of Si-rich C-S-H compared to URC. QRC3 has superior strength properties due to the higher formation of Si-rich C-S-H than QRC1. Thus, QRA quality control indicates a significant transformation of the C-S-H phase that significantly contributes to an improved ITZ.[54]

Finally, quality-controlled RA can produce RC with material properties similar to NC (except sorptivity). A high percentage of CH particles accounts for high ITZ porosity. Therefore, RC's sorptivity cannot be like NC when RA is only mechanically treated to control its quality. In addition, varying the mixture proportions can be used in other trials to achieve the target strength of a QRC1. The next study will examine how charges, drum revolutions, and varying feeding mass affect TRA material properties. Overall, the present study achieves its objective and is justified.

CONCLUSIONS

This study examines the performance of quality-controlled recycled concrete aggregates (QRAs) with fly-ash-based cement. The physical and mechanical properties of recycled concrete aggregate (RA) are determined after mechanical treatment with different charges and drum revolutions. Based on its performance index (PI), a ranking for each treated recycled concrete aggregate (TRA) is assigned. The TRA with the highest three ranks is used to prepare the mixture proportions. Based on the experimental observation, the following conclusions are drawn.

The present research successfully develops the concrete composed of 100% RA with fly-ash-based cement. Quality-controlled recycled aggregate concrete (QRC) has physical,

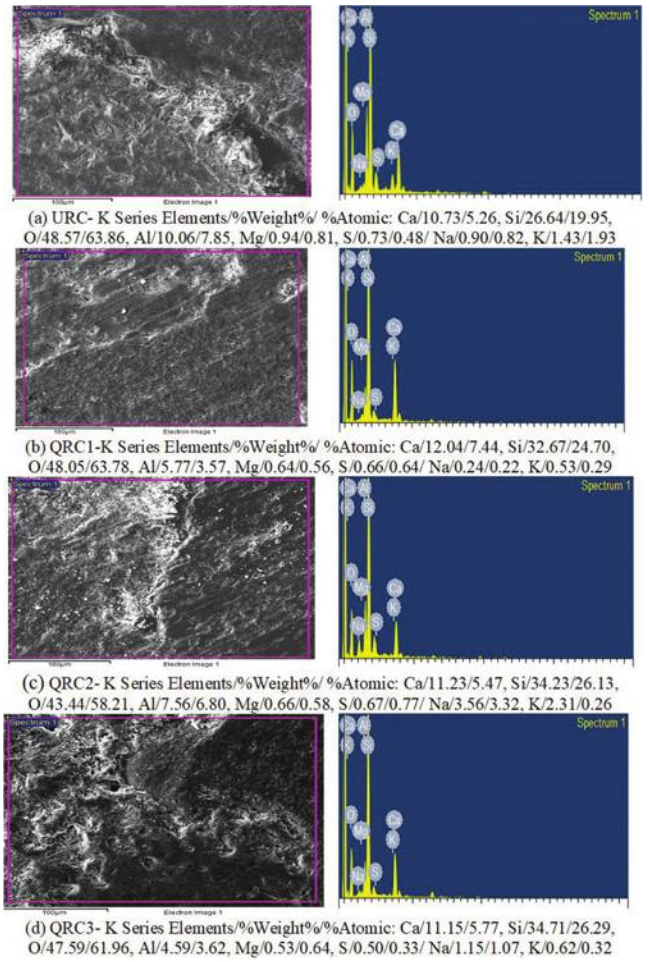

Fig. 13—EDX analysis for elemental composition of URC, QRC1, QRC2, and QRC3 at OITZ.

mechanical, and durability properties superior to the concrete composed of untreated recycled concrete aggregate (URC), and these properties are closer to natural aggregate concrete (NC) (except sorptivity). The compressive strength, splitting tensile strength, flexural strength, fracture energy, and modulus of elasticity (MOE) of QRC are higher than those of URC by 18.0, 16.8, 60.0, 27.17, and 43.46%, respectively. The abrasion resistance of a QRC is observed to be approximately 60% higher than URC. Scanning electron microscope (SEM) image and energy-dispersive X-ray (EDX) analysis prove that quality control of RA produces denser old interfacial transition zones (OITZs) with fewer microvoids. The QRA improves not only the pore structure but also the weak mortar structure attached to the aggregate.

There is also a strong correlation between the compressive strength and splitting tensile strength, flexural strength, fracture energy, and MOE of QRC. The mechanical and durability properties of QRC are in close agreement with NC, standard requirements, and the reported values. Therefore, the present research concludes that QRA can be used to compute the mixture proportions for concrete (certainly up to medium-strength concrete) according to the Indian standard or the international standard. Therefore, the standard mixture proportion procedure of NA can be applied to the QRA to achieve the target strength and other mechanical and durability properties of recycled aggregate concrete (RC) closer to NC (except sorptivity).

At present, QRC has failed to obtain a sorptivity equivalent to NC. Thus, this research also concludes that an RC will never have a similar sorptivity to NC until the microstructure and chemical composition of the adhered mortar are changed. Future studies will consider these factors in improving the sorptivity of RC.

AUTHOR BIOS

ACI member **Amit Kumar** *is a Research Scholar in the Department of Civil Engineering, National Institute of Technology Patna, Patna, Bihar, India. He received his MTech from Rajiv Gandhi Proudyogiki Vishwavidyalaya (RGPV), Bhopal, Madhya Pradesh, India. His research interests include the mechanical and durability properties of recycled aggregate concrete.*

Gyani Jail Singh *is an Assistant Professor in the Department of Civil Engineering, National Institute of Technology Patna. He received his PhD from Indian Institute of Technology Banaras Hindu University (BHU), Varanasi, Uttar Pradesh, India. His research interests include mechanical and durability properties, and structural performance of concrete.*

Priyanshu Raj *is a Postgraduate Student in the Department of Civil Engineering, National Institute of Technology Patna. He received his BTech from Jaipur Engineering College and Research Centre University, Jaipur, Rajasthan, India. His research interests include the mechanical and durability properties of recycled aggregate concrete.*

Rajesh Kumar *is a Professor in the Department of Civil Engineering, Indian Institute of Technology (BHU) Varanasi. He received his PhD from Indian Institute of Technology Kharagpur, Kharagpur, West Bengal, India. His research interests include the performance of concrete and composite materials.*

REFERENCES

1. Kim, J., "Influence of Quality of Recycled Aggregates on the Mechanical Properties of Recycled Aggregate Concretes: An Overview," *Construction and Building Materials*, V. 328, Apr. 2022, Article No. 127071.

2. Martín-Morales, M.; Zamorano, M.; Ruiz-Moyano, A.; and Valverde-Espinosa, I., "Characterization of Recycled Aggregates Construction and Demolition Waste for Concrete Production Following the Spanish Structural Concrete Code EHE-08," *Construction and Building Materials*, V. 25, No. 2, Feb. 2011, pp. 742-748. doi: 10.1016/j.conbuildmat.2010.07.012

3. Duan, Z. H., and Poon, C. S., "Properties of Recycled Aggregate Concrete Made with Recycled Aggregates with Different Amounts of Old Adhered Mortars," *Materials & Design*, V. 58, June 2014, pp. 19-29. doi: 10.1016/j.matdes.2014.01.044

4. Adams, M. P., and Jayasuriya, A., "Guideline Development for Use of Recycled Concrete Aggregates in New Concrete (ACI CRC 18.517)," ACI Foundation Concrete Research Council, Farmington Hills, MI, 2019, 89 pp.

5. Neville, A. M., *Properties of Concrete*, fourth edition, Pearson, London, UK, 1995.

6. Kumar, A., and Singh, G. J., "Improving the Physical and Mechanical Properties of Recycled Concrete Aggregate: A State-of-the-Art Review," *Engineering Research Express*, V. 5, No. 1, Mar. 2023, Article No. 012007.

7. Purushothaman, R.; Amirthavalli, R. R.; and Karan, L., "Influence of Treatment Methods on the Strength and Performance Characteristics of Recycled Aggregate Concrete," *Journal of Materials in Civil Engineering*, ASCE, V. 27, No. 5, May 2015, p. 04014168.

8. Pandurangan, K.; Dayanithy, A.; and Om Prakash, S., "Influence of Treatment Methods on the Bond Strength of Recycled Aggregate Concrete," *Construction and Building Materials*, V. 120, Sept. 2016, pp. 212-221. doi: 10.1016/j.conbuildmat.2016.05.093

9. Ahmad, S.; Maslehuddin, M.; Shameem, M.; Faysal, R. M.; and Adekunle, S. K., "Effect of Abrasion and Chemical Treatment of Recycled Aggregate on the Workability, Strength, and Durability Properties of Concrete," *European Journal of Environmental and Civil Engineering*, V. 26, No. 8, 2022, pp. 3276-3291.

10. Alqarni, A. S.; Abbas, H.; Al-Shwikh, K. M.; and Al-Salloum, Y. A., "Treatment of Recycled Concrete Aggregate to Enhance Concrete Performance," *Construction and Building Materials*, V. 307, Nov. 2021, Article No. 124960. doi: 10.1016/j.conbuildmat.2021.124960

11. Dilbas, H.; Çakır, Ö.; and Atiş, C. D., "Experimental Investigation on Properties of Recycled Aggregate Concrete with Optimized Ball Milling Method," *Construction and Building Materials*, V. 212, July 2019, pp. 716-726. doi: 10.1016/j.conbuildmat.2019.04.007

12. Principigallo, A., "Effective Water in Concrete with Recycled Aggregate," *ACI Materials Journal*, V. 115, No. 6, Nov. 2018, pp. 845-854. doi: 10.14359/51706842

13. ACI Committee E701, "Aggregates for Concrete (ACI Education Bulletin E1-07)," American Concrete Institute, Farmington Hills, MI, 2007, 29 pp.

14. Kurda, R.; de Brito, J.; and Silvestre, J. D., "Influence of Recycled Aggregates and High Contents of Fly Ash on Concrete Fresh Properties," *Cement and Concrete Composites*, V. 84, Nov. 2017, pp. 198-213. doi: 10.1016/j.cemconcomp.2017.09.009

15. Brand, A. S.; Roesler, J. R.; and Salas, A., "Initial Moisture and Mixing Effects on Higher Quality Recycled Coarse Aggregate Concrete," *Construction and Building Materials*, V. 79, Mar. 2015, pp. 83-89. doi: 10.1016/j.conbuildmat.2015.01.047

16. Quattrone, M.; Cazacliu, B.; Angulo, S. C.; Hamard, E.; and Cothenet, A., "Measuring the Water Absorption of Recycled Aggregates, What Is the Best Practice for Concrete Production?" *Construction and Building Materials*, V. 123, Oct. 2016, pp. 690-703. doi: 10.1016/j.conbuildmat.2016.07.019

17. Mefteh, H.; Kebaïli, O.; Oucief, H.; Berredjem, L.; and Arabi, N., "Influence of Moisture Conditioning of Recycled Aggregates on the Properties of Fresh and Hardened Concrete," *Journal of Cleaner Production*, V. 54, Sept. 2013, pp. 282-288. doi: 10.1016/j.jclepro.2013.05.009

18. Poon, C. S.; Shui, Z. H.; Lam, L.; Fok, H.; and Kou, S. C., "Influence of Moisture States of Natural and Recycled Aggregates on the Slump and Compressive Strength of Concrete," *Cement and Concrete Research*, V. 34, No. 1, Jan. 2004, pp. 31-36. doi: 10.1016/S0008-8846(03)00186-8

19. Tangchirapat, W.; Buranasing, R.; and Jaturapitakkul, C., "Use of High Fineness of Fly Ash to Improve Properties of Recycled Aggregate Concrete," *Journal of Materials in Civil Engineering*, ASCE, V. 22, No. 6, June 2010, pp. 565-571. doi: 10.1061/(ASCE)MT.1943-5533.0000054

20. Kou, S. C.; Poon, C. S.; and Chan, D., "Influence of Fly Ash as Cement Replacement on the Properties of Recycled Aggregate Concrete," *Journal of Materials in Civil Engineering*, ASCE, V. 19, No. 9, Sept. 2007, pp. 709-717. doi: 10.1061/(ASCE)0899-1561(2007)19:9(709)

21. Bhasya, V., and Bharatkumar, B. H., "Mechanical and Durability Properties of Concrete Produced with Treated Recycled Concrete Aggregate," *ACI Materials Journal*, V. 115, No. 2, Mar. 2018, pp. 209-217. doi: 10.14359/51701239

22. Rashid, K.; Rehman, M. U.; de Brito, J.; and Ghafoor, H., "Multi-Criteria Optimization of Recycled Aggregate Concrete Mixes," *Journal of Cleaner Production*, V. 276, Dec. 2020, Article No. 124316. doi: 10.1016/j.jclepro.2020.124316

23. IS 383:2016, "Coarse and Fine Aggregate for Concrete—Specification," Bureau of Indian Standards, New Delhi, India, 2016, 21 pp.

24. IS 10262:2019, "Concrete Mix Proportioning—Guidelines," Bureau of Indian Standards, New Delhi, India, 2019, 44 pp.

25. Mi, R.; Pan, G.; and Kuang, T., "Reducing the Carbonation Zone and Steel Corrosion Zone Widths of Recycled Aggregate Concrete by Optimizing Its Mixing Process," *Journal of Materials in Civil Engineering*, ASCE, V. 33, No. 5, May 2021, p. 04021061.

26. IS 516 (Part 1/Sec 1):2021, "Hardened Concrete—Methods of Test: Part 1 – Testing of Strength of Hardened Concrete: Section 1 – Compressive, Flexural and Split Tensile Strength," Bureau of Indian Standards, New Delhi, India, 2021, 20 pp.

27. ASTM C496/C496M-04, "Standard Test Method for Splitting Tensile Strength of Cylindrical Concrete Specimens," ASTM International, West Conshohocken, PA, 2004, 5 pp.

28. ASTM C78/C78M-18, "Standard Test Method for Flexural Strength of Concrete (Using Simple Beam with Third-Point Loading)," ASTM International, West Conshohocken, PA, 2018, 5 pp.

29. ASTM C469-02, "Standard Test Method for Static Modulus of Elasticity and Poisson's Ratio of Concrete in Compression," ASTM International, West Conshohocken, PA, 2002, 5 pp.

30. RILEM, "Determination of the Fracture Energy of Mortar and Concrete by Means of Three-Point Bend Tests on Notched Beams," *Materials and Structures*, V. 18, No. 4, July 1985, pp. 287-290.

31. ASTM C642-97, "Standard Test Method for Density, Absorption, and Voids in Hardened Concrete," ASTM International, West Conshohocken, PA, 1997, 3 pp.

32. ASTM C1585-04, "Standard Test Method for Measurement of Rate of Absorption of Water by Hydraulic-Cement Concretes," ASTM International, West Conshohocken, PA, 2004, 6 pp.

33. IS 516 (Part 5):2018, "Hardened Concrete—Methods of Test: Part 5 – Non-destructive Testing of Concrete," Bureau of Indian Standards, New Delhi, India, 2018.

34. ASTM C1202-19, "Standard Test Method for Electrical Indication of Concrete's Ability to Resist Chloride Ion Penetration," ASTM International, West Conshohocken, PA, 2019, 8 pp.

35. IS 15658:2006, "Precast Concrete Blocks for Paving—Specification," Bureau of Indian Standards, New Delhi, India, 2006, 27 pp.

36. IS 2386 (Part III)-1963, "Methods of Test for Aggregates for Concrete: Part III – Specific Gravity, Density, Voids, Absorption and Bulking (Reaffirmed 2021)," Bureau of Indian Standards, New Delhi, India, 1963, 22 pp.

37. ASTM C597-09, "Standard Test Method for Pulse Velocity Through Concrete," ASTM International, West Conshohocken, PA, 2009, 4 pp.

38. Singh, G. J.; Kumar, V.; Singh, B. N.; and Kumar, R., "Impact of Drying the Concrete before Its Complete Curing: Plain and Fly Ash–Based Cement Concrete," *Journal of Materials in Civil Engineering*, ASCE, V. 34, No. 2, Feb. 2022, p. 04021442. doi: 10.1061/(ASCE)MT.1943-5533.0004290

39. ACI Committee 318, "Building Code Requirements for Structural Concrete (ACI 318-08) and Commentary (ACI 318R-08)," American Concrete Institute, Farmington Hills, MI, 2008, 473 pp.

40. Xiao, J.-Z.; Li, J.-B.; and Zhang, C., "On Relationships between the Mechanical Properties of Recycled Aggregate Concrete: An Overview," *Materials and Structures*, V. 39, No. 6, July 2006, pp. 655-664. doi: 10.1617/s11527-006-9093-0

41. IS 456:2000, "Plain and Reinforced Concrete—Code of Practice (Reaffirmed 2005)," Bureau of Indian Standards, New Delhi, India, 2000, 114 pp.

42. Zhou, C., and Chen, Z., "Mechanical Properties of Recycled Concrete Made with Different Types of Coarse Aggregate," *Construction and Building Materials*, V. 134, Mar. 2017, pp. 497-506.

43. Siregar, A. P. N.; Pasaribu, E. L.; and Suarnita, I. W., "The Effect of Coarse Aggregate Hardness on the Fracture Toughness and Compressive Strength of Concrete," *MATEC Web of Conferences*, V. 258, 2019, Article No. 04011.

44. Butler, L.; West, J. S.; and Tighe, S. L., "The Effect of Recycled Concrete Aggregate Properties on the Bond Strength between RCA Concrete and Steel Reinforcement," *Cement and Concrete Research*, V. 41, No. 10, Oct. 2011, pp. 1037-1049. doi: 10.1016/j.cemconres.2011.06.004

45. Cabral, A. E. B.; Schalch, V.; Dal Molin, D. C. C.; and Ribeiro, J. L. D., "Mechanical Properties Modeling of Recycled Aggregate Concrete," *Construction and Building Materials*, V. 24, No. 4, Apr. 2010, pp. 421-430.

46. Dilbas, H., and Çakır, Ö., "Physical and Mechanical Properties of Treated Recycled Aggregate Concretes: Combination of Mechanical Treatment and Silica Fume," *Journal of Materials in Civil Engineering*, ASCE, V. 33, No. 6, June 2021, p. 04021096. doi: 10.1061/(ASCE)MT.1943-5533.0003658

47. Klink, S. A., "Aggregates, Elastic-Modulus, and Poisson's Ratio of Concrete," *ACI Journal Proceedings*, V. 83, No. 6, Nov.-Dec. 1986, pp. 961-965.

48. AASHTO PP 84-17, "Standard Practice for Developing Performance Engineered Concrete Pavement Mixtures," American Association of State Highway and Transportation Officials, Washington, DC, 2017, 67 pp.

49. Tam, V. W. Y., and Tam, C. M., "Assessment of Durability of Recycled Aggregate Concrete Produced by Two-Stage Mixing Approach," *Journal of Materials Science*, V. 42, No. 10, May 2007, pp. 3592-3602. doi: 10.1007/s10853-006-0379-y

50. Liu, J.; Xing, F.; Dong, B.; Ma, H.; and Pan, D., "Study on Surface Permeability of Concrete under Immersion," *Materials (Basel)*, V. 7, No. 2, Feb. 2014, pp. 876-886. doi: 10.3390/ma7020876

51. Kumar, A.; Singh, G. J.; Kumar, S. B.; and Kumar, R., "Performance-Based Quality Optimization Approach for Mechanically Treated Recycled Concrete Aggregates," *Journal of Materials in Civil Engineering*, ASCE, V. 35, No. 9, Sept. 2023, p. 04023315. doi: 10.1061/JMCEE7.MTENG-15284

52. Kumar, A., and Singh G. J., "Recycled Concrete Aggregate Classification Based on Quality Parameters and Performance," *Iranian Journal of Science and Technology, Transactions of Civil Engineering*, V. 47, No. 6, Dec. 2023, pp. 3211-3232.

53. Kavitha, O. R.; Shanthi, V. M.; Arulraj, G. P.; and Sivakumar, V. R., "Microstructural Studies on Eco-Friendly and Durable Self-Compacting Concrete Blended with Metakaolin," *Applied Clay Science*, V. 124-125, May 2016, pp. 143-149. doi: 10.1016/j.clay.2016.02.011

54. Al-Bayati, H. K. A.; Tighe, S. L.; and Baaj, H., "Effect of Different Treatment Methods on the Interfacial Transition Zone Microstructure to Coarse Recycled Concrete Aggregate," *TAC 2016: Efficient Transportation - Managing the Demand - 2016 Conference and Exhibition of the Transportation Association of Canada*, 2016, 29 pp.

ACI MATERIALS JOURNAL TECHNICAL PAPER

Title No. 121-M03

Interfacial Evolution between Graphene and Cementitious Composites

by Zhenyu Zhang, Yao Yao, Hu Liu, Dong Zhang, and Yan Zhuge

Carbon-based nanomaterials such as graphene oxide sheet-reinforced cementitious composites have attracted extensive interest owing to their improved post-fire mechanical properties. However, the role of graphene in anti-thermal detriment is still unclear. In the current study, the mechanical characteristics, pore structure, and interface evolution of graphene-toughened cement-based materials under high temperatures are investigated. Scanning electron microscope analysis showed that graphene implanted in the cement matrix had out-of-plane deformation at elevated temperature. The deformation caused the evolution of the interface between graphene and the cement-based material with respect to temperature. Correspondingly, the toughening effect of graphene on cement-based materials decreased first and then increased. The reinforced domain of graphene switched from mesopores to capillary pores when the temperature was beyond 400°C, contributing to the enhanced reinforcement efficiency of the cement mortar. The interfacial evolution process with an in-depth analysis based on multiple scales would benefit from optimizing the design of graphene composites at high temperatures.

Keywords: cementitious materials; elevated temperature; graphene; interface evolution; thermal detriment.

INTRODUCTION

Graphene and its derivatives have attracted extensive interest in civil engineering due to their modification of cementitious materials and functional application in infrastructure.[1-7] Due to the extraordinary mechanical strength[8-10] and super-high aspect ratio,[11,12] a small addition of graphene can significantly improve the mechanical properties and durability of concrete at room temperature.[13-17] These nanomaterials can act as seeding sites to accelerate cement hydration during the precipitation process. Graphene sheets anchored into the cement hydration products form an extensive distributed strengthening network and contribute to a defectless microstructure.[18-20]

It is noted that graphene and its derivatives not only have a good toughening effect on cement-based materials at room temperature, but also reduce the damage and deterioration under high temperatures. Concrete samples with graphene oxide (GO) presented better anti-spalling performance than neat samples, and the relative residual compressive strength of GO-modified specimens was noticeably higher than control groups after exposure to 400 and 600°C.[21] Chu et al.[22] pointed out that, at and after high temperatures, the concrete samples with graphene sulfonate nanosheets (GSN) always presented better mechanical performance than that of concrete samples without GSN. The porosity of concrete with and without GSN after 1000°C increased by 293 and 301% more than that of concrete at ambient temperature. Research was performed to find out the anti-thermal mechanism of graphene-reinforced concrete. According to Jing et al.,[23] the enhanced thermal propagation and lower temperature gradient restrict the development of thermal damages. Molecular dynamics simulation discovered that rough multilayered GO sheets were helpful in stabilizing the calcium silicate hydrate (C-S-H) structure by contributing to the good compatibility between C-S-H gel.[24] In addition, chemical alteration was found in graphene-reinforced concrete samples with the promotion effect of ordered crystal formation.[25] Thus, refinement of pore structures, regulation of the thermal stress gradient, and crack inhibition are commonly accepted fire-resistant mechanisms of the graphene-reinforced cement matrix. However, a well-bonded graphene and cement matrix at elevated temperature is hardly achieved in experiments. In previous studies, the interface evolution between graphene and the cement matrix, stemming from different thermal expansion coefficients, is usually neglected.[22,26] Under spontaneously and thermally induced strains, both one- and two-dimensional ripples and in-plane rotation in graphene sheets were observed in experiments,[26,27] which might result in changes in the interface between graphene and the cement matrix.

RESEARCH SIGNIFICANCE

There is still a lack of comprehension of the effect of graphene on the thermal resistance of concrete mechanisms. How the interface evolution of graphene and cement composites affects the cementitious microstructure and macroscopic performance remains to be investigated, which is helpful to nano-reinforced high-performance material design under high temperatures. Specifically, how does the interface evolve between graphene sheets and the cement matrix at different temperatures? How does graphene affect the pore structure and crack evolution with temperature continuously rising? Generally, the restricted thermal dilatation and evaporated water (usually evaporated free water, physically and part of chemically bound water) caused the development of thermal stress and pore pressure from 200 to 400°C, which plays a significant role in the deterioration process of cementitious microstructure.[28,29] At 600 to 800°C,

ACI Materials Journal, V. 121, No. 1, January 2024.
MS No. M-2022-270.R3, doi: 10.14359/51739199, received June 13, 2023, and reviewed under Institute publication policies.

Table 1—Properties of ordinary portland cement

Mixture	Cement	Water	Graphene	HRWRA	Silica sand
GC00	100	35	—	0.1	120
GC01	100	35	0.1	0.1	120
GC02	100	35	0.2	0.1	120

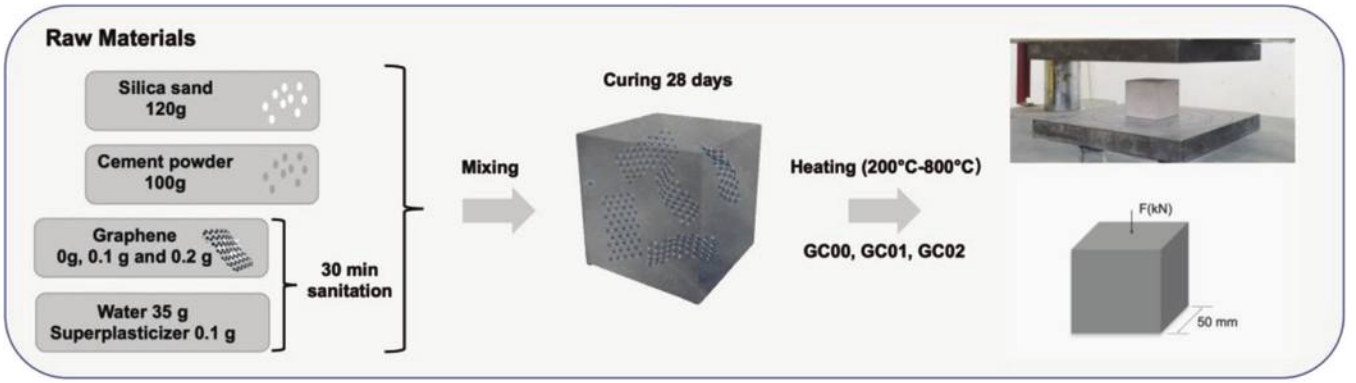

Fig. 1—Experimental setup and procedures.

most of the hydration products degrade and form a porous microstructure.[30]

The focus of this work is to investigate the role of graphene in the post-fire behavior of cement-based materials. For this purpose, experiments were performed on cement mortar samples at different temperatures.

EXPERIMENTAL INVESTIGATION

Materials and mixtures

Portland cement P.O 42.5R meeting the criteria of GB 175-2007[31] was adopted. Table 1 and Fig. 1 show the mixture proportions of the materials. Figure 2 reveals the features of the graphene sheet used in the present study. For dispersion, graphene, polycarboxylate ether (PCE), and high-range water-reducing admixtures (HRWRAs) were first added to water. Sonication (500 W, 30 minutes) was used to ensure the uniform dispersion of graphene sheets. By using a spectrophotometer, the ultraviolet-visible spectroscopy (UV-Vis) absorption spectra of each suspension were measured between 200 and 700 nm to comprehend the dispersion impact of graphene sheets. According to the Beer-Lambert law, greater absorbency corresponds to more effective dispersion of graphene sheets in water. The absorbance spectra of graphene suspension in water with and without dispersants are shown in Fig. 2. There is an absorption peak of graphene sheet suspension at 260 nm (the line in Fig. 2), which represents the particular absorption peak of each graphene for all spectra. With the addition of PCE and HRWRA, the graphene sheet suspension reaches its maximal absorption peak. When the inclusion of HRWRA dominates dispersion, graphene suspension absorbency is diminished. The minimal absorption of the graphene suspension's dispersion effect is indicative of its weak dispersion effect. Figure 3(a) presents uniformly dispersed graphene sheets with HRWRA after 30 minutes of sonication. The aggregations of graphene sheets without PCE and HRWRA as the surfactant are shown in Fig. 3(b). After sonication,

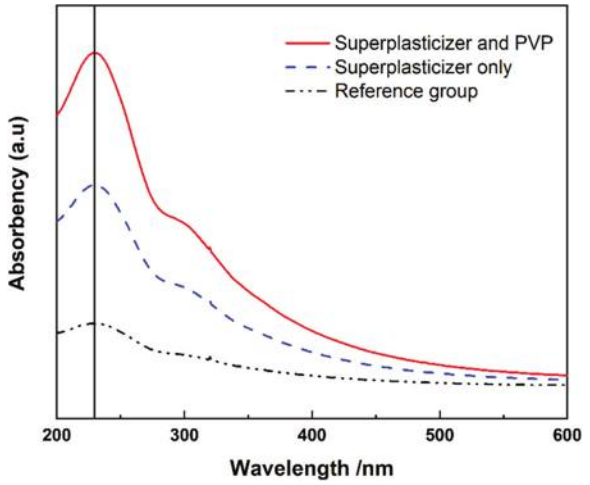

Fig. 2—UV-Vis absorbance spectra of graphene sheet suspension with polyvinylpyrrolidone (PVP) and HRWRA.

new cementitious composites with a water-cement ratio (*w*/*c*) of 0.35 were made by mixing the cement and silica sand with the prepared solutions in a cement paste mixer. After mixing, the material was placed into molds to prepare samples with a size of 50 x 50 x 50 mm. The cement mortar specimens were removed from the molds after curing in the laboratory condition for 1 day and then stored in a moist room for 27 days with a relative humidity of 95%. The thickness of graphene is approximately 1.5 nm, with a maximum diameter of up to 10 to 15 μm; the atomic force microscope (AFM) analysis results are shown in Fig. 3(d). The average silica sand particle size is 110 μm.

Heating procedure

The specimens were placed in a furnace and heated at a rate of 1°C/min from 25°C to the target temperature (200, 400, 600, and 800°C). To homogenize the interior temperature, the target temperature was held constant for 2 hours. The specimens were then cooled down naturally in the

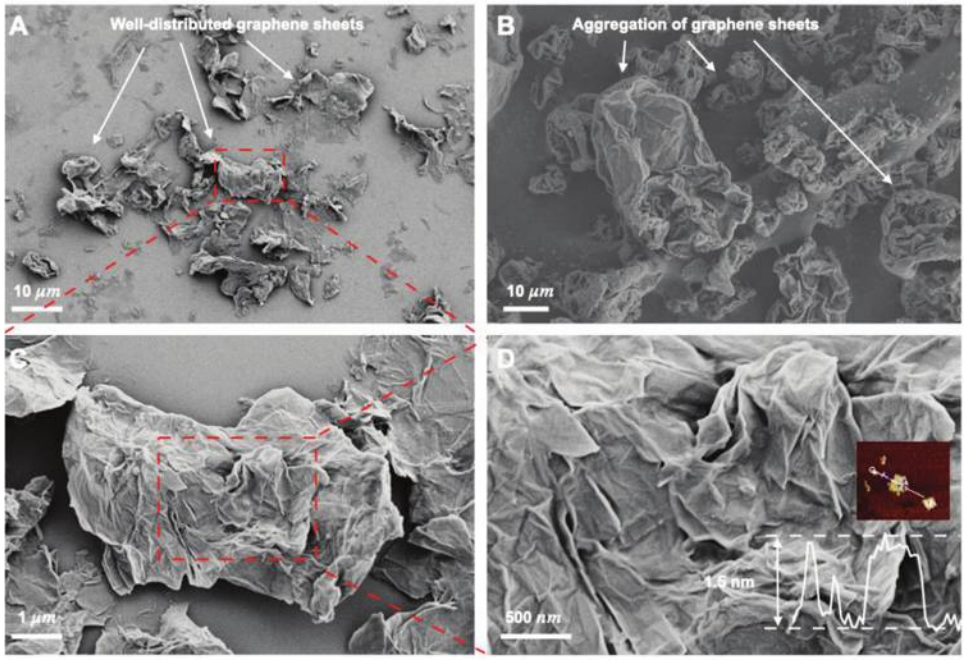

Fig. 3—SEM images of graphene sheet morphology and AFM analysis result.

oven at a moderate cooling rate. The specimens were then spontaneously cooled to room temperature in the furnace for testing and characterization. A hydraulic press machine with a loading rate of 100 kN/min was used to determine the residual compressive strength. The peak loads were measured, and the compressive strength was calculated as the average of three specimens.

Microstructure analysis

To explore the porosity and pore-size distribution of all the samples exposed to different temperatures, a mercury intrusion porosimetry (MIP) system was used to evaluate the pore-structure evolution in cement paste. All the samples were first sliced to a size of 10 x 10 x 10 mm. To avoid additional hydration, the sample was submerged in ethanol for 24 hours. The samples were then removed and put in a vacuum-drying oven at 60°C for 48 hours. The pressure gradually rose from 0.003 to 0.15 MPa during the test, then the penetrometer was taken out of the low-pressure chamber. The penetrometer was placed in the high-pressure chamber after the weight was measured. Mercury pressure was raised to the maximum of 227 MPa. The mercury was driven into the pores of the samples when the pressure increased. The highest volume of intruded mercury can be used to assess the sample's porosity. After completely preparing the samples with grinding and polishing operations, a scanning electron microscope (SEM) working at a 5 kV accelerating voltage was used to observe microstructural changes of different samples at different temperatures.

EXPERIMENTAL RESULTS AND DISCUSSION

Mechanical properties and microstructure analysis

As shown in Fig. 4(a) and (c), the presence of graphene in cement mortar not only played a significant role in the reinforcement effect on cement mortar samples at room temperature, but also effectively mitigated the thermal-detriment phenomenon under high temperatures. The compressive strength of these samples with 0.1 wt. % (GC01) and 0.2 wt. % (GC02) graphene improved by 10.7% and 24.7%, respectively, compared to neat cement mortar (GC00) at 25°C (Fig. 4(a)). This is consistent with the observations in the literature.[16,32] With increasing temperature, the compressive performance of GC00, GC01, and GC02 presented a similar trend. After 200°C, all samples showed better mechanical properties due to the rehydration of cement particles.[29,33] After heating up to 400°C, the residual mechanical strength of all samples started to decrease. The significant deterioration of mechanical properties occurred after exposure to 800°C. As shown in Fig. 4(c), the relative residual compressive strength enhanced with a higher content of graphene at 200 to 400°C or 600 to 800°C. However, the reinforcement effect of graphene on the cement matrix showed varied trends with increasing temperature. When exposed to 200 and 400°C, graphene-reinforced samples had a decreased reinforcement efficiency, while GC01 and GC02 presented enhanced reinforcement impact when heated up to 600 and 800°C.

Pore-structure evolution

Figures 5 to 7 show the pore-structure evolution at different temperatures for all the samples. Before thermal treatment, due to the compact action of graphene on the microstructure of cement hydration products, GC02 showed lower microporosity than GC01 and GC00 (Fig. 5 and 6(a)). As the temperature rose, total cumulative intrusion curves demonstrated a consistent increasing trend, and the pore access domain that was altered by heat seemed to switch from mesopores to the outer porosity of C-S-H, which corresponded to the inflection point of approximately 500 to 1100 nm in Fig. 6(c) to (e). The reference attributed these phenomena to several factors: 1) recrystallization, which

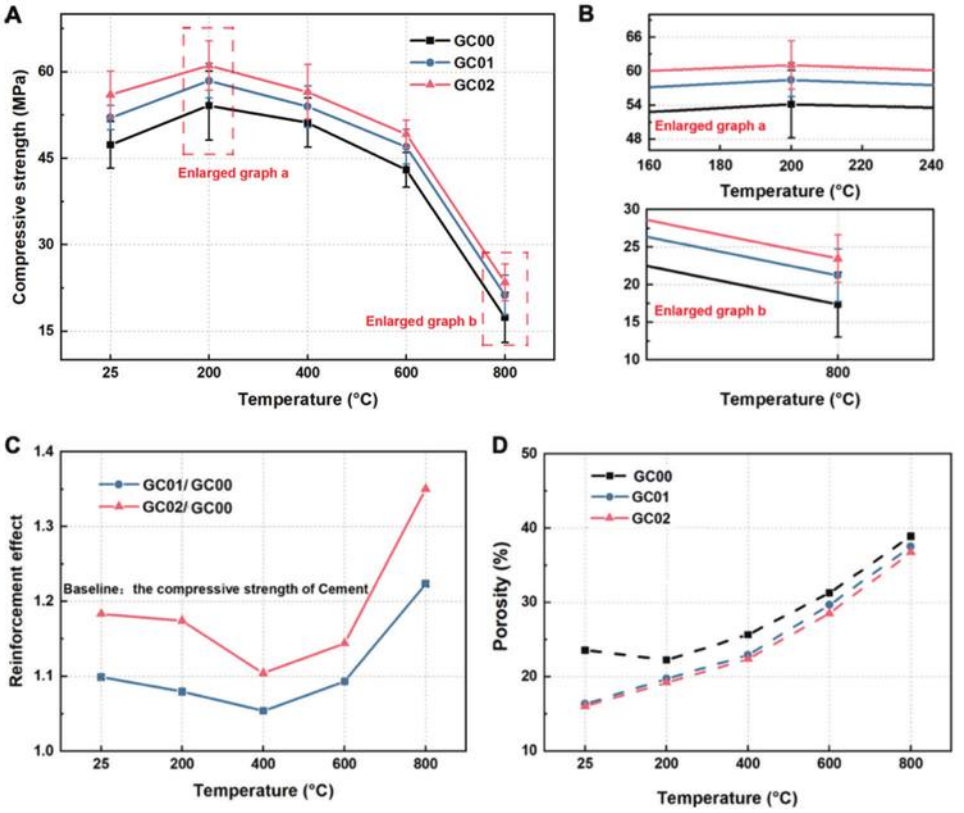

Fig. 4—Strength and porosity of cement specimens before and after exposure to different temperatures.

causes a decrease in the volume of C-S-H[30]; 2) significant changes in the shape of calcium hydroxide crystals[34]; and 3) fracturing at the specimen's edges when heated to 600°C.[35] Interestingly, the cumulative intrusion volume curves of GC01 and GC02, larger than 100 nm, remained lower than those of the reference samples, which explains why the strength of the specimens with graphene was always higher than the ones without graphene. The situation with cumulative intrusion volume curves (ranging from 5 to 100 nm) is more complex, as depicted in Fig. 6(f) to (j). The specimens reinforced with graphene exhibited a reinforcement effect similar to that shown in Fig. 4(c). Specifically, at 400°C, there was a higher intrusion volume observed between 5 and 100 nm, followed by a lower intrusion volume than the reference when heated beyond 400°C.

More significant information concerning pore-structure degradation and the effect of graphene on this process was provided by the differential curves. Overall, thermal treatments resulted in damage development and created significant capillary pore distribution peaks (500 to 1100 nm) in all samples. From 25 to 200°C, there was only one distribution peak in each sample (approximately 20 to 100 nm), as shown in Fig. 6(f) and (g). When the temperature was beyond 400°C, thermal damage generated extra pore volume and introduced a new distribution peak for all samples with the size class of approximately 0.5 to 1.1 μm. They were associated with the decomposition and shrinkage of hydration products and the development of cracks, as described in Zhang et al.[30] Beyond 600°C, the recrystallization and decomposition of C-S-H[25,36] are generally regarded as the most important factors causing a porous microstructure and the failure of cement composites. As a result of the introduced capillary pores, the compressive strength started to decrease, as shown in Fig. 4(a). When the temperature continually rose to 800°C, the diameter of capillary pores from thermal degradation and thermal damage was up to 1.2 to 8 μm. At this stage, the dehydration of C-S-H and CH was the main reason that contributed to the dramatic increase in porosity (from 29 to 39%).

Furthermore, the pore regulation effect of graphene on cement mortar at elevated temperature was evident by the analysis of the differential curves. From Fig. 6(f) and (g), the differential curve peaks strength (from 5 to 100 nm) of GC02 gradually increased beyond that of the reference group. When the temperature increased to 400°C (Fig. 6(h)), the differential curves between 30 to 50 nm of both GC01 and GC02 stayed at the top of the neat cement mortar curve. This indicated that more mesopores were generated in graphene groups when exposed to 200 and 400°C. In addition, the phenomenon that GC02 possessed a larger peak diameter (39 nm) than GC01 (32 nm) also suggested graphene inside cement mortar might have a negative impact on the restriction of mesopores, resulting in decreased reinforcement efficiency. During this process, the accumulated mesopores gradually merged into capillary pores with the appearance of another capillary pore distribution peak. The compressive strength of all samples started to decrease at this moment, as shown in Fig. 4(a). The nanopore regulating function of graphene was further diminished following the formation of capillary pore distribution peaks, and the distribution curves (approximately 100 nm) of all samples overlapped when exposed to 800°C. The overlapped pore differential

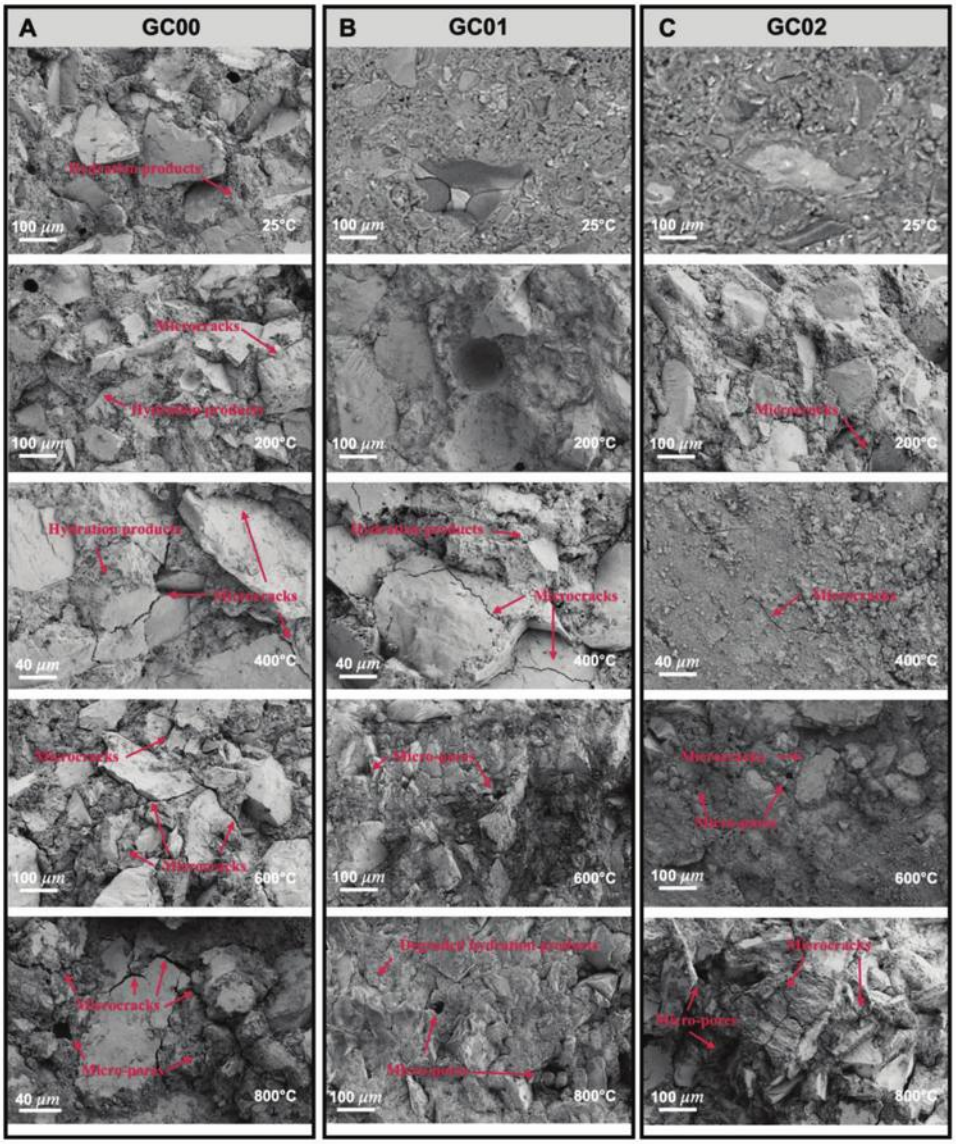

Fig. 5—SEM analysis of specimens before and after exposure to high temperatures: (a) GC00; (b) GC01; and (c) GC02.

curves (approximately 100 nm) of all samples illustrated that graphene lost control of nanoscale damage.

Although its nanopore regulation effect was continually being weakened, graphene showed a significant inhibition toward the development of capillary pores (500 to 1100 nm). According to Fig. 6(h) to (j), the pore differential curves of GC01 and GC02 were kept to the left of the reference group curve, even at 800°C. The smaller differential curve peaks and diameters hinted that graphene may have a positive influence on capillary pore inhibition when the temperature was beyond 400°C.

When exposed to elevated temperature, the pore volume fraction content of both coarse mesopores and intermediate capillary pores gradually increased, while that of thin mesopores decreased. However, samples with a higher content of graphene presented better mitigation of pore volume evolution. For temperatures lower than 400°C (Fig. 6(a) to (d)), the pore volume fraction of the capillary pore (>100 nm) of GC01 and GC02 was always lower than GC00, and graphene-toughened samples showed smaller diameters of differential peaks than GC00 (Fig. 6(f) to (j)). Notably, when heated beyond 400°C, the regulatory effect of graphene on mesopores and intermediate capillary pores continually weakened, with gradual overlapping of peaks between 5 and 100 nm. In contrast, the smaller differential peak (between 1000 and 10,000 nm) diameters of GC01 and GC02 than those of the control group suggested that the reinforced domain of graphene shifted from mesopores to capillary pores. The shift was strongly associated with the interface evolution of graphene and the cement matrix.

Interface evolution of graphene and cement matrix

The representative high-resolution SEM images containing graphene are shown in Fig. 8 for a better understanding of the interface evolution between graphene and the matrix with temperature changes. At ambient temperature, graphene anchored in the cement matrix presented stretching morphology (Fig. 8(a)) and played an important role in pore-structure regulation, contributing to the improved compressive strength of graphene-reinforced groups. When it was exposed to elevated temperature, because graphene sheets exhibited an in-plane rotation and

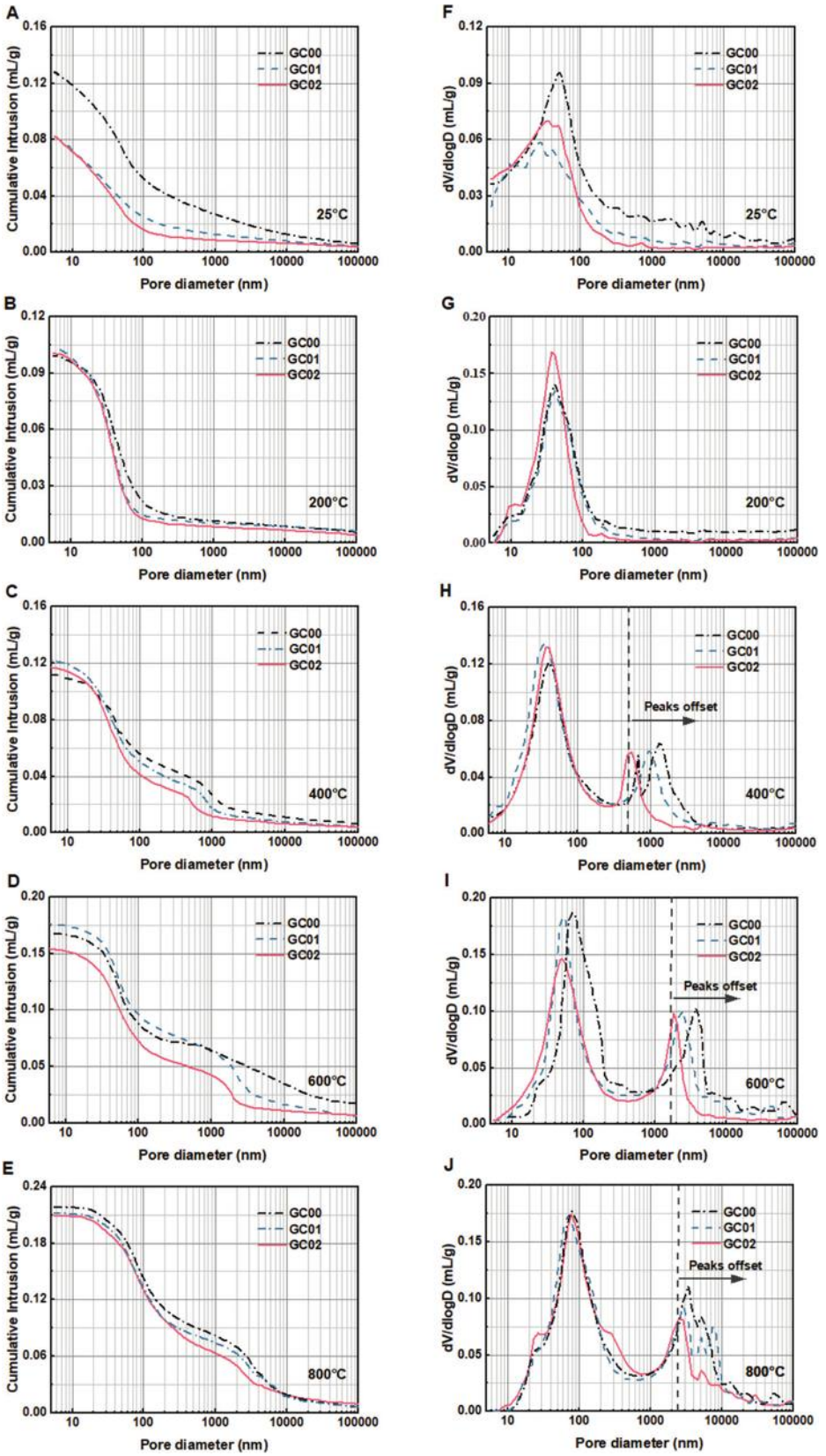

Fig. 6—(a) to (e) Cumulative intrusion volume curves; and (f) to (j) pore distribution curves before and after exposure to high temperatures.

out-of-plane rippling,[26,27] some ripples appeared on the mixture of graphene sheets and hydration products, as shown in Fig. 8(b). According to Bao et al.,[27] the thermal rippling could reach up to 30 nm. Interestingly, the MIP results in Fig. 6(f) to (g) show a similar trend. When heated up to 200°C, the mesopore (25 to 50 nm) content of GC02 increased significantly and had a higher peak intensity than GC01 and GC00. Additionally, the addition of graphene

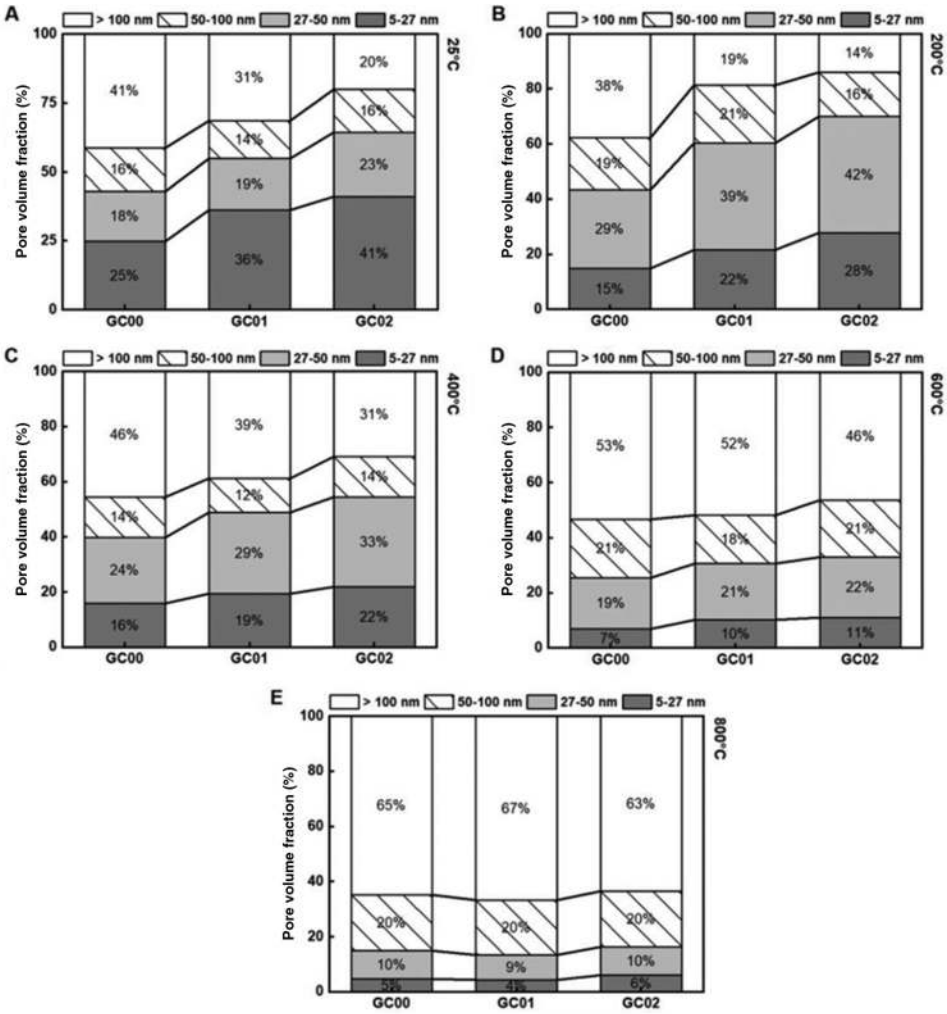

Fig. 7—Pore volume fraction of specimens at ambient temperature (25°C) and after exposure to 200, 400, 600, and 800°C.

reinforcement (GC01 with 20% and GC02 with 19%) resulted in a greater increase in pore size between 27 and 50 nm compared to samples without graphene (GC00 with 11%), as shown in Fig. 7(a) to (b). It is reasonable to attribute the additional mesopores in the cement matrix of approximately 25 to 50 nm to the thermal deformation of graphene. Element line scanning also verified the presence of graphene ripples in Fig. 8(g), as illustrated in Fig. 9(a).

When heated up to 400°C, the continual thermal deformation (Fig. 8(c) and (d)) further widened the mesopores and microcracks around the interface of graphene and the cement matrix. It should be noted that the graphene (Fig. 8(d)) partially debonded from the cement matrix, introducing nanoscale cracks and extra mesopores, as mentioned earlier. However, as the authors discussed in the section "Pore-structure evolution," due to the accumulation and merging of mesopores, the appearance of another capillary pore distribution peak gradually resulted in the diminishing of the nanopore regulating function of graphene. The reinforcement efficiency of graphene-reinforced samples presented a decreasing reinforcement trend, as shown in Fig. 4(c), which was illustrated in Fig. 9(b). Nevertheless, the graphene was still embedded in the hydration product, which could still play a role in controlling the development of large-scale capillary pore sizes, as shown in Fig. 6(h).

When the temperature increased beyond 600°C, the graphene sheets continually debonded from the matrix and formed several wrinkle morphologies in Fig. 8(e). Through Fig. 8(i), it is found that the ripples are the combination of C-S-H and graphene with the high strength of silicon and carbon elements. When the cement samples were heated to 800°C, most of the hydration products decomposed and recrystallized,[30,37] forming a porous cement matrix. Interestingly, the embedded graphene in the cement matrix acted as a frame that restricted the propagation of pores and cracks, as shown in Fig. 8(f), which was illustrated in Fig. 9(c). The influence of interface evolution on the microstructure was revealed by quantitative analysis. For all the samples, the distribution peaks between 10 and 100 nm overlap in Fig. 6(j). When the temperature was raised to 600 to 800°C, graphene gradually fell off from the cement-based matrix, which gradually weakened the control effect of graphene on nanopores. However, because graphene was not completely stripped from the matrix, the groups with graphene still had smaller pore-size distributions at the stage of 0.4 to 10 μm compared with GC00. Therefore, the graphene at 600 and 800°C showed a better reinforcement effect in cement mortar.

In summary, when all samples were exposed to elevated temperature, due to the out-of-plane deformation of

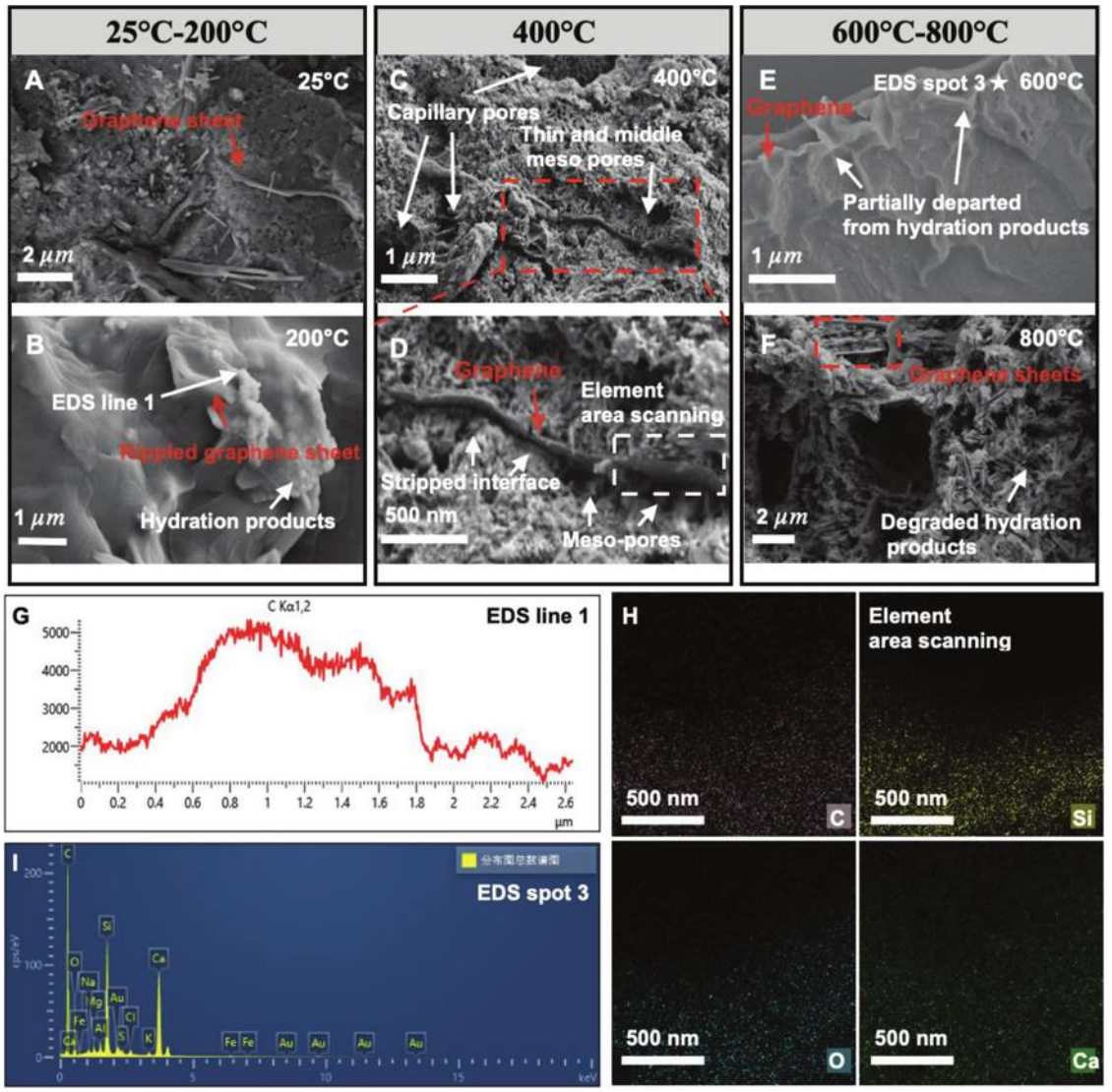

Fig. 8—(a) to (f) SEM micrographs of interface between graphene and cement matrix before and after exposure to high temperatures; and (g) to (i) energy-dispersive X-ray spectroscopy (EDS) results.

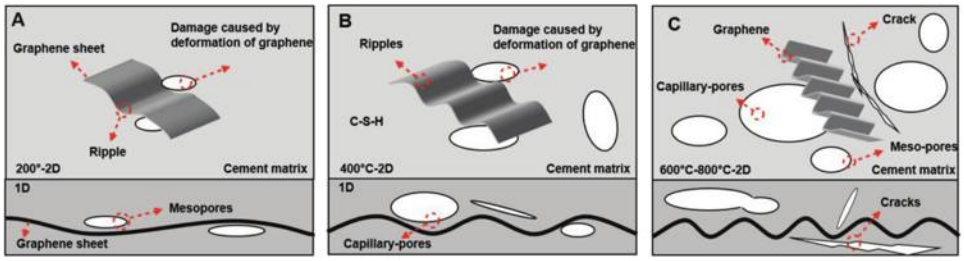

Fig. 9—Schematic diagram of interface development of graphene and cement matrix at different temperatures.

graphene, the interface of graphene and cement gradually departed and introduced damage inside the cement matrix. The pore volume fraction content of coarse mesopores and intermediate capillary pores inside graphene groups grew progressively, whereas thin mesopores decreased and resulted in the decreased graphene reinforcement efficiency from 200 to 400°C. The enlarged mesopores of graphene groups compared with the reference group before 400°C is one of the keys that reduced the graphene reinforcement effect on cement mortar (Fig. 9(a) and (b)). With increasing temperature, the graphene sheets gradually debonded from the matrix and formed several wrinkle morphologies, as shown in Fig. 8(e). However, according to the SEM analysis (Fig. 8(f)), graphene sheets still presented an anti-damage effect and showed a superior mitigation effect on capillary pore volume evolution (from 500 to 1100 nm), as shown in Fig. 6(h) to (j). Beyond 400°C, the superior capillary pore volume (from 500 to 1100 nm) inhibition effect contributed to better post-fire mechanical strength properties of the graphene groups (Fig. 9(b) and (c)). In other words, when

graphene was heated over 400°C, its regulating impact on mesopore and intermediate capillary pores gradually weakened, with progressive overlapping of peaks between 5 and 100 nm. GC01 and GC02 had lower differential peak sizes (within 1000 to 10,000 nm) than the control group, showing that the reinforced domain of graphene switched from mesopores to capillary pores. The change was strongly linked to the development of the graphene-cement matrix contact.

CONCLUSIONS

The mechanical properties, phase composition, and pore-structure evolution of graphene-toughened cement-based materials under high temperatures were investigated. The main findings are listed as follows:

1. The experimental results show that the incorporation of graphene can effectively improve the high-temperature performance of cement-based materials, and the toughening effect of cement-based materials presents two distinct stages.

2. Graphene embedded in a cement matrix undergoes out-of-plane deformation under the effect of temperature. This deformation led to the continuous evolution of the interface between graphene and the cement-based material, which affected the evolution of the cement-based microstructure, finally resulting in the change in the macroscopic toughening effect.

3. After exposure to 200°C, ripples could be observed at the interface between graphene and hydration products, which contrasted with the tightly bound interface between graphene and hydration products at room temperature. Mercury intrusion porosimetry (MIP) results indicated the thin mesopores gradually transformed into middle mesopores when the temperature was heated to 200 and 400°C. Further deterioration of the interface was observed with elevated temperature because of the graphene deformation up to 400°C.

4. After the samples were exposed to 600°C, cracks and pores were introduced at the interface due to thermally mismatched graphene and the cement matrix, resulting in a complete loss of the control of nanopores. Mechanical and MIP experiments show that the development of capillary pores is controlled in graphene-reinforced samples at this stage, revealing the restriction on the capillary development of graphene.

AUTHOR BIOS

Zhenyu Zhang *was a Research Assistant in the School of Civil Engineering at Xi'an University of Architecture and Technology, Xi'an, Shaanxi, China. He is currently a PhD Student in the School of Civil and Environmental Engineering at Nanyang Technological University, Singapore. He received his BS from Hunan Agricultural University, Changsha, Hunan, China, in 2018 and his MS from Xi'an University of Architecture and Technology in 2022. His research interests include the performance of advanced green construction materials and functional building materials.*

Yao Yao *is Chair Professor of the School of Civil Engineering at Xi'an University of Architecture and Technology. He received his BS from Tongji University, Shanghai, China, in 1999; his MS from Nanyang Technological University in 2002; and his PhD from Northwestern University, Evanston, IL, in 2008. His research interests include the mechanical properties of advanced materials and the reliability of structures under extreme load.*

Hu Liu *is an Associate Professor in the School of Chemistry and Chemical Engineering at Xi'an University of Architecture and Technology. He received his BS from Lanzhou University, Lanzhou, Gansu, China, in 2010; his MS from Xinjiang University, Ürümqi, Xinjiang, China, in 2013; and his PhD from Harbin Institute of Technology, Harbin, Heilongjiang, China, in 2019. His research interests include advanced functional building materials and functional precious metal nanomaterials.*

Dong Zhang *is an Associate Professor in the Department of Civil and Environmental Engineering at Fuzhou University, Fuzhou, Fujian, China. He received his BS and MS from Central South University, Changsha, Hunan, China, in 2008 and 2011, and his PhD from Nanyang Technological University in 2020. His research interests include ultra-high-performance concrete (UHPC) and advanced functional building materials.*

Yan Zhuge *is a Professor in the Department of Structural Engineering at the University of South Australia, Adelaide, SA, Australia. She received her BEng (Hons) in civil engineering and her master's in structural engineering from Beijing, China, and her PhD in structural engineering from Queensland University of Technology (QUT), Brisbane, QLD, Australia. Her research interests include green concrete materials, fiber composite structures, and seismic retrofitting of masonry structures.*

ACKNOWLEDGMENTS

The authors would like to acknowledge the financial support from the National Natural Science Foundation of China (No. 11772257), Natural Science Foundation of Shaanxi Province (No. 2020JM-103 and 2021JM-356), and Fundamental Research Funds for the Central Universities (No. G2019KY05212). The authors declare that they have no conflict of interest.

REFERENCES

1. Zhao, L.; Guo, X.; Song, L.; Song, Y.; Dai, G.; and Liu, J., "An Intensive Review on the Role of Graphene Oxide in Cement-Based Materials," *Construction and Building Materials*, V. 241, Apr. 2020, Article No. 117939. doi: 10.1016/j.conbuildmat.2019.117939

2. Lin, Y., and Du, H., "Graphene Reinforced Cement Composites: A Review," *Construction and Building Materials*, V. 265, Dec. 2020, Article No. 120312. doi: 10.1016/j.conbuildmat.2020.120312

3. Mohan, V. B.; Lau, K.-T.; Hui, D.; and Bhattacharyya, D., "Graphene-Based Materials and Their Composites: A Review on Production, Applications and Product Limitations," *Composites Part B: Engineering*, V. 142, June 2018, pp. 200-220. doi: 10.1016/j.compositesb.2018.01.013

4. Krystek, M.; Ciesielski, A.; and Samorì, P., "Graphene-Based Cementitious Composites: Toward Next-Generation Construction Technologies," *Advanced Functional Materials*, V. 31, No. 27, July 2021, Article No. 2101887. doi: 10.1002/adfm.202101887

5. Yao, Y.; Zhang, Z.; Liu, H.; Zhuge, Y.; and Zhang, D., "A New In-Situ Growth Strategy to Achieve High Performance Graphene-Based Cement Material," *Construction and Building Materials*, V. 335, June 2022, Article No. 127451. doi: 10.1016/j.conbuildmat.2022.127451

6. Lu, D.; Ma, L.-P.; Zhong, J.; Tong, J.; Liu, Z.; Ren, W.; and Cheng, H.-M., "Growing Nanocrystalline Graphene on Aggregates for Conductive and Strong Smart Cement Composites," *ACS Nano*, V. 17, No. 4, Feb. 2023, pp. 3587-3597. doi: 10.1021/acsnano.2c10141

7. Lu, D.; Huo, Y.; Jiang, Z.; and Zhong, J., "Carbon Nanotube Polymer Nanocomposites Coated Aggregate Enabled Highly Conductive Concrete for Structural Health Monitoring," *Carbon*, V. 206, Mar. 2023, pp. 340-350. doi: 10.1016/j.carbon.2023.02.043

8. Zhu, Y.; Murali, S.; Cai, W.; Li, X.; Suk, J. W.; Potts, J. R.; and Ruoff, R. S., "Graphene and Graphene Oxide: Synthesis, Properties, and Applications," *Advanced Materials*, V. 22, No. 35, Sept. 2010, pp. 3906-3924. doi: 10.1002/adma.201001068

9. Geim, A. K., "Graphene: Status and Prospects," *Science*, V. 324, No. 5934, June 2009, pp. 1530-1534. doi: 10.1126/science.1158877

10. Kinloch, I. A.; Suhr, J.; Lou, J.; Young, R. J.; and Ajayan, P. M., "Composites with Carbon Nanotubes and Graphene: An Outlook," *Science*, V. 362, No. 6414, Nov. 2018, pp. 547-553. doi: 10.1126/science.aat7439

11. Lin, C.; Wei, W.; and Hu, Y. H., "Catalytic Behavior of Graphene Oxide for Cement Hydration Process," *Journal of Physics and Chemistry of Solids*, V. 89, Feb. 2016, pp. 128-133. doi: 10.1016/j.jpcs.2015.11.002

12. Zhao, L.; Guo, X.; Liu, Y.; Zhao, Y.; Chen, Z.; Zhang, Y.; Guo, L.; Shu, X.; and Liu, J., "Hydration Kinetics, Pore Structure, 3D Network Calcium Silicate Hydrate, and Mechanical Behavior of Graphene Oxide Reinforced Cement Composites," *Construction and Building Materials*, V. 190, Nov. 2018, pp. 150-163.

13. Nasibulin, A. G.; Koltsova, T.; Nasibulina, L. I.; Anoshkin, I. V.; Semencha, A.; Tolochko, O. V.; and Kauppinen, E. I., "A Novel Approach to Composite Preparation by Direct Synthesis of Carbon Nanomaterial on Matrix or Filler Particles," *Acta Materialia*, V. 61, No. 6, Apr. 2013, pp. 1862-1871. doi: 10.1016/j.actamat.2012.12.007

14. Lin, J.; Shamsaei, E.; de Souza, F. B.; Sagoe-Crentsil, K.; and Duan, W. H., "Dispersion of Graphene Oxide–Silica Nanohybrids in Alkaline Environment for Improving Ordinary Portland Cement Composites," *Cement and Concrete Composites*, V. 106, Feb. 2020, Article No. 103488.

15. Shang, Y.; Zhang, D.; Yang, C.; Liu, Y.; and Liu, Y., "Effect of Graphene Oxide on the Rheological Properties of Cement Pastes," *Construction and Building Materials*, V. 96, Oct. 2015, pp. 20-28. doi: 10.1016/j.conbuildmat.2015.07.181

16. Long, W.-J.; Wei, J.-J.; Xing, F.; and Khayat, K. H., "Enhanced Dynamic Mechanical Properties of Cement Paste Modified with Graphene Oxide Nanosheets and Its Reinforcing Mechanism," *Cement and Concrete Composites*, V. 93, Oct. 2018, pp. 127-139. doi: 10.1016/j.cemconcomp.2018.07.001

17. Saafi, M.; Tang, L.; Fung, J.; Rahman, M.; and Liggat, J., "Enhanced Properties of Graphene/Fly Ash Geopolymeric Composite Cement," *Cement and Concrete Research*, V. 67, Jan. 2015, pp. 292-299. doi: 10.1016/j.cemconres.2014.08.011

18. Shamsaei, E.; de Souza, F. B.; Yao, X.; Benhelal, E.; Akbari, A.; and Duan, W., "Graphene-Based Nanosheets for Stronger and More Durable Concrete: A Review," *Construction and Building Materials*, V. 183, Sept. 2018, pp. 642-660.

19. Li, G.; Yuan, J. B.; Zhang, Y. H.; Zhang, N.; and Liew, K. M., "Microstructure and Mechanical Performance of Graphene Reinforced Cementitious Composites," *Composites Part A: Applied Science and Manufacturing*, V. 114, Nov. 2018, pp. 188-195.

20. Qureshi, T. S., and Panesar, D. K., "Nano Reinforced Cement Paste Composite with Functionalized Graphene and Pristine Graphene Nanoplatelets," *Composites Part B: Engineering*, V. 197, Sept. 2020, Article No. 108063. doi: 10.1016/j.compositesb.2020.108063

21. Mohammed, A.; Sanjayan, J. G.; Nazari, A.; and Al-Saadi, N. T. K., "Effects of Graphene Oxide in Enhancing the Performance of Concrete Exposed to High-Temperature," *Australian Journal of Civil Engineering*, V. 15, No. 1, 2017, pp. 61-71. doi: 10.1080/14488353.2017.1372849

22. Chu, H.-Y.; Jiang, J.-Y.; Sun, W.; and Zhang, M., "Effects of Graphene Sulfonate Nanosheets on Mechanical and Thermal Properties of Sacrificial Concrete during High Temperature Exposure," *Cement and Concrete Composites*, V. 82, Sept. 2017, pp. 252-264. doi: 10.1016/j.cemconcomp.2017.06.007

23. Jing, G.; Ye, Z.; Wu, J.; Wang, S.; Cheng, X.; Strokova, V.; and Nelyubova, V., "Introducing Reduced Graphene Oxide to Enhance the Thermal Properties of Cement Composites," *Cement and Concrete Composites*, V. 109, May 2020, Article No. 103559. doi: 10.1016/j.cemconcomp.2020.103559

24. Lu, L.; Zhang, Y.; and Yin, B., "Structure Evolution of the Interface between Graphene Oxide-Reinforced Calcium Silicate Hydrate Gel Particles Exposed to High Temperature," *Computational Materials Science*, V. 173, Feb. 2020, Article No. 109440. doi: 10.1016/j.commatsci.2019.109440

25. Li, G., and Zhang, L. W., "Microstructure and Phase Transformation of Graphene-Cement Composites under High Temperature," *Composites Part B: Engineering*, V. 166, June 2019, pp. 86-94. doi: 10.1016/j.compositesb.2018.11.127

26. Gao, W., and Huang, R., "Thermomechanics of Monolayer Graphene: Rippling, Thermal Expansion and Elasticity," *Journal of the Mechanics and Physics of Solids*, V. 66, May 2014, pp. 42-58. doi: 10.1016/j.jmps.2014.01.011

27. Bao, W.; Miao, F.; Chen, Z.; Zhang, H.; Jang, W.; Dames, C.; and Lau, C. N., "Controlled Ripple Texturing of Suspended Graphene and Ultrathin Graphite Membranes," *Nature Nanotechnology*, V. 4, No. 9, Sept. 2009, pp. 562-566. doi: 10.1038/nnano.2009.191

28. Zhang, D.; Dasari, A.; and Tan, K. H., "On the Mechanism of Prevention of Explosive Spalling in Ultra-High Performance Concrete with Polymer Fibers," *Cement and Concrete Research*, V. 113, Nov. 2018, pp. 169-177. doi: 10.1016/j.cemconres.2018.08.012

29. Zhang, D.; Tan, K. H.; Dasari, A.; and Weng, Y., "Effect of Natural Fibers on Thermal Spalling Resistance of Ultra-High Performance Concrete," *Cement and Concrete Composites*, V. 109, May 2020, Article No. 103512. doi: 10.1016/j.cemconcomp.2020.103512

30. Zhang, Q.; Ye, G.; and Koenders, E., "Investigation of the Structure of Heated Portland Cement Paste by Using Various Techniques," *Construction and Building Materials*, V. 38, Jan. 2013, pp. 1040-1050. doi: 10.1016/j.conbuildmat.2012.09.071

31. GB 175-2007, "Common Portland Cement," General Administration of Quality Supervision, Inspection and Quarantine of the People's Republic of China, Beijing, China, 2007.

32. Lu, Z.; Hanif, A.; Sun, G.; Liang, R.; Parthasarathy, P.; and Li, Z., "Highly Dispersed Graphene Oxide Electrodeposited Carbon Fiber Reinforced Cement-Based Materials with Enhanced Mechanical Properties," *Cement and Concrete Composites*, V. 87, Mar. 2018, pp. 220-228. doi: 10.1016/j.cemconcomp.2018.01.006

33. Sikora, P.; Abd Elrahman, M.; Chung, S.-Y.; Cendrowski, K.; Mijowska, E.; and Stephan, D., "Mechanical and Microstructural Properties of Cement Pastes Containing Carbon Nanotubes and Carbon Nanotube-Silica Core-Shell Structures, Exposed to Elevated Temperature," *Cement and Concrete Composites*, V. 95, Jan. 2019, pp. 193-204.

34. Handoo, S. K.; Agarwal, S.; and Agarwal, S. K., "Physicochemical, Mineralogical, and Morphological Characteristics of Concrete Exposed to Elevated Temperatures," *Cement and Concrete Research*, V. 32, No. 7, July 2002, pp. 1009-1018. doi: 10.1016/S0008-8846(01)00736-0

35. Kim, K. Y.; Yun, T. S.; and Park, K. P., "Evaluation of Pore Structures and Cracking in Cement Paste Exposed to Elevated Temperatures by X-Ray Computed Tomography," *Cement and Concrete Research*, V. 50, Aug. 2013, pp. 34-40. doi: 10.1016/j.cemconres.2013.03.020

36. Jia, Z.; Chen, C.; Shi, J.; Zhang, Y.; Sun, Z.; and Zhang, P., "The Microstructural Change of C-S-H at Elevated Temperature in Portland Cement/GGBFS Blended System," *Cement and Concrete Research*, V. 123, Sept. 2019, Article No. 105773. doi: 10.1016/j.cemconres.2019.05.018

37. Alonso, C., and Fernandez, L., "Dehydration and Rehydration Processes of Cement Paste Exposed to High Temperature Environments," *Journal of Materials Science*, V. 39, No. 9, May 2004, pp. 3015-3024. doi: 10.1023/B:JMSC.0000025827.65956.18

ACI MATERIALS JOURNAL TECHNICAL PAPER

Title No. 121-M04

Durability of Reinforced Concrete Caisson Parapet Beam Exposed to Mediterranean Seawater after 500 Days

by Igor Lapiro, Rami Eid, and Konstantin Kovler

The penetration of chloride ions causes degradation of reinforcing bars, which directly affects the service life of the element. In this study, four different alternatives for the construction of a reinforced concrete (RC) caisson parapet beam are investigated: conventional RC, the addition of a corrosion inhibitor to concrete, and the use of glass fiber-reinforced bars (GFRP) and galvanized steel instead of steel bars. The durability of the RC element under marine environment was studied based on measurements performed both in-place and in well-controlled laboratory conditions on specimens prepared in the laboratory, as well as specimens taken from the actual structural element.

It was concluded that the exposure of fresh concrete to seawater splash has no effect on mechanical properties. In addition, galvanized rods were found to be a less effective protection strategy compared to the other alternatives studied. GFRP bars, however, provide better protection than the other tested alternatives, although chloride ion penetration in these bars was found to be more accelerated in an alkaline environment compared to a chloride environment.

In contrast to the prevailing approach, which considers plain concrete and according to which the electrical resistance of the concrete decreases because of chloride penetration, this study found that electrical resistance in the reinforced element is increased due to an increase in the amount of corrosion products formed between steel and concrete if no cracks occur.

Furthermore, it was found that the potential measured using the half-cell method in all the alternatives slowly increased with time, as well as the corrosion risk in the three alternatives with reinforcing steel. The remaining question is whether this change of potential is a direct characteristic of the corrosion risk. Therefore, more research in this direction is needed.

Keywords: corrosion; durability; galvanized steel; glass fiber-reinforced bars (GFRP) bars; inhibitor; marine structures.

INTRODUCTION

A significant section of the world's population lives in a marine environment. Accordingly, the infrastructure serving this population is exposed to marine environmental conditions.[1] These environmental conditions contain chemicals that can damage the concrete or initiate corrosion of reinforcing bars.[2] Indeed, corrosion of steel-reinforced concrete (RC) is one of the major deterioration mechanisms causing economic and social losses.[3] RC structures start deteriorating mainly because of chloride-induced corrosion, sulfate-induced corrosion, and carbonation.[4] Furthermore, the concrete itself will be vulnerable if exposed to seawater and will be in conditions of wetting and drying with an aqueous solution containing mainly dissolved sodium chloride and magnesium sulfate. On average, seawater contains approximately 35 g/L (0.291 lb/gal.) of dissolved salts.[5] However, this is variable and depends on specific geographic locations. The concentrations of major ions (Cl^-, Na^+, SO_4^{2-}, Mg^{2+}, K^+, and Ca^{2+}) in the Eastern Mediterranean are 21,200, 11,800, 2950, 1403, 463, and 423 mg/L (0.176, 0.098, 0.024, 0.012, 0.0038, and 0.0035 lb/gal.), respectively.[6] The effects of harmful elements in the seawater and sediments, both in and around the sea, on the properties of the concrete must be taken into account.[7] The chemical reactions of seawater with concrete are mainly due to attack by magnesium sulfate ($MgSO_4$). The mode of this attack is crystallization. Potassium and magnesium sulfates (K_2SO_4 and $MgSO_4$) present in saltwater can cause sulfate attack in concrete due to the possibility of their reaction with calcium hydroxide ($Ca(OH)_2$), which is present in the hardened cement paste formed by the hydration of cement minerals, mainly dicalcium silicate (C_2S) and tricalcium silicate (C_3S).

The simplest way to reduce the risk of corrosion is to ensure an adequate cover depth of at least 40 mm (1.576 in.) and that the concrete itself will be impermeable to harmful substances.[8] To prevent the decay of concrete under this cover layer, it is proposed to improve the concrete mixture by adding pozzolanic mineral components. Pozzolanic additives are used in a dual role: the first as micro fillers and the second as a bonding material.[9,10] Despite the reduction of pores and diffusion coefficient, pozzolanic materials do not affect the corrosion process itself. Therefore, as soon as chlorides contact the reinforcing bars, corrosion develops.[11]

There are additional corrosion protection measures that are not limited to the use of membrane-type coatings applied to the concrete surface, such as painting of concrete, impregnation of concrete with materials intended to reduce its permeability, addition of corrosion inhibitors to concrete, use of corrosion-resisting materials (for example, stainless steels) as replacement for conventional steel reinforcement, cathodic protection of the reinforcement, and application of hot-dip galvanizing coatings to the reinforcement itself. Of these methods, the use of coated steel reinforcement has been widely accepted as an economical and convenient tool for providing corrosion protection in many types of concrete construction. For example, bar zinc coating provides not only simple barrier protection, but also additional cathodic

ACI Materials Journal, V. 121, No. 1, January 2024.

MS No. M-2022-287.R, doi: 10.14359/51740260, received June 14, 2023, and reviewed under Institute publication policies.

protection in which the coating acts as a sacrificial anode in cases where the underlying steel is exposed.

In ordinary concrete, uncoated steel bar depassivates once the pH level drops below ~11.5, though in chloride-contaminated concrete, this depassivation occurs at higher pH levels. In contrast, zinc-coated steel in concrete remains passivated to pH levels of approximately 9.5, thereby offering substantial protection against the effects of carbonation of concrete. In concrete with very high chloride levels, the life of the zinc coating may be somewhat reduced due to early depassivation of the zinc. In these circumstances, however, although the longevity of the galvanized coating may be reduced, the overall life of the reinforcement would still be somewhat longer than that of conventional steel in equivalent concrete and exposure conditions due to the inherently higher chloride tolerance of the zinc coating. Therefore, even zinc coatings do not guarantee long-term durability in a marine environment.

Some researchers suggest using corrosion inhibitors to improve the protection of the reinforcement bars. By definition, a corrosion inhibitor is basically any chemical that lowers the rate of corrosion formation. The presence of the inhibitor should be in an appropriate concentration, without significantly altering the concrete properties and mechanical properties of the steel. Due to their low cost and simple application method (addition to the concrete mixture or spraying over the surface of the element), corrosion inhibitors may be a good alternative to the classical protection and repair method.[12] A mixed inhibitor that consisted of amines and alkanolamines versus a zinc oxide-only inhibitor were examined in the work[13]; it was found that both functioned almost identically. In both cases (1 to 3% by weight inhibitor of the cement weight under exposure conditions of direct 12 volts voltage at medium of 5% NaCl), cracks were formed in the reinforced concrete already after 175 days. Based on these results, it can be estimated that galvanic coating can be equivalent to the mixed inhibitor which further encourages their use. Migratory corrosion inhibitors prevent steel corrosion by creating a thin layer of barrier film that protects the bar surface through an adsorption mechanism. Alkanolamines and their salts are used as organic inhibitors in concrete. The effectiveness of corrosion inhibitors varies according to the number of chlorides in the pore water. If concentration of chlorides is high, the inhibitory function decreases. This means that the chloride concentration will indicate the duration of the inhibitor service.[14]

Another anti-corrosion option is to avoid using steel bars and replacing them with glass fiber-reinforced polymer (GFRP) bars.[15] Beyond the high cost problems compared to conventional construction in carbon steel, the main obstacle in using GFRP bars is because it is considered a new material in civil engineering and, consequently, insufficient data on its performance for long-term exposures.[16] A few studies conducted in this field have shown impairment of long-term mechanical properties. Depending on the type of GFRP reinforcement, the strength of the bars may decrease two to three times in the long term defined between 50 and 120 years.[17] This decrease is explained by an alkaline reaction that can occur due to a combination of temperature effect and the constant tensile strength of fibers and matrix.[18,19] Most studies try to examine the elements in the short term and reflect the results on the long term. However, there may also be a scenario according to which an initial damage caused to the concrete due to the mistakes in primary design, execution, and maintenance (such as improper curing) in the short term is maintained for an extended period so that, in fact, the initial damage becomes the most severe.[20]

The current study deals with durability of reinforced concrete elements under marine environmental conditions and includes both measurements performed in-place and in well-controlled laboratory conditions on specimens prepared in the laboratory, as well as specimens taken from the actual structural element. The use of several alternatives (adding migrating corrosion inhibitor[21] and replacing conventional steel reinforcing bars with those made of galvanized steel and GFRP) is examined to shed light on their effectiveness.

RESEARCH SCOPE

This study investigates the effectiveness of four alternatives of construction of a marine structure (caisson parapet beam) under seawater attack. These alternatives include concrete with and without corrosion inhibitor, and different types of reinforcement (conventional steel, galvanized steel, and GFRP). The results of the in-place investigation are analyzed and compared to those obtained in the laboratory. The alternatives are:

a) Reference concrete with a cover thickness of 75 mm (2.955 in.) and conventional steel reinforcement—the alternative that meets the current standard requirements for durability of reinforced concrete elements in the splash zone.

b) Concrete containing corrosion inhibitor, concrete cover thickness of 40 mm (1.576 in.), and conventional steel reinforcement.

c) Concrete without corrosion inhibitor, concrete cover thickness of 40 mm (1.576 in.), and galvanized reinforcement steel.

d) Concrete without corrosion inhibitor, concrete cover thickness of 40 mm (1.576 in.), and GFRP reinforcing bars.

RESEARCH SIGNIFICANCE

Conventional concrete construction in a marine environment shows often unsatisfactory performance. The research goal is to examine different alternatives to conventional construction of RC concrete caisson parapet beam exposed to seawater attack.

This study describes the results of studying the accelerated degradation process in RC elements exposed to marine environments in laboratory conditions and compares it with a case study in field conditions. Several standard methods for studying durability of RC under seawater attack exist, but comparing their results is not trivial and can lead to inconsistency. In this study, to create similarity in corrosive conditions causing degradation of the reinforced concrete in the laboratory and in-place, the climatic parameters under natural environmental conditions on site were thoroughly measured.

Table 1—Concrete compositions

Sample	Content, kg/m³							Maximum aggregate size, mm	*w*/*c*	*w*/*b*	Air content, %	Unit weight, kg/m³	Slump, mm
	C	W	F	S	I	Aggregates* Fine	Aggregates* Coarse						
N	322	141	81	3	—	1034	804	14	0.43	0.34	1.1	2387	119
I	396	166	99	4	1	740	991	14	0.41	0.33	1.9	2397	115

*Type of aggregates—coarse: dolomite rock, fine: quartz.

Note: C is cement; W is water; F is fly ash; S is superplasticizer; I is corrosion inhibitor; *w*/*c* is water-cement ratio; *w*/*b* is water-binder ratio; N and I is concrete mixtures without and with corrosion inhibitor, respectively; 1 kg/m³ = 1.685555 lb/yd³; 1 mm = 0.0394 in.

CONCRETE MIXTURE DESIGN, CASTING, AND CURING

Two concrete mixture designs are described hereafter. The laboratory samples were prepared from the same concrete mixer (batch) from which the caisson parapet beam was cast in the field. A mixture marked 'N' was a concrete mixture without a corrosion inhibitor. The mixture marked with 'I' included a corrosion inhibitor. The fresh concrete was taken from the mixer on the day of the caisson parapet casting. Compressive, splitting, flexural, pullout (bond), and embedded reinforcement bar tension tests were performed at ages of 7, 28, and 90 days for the two mixtures. All specimens were demolded after 24 hours and kept in two different curing conditions. Half of the specimens were immersed in water and the others in the 3.5 wt% NaCl solution. The specimens cured in the salt solution for 28 days made of the mixture without and with a corrosion inhibitor were marked 'NS' and 'IS', respectively. After this period, all samples were kept in the air under temperature (T) = 21 ± 2°C (69.8 ± 3.6°F) and relative humidity (RH) = 65 ± 5%, until the age of 90 days. After being air-cured, the specimens were cured in the same type of wet conditions (immersed in water and the salt solution) for 24 hours before the mechanical tests (compressive, bond, and splitting strength) to achieve identical humidity conditions in all samples. CEM III 42.5N cement and migrating corrosion inhibitor based on amines and alkanolamines were used in this work. The concrete mixture compositions are shown in Table 1. The water-cement ratio (*w*/*c*) and water-binder ratio (*w*/*b*) have a direct correlation with the density and porosity of cement paste at the onset of hydration. The mechanical characteristics of concrete are directly influenced by these ratios. A decrease in these ratios leads to stronger, more resilient, and more sustainable concrete. Concrete with lower water content results in insufficient water for complete hydration, resulting in an increase in compressive strength as *w*/*c* or *w*/*b* decreases.[22] This is the reason why in this study, the authors chose to work in combination with CEM III 42.5N type cement and another addition of fly ash.

Specimen types

The dimensions of the samples were made based on the requirements of the EN 12390-1 standard. Standard concrete cubes of 100 x 100 x 100 mm (3.94 x 3.94 x 3.94 in.) were used for measuring the compressive strength. Concrete cubes for measuring the splitting tensile strength were 70 x 70 x 70 mm (2.755 x 2.755 x 2.755 in.), and concrete prisms with dimensions 280 x 70 x 70 mm (11.023 x 2.755 x 2.755 in.) were tested for flexural strength. Pullout and tensile strength tests were performed on conventional carbon steel and 12 mm (0.472 in.) GFRP bars embedded in the center of 70 x 70 x 70 mm (2.755 x 2.755 x 2.755 in.) concrete cubes (Fig. 1). The bar in the pullout test was embedded 40 mm (1.5748 in.) inside the concrete cube on one side only. In the tensile strength test, the concrete cube was located in the center, while the bar extended from both ends by 150 mm (5.90551 in.). Three samples were taken from the beam in the field. The dimensions of the cylinders were 74 mm (2.913 in.) diameter and 100 mm (3.937 in.) in height.

Exposure conditions

Site exposure—For the in-place studies of concrete durability, the caisson parapet beam built in 2019 in the Bay Port of Haifa (35°02'N, 32°82'E), in the Eastern Mediterranean, was selected (Fig. 2). During the authors' observations, the average annual temperature was 20.5°C (68.9°F) and the average annual precipitation was 24.41 mm (0.961 in.) (Fig. 2(b)). The average wind speed measured was 3.9 m/s (153.543 in./s) and the maximum wind value was 4.9 m/s (192.913 in./s) and was directed north or northwest. The height of the measured waves ranged from 0.5 to 1.6 m (19.685 to 62.992 in.), mainly from W (258.75 to 281.25 degrees) to WNW (281.25 to 303.75 degrees). Approximately 70% of the annual waves come from these directions. These conditions are considered as representing mild to moderate exposure.

Laboratory exposure—After 28 days of water curing, the specimens for pullout and tension tests were fully submerged in a 3.5% NaCl solution in individual containers. The specimens were subjected to wetting and drying cycles to sustain initiation and propagation corrosion. Both the wetting and drying cycles were carried out at 21 ± 2°C (69.8 ± 3.6°F) and controlled RH 65 ± 5%. All samples were exposed for monthly wetting-and-drying cycles (in total, there were 16 complete cycles of wetting and drying).

Corrosion measurement methods

To examine the development of corrosion at the site, a measuring area of 2 x 1 m (78.74 x 39.37 in.) was marked for each part of the caisson parapet beam. Each area was divided into a grid of 20 x 20 cm (7.874 x 7.874 in.) that matches the spacing of the reinforcement bars. The test is performed according to ASTM C876 for $Cu/CuSO_4$ (CSE) half-cell.[23]

Electrical resistance was measured by an Ohm meter device, with the negative pole connected directly to the reinforcing rod in the concrete and the positive pole connected

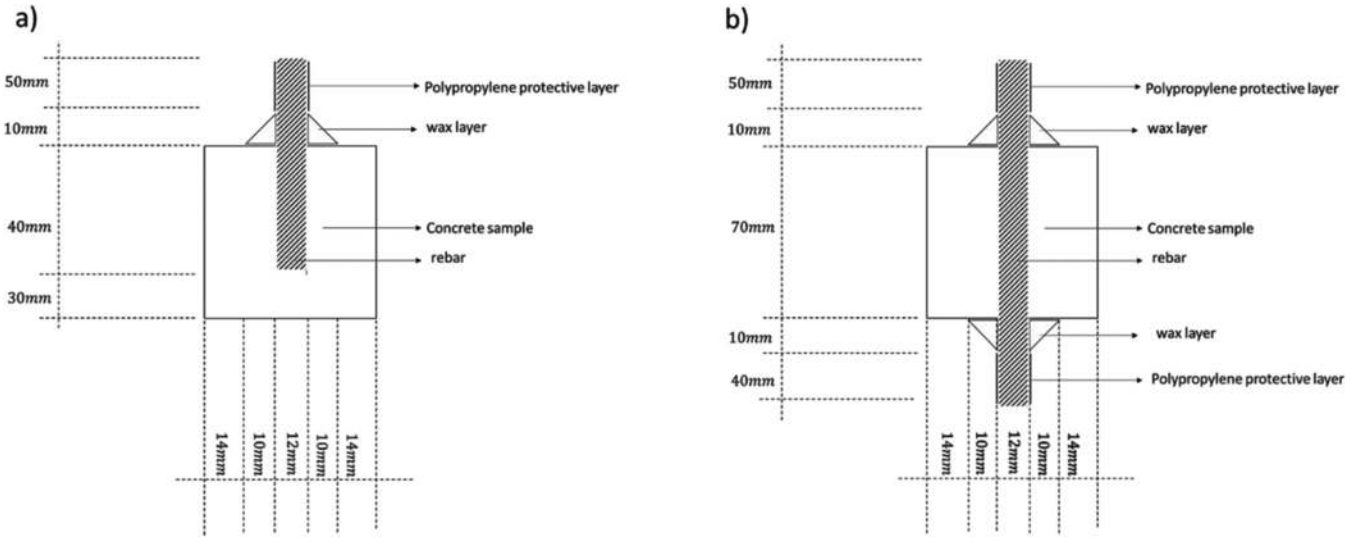

Fig. 1—(a) Pullout; and (b) tensile testing schemes. (Note: 1 mm = 0.0394 in.)

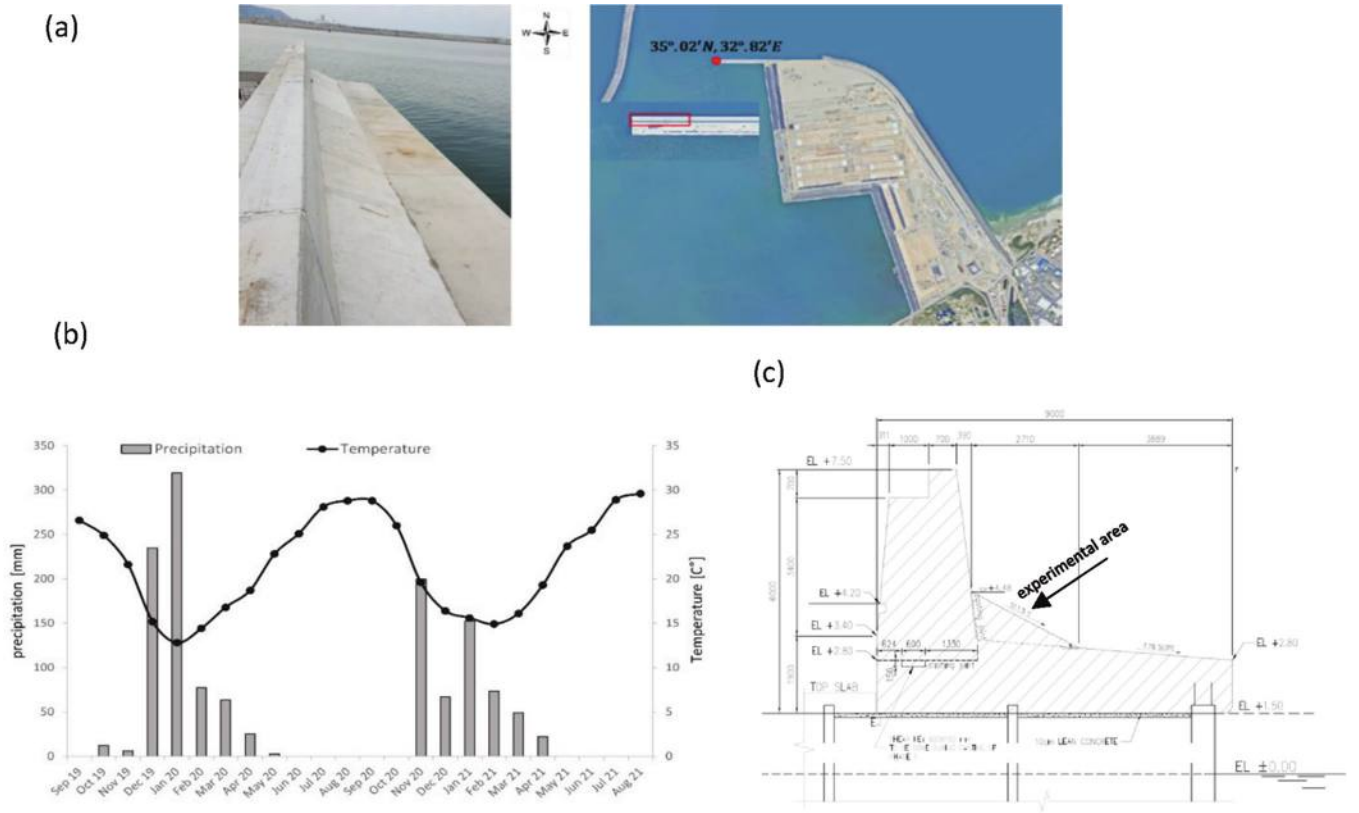

Fig. 2—(a) Observation area and its coordinates; (b) dependence of precipitation and temperature versus time in field conditions; and (c) cross section of parapet beam constructed above caisson. (Note: 1 mm = 0.0394 in.; (°C × 9/5) + 32 = °F.)

to a damp sponge (Fig. 3(a)). Measurements were made in six points along a 1 m (39.37 in.) rod embedded in concrete. In addition, on each day of the experiment, measurements were also made in concrete without metal rods to analyze the change in the properties of the concrete. The average results are shown in Fig. 3(b).

RESULTS AND DISCUSSION

Compressive, splitting, and flexural strength

Concrete is vulnerable to attack when exposed to seawater, especially when there are cycles of wetting and drying in an aqueous solution containing dissolved sodium chloride and magnesium sulfate. As mentioned earlier, these harmful substances exist not only in the seawater but also in rainwater and even in soils and sediments.[24] Information about the influence of marine environments on concrete properties is contradictory. For example, a negative effect of approximately 6% on the compressive strength of the concrete due to curing in seawater was reported.[25] In contrast, no effect at all was observed elsewhere.[26] For this reason, in the first stage, the effect of the marine environment on the specimens through their curing in the saltwater was studied. All

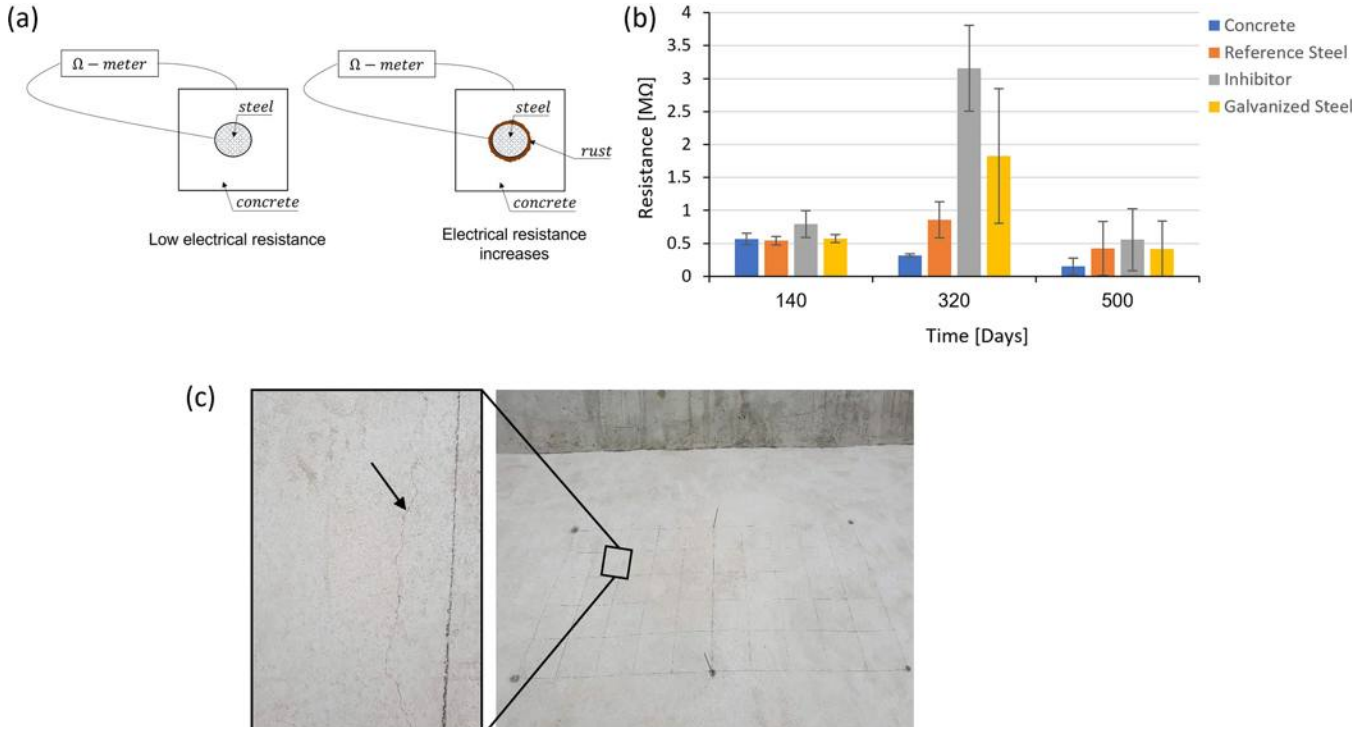

Fig. 3—Testing electrical resistance of concrete: (a) scheme of measuring electrical resistance on reinforced concrete sample with and without corrosion; (b) results of electrical resistance measurements at 140, 320, and 500 days after casting of concrete alone versus electrical resistance of concrete with reference steel, inhibitor, and galvanized steel; and (c) typical image of crack formation after 500 days in all types of areas in field measurement.

specimens were tested at 7, 28, and 90 days after casting for compressive, splitting, and bending strength. Control specimens were exposed to standard curing without the presence of saltwater. By comparing the test results of specimens with different curing conditions, a similar trend was observed for each of the examined days and no significant differences were observed in any of the strengths tested (Fig. 4).

To compare the laboratory compressive strength to that in the field conditions, cylinders were drilled and extracted from the caisson parapet 2 years after the day of casting. The obtained compressive strength was 43.5 ± 5.0 MPa (6309.142 ± 725.189 psi)—that is, significantly lower than that obtained in the laboratory conditions (71.5 ± 0.5 MPa [10,370.2 ± 72.5189 psi]). This significant difference probably occurs due to the poor curing conditions in the large elements in-place compared to the well-controlled curing of the small samples in the lab.[27] It is necessary to note the difference in the dimensions of laboratory samples compared to samples taken from the field, but according to the previous studies, the effect of the dimensions of the samples tested in this experiment was very small compared to the effect of curing.[28,29]

Corrosion tests—impact on mechanical performance

On-site measurements—The half-cell potential is also known as open circuit potential and measures the difference of electrochemical potential versus reference electrode at each measurement point so that potential maps can be obtained. Analysis of results is based on the following values introduced in ASTM C876-15[23] and Kendall et al.[30]: a) if potentials over an area are higher than −0.20 V CSE, there is a greater than 90% probability that no reinforcing steel corrosion is occurring in that area at the time of measurement; b) if potentials over an area are in the range of −0.20 to −0.35 V CSE, corrosion activity of the reinforcing steel in that area is uncertain; and finally, c) if potentials over an area are smaller than −0.35 V CSE, there is a greater than 90% probability that reinforcing steel corrosion is occurring in that area at the time of measurement. Regarding galvanized steel—at a direct connection of the steel to the zinc coating, these values can be more negative than ~135 to 150 millivolts.[31] In the authors' experiment, the stainless electrode was directly connected to the steel rod by welding. That is why the more suitable potential value for analysis would be that of black steel.

Measurements were performed every 6 months after 140 days from the casting of the elements (Fig. 5(a) to (d)). The measurements presented in Fig. 5(d) were made to determine the reference areas that describe the concrete conditions on the day of the measurement, because the element is exposed to the environment in which the conditions change in time. Over time, the electric potential in these reference areas has risen to more positive values. This may indicate increasing probability of corrosion in the areas containing steel because of penetration and accumulation of chlorides.

A calculation of the areas suspected of corrosion with different probability is shown in Fig. 6 for each time point. In this figure, "a" refers to the control RC, "b" refers to the RC containing corrosion inhibitor, and "c" refers to concrete reinforced with galvanized reinforcement steel, while "d" is not shown because corrosion cannot occur in GFRP rods.

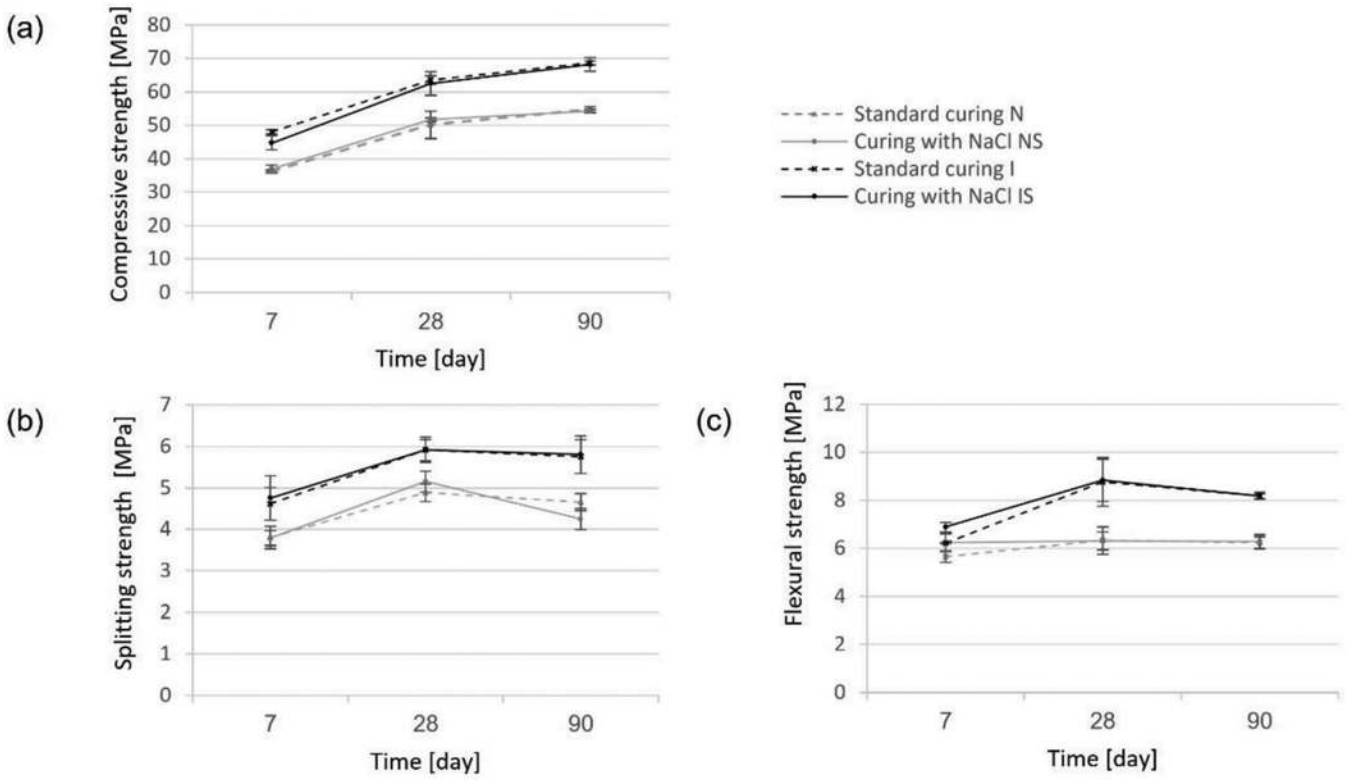

Fig. 4—(a) Compressive; (b) splitting; and (c) flexural strength test results. 'N' is concrete mixture without corrosion inhibitor; 'I' includes corrosion inhibitor. 'N' + salt solution or 'I' + salt solution, marked 'NS' or 'IS', respectively. Values are expressed as mean ± STD, n = 3 specimens. (Note: 1 MPa = 145 psi.)

The measurement after 140 days from casting showed that, for the control RC section, 10.6% of the area suspected of corrosion process with a probability of 90% was already observed—mainly in places where cracks appeared. Moreover, in this control section, the rest of the surface showed a 50% corrosion probability. For the section made of RC containing corrosion inhibitor, the 90% corrosion probability area was like that in the control RC. However, unlike the control section, 59.7% of the RC containing corrosion inhibitor section indicated only 10% probability of corrosion. Figure 6 shows that after 140 days, 60.6% of the area of concrete reinforced with galvanized reinforcement steel indicated 90% probability of corrosion. This was the section with the highest corrosion potential at this time. In the section with GFRP reinforcing bars, the measurements showed uniform values of half-cell potential, between −300 and −350 mV. The authors would like to mention that the difference of ±50 mV in the maps of half-cell potential is small and indicates a measurement error.

In the measurements conducted after 320 days in the reference section, 48.5% of the measurement area showed a 90% probability of corrosion, and 51.5% had a 50% corrosion probability. These results demonstrate a relatively high corrosion risk in the reference section. As mentioned previously, the focal points of corrosion were the long cracks that appeared in the element, and this contributed to the larger distribution of corrosion in the reference section compared with the area measured at the age of 140 days. In the section made of RC containing corrosion inhibitor, only 9% of the area had a 90% probability of corrosion and 56.7% of the area had a 10% probability of corrosion. Also in this area, the high-corrosion-probability locations were the places with cracks. In the section with galvanized steel, 16.7% of the area had a 90% corrosion probability, while 83.3% of the area showed a 50% corrosion risk. As in the previous cases, the cracks in this section triggered the spreading of higher corrosion potential area.

For the measurements carried out after 500 days in the reference section, a reduction was observed in the 90% corrosion probability area, which decreased to 15.2%. This phenomenon can be linked to the filling effect that occurs in the concrete by corrosion products. At the same time, the area with a 50% corrosion probability increased up to 84.8%. In the section containing corrosion inhibitor, the 90% corrosion risk area dropped down to zero from 9% (compared with the measurements at 320 days). The reduction in the high-corrosion-potential area can be explained by the filling effect mentioned previously. At the same time, an increase in the 50% corrosion probability area (up to 60.6%), accompanied by some decrease in the 10% corrosion risk area. This trend seems to be a result of the inhibitor fading effect: it is known that while the migrating inhibitors can be effective in extending the service life of the structure, they can gradually degrade or fade over time. The area with galvanized bars showed a 90% corrosion potential before the corrosion probability decreased to 50%, and here, the phenomenon can be attributed to filling by corrosion products. For the measurements in concrete containing GFRP reinforcing bars, the half-cell potential was more or less uniformly distributed over the experimental section at ±50 mV.

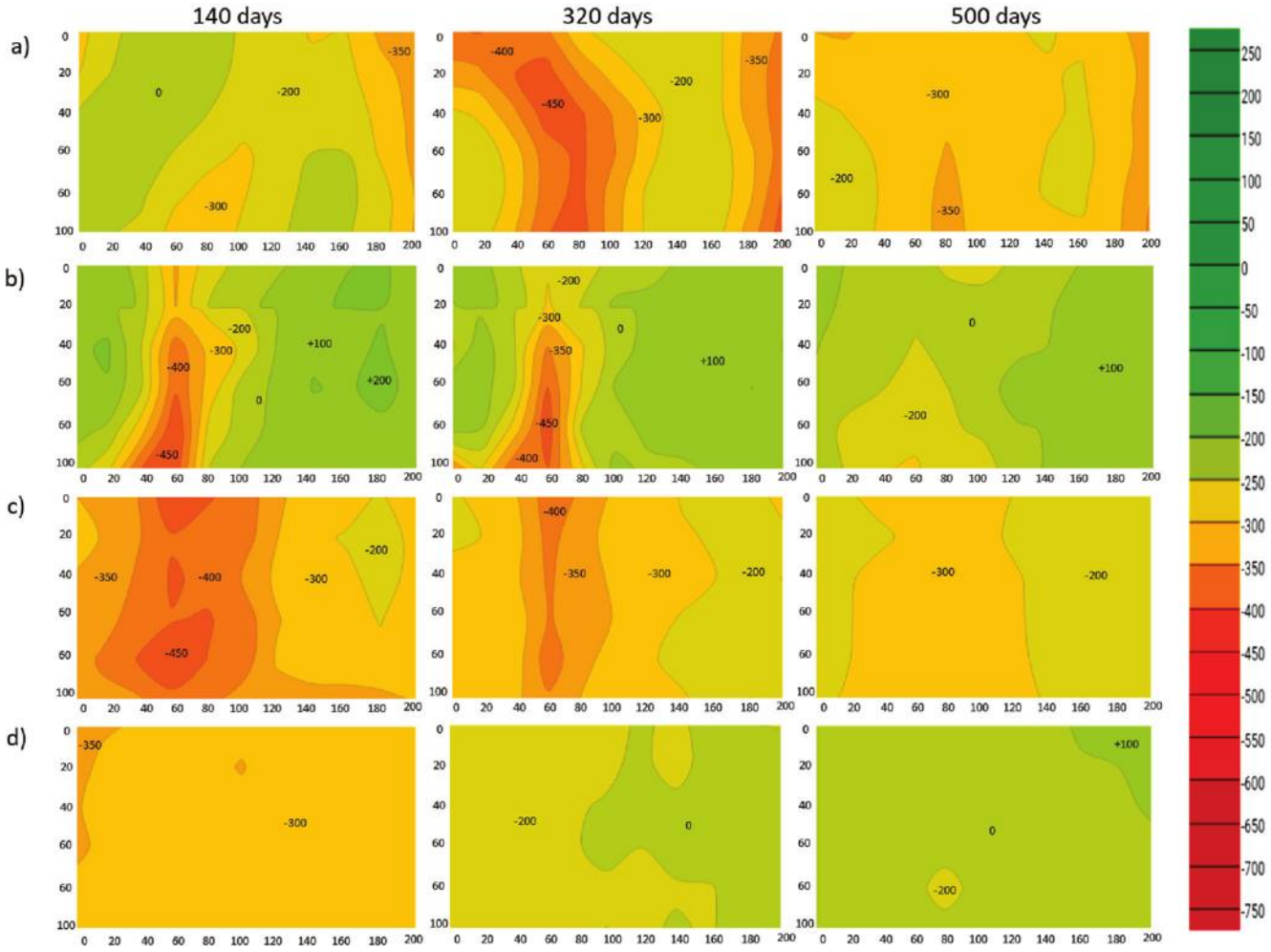

Fig. 5—Site (200 x 100 cm) mapping of half-cell potential measurement results in mV (color bar on right side of figure): (a) reference concrete with concrete cover thickness of 75 mm and conventional steel reinforcement; (b) concrete containing corrosion inhibitor, cover thickness of 40 mm, and conventional steel reinforcement; (c) concrete without corrosion inhibitor, cover thickness of 40 mm, and galvanized reinforcement steel; and (d) concrete without corrosion inhibitor, cover thickness of 40 mm, and GFRP reinforcement bars. (Note: 1 cm= 0.394 in; 1 mm = 0.0394 in.)

Another parameter that can help in estimating corrosion potential is the electrical resistance of the concrete. As can be seen in Fig. 3(a), the formation of an oxide layer increases the electrical resistance of the sample; however, penetration of chloride ions decreases the electrical resistance, which confirms the findings of the work.[32] This is contrary to the prevailing view that corrosion in reinforced concrete and electrical resistance of concrete have an inverse relationship—that is, the lower the electrical resistance of concrete, the higher the corrosion rate of a steel reinforcing bar. It is worth mentioning that it was also found in the work that concrete resistance affected not only the corrosion rate but also the corrosion potential.[32]

Figure 3(b) shows the electrical resistance measurements of the concrete alone versus the electrical resistance of the concrete together with the steel reinforcing bars, with inhibitor, and concrete with galvanized steel bars. As can be seen, the electrical resistance of the concrete alone decreases over time during the exposure to environmental conditions (please refer to the concrete resistance results on day 140 compared to day 320 and 500).

In the measurements taken 140 days after casting, an insignificant difference in the resistance was observed between the experimental areas. After 320 days, the concrete containing the reference reinforcement steel, inhibitor, and galvanized steel showed an increase in electrical resistance compared to the concrete alone; this is probably due to the formation of a dense oxide layer. This trend disappears in the measurements taken after 500 days. It can be explained by the chloride permeability of the concrete sample and the destruction of this layer. Cracks were also observed on site (Fig. 3(c)), which apparently allowed corrosion products to be released and prevented oxide layers from forming.

These results support the hypothesis that the formation of a dense oxide layer on steel bars insulates the steel and thus prevents the development of corrosion. This phenomenon has been described by Renpu,[33] who concluded that corrosion products form a cover film on a metal surface acting as passivating film because it can prevent electrochemical corrosion from continuous generation.

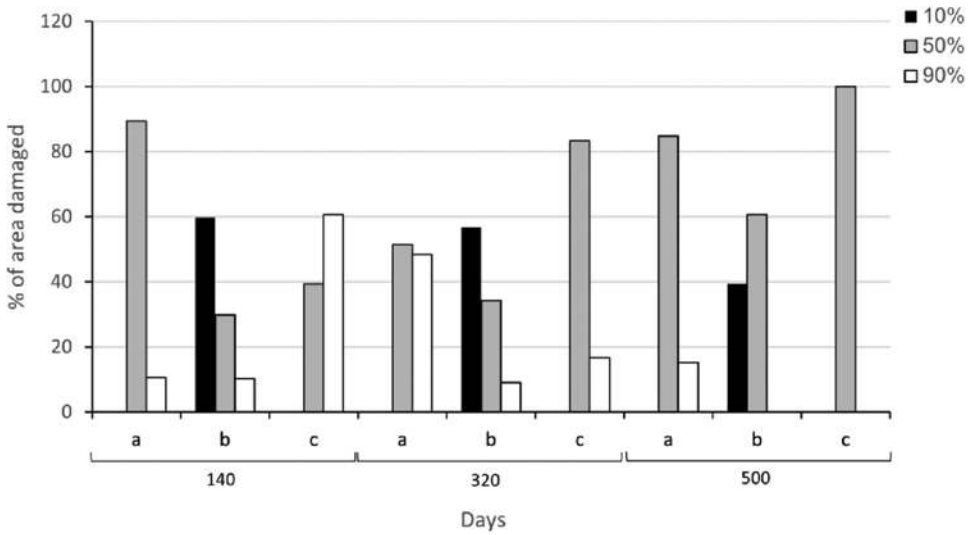

Fig. 6—Amount of corrosion suspect area according to Fig. 5: (a) reference concrete with concrete cover thickness of 75 mm and conventional steel reinforcement; (b) concrete containing corrosion inhibitor, cover thickness of 40 mm, and conventional steel reinforcement; and (c) concrete without corrosion inhibitor, cover thickness of 40 mm, and galvanized reinforcement steel. (Note: 1 mm = 0.0394 in.)

Laboratory tests

Impact of corrosion on bond strength—To examine the performance of specimens of the four aforementioned construction methods, the bond strength between steel bars and concrete was tested by a pullout test at several time points. Galvanized and GFRP bars showed no difference throughout the period examined. However, reference steel bars and bars located in specimens of concrete with corrosion inhibitor showed a steady increase in bond strength. Comparing the measurement performed on day 140 compared to day 500, the bond strength of the reference steel bars and those located at corrosion inhibitor concrete increased by 43% and 69%, respectively (Fig. 7). This increase can be explained by the formation of radial stresses of corrosion products (Fig. 8) and the development of higher friction between the steel bar and concrete in the early stages of corrosion formation to a stage where the stresses will overcome the tensile strength of the concrete and then cracks will form (Fig. 8). According to Coccia et al.,[34] the amount of corrosion products that will cause cracks is 0.5 to 0.6% of the bar weight. It should be noted that in this study the calculation of the loss the bar weight was based on Faraday's law only. However, there is evidence that this calculation requires consideration of a coefficient of adjustment that considers the porosity of the material.[35] Moreover, zinc in concrete undergoes passivation when the pH in concrete ranges from 8 to 12.5. The corrosion products formed are relatively insoluble in pH in these mediums and form a protective layer on the reinforcing steel.[36] To create stress, it is necessary to fill a gap of 10 to 30 µm (0.00039 to 0.00118 in.) that exists between the surface of the bar and the concrete.[37] According to the results of the pullout test, no increase in the bond strength was observed, which means that the galvanization showed protection during this period. A similar distinction was reported in Cheng et al.[38] However, unlike the current study, a steady decrease in the bond strength of the bar without galvanizing was observed. This is probably due to the samples that were examined at a later stage with higher amounts of corrosion.

Effect of corrosion on tensile strength of steel and GFRP reinforcing bars

Tensile tests were performed to examine the influence of marine environmental conditions combined with wetting and drying. Unlike other specimen types, GFRP bar samples were tested with a steel anchor installed at their ends where the bars in the other types (reference concrete; concrete with inhibitor and concrete reinforced by galvanized steel) went straight into the testing machine grips. All samples were tested at several time points to failure under uniaxial tensile loading at a rate of 500 N/min (112.4045 lbf/min) (Fig. 9). Comparing the specimens, it seems that the longer the exposure time, the lower are both the corresponding bar elongation and the tensile strength. At day 500, the tensile strength was decreased as follows: for the control bars—34%, for the bars in concrete with corrosion inhibitor and galvanized bars—32%, and for the GFRP bars—only 10%. It is important to note that the maximum scatter was observed in the GFRP bars where the standard deviation was 18.85 kN (4237.648 lbf), while in the other types of the standard deviation was approximately 2.75 kN (618.224 lbf). Similar results can be seen in previous studies that have shown a decrease in strength as a function of weight loss of the bars due to corrosion. When carbon steel bars lose approximately 12% of their weight, the capacity decreases by 30%.[39] Another study reported that a decrease of 30% in strength involved a decrease in the cross-sectional area by 30%—a similar percentage.[40] Additionally, a strength decrease of approximately 13% was observed for galvanized bars that were exposed to a 5% salt solution for 100 days.[41] This work reported that this decrease was reflected in the separations of the zinc layer on the surface of galvanized steel reinforcing bars, which was also observed in the current study during the preparation of the samples for the laboratory experiment

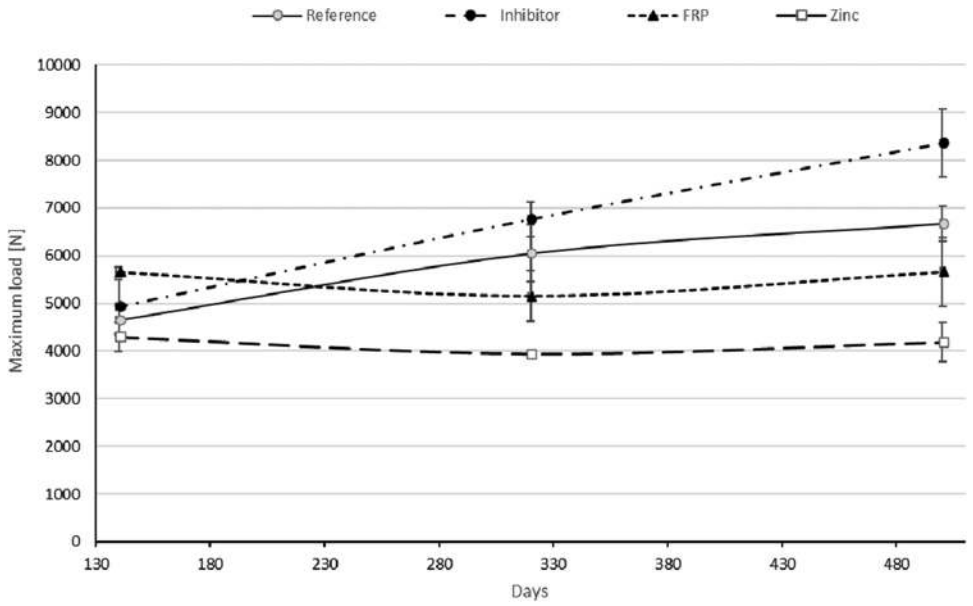

Fig. 7—Maximum load in bond strength test versus concrete age. (Note: 1 N= 0.224 lbf.)

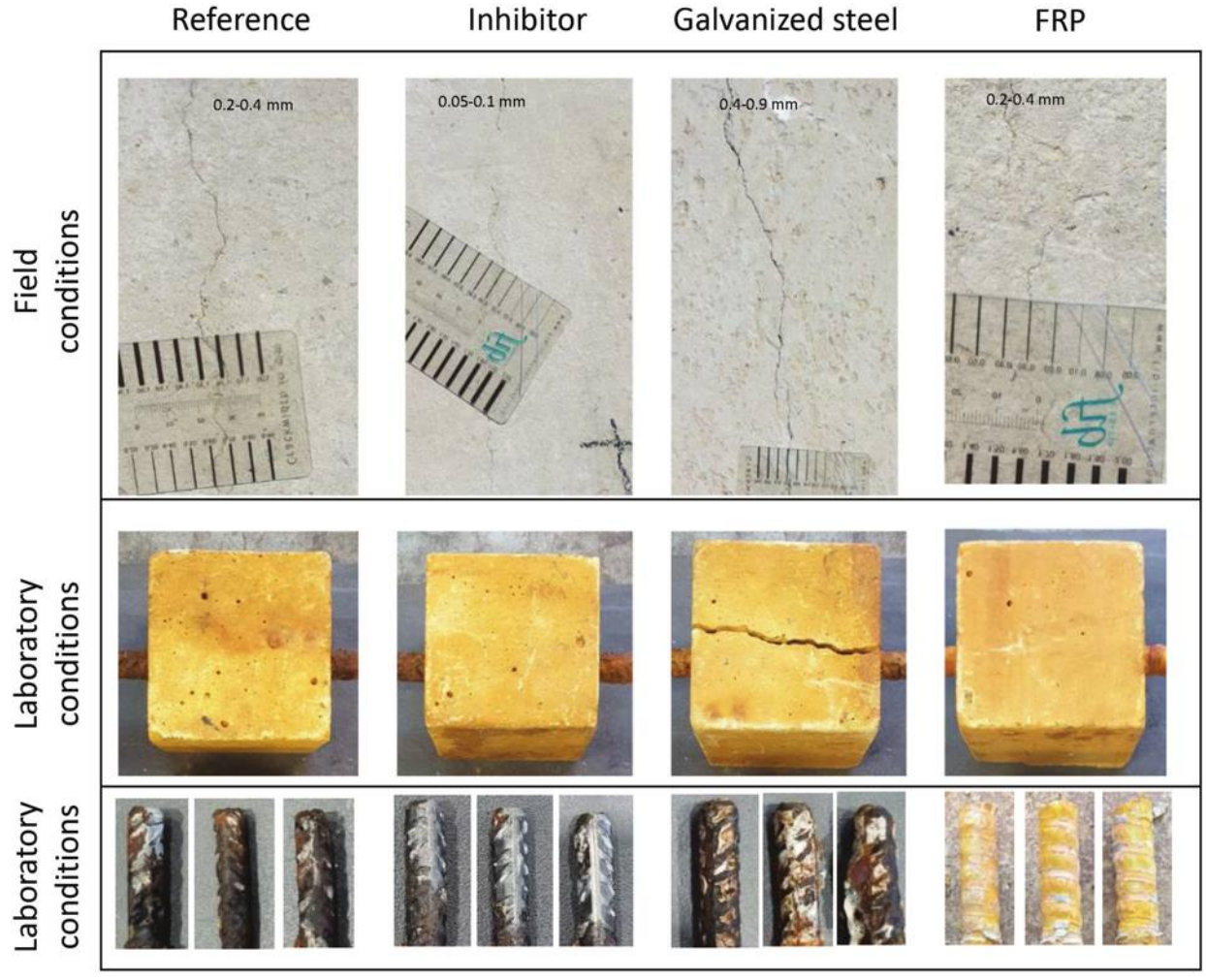

Fig. 8—Crack formation in field versus laboratory conditions and reinforcing bars after 500 days from pullout test.

and experiments in the field. In addition to the delamination of the zinc layer, an increase in corrosion can also occur due to zinc dilution, occurring as a result of selective corrosion in zinc-deficient areas, which was observed in the present study. Zinc is indeed an anode to steel, so it oxidizes if it is galvanized to steel. Beyond that, the zinc layer is selectively removed by corrosion of the steel—a process that can occur upon contact with NaCl solution. The impermeability of the

galvanic coating layer maintains a high electrical potential (more noble). As soon as a crack is formed in another area of the sample and the electric potential there decreases, an electron flow is created, which in turn increases the formation of corrosion products even in the seemingly opaque place.[41]

A study examining GFRP bars under an environmental condition of 60°C (140°F) and the presence of seawater, found that the bar's tensile strength decreased by 25% after approximately 140 days.[42] Other studies showed that though the alkaline reaction in the GFRP bar with a solution of distilled water containing 0.16% $Ca(OH)_2$, 1% Na(OH), and 1.4% K(OH) by weight, pH = 13, and 60°C (140°F) has insignificant effect on tensile strength, the properties of the bar-to-concrete interface were affected.[16,17] As of the time of writing this paper, there is no known evidence of a chemical change that can affect the strength of GFRP bars.[43] The degradation of GFRP bars is a complicated process associated with many accelerated factors, such as the presence of alkaline ions, humidity, and temperature.[17] Unlike other studies, which indicate that the degradation (observed by a decrease in tensile strength of GFRP bars by 20 to 25%) takes between 100 and 200 years,[17] the results of the present study present a decrease of 10% already after 500 days of exposure.

The electrical resistance of concrete is closely related to the level of moisture within the concrete and the number of ions present in the mixture in pore water.[44] For this reason, electrical resistance can also serve an indicator of degradation of the GFRP bars similar to carbon steel bars as described earlier (refer to black bars at Fig. 3(b)).

Considering the alternative based on the addition of a corrosion inhibitor to concrete, it is worth asking the question of how long the corrosion inhibitor may remain at a sufficient concentration for the optimal protection of the steel reinforcing bars. Moreover, is there any removal or rinsing of the inhibitor due to the process of wetting and drying? As mentioned earlier, based on the field measurements, at approximately 320 days after casting, the concrete with the inhibitor shows a tendency similar to the reference concrete. Based on the current observations, it can be concluded that the concentration of the inhibitor in the vicinity of the rod no longer provides protection. The results of testing the tensile strength of the steel bars show that the decrease in strength is proportional to the loss of their cross-sectional area. Thus, it can be concluded that in case of wetting and drying, a process of rinsing and removal of the active substance (inhibitor) occurs and prevents achievement of optimal protection of the steel. This explains an almost identical degradation obtained for the bars embedded in concrete without corrosion inhibitor. It is known that after corrosion initiation, with increasing NaCl concentration, the inhibitor cannot stop the corrosion but prevents an increase in the corrosion rate as long as the concentration of the inhibitor is sufficient.[12] In addition, it is known that inhibitor concentrations of 0.1% and 1% cannot prevent corrosion initiation in steel reinforcing bars, so using a 1:1 ratio between the maximum chloride content and the mass of inhibitor by cement weight is recommended.[12] This was not taken into account in the present study, and therefore, an immediate corrosion initiation and effect on tensile behavior can be seen.

SEM and EDS analysis

For a deeper understanding of the reason for the degradation of GFRP bars, scanning electron microscope (SEM) observations and energy-dispersive X-ray spectroscopy (EDS) analysis were performed on cross sections of three GFRP bars that were under three different conditions: GFRP bar without concrete cover exposed to NaCl solution (only exposed to air), GFRP bar without concrete cover not exposed to NaCl solution, and GFRP bar with concrete cover exposed to NaCl solution. Representative images that were taken at random locations within the epoxy matrix are shown in Fig. 10. Attention has been given to the areas around the edges, because degradation is possible due to a chemical attack that begins with a GFRP-concrete interface in the vicinity of a saline solution. SEM analysis showed no sign of deterioration in the GFRP bars. The glass fibers were intact without loss of cross-sectional area or dissolution. Similarly, the fibers were surrounded by an undamaged epoxy. Comparable results have been shown in previous work.[45]

EDS was performed at several selected locations of the three bar types described earlier with a focus on the bar perimeter to detect chemical changes. It can be seen from the results that the bar without cover and without direct exposure to salt, as expected, showed no presence of internal chlorides. In contrast, in the bars that have been exposed to chlorides, a presence of chlorides was observed (which decreases with the distance from the bar perimeter). An alkaline environment increases the permeability into the matrix compared to an alkali-free environment, as can be seen from the results of the two bars that were exposed to chlorides (Fig. 10). As was demonstrated in other studies,[19,42] an alkaline environment reduces the tensile strength of GFRP bars. Thus, it can be concluded that there is a chemical reaction that can also affect the permeability of chlorides, which ultimately creates a synergy effect resulting in the reinforcing bar deterioration.

Crack formation

Figure 8 shows that in the field conditions, cracks were observed in all four experimental alternatives studied. However, in the laboratory conditions, only the specimens with galvanized steel were cracked. This phenomenon can be explained by the fact that in field conditions, the main cracking is due to shrinkage. In the case of a large volume element, the shrinkage is more pronounced and leads to increased cracking regardless of the presence of corrosion. Figures 5(c) and 6 show that for galvanized steel, most of the area has a high probability of corrosion since the 140th day. This observation strengthens the conclusion that the galvanized steel samples in the laboratory are cracked following the formation of corrosion products. Potentiodynamic polarization curves, also known as Tafel curves, depict the correlation between the polarization current density and electrode potential. It comprises both the cathode polarization curve and the anode polarization curve and shows that the corrosion

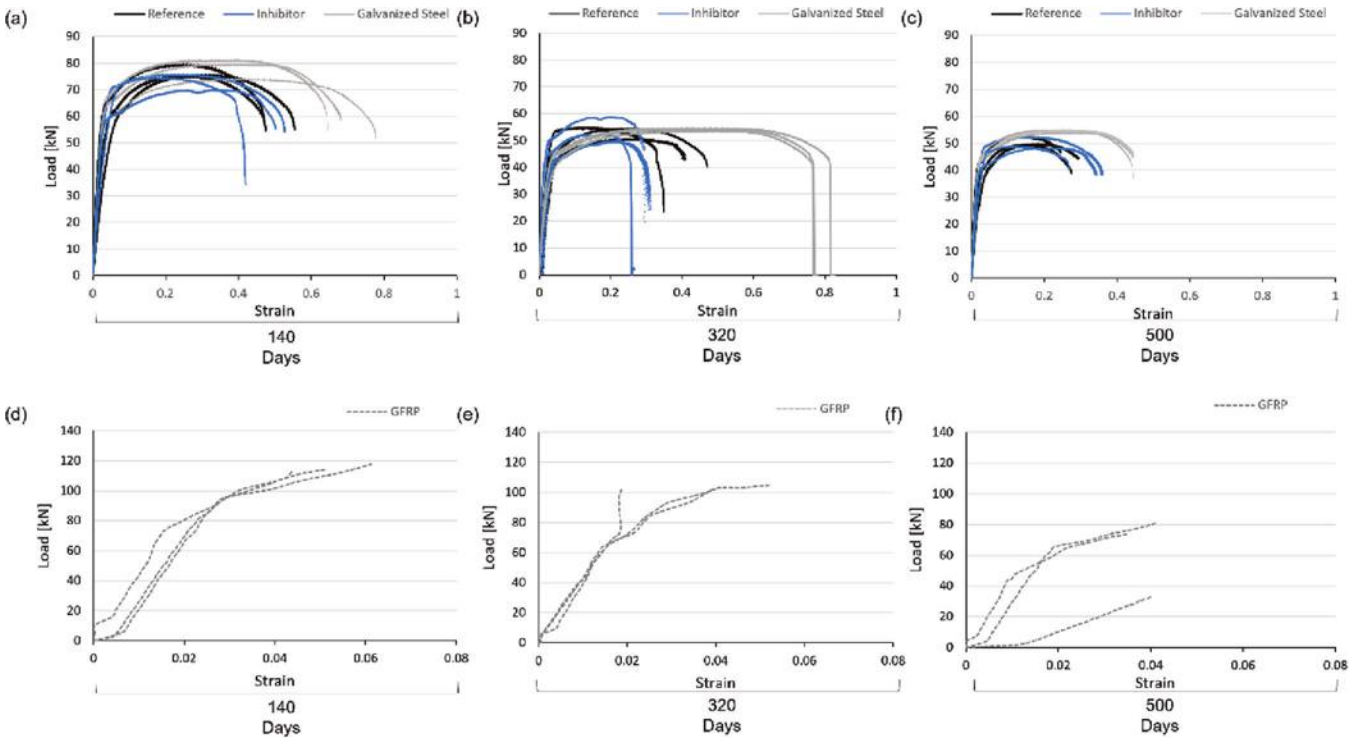

Fig. 9—Tensile tests of steel and GFRP reinforcing bars after: (a) and (d) 140 days; (b) and (e) 320 days; (c) and (f) and 500 days. GFRP results are shown in graph separately because of different scale. (Note: 1 kN = 224.8 lbf).

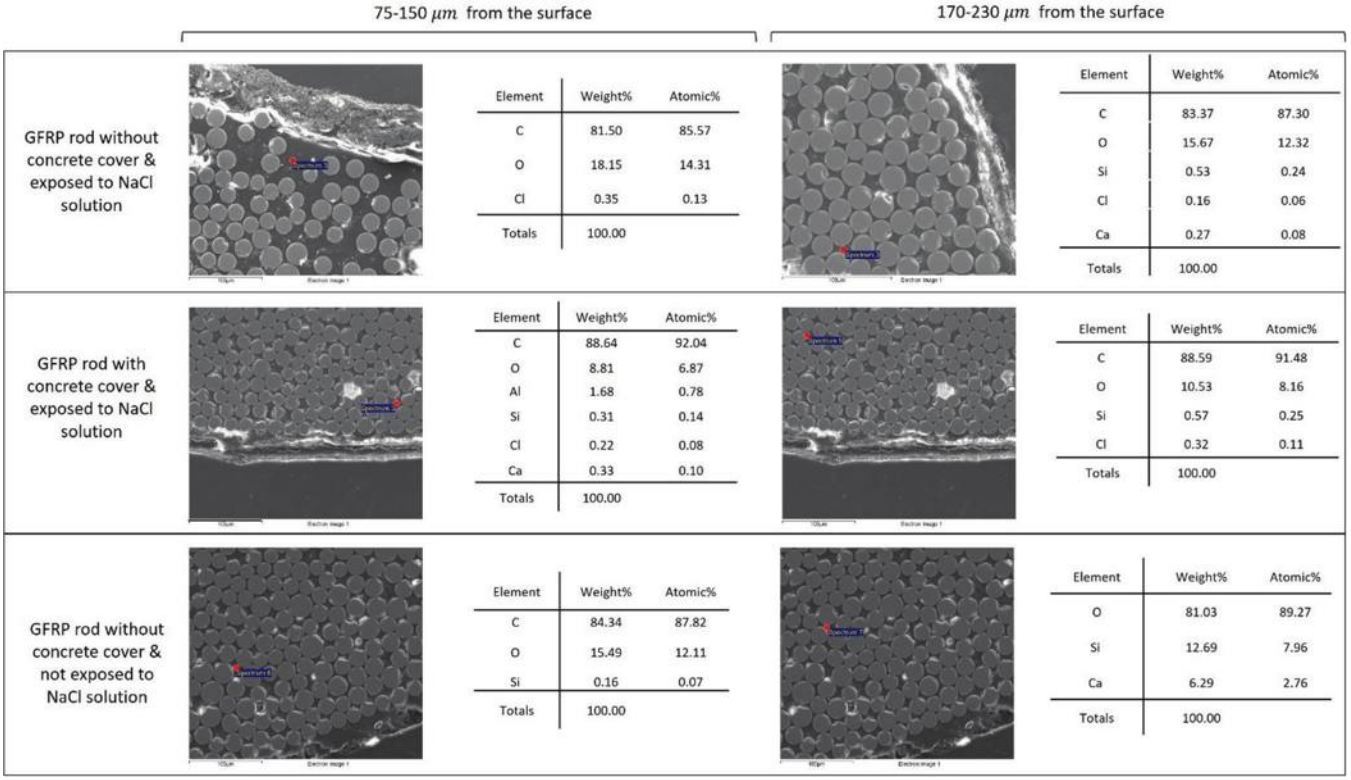

Element	Weight%	Atomic%
C	81.50	85.57
O	18.15	14.31
Cl	0.35	0.13
Totals	100.00	

Element	Weight%	Atomic%
C	83.37	87.30
O	15.67	12.32
Si	0.53	0.24
Cl	0.16	0.06
Ca	0.27	0.08
Totals	100.00	

Element	Weight%	Atomic%
C	88.64	92.04
O	8.81	6.87
Al	1.68	0.78
Si	0.31	0.14
Cl	0.22	0.08
Ca	0.33	0.10
Totals	100.00	

Element	Weight%	Atomic%
C	88.59	91.48
O	10.53	8.16
Si	0.57	0.25
Cl	0.32	0.11
Totals	100.00	

Element	Weight%	Atomic%
C	84.34	87.82
O	15.49	12.11
Si	0.16	0.07
Totals	100.00	

Element	Weight%	Atomic%
O	81.03	89.27
Si	12.69	7.96
Ca	6.29	2.76
Totals	100.00	

Fig. 10—SEM scans and EDS analysis performed on cross sections of three GFRP roads under different conditions: naked bar, exposed to NaCl solution (top line); naked bar, not exposed to NaCl solution (middle line); and reinforcing bar embedded in concrete, exposed to NaCl solution (bottom line). Measurement points located at distances of 75 to 150 μm and 170 to 230 μm from surface are marked as red dots. (Note: 1 μm = 3.93701 × 10^{-5} in.; full-color PDF can be accessed at www.concrete.org.)

rate of zinc is higher than carbon steel in pH = 12 solution, but lower in 3.5% NaCl solution.[38] It is known that the pH in concrete is more basic than 12 and therefore is expected to have a better protection performance by zinc, which was not actually obtained. This result can be explained, as noted earlier in the section "Effect of corrosion on tensile strength

of steel and GFRP reinforcing bars," by the fact that certain bar areas were exposed to the environment due to insufficient zinc coverage. Thus, bar galvanizing resulted in an adverse effect. It is known that the rate of zinc decomposition and its solubility in the porous water of concrete determines the rate of formation of corrosion products and therefore, also the time required for cracking the concrete. Corrosion products have larger volumes than the metals from which they are formed.[36] This volume expansion is responsible for cracking of concrete. Today, it is not clear how zinc corrosion products are formed and dispersed in concrete under different conditions. This lack of clarity is because corrosion products of steel that are not extremely soluble in concrete tend to remain in the metal-concrete interface. The corrosion products of zinc are more soluble and therefore may disperse farther from the interface.[46] In this study, despite the solubility of zinc, only one type of the samples (that containing galvanized steel) cracked after 500 days of wetting and drying cycles in seawater. This may indicate that due to an alkaline environment, the reaction products have formed in such a way that the concrete cover and protection of the steel is damaged; the steel rusts and the corrosion products create strong radial stresses that lead to cracking of the element.[36,47] This hypothesis conflicts with the results of bond strength. If the cracking occurred due to corrosion products, the bond strength measured before cracking was expected to increase. However, the bond strength did not change. An explanation for this could be that the adhesion force was measured over time frames that failed to capture the onset of cracking, as it occurred at high speed once the zinc layer had fully reacted.

CONCLUSIONS

In this study, four alternatives for construction of reinforced concrete elements exposed to marine environments were examined: using conventional reinforced concrete (RC) with thick concrete cover (75 mm), the addition of a corrosion inhibitor to concrete, and using glass fiber-reinforced polymer (GFRP) and galvanized steel instead of steel bars. This was made by monitoring a caisson parapet beam made of reinforced concrete exposed to seawater attack during 500 days after casting, in both natural environmental conditions (in the Mediterranean Sea) and in laboratory-simulated chloride attack. Wetting and drying cycles were applied in the lab to speed up the processes of degradation. Furthermore, the effect of concrete curing on its mechanical properties was examined. Degradation processes, including crack formation, in the field and laboratory conditions were compared. Based on the results of this study, it can be concluded:

- Saltwater curing did not show a negative effect on the strength and mechanical properties of the concrete. Thus, exposing young-age concrete to splash seawater is not expected to affect its mechanical properties.
- As expected, cracking accelerates corrosion.
- Galvanized steel bars under chloride attack do not provide adequate protection of reinforced concrete from corrosion: after 140 days of exposure on site, 60.6% of the selected area of concrete reinforced with galvanized reinforcement steel showed the highest corrosion potential (90% probability of corrosion); this result was also confirmed by observation of cracking in both field and laboratory conditions. At the same time, reinforcing by galvanized steel shows no change in the bond strength despite the corrosion process observed in the bars themselves. This can be explained by the fact that the oxide layer is dissolved in the pore water and released easily outside the concrete.
- In contrast to the prevailing approach (which considers the plain concrete, according to which the electrical resistance of the concrete decreases because of chloride penetration), this study found that electrical resistance in the reinforced concrete element increases due to an increase in the amount of corrosion products formed between steel and concrete, as long as cracking does not occur.
- Under chloride attack, tensile strength in the following types of reuinforcing bars embedded in concrete (the bars made of conventional and galvanized steel embedded in the reference concrete, and the bars made of conventional steel embedded in concrete containing corrosion inhibitor) decreased by approximately 30% already after 500 days, while the strength of GFRP bars decreased by approximately 10%. This means that GFRP bars yield significantly better protection than the other alternatives tested.
- It was also found that chloride ion permeability is more accelerated in the GFRP bars embedded in concrete compared to the bars exposed directly to the chloride environment. It is possible that an alkaline environment chemically damages the bar components, resulting in a decrease in the tensile strength. On the other hand, the bond strength was not affected.
- Under marine conditions, the bars embedded in concrete containing the corrosion inhibitor accelerated the rate of corrosion formation, especially at the first year of observation in place.
- At the same time, the electric potential measured using the half-cell method in all the alternatives (including in concrete containing GFRP bars) slowly increased over time (becoming more positive), as well as the corrosion risk in the three alternatives with reinforcing steel. The remaining question is whether this change of potential could be a direct characteristic of the corrosion risk. Therefore, more research in this direction is needed.

AUTHOR BIOS

Igor Lapiro *is a PhD Student in civil and environmental engineering at the Technion – Israel Institute of Technology, Haifa, Israel, where he received his MSc in civil engineering. His research interests include the durability and sustainability of reinforced concrete structures, corrosion inhibitors, and reinforcement steel substitutes.*

ACI member **Rami Eid** *is a Senior Lecturer at the Department of Civil Engineering at Braude College of Engineering, Karmiel, Israel. He received his PhD in structural engineering from the Technion – Israel Institute of Technology. He is a member of ACI Committee 440, Fiber-Reinforced Polymer Reinforcement, and Joint ACI-ASCE Committee 441, Reinforced Concrete Columns. His research interests include structural behavior of reinforced concrete structures under static and seismic loading.*

ACI member **Konstantin Kovler** *is Associate Professor at the Faculty of Civil and Environmental Engineering at the Technion – Israel Institute of*

Technology. He received his PhD in structural engineering from Moscow State University of Civil Engineering, Moscow, Russia. He is a member of ACI Committees 236, Materials Science of Concrete, and 241, Nanotechnology of Concrete. His research interests include durability of concrete and sustainable construction.

ACKNOWLEDGMENTS

This study was funded by the Coastal and Marine Engineering Research Institute (CAMERI), Technion – Israel Institute of Technology.

The authors are thankful to A. Elgaba and S. Ofir from the Israeli Port Company for providing logistic help in the experimental studies in the Gulf Port of Haifa, and to E. Itzhak and E. Gershengoren for the help in conducting the experiments in the lab and in place. The generous help of P. Merkt from FiReP International AG (Switzerland) and B. Halamish from Keshet Technologies (Israel) in preparation of the GFRP reinforcing bars for testing is highly appreciated. The authors declare that they have no conflict of interest.

REFERENCES

1. Alexander, M., *Marine Concrete Structures: Design, Durability and Performance*, Woodhead Publishing, 2016.

2. Qu, F.; Li, W.; Dong, W.; Tam, V. W. Y.; and Yu, T., "Durability Deterioration of Concrete Under Marine Environment From Material to Structure: A Critical Review," *Journal of Building Engineering*, V. 35, Mar. 2021, p. 102074. doi: 10.1016/j.jobe.2020.102074

3. Angst, U. M., "Challenges and Opportunities in Corrosion of Steel in Concrete," *Materials and Structures/Materiaux et Constructions*, V. 51, No. 1, 2018, pp. 1-20.

4. Zhou, Y.; Gencturk, B.; Willam, K.; and Attar, A., "Carbonation-Induced and Chloride-Induced Corrosion in Reinforced Concrete Structures," *Journal of Materials in Civil Engineering*, ASCE, V. 27, No. 9, 2015, p. 04014245. doi: 10.1061/(ASCE)MT.1943-5533.0001209

5. ASTM D1141-98, "Standard Practice for the Preparation of Substitute Ocean Water (Reapproved 2008)," ASTM International, West Conshohocken, PA, 1998, 3 pp.

6. Lenntech, "Composition of Seawater," Miami, FL, http://www.lenntech.com/composition-seawater.htm. (last accessed Nov. 21, 2023)

7. Mamane, Y., and Gottlieb, J., "Ten Years of Precipitation Chemistry in Haifa, Israel," *Water, Air, and Soil Pollution*, V. 82, No. 3-4, 1995, pp. 549-558. doi: 10.1007/BF00479411

8. Asamoto, S.; Sato, J.; Okazaki, S.; Chun, P.; Sahamitmongkol, R.; and Nguyen, G. H., "The Cover Depth Effect on Corrosion-Induced Deterioration of Reinforced Concrete Focusing on Water Penetration: Field Survey and Laboratory Study," *Materials (Basel)*, V. 14, No. 13, 2021, p. 3478. doi: 10.3390/ma14133478

9. Gonen, T., and Yazicioglu, S., "The Influence of Mineral Admixtures on the Short and Long-Term Performance of Concrete," *Building and Environment*, V. 42, No. 8, 2007, pp. 3080-3085. doi: 10.1016/j.buildenv.2006.10.019

10. Setina, J.; Gabrene, A.; and Juhnevica, I., "Effect of Pozzolanic Additives on Structure and Chemical Durability of Concrete," *Procedia Engineering*, V. 57, 2013, pp. 1005-1012. doi: 10.1016/j.proeng.2013.04.127

11. Ibrahim, M.; Kalimur Rahman, M.; Megat Johari, M. A.; Nasir, M.; and Adeoluwa Oladapo, E., "Chloride Diffusion and Chloride-Induced Corrosion of Steel Embedded in Natural Pozzolan-Based Alkali Activated Concrete," *Construction and Building Materials*, V. 262, 2020, p. 120669. doi: 10.1016/j.conbuildmat.2020.120669

12. Söylev, T. A., and Richardson, M. G., "Corrosion Inhibitors for Steel in Concrete: State-of-the-Art Report," *Construction and Building Materials*, V. 22, No. 4, 2008, pp. 609-622. doi: 10.1016/j.conbuildmat.2006.10.013

13. Saraswathy, V., and Song, H. W., "Improving the Durability of Concrete by Using Inhibitors," *Building and Environment*, V. 42, No. 1, 2007, pp. 464-472. doi: 10.1016/j.buildenv.2005.08.003

14. Aliofkhazraei, M., ed., *Corrosion Inhibitors, Principles and Recent Applications*, IntechOpen Limited, London, UK, 2018.

15. Wang, Y. C.; Wong, P. M. H.; and Kodur, V., "An Experimental Study of the Mechanical Properties of Fibre Reinforced Polymer (FRP) and Steel Reinforcing Bars at Elevated Temperatures," *Composite Structures*, V. 80, No. 1, 2007, pp. 131-140. doi: 10.1016/j.compstruct.2006.04.069

16. Micelli, F., and Nanni, A., "Durability of FRP Rods for Concrete Structures," *Construction and Building Materials*, V. 18, No. 7, 2004, pp. 491-503. doi: 10.1016/j.conbuildmat.2004.04.012

17. Robert, M.; Cousin, P.; and Benmokrane, B., "Durability of GFRP Reinforcing Bars Embedded in Moist Concrete," *Journal of Composites for Construction*, ASCE, V. 13, No. 2, 2009, pp. 66-73. doi: 10.1061/(ASCE)1090-0268(2009)13:2(66)

18. Gudonis, E.; Timinskas, E.; Gribniak, V.; Kaklauskas, G.; Arnautov, A. K.; and Tamulėnas, V., "FRP Reinforcement for Concrete Structures: State-of-the-Art Review of Application and Design," *Engineering Structures and Technologies*, V. 5, No. 4, 2014, pp. 147-158. doi: 10.3846/2029882X.2014.889274

19. Wu, W.; He, X.; Yang, W.; Dai, L.; Wang, Y.; and He, J., "Long-Time Durability of GFRP Bars in the Alkaline Concrete Environment for Eight Years," *Construction and Building Materials*, V. 314, 2022, p. 125573. doi: 10.1016/j.conbuildmat.2021.125573

20. De Schutter, G., *Damage to Concrete Structures*, CRC Press, London, UK, 2012, 210 pp.

21. Griffin, D. F., "Corrosion Inhibitors for Reinforced Concrete," *Corrosion of Metals in Reinforced Concrete*, SP-49, L. Pepper, R. G. Pike, and J. A. Willett, eds., American Concrete Institute, Farmington Hills, MI, 1975, pp. 95-102.

22. Aïtcin, P. C., "The Importance of the Water-Cement and Water-Binder Ratios," *Science and Technology of Concrete Admixtures*, Woodhead Publishing, 2016, pp. 3-13.

23. ASTM C876-15, "Standard Test Method for Corrosion Potentials of Uncoated Reinforcing Steel in Concrete," ASTM International, West Conshohocken, PA, 2015, 8 pp.

24. Dhondy, T.; Remennikov, A.; and Shiekh, M. N., "Benefits of Using Sea Sand and Seawater in Concrete: A Comprehensive Review," *Australian Journal of Structural Engineering*, V. 20, No. 4, 2019, pp. 280-289. doi: 10.1080/13287982.2019.1659213

25. Islam, M. M., and Islam, S. M., "Suitability of Sea Water on Curing and Compressive Strength of Structural Concrete," *Journal of Civil Engineering*, V. 40, No. 1, 2012, pp. 37-45.

26. Alaejos, P., and Bermúdez, M. A., "Influence of Seawater Curing in Standard and High-Strength Submerged Concrete," *Journal of Materials in Civil Engineering*, ASCE, V. 23, No. 6, 2011, pp. 915-920. doi: 10.1061/(ASCE)MT.1943-5533.0000231

27. Taylor, P. C., *Curing Concrete*, CRC Press, London, UK, 2013, 184 pp.

28. Luga, E., "The Effect of Concrete Sample Size in the Compressive Strength Value of Concrete," 2020 UBT International Conference, Lipjan, Kosovo, 2020.

29. Ariöz, Ö.; Tuncan, M.; Ramyar, K.; Tuncan, A.; Karasu, B.; Kilinç, K.; and Mortaja, W., "Specimen Size and Shape Effects on Measured Compressive Strength of Concrete," SERES'09 I. International, Ceramic, Glass, Porcelain Enamel, Glaze and Pigment Congress, Eskisehir, Turkey, 2009, pp. 1044-1052.

30. Kendall, A.; Keoleian, G. A.; and Helfund, G. E., "Integrated Life Cycle Assessment and Life Cycle Cost Analysis Model for Concrete Bridge Deck Applications," *Journal of Infrastructure Systems*, ASCE, V. 14, No. 3, 2008, pp. 214-222. doi: 10.1061/(ASCE)1076-0342(2008)14:3(214)

31. Zhang, J., and Baldock, B., "Condition Assessment and Corrosion Mitigation of Galvanized Steel Reinforcement in Concrete Structures," National Research Council of Canada, Ottawa, ON, Canada, 2015.

32. Azarsa, P., and Gupta, R. "Electrical Resistivity of Concrete for Durability Evaluation: A Review," *Advances in Materials Science and Engineering*, V. 2017, 2017. doi: 10.1155/2017/8453095

33. Renpu, W., "Oil and Gas Well Corrosion and Corrosion Prevention," *Advanced Well Completion Engineering*, 2011, pp. 617-700.

34. Coccia, S.; Imperatore, S.; and Rinaldi, Z., "Influence of Corrosion on the Bond Strength of Steel Rebars in Concrete," *Materials and Structures/Materiaux et Constructions*, V. 49, No. 1-2, 2016, pp. 537-551.

35. Torres-Acosta, A. A., and Castro-Borges, P., "Corrosion-Induced Cracking of Concrete Elements Exposed to a Natural Marine Environment for Five Years," *Corrosion*, V. 69, No. 11, 2013, pp. 1122-1131. doi: 10.5006/0844

36. Tan, Z. Q., and Hansson, C. M., "Effect of Surface Condition on the Initial Corrosion of Galvanized Reinforcing Steel Embedded in Concrete," *Corrosion Science*, V. 50, No. 9, 2008, pp. 2512-2522. doi: 10.1016/j.corsci.2008.06.035

37. Lu, C. H.; Liu, R. G.; and Jin, W. L., "A Model for Predicting Time to Corrosion-Induced Cover Cracking in Reinforced Concrete Structures," *Fracture Mechanics of Concrete and Concrete Structures — Assessment, Durability, Monitoring and Retrofitting of Concrete Structures*, 2010, pp. 967-975.

38. Cheng, A.; Huang, R.; Wu, J. K.; and Chen, C. H., "Effect of Rebar Coating on Corrosion Resistance and Bond Strength of Reinforced Concrete," *Construction and Building Materials*, V. 19, No. 5, 2005, pp. 404-412. doi: 10.1016/j.conbuildmat.2004.07.006

39. Almusallam, A. A., "Effect of Degree of Corrosion on the Properties of Reinforcing Steel Bars," *Construction and Building Materials*, V. 15, No. 8, 2001, pp. 361-368. doi: 10.1016/S0950-0618(01)00009-5

40. Cairns, J.; Plizzari, G. A.; Du, Y.; Law, D. W.; and Franzoni, C., "Mechanical Properties of Corrosion-Damaged Reinforcement," *ACI Materials Journal*, V. 102, No. 4, July-Aug. 2005, pp. 256-264.

41. Ismail, M.; Muhammad, B.; Hamzah, E.; and Keong, T. W., "Corrosion Behaviour of Dual-Phase and Galvanized Steels in Concrete," *Anti-Corrosion Methods and Materials*, V. 59, No. 3, 2012, pp. 132-138. doi: 10.1108/00035591211224672

42. Aydın, F., and Arslan, Ş., "Investigation of the Durability Performance of FRP Bars in Different Environmental Conditions," *Advances in Concrete Construction*, V. 12, No. 4, 2021, pp. 295-302.

43. Gooranorimi, O., and Nanni, A., "GFRP Reinforcement in Concrete after 15 Years of Service," *Journal of Composites for Construction*, ASCE, V. 21, No. 5, 2017, p. 04017024. doi: 10.1061/(ASCE)CC.1943-5614.0000806

44. Jia, D.; Guo, Q.; Mao, J.; and Lv, J., "Durability of Glass Fibre-Reinforced Polymer (GFRP) Bars Embedded in Concrete Under Various Environments I: Experiments and Analysis," *Composite Structures*, V. 234, Feb. 2020, p. 111687. doi: 10.1016/j.compstruct.2019.111687

45. Tatar, J., and Brenkus, N. R., "Performance of FRP-Strengthened Reinforced Concrete Bridge Girders after 12 Years of Service in Coastal Florida," *Journal of Composites for Construction*, ASCE, V. 25, No. 4, 2021, pp. 1-14. doi: 10.1061/(ASCE)CC.1943-5614.0001134

46. Zhang, X. G., *Corrosion and Electrochemistry of Zinc*, Springer Science & Business Media, 1996.

47. Zhao, Y., and Jin, W., "Steel Corrosion in Concrete," *Steel Corrosion-Induced Concrete Cracking*, 2016, pp. 19-29.

ACI MATERIALS JOURNAL TECHNICAL PAPER

Title No. 121-M05

High-Volume Fly Ash Engineered Cementitious Composite for Underground and Hydraulic Engineering

by Xiaoqin Li, Li Zhang, Wenlu Wen, Shihua Li, and Xu Zhou

*Engineered cementitious composites (ECCs) have excellent toughness and crack-control abilities compared to other cement-based materials, which can be used in underground and hydraulic engineering. Nevertheless, excellent impermeability and workability and low drying shrinkage are also required. Two groups of ECC mixture proportions with high fly ash-cement (*FA/c*) and water-cement ratios (*w/c*) were chosen as baselines, and silica fume (SF) and a shrinkage-reducing agent (SRA) were introduced to improve the impermeability, workability, and mechanical behaviors. The workability laboratory evaluation indexes of ECC were also discussed. ECC mixture proportions with excellent workability (pumpability and sprayability), high toughness (ultimate tensile strain ε_{tp} over 3.5%), good impermeability (permeability coefficient* K *= 1.713 × 10^{-11} m/s), and low drying shrinkage (drying shrinkage strain ε_{st} = 603.6 × 10^{-6}) were finally obtained. Then, flexural and shear tests were carried out for the material flexural/shear strength and toughness evaluations, giving the characteristic material properties for the final ECC mixture proportions.*

Keywords: engineered cementitious composite (ECC); high-volume fly ash; impermeability; low drying shrinkage; toughness; workability.

INTRODUCTION

The importance of controlling crack width has gained much attention in underground and hydraulic engineering. Normal concrete (NC) behaves brittlely, with poor crack-control abilities due to its low toughness, of which the ultimate tensile strain is only approximately 0.01% and the relevant NC local crack width may exceed 0.6 mm.[1,2] Due to the low toughness and poor crack-control abilities, underground tunnel lining deterioration, spalling of concrete debris, and water leakages may occur, especially when the tunnel is exposed to an aggressive environment.[3,4] Nevertheless, for hydraulic structures, including dams, spillways, and sluices, concrete cracking may also induce structural damage.[5,6] To solve these problems, engineered cementitious composites (ECCs) could be introduced, which exhibit strain-hardening behavior under uniaxial tensile loading conditions. The tensile strain capacity of ECC ranges from 3 to 7%, which is 300 to 700 times that of NC.[7] More importantly, the high tensile ductility of ECC is achieved by forming multiple tight microcracks instead of large localized cracks,[5,7] and the crack width is typically less than 80 µm, even when the tensile strain is up to 5%.[8] Also, the cement industry accounts for 5 to 8% of worldwide CO_2 emissions, and approximately 0.94 tons of CO_2 are released into the atmosphere while manufacturing 1 ton of cement.[9,10] Industrial by-product fly ash (FA) can replace a large portion of cement in ECC to enhance tensile ductility[9] and also offers environmental advantages compared to processing cement, such as reducing the energy investment and CO_2 release.[11] Aggregates with sizes larger than average fiber spacing can cause poor fiber dispersion, which leads to a reduction in the number of effective fibers at the failure crack, resulting in a decrease in tensile strength. As the particle size of FA is less than 10 µm, which is much smaller than average fiber spacing, adding FA can improve fiber dispersion homogeneity in the fresh state and also improve ECC tensile ductility.[12] Moreover, it was pointed out by Şahmaran and Li[13] that for high-volume FA ECC, the crack width may be reduced to 10 to 30 µm, sometimes even lower than 10 µm—much smaller than the 80 µm discussed earlier[8]—which is beneficial to the structural durability, too.

Based on its excellent mechanical properties and advantages in reducing CO_2 emissions, high-volume FA ECC has been extensively investigated for repairing waterproofing structures, such as bridges,[14] dams,[15] and tunnels.[16] When a large amount of ECC needs to be applied in new building structures, the pumpability and sprayability are required. However, few research studies have given a detailed discussion on ECC workability, and little attention has been paid regarding the proper laboratory evaluation indexes for ECC. In addition, for ECC used in underground and hydraulic engineering, high impermeability is also required, which is of crucial importance to the material durability.[17] Nevertheless, to obtain ECC that exhibits desirable pseudo-strain-hardening behavior and improved elastic modulus, only a small amount of fine sand is allowed to be applied in the matrix to control fracture toughness.[18] As a result of this requirement, a high drying shrinkage strain may develop during setting and hardening of the composite,[19] which is not expected in underground and hydraulic engineering as it may induce lining cracks, cavities in tunnel linings, and water leakage. Based on the previous discussions, the impermeability, workability, drying shrinkage strain, and mechanical properties for high-volume FA ECC, as well as proper workability laboratory evaluation indexes, should be comprehensively evaluated before being used in underground and hydraulic engineering.

Generally, the permeability coefficient *K* is required to be less than 2.610 × 10^{-11} m/s for underground and hydraulic

ACI Materials Journal, V. 121, No. 1, January 2024.
MS No. M-2022-296.R1, doi: 10.14359/51739200, received June 26, 2023, and reviewed under Institute publication policies.

Table 1—Investigated ECC mixture proportions (mass ratios to cement)

	No.	Cement	FA (Class F)	Water	Sand	HRWRA	PVA fiber	SF	SRA
E-1	E-1.0	1	1.72	1.03	0.7	0.006	0.055	0	0
	E-1.1	1	1.72	1.03	0.7	0.006	0.055	0.10	0.09
	E-1.2	1	1.72	1.03	0.7	0.006	0.055	0.15	0.09
	E-1.3	1	1.72	1.03	0.7	0.006	0.055	0.20	0.09
E-2	E-2.0	1	4.44	1.55	1.11	0.024	0.111	0.10	0.09
	E-2.1	1	4.44	1.55	1.11	0.024	0.111	0.15	0.09
	E-2.2	1	4.44	1.55	1.11	0.024	0.111	0.20	0.09

applications.[20] The impermeability is mainly related to its fiber content[21] and porosity.[22] The fiber content of ECC is typically close to or less than 2% by volume, which indicates that the effect of fiber content is small. The porosity of cement-based materials is usually related to the particle size of coarse aggregates,[23] mineral admixtures,[24,25] and the water-cement ratio (*w*/*c*).[22,26,27] Regardless of coarse aggregates, the effects of aggregate on porosity should not be considered for ECC. Therefore, mineral admixtures and *w/c* should be considered. According to existing research—for example, the test done by Ding et al.[28]—the optimal ECC mixture proportions[29] with a low *w*/*c* (0.57) could not satisfy the workability requirements, including pumpability and sprayability, which could not be easily improved. Although a high *w*/*c* might lead to poor impermeability, it could be improved by adding the by-product of the ferrosilicon industry, silica fume (SF), and other additional agents. Moreover, as the particle size of FA is less than 10 μm, it can be used as the filler to improve pore distributions and reduce porosity,[24] thereby reducing permeability. As there is no coarse aggregate in ECC, shrinkage-reducing agents (SRAs) should be introduced to reduce drying shrinkage by reducing the surface tension of concrete's fluid, resulting in a significant reduction of the magnitude of capillary stresses and shrinkage strains that occur when concrete loses moisture.[30] Adding SRAs could not only obtain a material with a low drying shrinkage strain, but also reduce the quantity of detrimental pores (pore diameter $d > 200$ nm) and increase the number of innocuous pores (pore diameter $d < 20$ nm), which is beneficial to the denseness of the inner paste structure and can improve the resistance to chemical attack and the durability of cement-based materials.[31]

Based on the previous discussions, high-volume FA ECC mixture proportions with high *w*/*c* should be adopted as the baselines to conduct empirical research rather than those with low *w*/*c*, and SF and SRA needed to be introduced. The influences of *w*/*c*, FA, SF, and SRA to the ECC material properties should be carefully investigated, giving the optimum ECC mixture proportions for underground and hydraulic engineering to have excellent mechanical behavior, the required workability, high impermeability, and low drying shrinkage strain. Also, the proper workability laboratory evaluation indexes that can be used to indirectly predict the quality of spraying need to be given. Moreover, the toughness evaluation and material characteristic parameters calibration should be carried out for the final optimized ECC.

RESEARCH SIGNIFICANCE

ECC has excellent toughness and crack-control abilities compared to other cement-based materials, which could be used in underground and hydraulic engineering to prevent tunnel lining deterioration, spalling of concrete debris, water leakages, and so on. Industrial by-product FA can be introduced to ECC to replace a large amount of cement, which can not only benefit the environment but also could enhance its tensile ductility. When a large amount of ECC needs to be applied in underground and hydraulic engineering, the pumpability and sprayability of ECC are required. Specifically, the significance of this investigation lies in optimizing a high fly ash-cement mass ratio (*FA*/*c*) and high *w*/*c* ECC mixture proportions with good workability (pumpability and sprayability) and impermeability and low drying shrinkage for underground and hydraulic engineering, and establishing proper workability laboratory evaluation indexes for ECC that can be used to indirectly predict the quality of spraying.

EXPERIMENTAL DESIGN

ECC mixture proportions design

To obtain ECC mixture proportions with excellent mechanical properties, impermeability, and workability, two ECC mixture proportions with high *FA*/*c* (1.72, 4.44) and *w*/*c* (1.03, 1.55)[29] were chosen as the baselines, which were named E-1.0 and E-2.0, respectively, in Table 1, of which the ultimate tensile strain ε_{tp} is over 3%. SF, with its high content of glass-phase silicon dioxide (SiO_2), consists of very small spherical particles that could be added to ECC mixture proportions to solve the problem of the early-strength reduction that results from adding high-volume FA due to its slow pozzolanic reactivity.[21] Adding SF aids pumping by reducing torque viscosity while also providing enhanced sprayability by maintaining an appropriate level of flow resistance so that the balance between fluidity and cohesion of fresh cement-based materials can be obtained for better pumpability and sprayability.[32] The suggested SF-cement mass ratio (*SF*/*c*) was in the range of 8 to 20%[32]; therefore, three *SF*/*c*—10%, 15%, and 20%—were investigated. As suggested by Gao et al.,[19] when the SRA-cement mass ratio (*SRA*/*c*) was 9%, the drying shrinkage strain of ECC might meet the requirements of NC in engineering. The 9% *SRA*/*c* was chosen to improve the ECC's anti-drying-shrinkage ability. The investigated ECC mixture proportions are listed in Table 1.

Table 2—Physical properties of P.O 42.5 portland cement

Physical properties	Loss on ignition (LOI), %	Specific surface, m^2/kg	Specific gravity
P.O 42.5 portland cement	1.38	368	3.15

Table 3—Chemical properties of P.O 42.5 portland cement

Mineral composition	SiO_2	Fe_2O_3	Al_2O_3	CaO	MgO	SO_3
Mass percent, %	20.8	3.6	4.62	61.61	2.12	2.71

Table 4—Material properties of cement

	Compressive strength, MPa		Bending strength, MPa	
Curing time	3 days	28 days	3 days	28 days
Specified value	≥17.0	≥42.5	≥3.5	≥6.5
Actual value	18.9	45.3	4.2	7.8

Raw materials

Materials used to prepare ECC mixtures include P.O 42.5 portland cement, SF, FA (Class F), quartz sand with the particle size ranging from 0.2 to 0.4 mm, water, high-range water-reducing admixture (HRWRA), polyvinyl alcohol (PVA) fibers, and SRA (I). Detailed information of the materials is listed in Tables 2 to 6.

Experimental research

The workability, impermeability, mechanical properties, and drying shrinkage tests were conducted based on the ECC mixture proportions mentioned in Table 1. All specimens were stored for 24 hours at room temperature before demolding, then cured in a standard curing room with a temperature of 20 ± 2°C and a humidity of 95% for 28 days.

Workability investigation—The workability of fresh cement-based materials, including pumpability and sprayability, is related to the material fluidity and cohesion. Generally, pumpable materials require high fluidity and low cohesion, and the slump (S_L) is usually used to evaluate the fluidity of cement-based materials, which needs to be controlled in the range of 140 to 200 mm.[33,34] The slump flow (S_t) and funnel flow time (t) of the pumpable concrete are used as the laboratory evaluation indexes for cohesion evaluation, of which S_t should be in the range of 400 to 600 mm, and the required range of t is 4 to 10 seconds.[35] The sprayability additionally requires that, once a fresh cement-based material is sprayed onto the surface of the substrate, it should be viscous enough to stay adhered to the substrate and remain cohesive without composite ingredient segregation.[36] The S_L of freshly sprayable materials should be controlled in the range of 100 to 200 mm.[35] Meanwhile, the sprayability decreases with the increase in fluidity and increases with cohesion, indicating that a sprayable ECC needs to maintain a balance between fluidity and cohesion.[37] To achieve a balance between fluidity and cohesion, the ratio of slump to slump flow (S_L/S_t) of fresh ECC with good workability is approximately 0.45.[38] The workability requirements for fresh ECC with good pumpability and sprayability are given in Table 7.

Table 5—Material properties of FA (Class F) and SF

Material properties	FA (Class F)	SF
Amount retained on 45 μm sieve, %	8.10	—
Specific gravity	2.51	2.24
LOI, %	4.22	1.98
Moisture content, %	0.80	0.40
Water required, percent of control, %	90.00	121.00
Mass fraction of SiO_2, %	55.08	94.00
Mass fraction of Al_2O_3, %	28.40	0.60
Mass fraction of Fe_2O_3, %	4.54	0.90

Table 6—Material parameters of PVA fiber

Tensile strength, MPa	Elastic modulus, GPa	Length, mm	Diameter, μm	Density, g/cm^3	Elongation, %
1620	42.8	12	39	1.3	7

Table 7—Workability requirements for pumpable and sprayable fresh ECC

Evaluations	Fluidity	Cohesion		
Indexes	S_L, mm	S_t, mm	t, seconds	S_L/S_t
Required range	140 to 200	400 to 600	4 to 10	0.450

The slump, slump flow, and funnel flow tests were carried out for all of the fresh ECC listed in Table 1,[35,39] and the data were compared with the requirements in Table 7. For the slump and slump flow tests, the fresh ECC was evenly placed into the slump barrel in three installments and vibrated with a vibrator. The slump barrel was lifted steadily, and the lifting process was controlled in 3 to 7 seconds. When the ECC no longer slumped or the slump time reached 30 seconds, the vertical distance between the slump barrel and the top surface of ECC was measured and reported as the ECC S_L in mm, and the test was completed in 150 seconds. When the fresh ECC no longer slumped or the slump time reached 50 seconds, the two corresponding diameters of the flowed fresh ECC were measured in two orthogonal directions. The S_t in mm of ECC is the average value of the two diameters, and the test was completed in 4 minutes. For the funnel flow test, the slump barrel was inverted on the bracket and the sealing cover was closed. The fresh ECC was put into the slump barrel and vibrated with a vibrator until it was uniformly distributed. Then, the sealing cover was opened, and a timer was used to measure the time interval between opening the sealing cover and ECC emptying from the slump barrel. The funnel flow test operation was taken twice, and the average value of the measured time intervals was the funnel flow time (t) in seconds.

Impermeability—Cylindrical ECC specimens sized Φ175 x 150 x Φ185 mm were made and cured for 27 days to conduct the ECC impermeability tests according to GB/T 50082-2009.[40] The specimens were sealed with paraffin and kept standing for 1 day before impermeability tests, where

the specimens were fixed onto the concrete permeability apparatus.

The water pressurizing process of the concrete permeability apparatus took no more than 5 minutes, and the timing was started as soon as the proposed water pressure was reached. The water pressure was controlled at 1.2 ± 0.5 MPa within 24 hours, and the tested specimens were removed and then split in half lengthwise to determine the water penetration height. The average penetration height of water D_m was taken from 10 equidistant spots along each face of the split specimen, and K (m/s) could be calculated according to Eq. (1)

$$K = aD_m^2/2TH \quad (1)$$

where D_m is the average penetration height of water, m; H is the water pressure, where 1 MPa is expressed as a height of 102 m, m; T is the constant pressure time, seconds; and a is the water absorption rate, which is generally taken as 0.03. K is required to be less than 2.610×10^{-11} m/s for underground and hydraulic applications.[20]

Mechanical properties—Cubic specimens sized 100 mm were used for uniaxial compression tests. The compression tests were performed on a 1000 kN-capacity servo-hydraulic universal testing system with controlled monotonic loading, with a speed of 0.15 mm/min for obtaining the compressive strength (f_c). The 330 mm long x 60 mm wide x 15 mm thick dumbbell-shaped specimens were used in the uniaxial tensile tests, shown in Fig. 1, and the tests were carried out on the electro-servo universal testing machine to obtain the tensile strain (ε_t) and tensile stress (σ_t). Monotonic loading and displacement control with a speed of 0.15 mm/min were used in the uniaxial tensile tests.

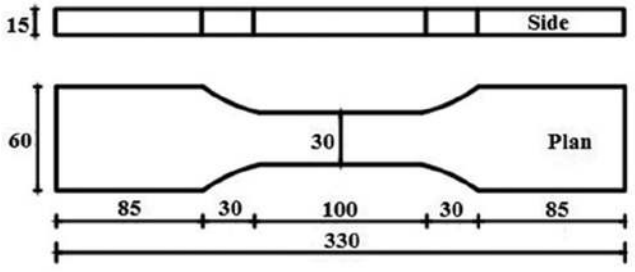

Fig. 1—Dumbbell specimens for ECC direct tension tests (mm).

Drying shrinkage tests—Specimens of 100 x 100 x 510 mm and a horizontal length comparator with a 540 mm survey scaled distance and 0.001 mm resolution were used for drying shrinkage tests.[40] The shrinkage tests were performed at a room temperature of 20 ± 2°C and relative humidity of 60 ± 5%. The length of the specimens during the curing time was measured, and the drying shrinkage strain ε_{st} could be calculated based on Eq. (2)

$$\varepsilon_{st} = (L_0 - L_t)/L_b \quad (2)$$

where L_0 is the length of the specimen at the beginning, mm; L_t is the length of the specimen after 28 days, mm; and L_b is 540 mm. The resolution of ε_{st} should be 1.0×10^{-6}. The 28-day drying shrinkage strain ε_{st} of cement-based materials used in underground and hydraulic practical engineering should be lower than 800×10^{-6}.[41]

ECC MIXTURE PROPORTIONS OPTIMIZATION BASED ON TEST RESULTS

General test results

Based on the workability, impermeability, and drying shrinkage requirements listed in the "Experimental research" section, the empirical results are evaluated in Table 8.

Test results discussion and analysis

Mechanical properties—According to Table 8, the f_c were all over 30 MPa, of which the f_c of E-2.2 achieved 43.67 MPa. The tensile stress-strain curves of each group are shown in Fig. 2, and it could be observed clearly that each group had obvious strain hardening, and the ultimate tensile strain was in the range of 3.25 to 4.12%.

The mechanical properties of the E-1 and E-2 series were all good, but the workability and impermeability of the specimens were quite different from each other, which are of crucial importance when a large amount of ECC is applied in underground and hydraulic engineering. Therefore, the effects of adding SF to ECC workability and impermeability need to be further discussed.

Workability—The relationship between SF content and workability evaluation indexes (slump, slump flow, flow time, and the S_L/S_t) of the E-1 and E-2 series is shown in Fig. 3.

Table 8—Test results of ECC performance evaluation indexes

	Workability (pumpability and sprayability)				Mechanical properties			Impermeability	Drying shrinkage
No.	S_L, mm	S_t, mm	t, seconds	S_L/S_t	f_c, MPa	ε_{tp}, %	σ_{tp}, MPa	$K \times 10^{-11}$, m/s	$\varepsilon_{st} \times 10^{-6}$
E-1.0	218☒	608☒	3.41☒	0.361☒	34.23	3.73	3.25	3.189☒	1021.3☒
E-1.1	197☑	543☑	4.23☑	0.363☒	37.85	3.45	3.46	2.358☑	945.2☒
E-1.2	188☑	436☑	5.38☑	0.432☑	38.42	3.16	3.78	1.912☑	739.1☑
E-1.3	183☑	387☒	5.46☑	0.473☑	38.63	2.98	4.11	1.657☑	811.4☒
E-2.0	188☑	458☑	5.33☑	0.410☒	36.90	4.41	3.48	2.227☑	835.6☒
E-2.1	178☑	425☑	5.48☑	0.418☑	41.18	4.02	3.92	1.902☑	846.5☒
E-2.2	174☑	412☑	5.73☑	0.423☑	43.67	3.80	4.12	1.713☑	603.6☑

Note: ☑ stands for test results satisfy requirements; ☒ stands for test results do not satisfy requirements.

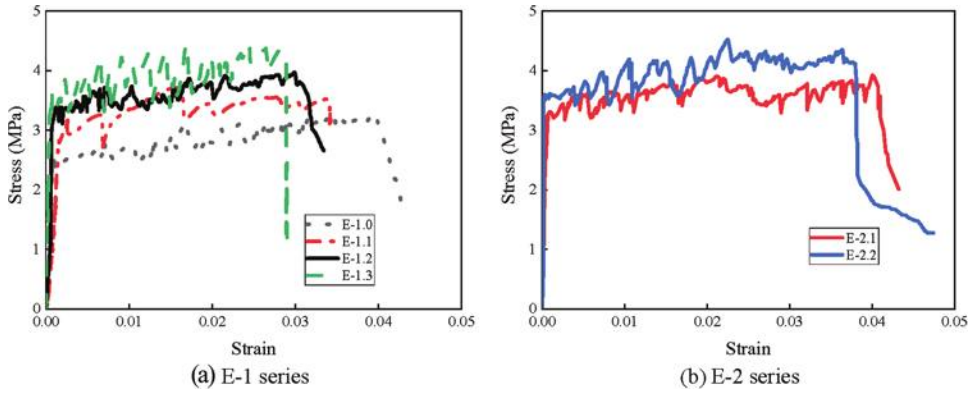

Fig. 2—Tensile stress-strain curves.

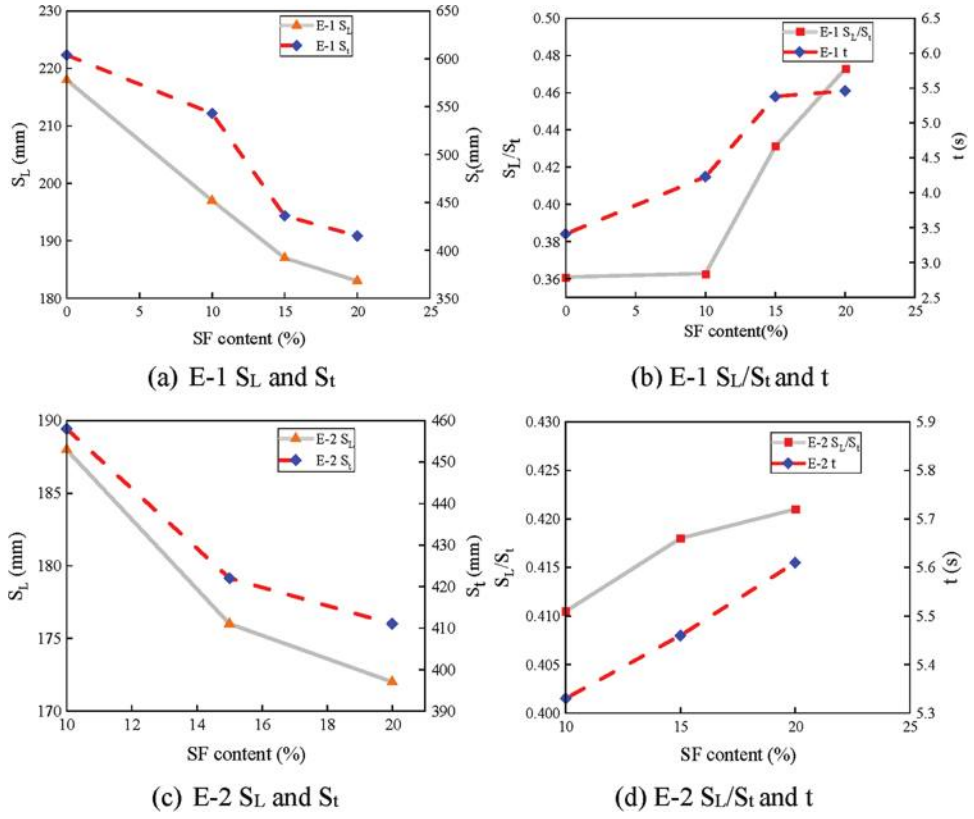

Fig. 3—Relationships between SF content and workability evaluation indexes.

It can be seen from Fig. 3 that the S_L decreased gradually with the increase in SF content, indicating that the fluidity decreased as the amount of SF increased. However, the S_t decreased and the t increased as SF was added, indicating that the cohesion increased with the increase in SF. For the E-1 series, the S_L of E-1.0 was 218 mm, which exceeded the upper limit of S_L (200 mm) according to Table 7. The S_t of E-1.3 is only 387 mm, which cannot satisfy the required lower limit 400 mm. The S_L, S_t, and t of groups E-1.1 and E-1.2 were in the required ranges. In addition, the S_L/S_t of E-1.2 was 0.432, which was closer to 0.450. For the E-2 series, the S_L, S_t, and t were all within the required range. In addition, the S_L/S_t of E-2.2 was 0.423, which was the closest to the suggested 0.450. The use of SF can effectively improve both the pumpability and sprayability of high-w/c ECC. The extremely fine SF particles can improve sprayability in a pozzolanic admixture by maintaining proper cohesion and increasing the thickness of sprayed cement-based materials, minimizing the rebound degree.[37] At the same time, fine SF can help form a lubricating layer on the surface of the mixture, resulting in reduced pumping resistance, which has a positive effect on pumpability.

Impermeability—The average permeability height H and the K of each group are listed in Table 9. It can be observed that as more SF was added, lower H and K values were achieved. The SF hydrated with the cement, which improved the microstructure uniformity and reduced the ECC's porosity by forming additional calcium silicate hydrate (C-S-H).[32] Also, adding SF might increase the density of the cement matrix. For the E-2 series, the impermeability was better than that of the E-1 series under the same SF mass ratio—even their w/c were close to each other—because FA mass ratios were higher for the E-2 series, and plenty of C-S-H was produced through pozzolanic reactions, making

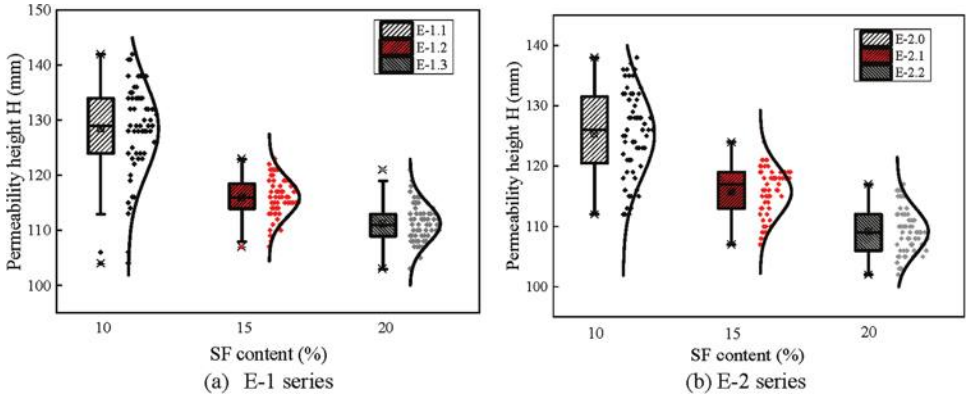

Fig. 4—Box plots for relationships between SF content and H.

Table 9—Average *H* and *K* of each group

Series	No.	*H*, m	$K \times 10^{-11}$, m/s
E-1	E-1.0	148.9	3.189
	E-1.1	128.9	2.358
	E-1.2	116.1	1.912
	E-1.3	108.1	1.657
E-2	E-2.0	125.3	2.227
	E-2.1	115.8	1.902
	E-2.2	109.9	1.713

Table 10—Porosity and pore density test results

Series	No.	Pore density, psc./μm²	Porosity, %
E-1	E-1.0	0.017	15.43
	E-1.1	0.013	12.76
	E-1.2	0.011	9.31
	E-1.3	0.009	7.16
E-2	E-2.0	0.012	12.01
	E-2.1	0.009	8.99
	E-2.2	0.007	6.98

Note: psc is pore space.

the cement matrix denser and the pores finer. Meanwhile, the pozzolanic reaction takes some of the free water in the system, which indirectly reduces the porosity.[42]

Box plots were used to analyze the dispersion of each group's *H*, as shown in Fig. 4. It was found that the median and average values of *H* of E-1 were nearly located at the middle of the box plot. The *H* distributions of E-1.2 and E-1.3 were closer to normal distributions compared with E-1.1. However, for E-1.3, there was an exceptional datum, and the *H* was higher, indicating poor impermeability. Although E-1.2 also has an exceptional datum, it was with a lower *H*, indicating good impermeability. It can be seen from Fig. 4(b) that the *H* distribution of E-2.2 was closer to the normal distributions compared with E-2.0 and E-2.1. The median and average values of *H* for E-2.2 were nearly located at the middle of the box plot.

To further explore the influence of SF on ECC impermeability, the porosity of the E-1 and E-2 series was analyzed, and the relationship between SF content and porosity was obtained accordingly. Scanning electron microscopy (SEM) was used to investigate the porosity of the E-1 and E-2 series. The 3 x 3 x 1 mm specimens for SEM were obtained from the compressive strength tests and coated with gold using a coating machine to progress the characteristics of electricity transmission. The SEM images were taken at 1000 magnification levels to observe the porosity of ECC and are shown in Fig. 5. Based on the image processing software used, microscopic parameters such as the area and the number of pores were extracted. The porosity was obtained by dividing the area of the pores by the total area. The ECC porosity and pore density of each group are listed in Table 10.

It can be seen from Table 10 that the ECC porosity and pore density decreased with the increase in SF content. The higher the *SF*/*c* used, the lower the porosity and pore density. It is well known that the durability of cement-based materials largely depends on the possibility of penetration of hazardous ions into the material with water as the medium.[17] Therefore, combined with the aforementioned test results, adding SF might also improve ECC durability.

ECC mixture proportions optimization

Based on Table 8 and the discussion of the test results, E-1.2 and E-2.2 satisfy the workability evaluation indexes for underground and hydraulic engineering, of which the S_L is in the range of 140 to 200 mm to ensure proper fluidity, the S_t is in the range of 400 to 600 mm, the *t* should be in the range of 4 to 10 seconds to ensure cohesion, and the S_L/S_t is generally approximately 0.45 to ensure the balance between fluidity and cohesion. Also, for E-1.2 and E-2.2, the ultimate tensile strain ε_{tp} was greater than 3%, *K* was lower than 2.610×10^{-11} m/s, and drying shrinkage strain ε_{st} was lower than 800×10^{-6}.

To optimize the final ECC mixture proportions, spray tests were carried out on E-1.2 and E-2.2. During the spray tests, fresh ECC was sprayed with air pressure of 100 psi (0.69 MPa). The distance between the spray gun and concrete surface was approximately 0.2 to 0.5 m, and the spray thickness was 20 mm. The mass of ECC attached to the concrete surface (m_1) and the mass of the rebound ECC (m_2) were obtained. The value of $m_2/(m_1 + m_2)$ was calculated as the rebound rate. It can be seen in Fig. 6 that both E-1.2 and E-2.2 could be pumped and sprayed, which further

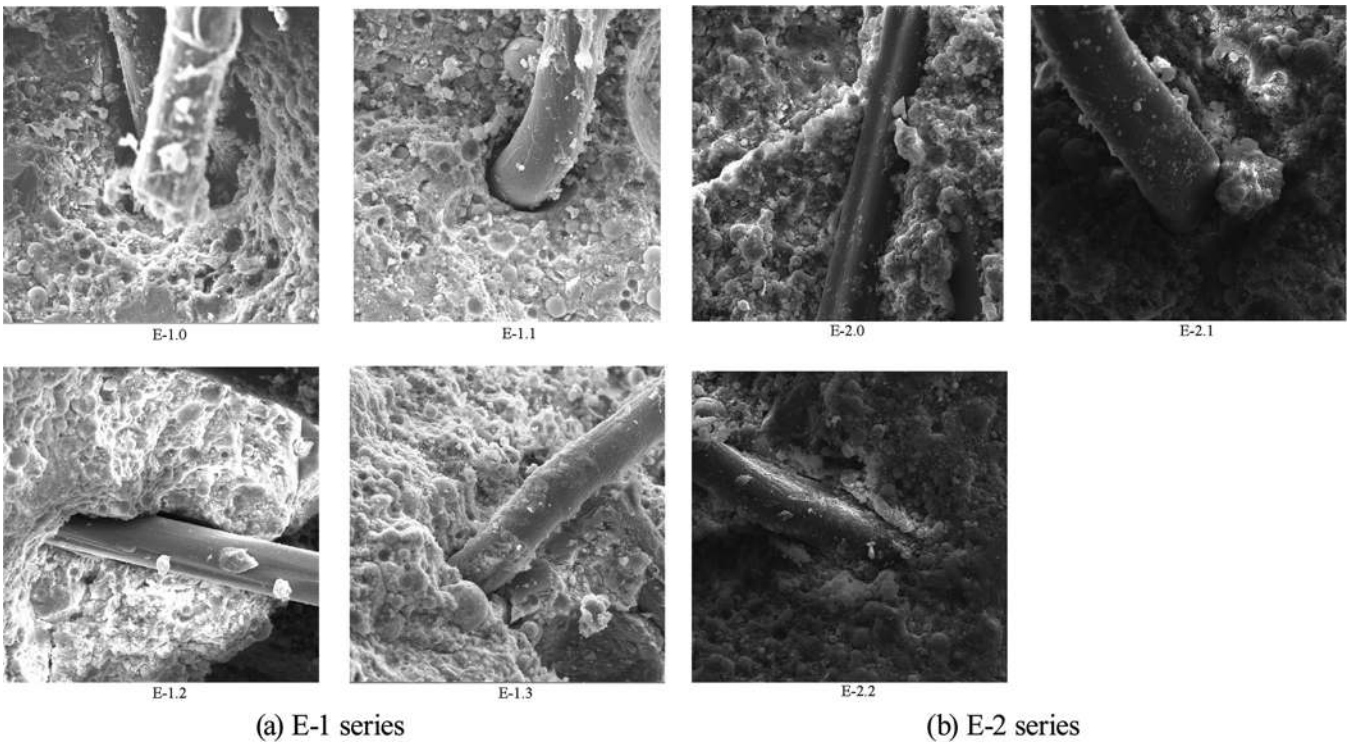

Fig. 5—SEM images of E-1 and E-2 series.

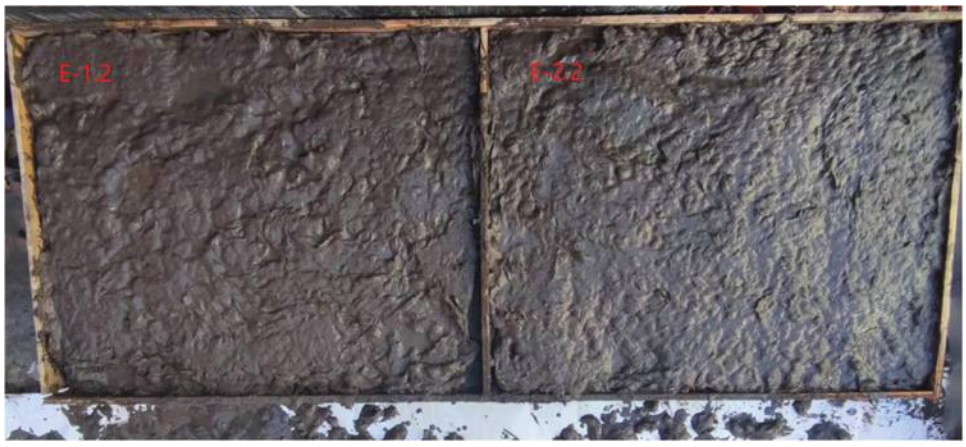

Fig. 6—Spray tests of: (left) E-1.2; and (right) E-2.2.

demonstrated the reliability of the workability evaluation indexes. However, the rebound rate of E-2.2 was 7.89% lower than that of E-1.2 (18.92%), indicating that E-2.2 had better workability.

In addition, a radar chart of all the issues regarding ECC material properties discussed is given in Fig. 7, which indicates that the mechanical properties, impermeability, and anti-drying-shrinkage ability of E-2.2 were better than those of E-1.2. Therefore, the E-2.2 ECC mixture proportions (F/c = 4.44, SF/c = 0.20, SRA/c = 9%, and fiber volume content V_f = 2%) having excellent workability (pumpability and sprayability), high toughness (the ultimate tensile strain ε_{tp} is greater than 3.5%), high tensile ductility achieved by forming multiple tight microcracks instead of localized large cracks (as shown in Fig. 8), good impermeability ($K = 1.713 \times 10^{-11}$ m/s < 2.610×10^{-11} m/s), and low drying shrinkage strain ($\varepsilon_{st} = 603.6 \times 10^{-6} < 800 \times 10^{-6}$) were the final optimized ECC mixture proportions.

TOUGHNESS EVALUATION AND CHARACTERISTIC PARAMETERS CALIBRATION OF OPTIMIZED ECC

Toughness evaluation

Though the toughness evaluation of ECC could be carried out using the uniaxial tensile test, this method was complicated and time-consuming—advanced equipment was required and improper operation may have a great impact on test results. The operations of the four-point bending test were easy to conduct and are more widely used to evaluate the toughness of ECC. In addition, in tunnel engineering, direct shear failure caused by creep slip and dislocation of active faults will lead to tunnel lining cracking and even collapse of the whole structure, which seriously endangers

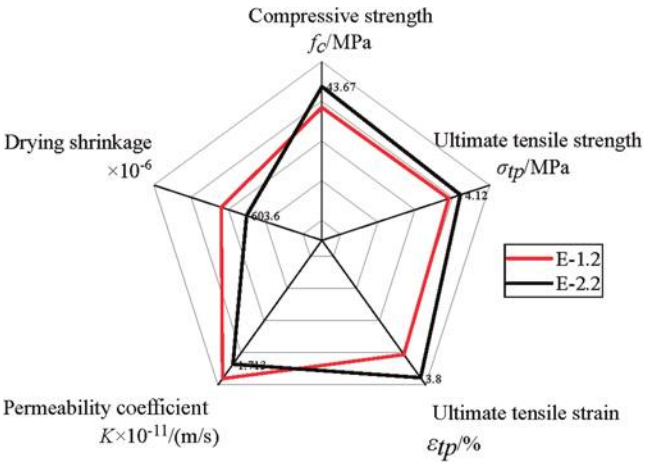

Fig. 7—Radar chart for PVA-ECC test results (E-1.2 and E-2.2).

Fig. 8—ECC multiple tight microcracks of E-2.2 direct tension test specimen.

the safety of the tunnel structure.[43] Thus, shear toughness is also a key parameter of ECC when used in underground and hydraulic engineering. Therefore, the toughness of the optimized ECC (E-2.2) was evaluated by combining the four-point bending test and the shear test.

Four-point bending tests were carried out according to ASTM C1609/C1609M-06,[39] and the flexural toughness was evaluated by the flexural toughness index (I_m) proposed by Naaman and Reinhardt.[44] The method stated in ASTM C1018 can only determine the toughness indexes I_5, I_{10}, and I_{20}. However, Said and Razak[45] pointed out that toughness indexes I_5, I_{10}, I_{20}, I_{30}, I_{40}, I_{50}, I_{60}, and I_{70} for ECC may be evaluated because of the high ductility and high deflection. Thus, according to the four-point bending test, the load-deflection relationship of E-2.2 shown in Fig. 9 and I_m and I_{MOR} can be calculated as follows

$$I_m = \int_0^{\frac{m+1}{2}} P(\delta)d\delta / \int_0^{\delta} P(\delta)d\delta = S_{OACD}/S_{OAB} \quad (3)$$

$$I_{MOR} = \int_0^{\delta_{MOR}} P(\delta)d\delta / \int_0^{\delta} P(\delta)d\delta = S_{OACEF}/S_{OAB} \quad (4)$$

where δ is the deflection of midspan at the first crack; the values of m were taken as 5, 10, 20, 30, 40, 50, 60, and 70, respectively; and δ_{MOR} is the midspan deflection at ultimate load.

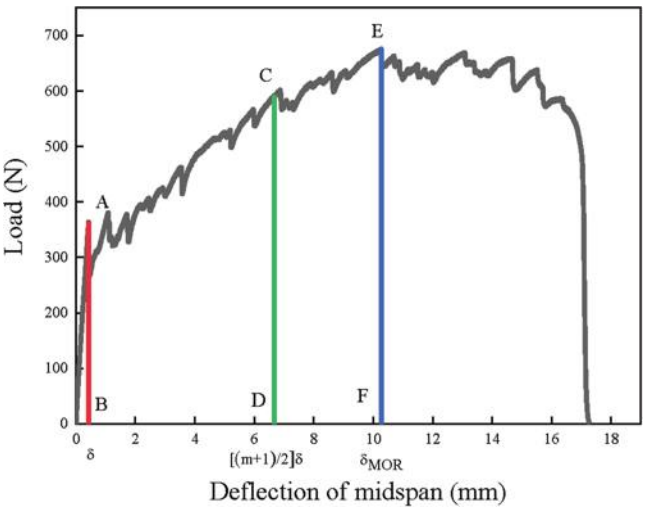

Fig. 9—Four-point bending test load-deflection curve (E-2.2).

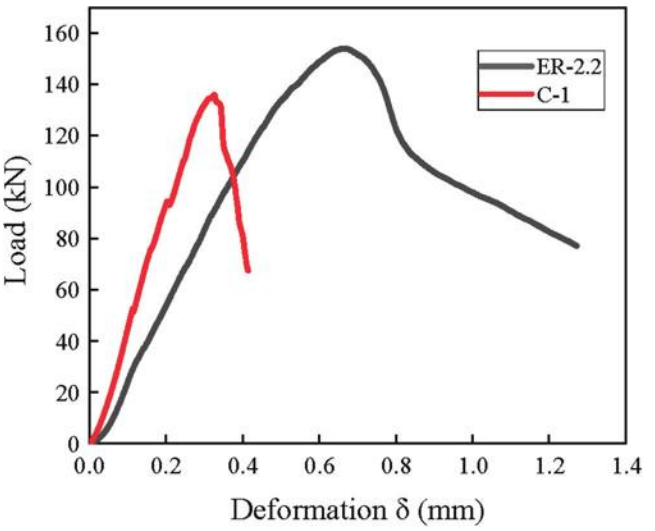

Fig. 10—Shear test load-deflection curves for E-2.2 and C-1.

NC of the same f_c as E-2.2 was set as the control group named C-1, and the shear tests were carried out according to CECS 13-2009.[46] The shear test load-deflection curves of E-2.2 and C-1 are shown in Fig. 10. According to Deng et al.,[47] the shear toughness before peak load (T_p) and the shear toughness after peak load ($R_{p,k}$) can be calculated as follows

$$T_p = \Omega_p/2bh^2 \quad (5)$$

$$R_{p,k} = \Omega_{p,k}/2bh\delta_{p,k}f_p \quad (6)$$

where Ω_p is the area under the load-deflection curve before the peak load; b and h are the width and height, respectively, of the shear specimen; δ_k is defined as K times δ_p; δ_p is the deflection corresponding to peak load; K is taken as 1.2, 1.5, and 2.0, respectively[47]; $\Omega_{p,k}$ is the area under the load-deflection curve from δ_p to δ_k; and f_p is the shear strength.

Table 11—Test results of four-point bending and shear tests

Test	Toughness evaluation index	Test result	
		E-2.2	C-1
Four-point bending test	I_5	5.1	—
	I_{10}	10.5	—
	I_{20}	22.4	—
	I_{30}	35.1	—
	I_{40}	49.7	—
	I_{50}	67.8	—
	I_{60}	78.9	—
	I_{70}	91.3	—
	I_{MOR}	110.9	—
	$2\delta_{MOR}/(\delta - 1)$	78.0	—
Shear test	T_p	3.048%	0.269
	$R_{p,1.2}$	0.93	0.17
	$R_{p,1.5}$	0.82	0.08
	$R_{p,2.0}$	0.37	—

The test results of the bending and shear tests are given in Table 11.

Said and Razak[45] pointed out that ECC having toughness indexes $I_m > m$ and $I_{MOR} > 2\delta_{MOR}/(\delta - 1)$ can be termed as strain-hardening-type materials. It can be seen from Table 11 that with the increase of the m, the difference between the I_m and m increased. Meanwhile, I_{MOR} was 110.9, which was far greater than $2\delta_{MOR}/(\delta - 1) = 78.0$, indicating that the toughness of the material increases with the increase in deformation. The T_p and $R_{p,k}$ reflect the shear toughness of ECC; the larger the values, the greater the shear toughness.[47] The T_p of ECC was 3.672%, which was approximately 15 times that of C-1 ($T_p = 0.269$), and the maximum residual shear toughness of E-2.2 ($R_{p,1.2} = 0.93$) was approximately 12 times that of C-1 ($R_{p,1.5} = 0.08$).

Combined with the ultimate tensile strain obtained from the uniaxial tensile test in this paper, the complete toughness evaluation of E-2.2 was finally obtained, as shown in Table 12.

Table 12—Toughness evaluation indexes for E-2.2

Test	Toughness evaluation index	Test result
Uniaxial compression tests	ε_{cp}	0.416%
Uniaxial tensile tests	ε_{tp}	3.80%
Four-point bending test	I_5	5.1
	I_{10}	10.5
	I_{20}	22.4
	I_{30}	35.1
	I_{40}	49.7
	I_{50}	67.8
	I_{60}	78.9
	I_{70}	91.3
	I_{MOR}	110.9
Shear test	T_p	3.048%
	$R_{p,1.2}$	0.93
	$R_{p,1.5}$	0.82
	$R_{p,2.0}$	0.37

Table 13—Material characteristic parameters for E-2.2

Characteristic parameter	Value
E_0, MPa	22.60
σ_{cp}, MPa	43.67
ε_{cp}, %	0.416
σ_{cu}, MPa	7.95
ε_{cu}, %	3.91
σ_{t0}, MPa	3.53
ε_{t0}, %	0.016
σ_{tp}, MPa	4.12
ε_{tp}, %	3.80
σ_{tu}, MPa	1.02
ε_{tu}, %	4.50
Density, kg/m^3	1950

Material characteristic parameters

Also, according to the previous test results, the material characteristic parameters of E-2.2 are given in Table 13, including the density ρ, elastic modulus E_0, uniaxial compression peak stress σ_{cp} and its corresponding strain ε_{cp}, uniaxial compression ultimate stress σ_{cu}, ultimate compression strain ε_{cu}, uniaxial tensile yield stress σ_{t0} and its yield strain ε_{t0}, ultimate tensile strength σ_{tp} and its corresponding strain ε_{tp}, as well as the tensile failure stress σ_{tu} and the failure strain ε_{tu}; these provide a basis for its engineering application and numerical simulation. A comparison of the mechanical properties of E-2.2 and the traditional cement-based material C-1 used in underground and hydraulic engineering is given in Fig. 11, where the f_c was the same. It could be intuitively found that the radar chart of E-2.2 was fuller than that of C-1, indicating that ECC (E-2.2) had excellent mechanical properties compared with the NC (C-1), especially for toughness.

CONCLUSIONS

To meet the requirements of underground hydraulic structures, an engineered cementitious composite (ECC) mixture ratio with a high water-cement ratio (w/c) and high fly ash (FA) content was adopted, and silica fume (SF) and shrinkage-reducing agent (SRA) were added to improve the ECC's performance. The conclusions of this study are summarized as follows:

1. High-FA ECC mixture proportions were adapted in this study. FA not only replaced a large portion of cement in ECC without sacrificing its mechanical properties and tensile ductility but also offered environmental advantages in processing cement.

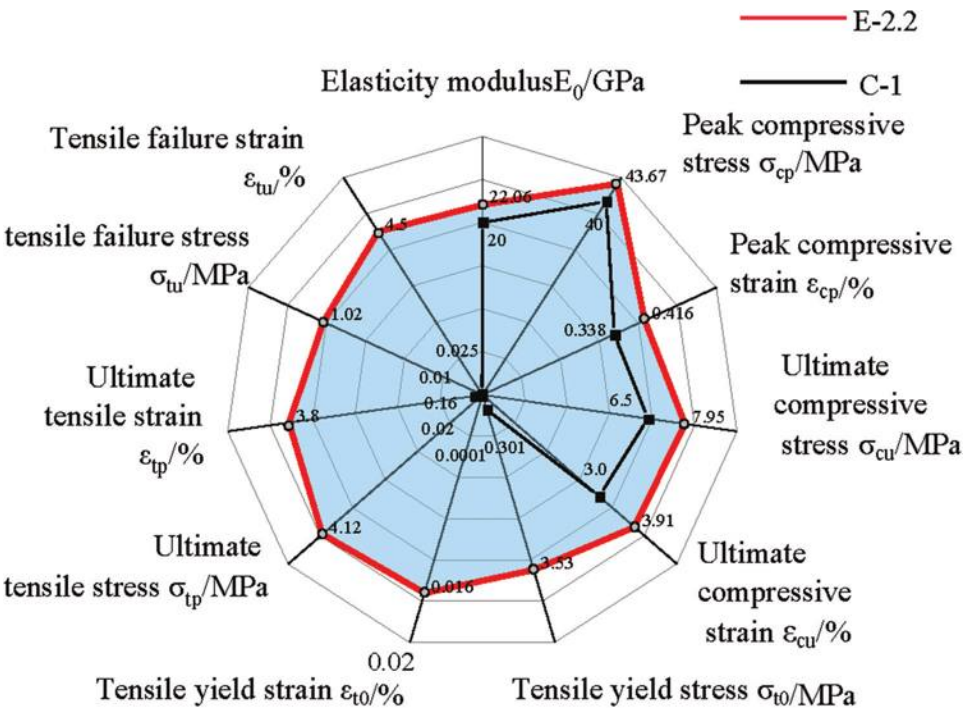

Fig. 11—Radar chart for PVA-ECC characteristic material parameters (E-2.2).

2. The workability evaluation indexes of fresh ECC were obtained, of which the slump S_L was in the range of 140 to 200 mm to ensure proper fluidity; the slump flow S_t was in the range of 400 to 600 mm; and funnel flow time t was 4 to 10 seconds to ensure cohesion; and the ratio of slump to slump flow (S_L/S_t) was generally approximately 0.45 to ensure the balance between fluidity and cohesion.

3. An ECC mixture proportion (E-2.2), with excellent workability (pumpability and sprayability), high toughness (the ultimate tensile strain ε_{tp} is greater than 3.5%), good impermeability (permeability coefficient $K = 1.713 \times 10^{-11}$ m/s $< 2.610 \times 10^{-11}$ m/s), and low drying shrinkage strain (drying shrinkage strain $\varepsilon_{st} = 603.6 \times 10^{-6} < 686.5 \times 10^{-6}$) was the result of the final optimization.

4. The use of SF can effectively improve both pumpability and sprayability of high-w/c ECC. The S_L decreased gradually with the increase of SF content, indicating that the fluidity decreases gradually. However, the S_t decreased and the t increased, indicating that the cohesion increases.

5. The more SF added, the lower the K value that could be achieved. Adding SF could increase the density of the cement matrix. The ECC porosity and pore density decreased with the increase of SF content.

6. Combined with the four-point bending test and shear test, the complete toughness evaluation for E-2.2 was established; the material characteristic parameters of E-2.2 are given in Table 13, which can be directly applied to future engineering.

AUTHOR BIOS

Xiaoqin Li *is a Professor in the Faculty of Civil Engineering and Mechanics at Kunming University of Science and Technology. She received her BS from Tsinghua University, Beijing, China, and her MS and PhD from The University of Edinburgh, Edinburgh, UK. Her research interests include ECCs and fiber-reinforced polymer (FRP)-strengthened structures.*

Li Zhang *is a Postgraduate Student in the Faculty of Civil Engineering and Mechanics at Kunming University of Science and Technology, Kunming, Yunnan, China. Her research interests include engineered cementitious composites (ECCs) and structural engineering.*

Wenlu Wen *is a Manager of QuakeSafe Technologies Co., Ltd., Kunming, Yunnan, China.*

Shihua Li *is a Director of YCIH Green High-Performance Concrete Company Limited, Kunming, Yunnan, China.*

Xu Zhou *is a Graduate Student in the Faculty of Civil Engineering and Mechanics at Kunming University of Science and Technology. His research interests include ECCs and structural engineering.*

ACKNOWLEDGMENTS

The authors gratefully acknowledge the funding support of the National Natural Science Foundation of China (Grant No. 52168028, 51968035) and Yunnan Youth Talent Project (No. [2020]150 YNWR-QNBJ-2020-049).

REFERENCES

1. Li, V. C., "Tailoring ECC for Special Attributes: A Review," *International Journal of Concrete Structures and Materials*, V. 6, No. 3, 2012, pp. 135-144.

2. Kim, Y. Y.; Fischer, G.; and Li, V. C., "Performance of Bridge Deck Link Slabs Designed with Ductile Engineered Cementitious Composite," *ACI Structural Journal*, V. 101, No. 6, Nov.-Dec. 2004, pp. 792-801.

3. Lee, C.-H.; Chiu, Y.-C.; Wang, T.-T.; and Huang, T.-H., "Application and Validation of Simple Image-Mosaic Technology for Interpreting Cracks on Tunnel Lining," *Tunnelling and Underground Space Technology*, V. 34, 2013, pp. 61-72. doi: 10.1016/j.tust.2012.11.002

4. Mashimo, H.; Isago, N.; Kitani, T.; and Endou, T., "Effect of Fiber Reinforced Concrete on Shrinkage Crack of Tunnel Lining," *Tunnelling and Underground Space Technology*, V. 21, No. 3-4, 2006, pp. 382-383. doi: 10.1016/j.tust.2005.12.194

5. Liu, H.; Zhang, Q.; Gu, C.; Su, H.; and Li, V. C., "Influence of Micro-Cracking on the Permeability of Engineered Cementitious Composites," *Cement and Concrete Composites*, V. 72, 2016, pp. 104-113. doi: 10.1016/j.cemconcomp.2016.05.016

6. FERC, "Engineering Guidelines for the Evaluation of Hydropower Projects," Office of Hydropower Licensing, Federal Energy Regulatory Commission, Washington, DC, 2013, https://www.ferc.gov/industries-data/hydropower/dam-safety-and-inspections/eng-guidelines. (last accessed Nov. 16, 2023)

7. Zhou, J.; Qian, S.; Ye, G.; Copuroglu, O.; van Breugel, K.; and Li, V. C., "Improved Fiber Distribution and Mechanical Properties of Engineered Cementitious Composites by Adjusting the Mixing Sequence," *Cement and Concrete Composites*, V. 34, No. 3, 2012, pp. 342-348. doi: 10.1016/j.cemconcomp.2011.11.019

8. Lepech, M. D., and Li, V. C., "Water Permeability of Engineered Cementitious Composites," *Cement and Concrete Composites*, V. 31, No. 10, 2009, pp. 744-753. doi: 10.1016/j.cemconcomp.2009.07.002

9. Yang, E.-H.; Yang, Y.; and Li, V. C., "Use of High Volumes of Fly Ash to Improve ECC Mechanical Properties and Material Greenness," *ACI Materials Journal*, V. 104, No. 6, Nov.-Dec. 2007, pp. 620-628.

10. Sherir, M. A. A.; Hossain, K. M. A.; and Lachemi, M., "Structural Performance of Polymer Fiber Reinforced Engineered Cementitious Composites Subjected to Static and Fatigue Flexural Loading," *Polymers*, V. 7, No. 7, 2015, pp. 1299-1330. doi: 10.3390/polym7071299

11. Wang, S., and Li, V. C., "Engineered Cementitious Composites with High-Volume Fly Ash," *ACI Materials Journal*, V. 104, No. 3, May-June 2007, pp. 233-241.

12. Qian, C. X., and Stroeven, P., "Development of Hybrid Polypropylene-Steel Fibre-Reinforced Concrete," *Cement and Concrete Research*, V. 30, No. 1, 2000, pp. 63-69. doi: 10.1016/S0008-8846(99)00202-1

13. Şahmaran, M., and Li, V. C., "Durability Properties of Micro-Cracked ECC Containing High Volumes Fly Ash," *Cement and Concrete Research*, V. 39, No. 11, 2009, pp. 1033-1043. doi: 10.1016/j.cemconres.2009.07.009

14. Zhang, X.; Liu, S.; Yan, C.; Wang, X.; and Wang, H., "Effects of Traffic Vibrations on the Flexural Properties of Newly Placed PVA-ECC Bridge Repairs," *Materials (Basel)*, V. 12, No. 20, 2019, Article No. 3337. doi: 10.3390/ma12203337

15. Marks, J., and Conklin, J., "Engineered Cementitious Composites: Applications and Impact of High Tensile, Self-Healing Concrete," University of Pittsburgh Swanson School of Engineering, Pittsburgh, PA, Session A5, 2013, Paper No. 3204.

16. Bäuml, M. F., and Wittmann, F. H., "Application of PVA-Fiber Reinforced Self-Compacting Concrete (ECC) for Repair of Concrete Structures," *Restoration of Buildings and Monuments*, V. 8, No. 6, 2002, pp. 591-604. doi: 10.1515/rbm-2002-5709

17. Cui, L., and Cahyadi, J. H., "Permeability and Pore Structure of OPC Paste," *Cement and Concrete Research*, V. 31, No. 2, 2001, pp. 277-282. doi: 10.1016/S0008-8846(00)00474-9

18. Li, V. C.; Mishra, D. K.; and Wu, H.-C., "Matrix Design for Pseudo-Strain-Hardening Fibre Reinforced Cementitious Composites," *Materials and Structures*, V. 28, No. 10, 1995, pp. 586-595. doi: 10.1007/BF02473191

19. Gao, S.; Wang, Z.; Wang, W.; and Qiu, H., "Effect of Shrinkage-Reducing Admixture and Expansive Agent on Mechanical Properties and Drying Shrinkage of Engineered Cementitious Composite (ECC)," *Construction and Building Materials*, V. 179, 2018, pp. 172-185. doi: 10.1016/j.conbuildmat.2018.05.203

20. GB 50108-2008, "Technical Code for Waterproofing of Underground Works," Ministry of Housing and Urban-Rural Development of the People's Republic of China, Beijing, China, 2008.

21. Zhang, P., and Li, Q., "Effect of Polypropylene Fiber on Durability of Concrete Composite Containing Fly Ash and Silica Fume," *Composites Part B: Engineering*, V. 45, No. 1, 2013, pp. 1587-1594. doi: 10.1016/j.compositesb.2012.10.006

22. Hamami, A. A.; Turcry, P.; and Aït-Mokhtar, A., "Influence of Mix Proportions on Microstructure and Gas Permeability of Cement Pastes and Mortars," *Cement and Concrete Research*, V. 42, No. 2, 2012, pp. 490-498. doi: 10.1016/j.cemconres.2011.11.019

23. Pereira, C. G.; Castro-Gomes, J.; and Pereira de Oliveira, L., "Influence of Natural Coarse Aggregate Size, Mineralogy and Water Content on the Permeability of Structural Concrete," *Construction and Building Materials*, V. 23, No. 2, 2009, pp. 602-608. doi: 10.1016/j.conbuildmat.2008.04.009

24. Niu, Q.; Feng, N.; Yang, J.; and Zheng, X., "Effect of Superfine Slag Powder on Cement Properties," *Cement and Concrete Research*, V. 32, No. 4, 2002, pp. 615-621. doi: 10.1016/S0008-8846(01)00730-X

25. Heikal, M.; El-Didamony, H.; and Morsy, M. S., "Limestone-Filled Pozzolanic Cement," *Cement and Concrete Research*, V. 30, No. 11, 2000, pp. 1827-1834. doi: 10.1016/S0008-8846(00)00402-6

26. Lee, C.-L.; Huang, R.; Lin, W.-T.; and Weng, T.-L., "Establishment of the Durability Indices for Cement-Based Composite Containing Supplementary Cementitious Materials," *Materials & Design*, V. 37, 2012, pp. 28-39. doi: 10.1016/j.matdes.2011.12.030

27. Yang, C. C., and Chiang, C. T., "On the Relationship between Pore Structure and Charge Passed from RCPT in Mineral-Free Cement-Based Materials," *Materials Chemistry and Physics*, V. 93, No. 1, 2005, pp. 202-207. doi: 10.1016/j.matchemphys.2005.03.044

28. Ding, Z.; Wen, J.; Li, X.; and Yang, X., "Permeability of the Bonding Interface between Strain-Hardening Cementitious Composite and Normal Concrete," *AIP Advances*, V. 9, No. 5, 2019, Article No. 055107. doi: 10.1063/1.5086915

29. Li, X.; Yang, X.; Ding, Z.; Du, X.; and Wen, J., "ECC Design Based on Uniform Design Test Method and Alternating Conditional Expectation," *Mathematical Problems in Engineering*, V. 2019, 2019, Article No. 9575897. doi: 10.1155/2019/9575897

30. Wu, Z. W., and Lian, H. Z., *High Performance Concrete*, Railway Publishing House, Beijing, China, 2008.

31. Rajabipour, F.; Sant, G.; and Weiss, J., "Interactions between Shrinkage Reducing Admixtures (SRA) and Cement Paste's Pore Solution," *Cement and Concrete Research*, V. 38, No. 5, 2008, pp. 606-615. doi: 10.1016/j.cemconres.2007.12.005

32. Thomas, M. D. A.; Hooton, R. D.; Scott, A.; and Zibara, H., "The Effect of Supplementary Cementitious Materials on Chloride Binding in Hardened Cement Paste," *Cement and Concrete Research*, V. 42, No. 1, 2012, pp. 1-7. doi: 10.1016/j.cemconres.2011.01.001

33. Ngo, T.-T.; Kadri, E.-H.; Cussigh, F.; and Bennacer, R., "Relationships between Concrete Composition and Boundary Layer Composition to Optimise Concrete Pumpability," *European Journal of Environmental and Civil Engineering*, V. 16, No. 2, 2012, pp. 157-177. doi: 10.1080/19648189.2012.666910

34. JGJ/T 10-2011, "Technical Specification for Construction of Concrete Pumping," Ministry of Housing and Urban-Rural Development of the People's Republic of China, Beijing, China, 2011.

35. JGJ/T 372-2016, "Technical Specification for Application of Sprayed Concrete," Ministry of Housing and Urban-Rural Development of the People's Republic of China, Beijing, China, 2016.

36. Kim, Y. Y.; Kong, H.-J.; and Li, V. C., "Design of Engineered Cementitious Composite Suitable for Wet-Mixture Shotcreting," *ACI Materials Journal*, V. 100, No. 6, Nov.-Dec. 2003, pp. 511-518.

37. Yun, K.-K.; Choi, S.-Y.; and Yeon, J. H., "Effects of Admixtures on the Rheological Properties of High-Performance Wet-Mix Shotcrete Mixtures," *Construction and Building Materials*, V. 78, 2015, pp, 194-202.

38. Shi, Y.; Matsui, I.; and Feng, N., "Effect of Compound Mineral Powders on Workability and Rheological Property of HPC," *Cement and Concrete Research*, V. 32, No. 1, 2002, pp. 71-78. doi: 10.1016/S0008-8846(01)00631-7

39. ASTM C1609/C1609M-06, "Standard Test Method for Flexural Performance of Fiber-Reinforced Concrete (Using Beam With Third-Point Loading)," ASTM International, West Conshohocken, PA, 2006, 8 pp.

40. GB/T 50082-2009, "Standard for Test Methods of Long-Term Performance and Durability of Ordinary Concrete," Ministry of Housing and Urban-Rural Development of the People's Republic of China, Beijing, China, 2009.

41. Zhang, J.; Gong, C.; Guo, Z.; and Zhang, M., "Engineered Cementitious Composite with Characteristic of Low Drying Shrinkage," *Cement and Concrete Research*, V. 39, No. 4, 2009, pp. 303-312. doi: 10.1016/j.cemconres.2008.11.012

42. Abd Elrahman, M., and Hillemeier, B., "Combined Effect of Fine Fly Ash and Packing Density on the Properties of High Performance Concrete: An Experimental Approach," *Construction and Building Materials*, V. 58, 2014, pp. 225-233. doi: 10.1016/j.conbuildmat.2014.02.024

43. Shahidi, A. R., and Vafaeian, M., "Analysis of Longitudinal Profile of the Tunnels in the Active Faulted Zone and Designing the Flexible Lining (for Koohrang-III Tunnel)," *Tunnelling and Underground Space Technology*, V. 20, No. 3, 2005, pp. 213-221. doi: 10.1016/j.tust.2004.08.003

44. Naaman, A., and Reinhardt, H., "Characterization of High Performance Fiber Reinforced Cement Composites – HPFRCC," *High Performance Fiber Reinforced Cement Composites 2 (HPFRCC 2): Proceedings of the Second International RILEM Workshop*, Taylor & Francis, London, UK, 1996, pp. 1-24.

45. Said, S. H., and Razak, H. A., "The Effect of Synthetic Polyethylene Fiber on the Strain Hardening Behavior of Engineered Cementitious Composite (ECC)," *Materials & Design*, V. 86, 2015, pp. 447-457. doi: 10.1016/j.matdes.2015.07.125

46. CECS 13-2009, "Standard Test Method for Fiber Reinforced Concrete," China Association of Engineering and Construction Standardization, Beijing, China, 2009.

47. Deng, M.; Liu, H.; Ma, F.; and Deng, C., "Double Shear Experiment of Highly Ductile Concrete Modified by Polyvinyl Alcohol and Shear Toughness Evaluation Method," *Acta Materiae Compositiae Sinica*, V. 37, No. 2, 2020, pp. 461-471.

ARE YOU A RESEARCHER?

SIGN UP FOR ORCID TODAY!

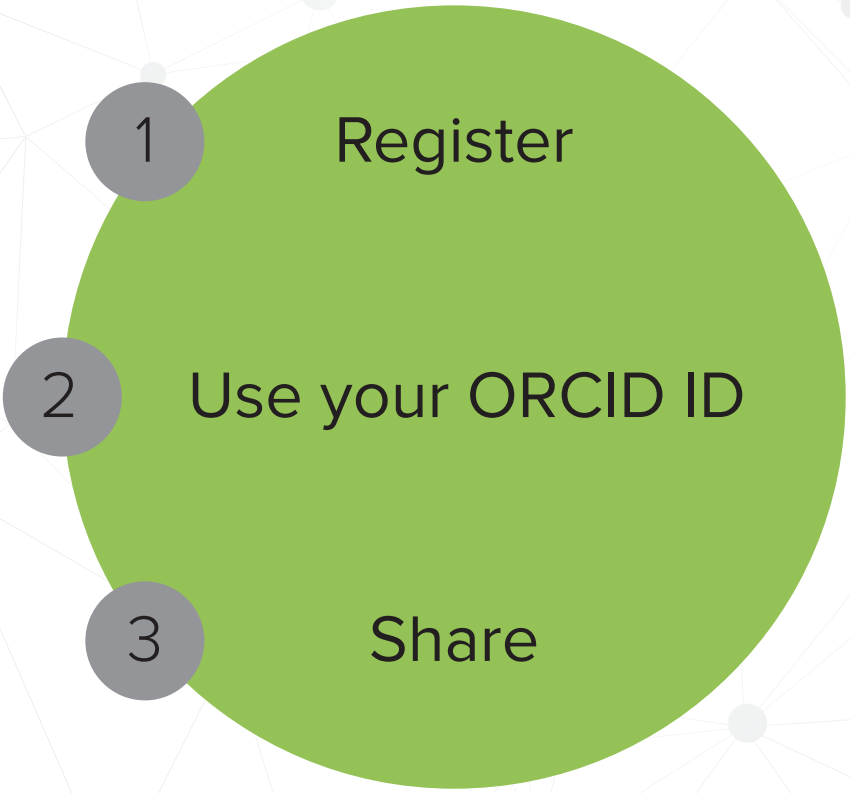

ORCID provides a digital identifier that distinguishes you from every other researcher and, through integration in key research workflows such as manuscript and grant submission, supports automated linkages between you and your professional activities, ensuring that your work is recognized.

ORCID services are FREE and it's as easy as **1-2-3**.

WWW.ORCID.ORG

ACI MATERIALS JOURNAL TECHNICAL PAPER

Title No. 121-M06

Proposed Mixture Design Method for High-Strength Geopolymer Concrete

by Jagad Gaurav, Chetankumar Modhera, and Dhaval Patel

*This research focuses on developing a mixture design for high-strength geopolymer concrete (HSGPC) complying with the high-strength concrete criteria mentioned in Indian standards. This study focuses on optimizing the content of alkaline activators and binders proportionately. The compressive strength of different proportions of geopolymer mortar was carried out meticulously to determine the optimal proportions of solution-binder (*S/B*) and sodium silicate-sodium hydroxide (*SS/SH*) ratios. The aforementioned ratios were optimized using the Technique for Order of Preference by Similarity to Ideal Solution (TOPSIS) analysis for further calculation. The mixture proportions for Grades M70, M80, M90, and M100 were determined and verified through experimental validation. To assess the suggested mixture design, a slump test was conducted to quantify the workability, subsequently followed by the evaluation of compressive strength after 24 hours, 7 days, and 28 days. After achieving the desired workability, promising compressive strength was observed as 76, 89, 93, and 104 MPa at 28 days. Finally, the mechanism of strength increment was investigated using various characterization techniques, such as X-ray diffraction (XRD) and scanning electron microscopy (SEM) equipped with energy-dispersive spectroscopy (EDS). The SEM/EDS analysis of the HSGPC proves the dense microstructures of different gel formations. The proposed mixture design procedure falls under the target strength-based method category. It has successfully yielded a strength of 104 MPa for ground-granulated blast-furnace slag (GGBS)-based geopolymer concrete incorporating coarse and fine aggregates.*

Keywords: ambient curing; high-strength geopolymer concrete (HSGPC); microstructural study; mixture design procedure.

INTRODUCTION

Interest in achieving sustainable development has grown over the past few decades. Infrastructural development has garnered much attention concerning its need and associated environmental impact. Concrete, a highly chosen material for construction, shared major concerns due to the presence of cement. Using geopolymer concrete (GPC) in construction reduces the carbon footprint as the cement is primarily responsible for the CO_2 emissions while manufacturing.[1] Research on replacing cement when producing concrete has grown since the 1970s. A 100% cement replacement was made possible due to the emergence of GPC, where cement was completely replaced with aluminosilicate material with alkaline activators. The development in research on GPC has rendered a distinguished identity to GPC rather than being an option for cement-based concrete.[2-4]

GPC is produced by mixing cementitious materials and alkaline activators in the presence of water.[5] The presence of silicates and aluminates governs the compatibility of cementitious material. Fly ash (FA), an industrial by-product, contains silicates and aluminates and was used initially to produce GPC in the presence of sodium hydroxide (SH) and sodium silicate (SS). The research highlighted the need for temperature curing for FA-based GPC. The existence of CaO in ground-granulated blast-furnace slag (GGBS) (also known as slag cement) allowed GPC to be cured in ambient curing.[1,6] By eliminating the requirement of temperature curing, GGBS-based GPC changed the way research on GPC was done.

After mixing the ingredients of GPC, polymerization starts with the OH hydroxyl groups dissolving Si-O-Si (siloxo) and Al-O-Si (sialate) bonds in an alkaline solution. Dissolution is followed by the coagulation-condensation stage, during which the dissolved ionic species interact with one another and alkali cations (Na or K), and silica monomers react with other monomers, culminating in the development of three-dimensional (3-D) polymeric networks.[7-9] The reaction is often amorphous to a semi-crystalline geopolymer comprising a 3-D alkali aluminosilicate network.[10] Precursors with a high calcium content generate calcium aluminosilicate hydrate (C-A-S-H) gels during the polymerization process, while those with lower calcium levels form sodium aluminosilicate hydrate (N-A-S-H) gels.[11,12] There has been much study in the area of GPC employing supplementary cementitious materials (SCMs) such as metakaolin,[11-13] FA,[14-16] and GGBS.[17-19] Several experts have recently concentrated on using waste products in geopolymer products, including marble sludge, rice husk ash, glass powder, and copper mine tailings recycled successfully as precursor powders or aggregates in the production of polymer binders, mortars, and concretes.[20-24] These waste-based polymer concretes demonstrated significant sustainability and environmental benefits in addition to having mechanical strengths, durability, and microstructural qualities comparable to or better than those of standard cementitious materials. It was particularly the case when ambient temperature curing was considered.[11,25]

Many factors must be considered when designing a GPC for standard compressive strength.[26] Factors that govern the mixture design of GPC are the source and the composition of aluminosilicate and the concentration of alkaline activators. The quality of water and the method of curing play an important role. Therefore, while manufacturing a GPC, the essential factors—such as the *SS*/*SH* ratio, solution-binder ratio (*S*/*B*), the molarity of the SH, time and curing temperature, water content, and the influence of calcium and other contaminants—were taken into account for experimental investigations by various

ACI Materials Journal, V. 121, No. 1, January 2024.
MS No. M-2022-313.R3, doi: 10.14359/51739201, received July 25, 2023, and reviewed under Institute publication policies.

researchers.[1,27-30] The present study attempts to incorporate the aforementioned parameters and converge the GPC mixture design procedure with the standard guidelines mentioned in IS 10262:2019[31] for high-strength concrete.

Research basis

The stature of designing a mixture for producing concrete of desired characteristics is rated very high. Mixture design reduces the trials, and hence the required resources. Various code provisions are available for designing ordinary portland cement (OPC)-based concrete. A systematic approach for designing a specific grade of GPC is yet to be established for the cast-in-place applications, as GPC falls under a special concrete category as cementless concrete. The research to date showcased the approach for designing the mixture for GPC under the following categories: a) target strength-based method; b) ratio-based method; c) performance-based method; d) factorial-based method; and e) hit-trial method.[32]

Generally, the target strength-based method is commonly employed for designing OPC-based concrete mixtures. Table 1 presents the reported efforts to create GPC through adherence to cement-based concrete's conventional mixture design process. The aforementioned methodologies employed in the mixture design process have produced GPC with a compressive strength of up to 92 MPa after 28 days.[42] However, it has been reported that when using GGBS in manufacturing GPC, the maximum compressive strength achieved was 85 MPa at 28 days.[17] The primary objective of this research is to establish an aggregate-based high-strength geopolymer concrete (HSGPC) mixture design procedure by a target strength-based method. The primary material used is GGBS, and the curing process can be carried out at ambient conditions. Incorporating FA and silica fume (SF) as supplementary materials is intended to mitigate the reactivity of GGBS. Furthermore, the subsequent section examines the significance of the ratio of alkaline solution to binders, the molarity of NaOH, and the silicates-to-hydroxide ratio.

Governing parameters for mixture design of GPC

The fundamental components of the GPC mixture design process include the molarity of sodium hydroxide, the Na_2SiO_3/NaOH ratio, and the S/B. It was reported that as the molecular weight percentage of SH (molarity of NaOH) increases in the alkaline solution, the compressive strength of GPC increases.[36] The molar concentration of SH exhibits a range of values between 8 and 16, as documented in the

Table 1—Different mixture design approaches for GPC

	CA used, mm				Concrete inside					28-day compressive strength, MPa	
Source material	10	20	Sand	Admixture	*s/b*	*SS/SH*	Molarity of SH	Method	Curing		Authors
FA and GGBS	✓	✓	✓	✓	0.4 to 0.8	1.5	14	ACI	Ambient	66.23	Reddy et al.[6]
FA, GGBS, and HPA	—	—	✓	—	0.55	2.5	12	PPM	90°C for 7 days	80.4	Ng and Foster[33]
FA and OPC	✓	—	✓	✓	0.76	2.5	16	IS	60°C for 72 hours	63	Ferdous et al.[34]
FA	✓	✓	✓	—	0.5	1, 1.5, 2	10, 12, 14	ACI	60°C for 24 hours	35	Montes et al.[35]
FA	✓	✓	✓	—	0.35	1	13	IS	60°C for 24 hours	37.2	Patankar et al.[36]
FA	✓	✓	✓	✓	0.4 to 0.8	1.5	1	ACI	60°C for 24 hours	54	Pavithra et al.[37]
FA	✓	✓	MS	—	0.38 to 0.80	2.5, 3.5	16	IS	60°C for 24 hours	33	Anuradha et al.[38]
MK	✓	✓	✓	—	0.31 to 0.76	1.03 to 6.34	—	Statistical analysis	Ambient	66	Lahoti et al.[39]
Slag and FA	✓	✓	✓	—	—	—	—	Taguchi	Ambient	85	Chen et al.[17]
High-calcium FA	✓	✓	✓	✓	0.45 to 0.60	1	5, 10, 15	ACI	Ambient	36	Phoo-ngernkham et al.[40]
GGBS	✓	✓	✓	✓	0.3 to 0.7	1 to 5	12	ACI	Air, water, and oven	52	Serag Faried et al.[41]
FA	✓	✓	✓	—	0.24 to 0.57	2.7 to 11	11.5 to 15.5	Taguchi	80°C for 24 hours	92.86	Luan et al.[42]
GGBS, FA, SF, and MK	✓	—	✓	✓	0.35 to 0.55	1.5 to 2.5	10 to 14	Taguchi	Ambient	61.15	Hadi et al.[43]
FA and GGBS	✓	✓	✓	—	0.5	2.25	14	IS	Ambient	30	Bhogayata et al.[44]
FA, GGBS, and SF	✓	✓	✓	✓	0.35 to 0.45	2 to 3	10 to 14	IS and Taguchi	Ambient	36	Dave et al.[45]
FA, GGBS, and SF	✓	✓	✓	✓	0.35 to 0.45	2 to 3	10 to 14	IS and Taguchi	Ambient	44.75	Dave and Bhogayata[46]
FA and cement	14, 10 mm		✓	✓	0.76	2.3	16	IS	60°C for 72 hours	65	Ferdous et al.[34]

Note: CA is coarse aggregate; HPA is kaolinite high-performance ash; PPM is particle packing model; MK is metakaolin; IS is IS 10262:2009; ACI is ACI 211.1-91; MS is manufactured sand.

Table 2—Chemical properties of binders

Particulars	CaO	SiO_2	Al_2O_3	Fe_2O_3	MgO	Na_2O	K_2O	SO_3	TiO_2
GGBS	38.09	32.19	8.59	2.80	5.50	0.26	0.40	8.89	1.30
FA	1.72	60.41	12.71	14.10	0.59	0.17	1.46	2.65	2.78
SF	1.60	90.00	0.40	0.40	0.00	0.50	2.20	0.40	0.00

literature and presented in Table 1. Additionally, an increased molar concentration in terms of the molarity of SH leads to increased viscosity of the alkaline solution, consequently causing the concrete to become more brittle.[36] Hence, optimizing the SH solution concentration is essential in the alkaline solution.

The alkaline solution includes a blend of SS and SH. It is reported that the *SS*/*SH* executed in the previously published literature is between 1 and 5, as shown in Table 1. It was noted that the geopolymerization process, gel formation, and viscosity of the alkaline solution could be affected by the *SS*/*SH* in the alkaline solution.[47] The compressive strength of GPC decreases as the *SS*/*SH* increases, and the decreased *SS*/*SH* yields similar results. It was also noted that the lower proportion of SH for the higher *SS*/*SH* and the lower percentage of SS for the lower *SS*/*SH* influenced the compressive strength of GPC.[48] Therefore, it is essential to prioritize the optimization of the *SS*/*SH* to attain the desired compressive strength of GPC.

The *s*/*b* exhibits a range of values from 0.2 to 1.0, as tabulated in Table 1. As the *S*/*B* decreases, the alkaline solution can not mix thoroughly with the dry concrete mixture. Conversely, the higher *s*/*b* generates high liquidized content in the concrete mixture, resulting in poor gel formation. Ultimately, the compressive strength of GPC decreases in both cases. Moreover, efforts have been undertaken to streamline the mixture design process of GPC by establishing a correlation between the *S*/*B* and the water-cementitious materials ratio (*w*/*cm*) of cement-based concrete according to the code provisions.[6,31,36,38,49-51] Hence, it is necessary to optimize the quantities of alkaline solutions and the molarity of the SH by preliminary investigation for the desired compressive strength of GPC.

RESEARCH SIGNIFICANCE

The maximum 28-day compressive strength was reported to be 92 MPa and 86 MPa for FA-based GPC[42] and GGBS-based GPC, respectively.[17] This paper aims to develop a mixture design methodology for HSGPC (M100) in line with the provisions of IS 10262:2019[31] by incorporating coarse and fine aggregates. The design approach aligns with the studies on mixture design procedures.[32] However, emphasis has been given to the determination of optimized *SS*/*SH* and *S*/*B* in addition to the molarity of NaOH. A comprehensive mixture design approach (with an example) has been detailed meticulously and supported with results of workability, compressive strength, and microstructural properties such as X-ray diffraction (XRD), scanning electron microscopy (SEM), and energy-dispersive spectroscopy (EDS) of HSGPC.

MATERIALS USED

The primary binding materials were GGBS, FA, and SF. Alkaline activators such as SH and SS were used to react with binders. The oxide composition of these binders is given in Table 2. Table 3 represents the physical properties of all the ingredients used in HSGPC. Sand obtained from the bed of the Nareshwar River (near Surat, Gujarat, India) was used as a fine aggregate conforming to Zone II. Aggregate with the size of 10 mm was used, and the grain-size distribution of coarse and fine aggregates is depicted in Fig. 1. The upper and lower limits for both sizes of aggregate have been fixed as per the guidelines mentioned in IS 383:2016[52] to achieve the maximum possible packing density. Approximately 98% pure SH flakes were used to initiate the polymerization process. The highly viscous and concentrated SS made GPC cohesive and provided additional silica content for forming Si-O-Al bonds.

Instead of ordinary potable water, a combination of alkaline activators was used while mixing. Therefore, when the solution is added to a dry concrete mixture, it inhibits the workability of GPC as it is inherently highly viscous. To avoid this problem, a naphthalene-based high-range water-reducing admixture (HRWRA) was used.[6,53] However, the water quantity available in alkaline activators is less than the

Table 3—Different properties of all materials of HSGPC

Material	Specific gravity	Different properties
Water	1.00	Normal potable water
HRWRA	1.08	Naphthalene-based HRWRA
FA	2.20	Fineness = 380 m^2/kg
SF	2.20	Fineness = 340 m^2/kg
NaOH	2.30	98% purity, industrial-grade
Na_2SiO_3	2.40	16.7% Na_2O, 34.40% SiO_2, and 48.9% H_2O
River sand	2.66	Fineness modulus = 2.8, Zone II sand
Coarse aggregate	2.75	Angular particles, fineness modulus = 6.15
GGBS	2.90	Fineness = 450 m^2/kg

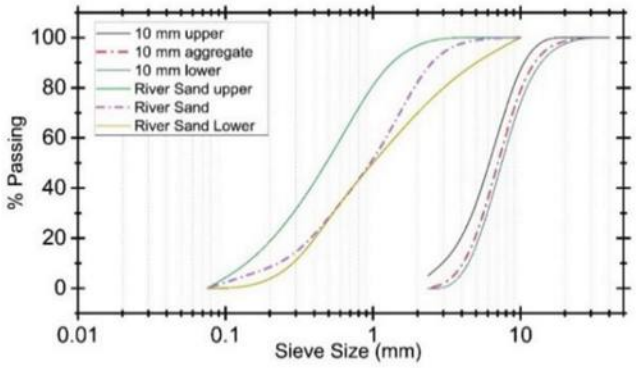

Fig. 1—Particle-size distribution of coarse and fine aggregates.

amount required in code provisions. To mitigate this issue, surplus water was added after removing the solid content of the alkaline activators. In addition, saturated surface-dry condition (SSD) aggregates were used to eliminate the water absorption effect of fine and coarse aggregates.

PROPOSED HSGPC MIXTURE DESIGN PROCEDURE

As discussed earlier, this research study aims to develop a mixture design procedure for HSGPC by channeling IS 10262:2019[31] as a target strength-based method. The binders react with alkaline activators such as SH and SS solutions. Laboratory testing of cast samples using a mixture ratio found by the absolute volume method validated the proposed mixture design. The mortar samples were cast to determine the optimization of the *SS*/*SH*, *S*/*B*, and molarity of SH. A thorough description is given in Step 4. The complete description of the procedure of the HSGPC mixture is described as follows. Figure 2 depicts the detailed flowchart of the mixture design calculation of HSGPC.

Step 1: Target average compressive strength at 28 days

A higher target mean compressive strength f_{ck}' must be used in the concrete mixture proportions to ensure the test results do not fall below the characteristic strength. Equations (1) and (2) provide the safety factor above a given suitable range of compressive strength.

$$f_{ck}' = f_{ck} + 1.65S \quad (1)$$

or

$$f_{ck}' = f_{ck} + X \quad (2)$$

whichever is higher, where f_{ck}' is the 28-day target average compressive strength; f_{ck}' is the 28-day characteristic compressive strength; S is the standard deviation; and X is a factor based on the grade of concrete.

Step 2: Approximate air content

The approximate air content entrapped in hardened concrete is adopted from Table 6 of IS 10262:2019.[31]

Step 3: Selection of water-cement ratio (*w*/*c*) and HRWRA content

Numerous parameters, including maximum particle size, particle shape, and aggregate gradation, determine the quantity of water needed to achieve a workable matrix. Moreover,

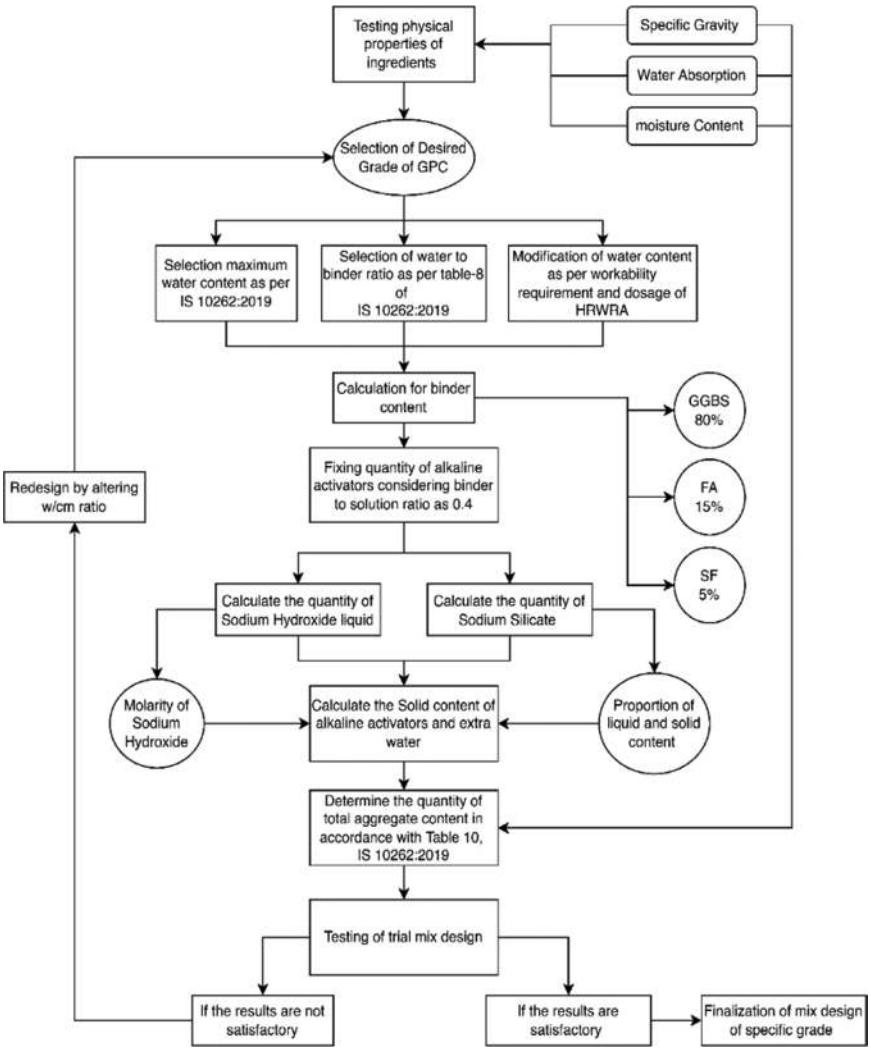

Fig. 2—Mixture design procedure for HSGPC according to IS 10262:2019.

binder content, chemical admixture, and the type of pozzolanic materials also affect the water demand for concrete. The water content of high-strength concrete without chemical admixtures is as per Table 7 of IS 10262:2019. The water content specified here is for a 50 mm slump. The requisition of the quantity of water content can be increased or decreased by approximately 3% for every increment or decrement of the 25 mm slump, or it can be calculated experimentally.[31] The aggregate particle size significantly affects the water demand, as per Table 8 of IS 10262:2019.[31]

Moreover, the compatibility of the HRWRA was examined by trial and error to fix the dosage and percentage reduction of the water by adding the HRWRA, according to Annex G (IS 10262:2019) and IS 9103:1999.[31,54] For this experimental investigation, a naphthalene-based HRWRA was used to reduce water content, and it was observed that adding 1% of HRWRA can reduce water by up to 30% with an adequate dosage and achieve better workability and cohesiveness.

Step 4: Fixing quantity of alkaline solution and extra water

As described earlier, 16 M NaOH solution was prepared by dissolving NaOH flakes in distilled water 1 day before casting. Later, the SS was added to the SH solution and mixed thoroughly. The quantity of water required in the SH solution was decided based on the solid content required to prepare a 16 M solution. For instance, to prepare a 16 M solution, 39% of solid NaOH content is needed; thus, the water quantity should be 61% of the total solution content. The SS used for this experimental work has 50.72% solid content; the rest was 49.28% water. Therefore, the extra water was calculated by subtracting the water presence in an alkaline solution. The required water content was deduced from the total water content as tabulated in Table 7 of IS 10262:2019.[31]

CALCULATION OF *SS*/*SH* AND *S*/*B*

Sixteen different proportions of mortar were prepared so that the quantities of GGBS, water, and sand remained the same. Only the quantity of the SS, SH, and the combination of SS and SH differed. The purpose of this division was to vary the *SS*/*SH* while keeping the *S*/*B* constant. The quantities of GGBS, sand, and water remained consistent across all 16 mixtures. The specific quantities used for each mixture are provided in Table 4. For each combination, mortar cubes were prepared and subjected to ambient curing. Compressive strength tests were conducted on these cubes after 7 and 28 days. Table 4 represents mortar cube compressive strength for these optimizations.

TOPSIS ANALYSIS

The Technique for Order of Preference by Similarity to Ideal Solution (TOPSIS) is a convenient and applicable approach for evaluating and prioritizing options using distance metrics. Hwang and Yoon introduced TOPSIS specifically to address decision-making challenges involving multiple attributes or criteria. It is a method commonly used in the field of multi-criteria/multi-attribute decision-making (MCDM/MADM). Initially, each parameter weight must be defined by the entropy method.[55] Afterward, the calculation should be followed by the following equations. Ultimately, it is based on the principle that the optimized value is closer than the positive ideal solution value and far away from the negative ideal solution value. The following steps need to be followed for the detailed explanation of TOPSIS analysis.

Step 1: Generate the evaluation matrix (M) comprising alternatives (P) and criteria (q). As per Eq. (3), calculate the M based on the X_{ij} for each criterion and alternatives.

$$M = (X_{ij})_{p\times q} \tag{3}$$

Table 4—Details of geopolymer mortar and compressive strength, MPa

Sample details	Designation	GGBS	Na_2SiO_3	NaOH	Sand	Water	Compressive strength, MPa	
		g					7 days	28 days
S/*B* = 0.35, *SS*/*SH* = 1.5	A	200	42.0	28.0	600	30	21.70	42.20
S/*B* = 0.35, *SS*/*SH* = 2	B	200	46.7	23.3	600	30	31.30	44.30
S/*B* = 0.35, *SS*/*SH* = 2.5	C	200	50.0	20.0	600	30	26.50	48.10
S/*B* = 0.35, *SS*/*SH* = 3	D	200	52.5	17.5	600	30	45.10	55.30
S/*B* = 0.4, *SS*/*SH* = 1.5	E	200	48.0	32.0	600	30	59.60	84.80
S/*B* = 0.4, *SS*/*SH* = 2	F	200	53.3	26.7	600	30	59.50	93.20
S/*B* = 0.4, *SS*/*SH* = 2.5	G	200	57.2	22.8	600	30	71.30	99.80
S/*B* = 0.4, *SS*/*SH* = 3	H	200	60.0	20.0	600	30	65.20	75.80
S/*B* = 0.45, *SS*/*SH* = 1.5	I	200	54.0	36.0	600	30	61.20	91.20
S/*B* = 0.45, *SS*/*SH* = 2	J	200	60.0	30.0	600	30	58.20	85.30
S/*B* = 0.45, *SS*/*SH* = 2.5	K	200	64.3	25.7	600	30	62.20	85.70
S/*B* = 0.45, *SS*/*SH* = 3	L	200	67.5	22.5	600	30	55.30	79.20
S/*B* = 0.5, *SS*/*SH* = 1.5	M	200	60.0	40.0	600	30	58.50	81.20
S/*B* = 0.5, *SS*/*SH* = 2	N	200	66.7	33.3	600	30	47.00	82.40
S/*B* = 0.5, *SS*/*SH* = 2.5	O	200	71.5	28.5	600	30	42.20	76.30
S/*B* = 0.5, *SS*/*SH* = 3	P	200	75.0	25.0	600	30	47.60	78.80

Step 2: Prepare a normalized matrix R_{ij} according to Eq. (4).

$$[R]_{ij} = \left[\frac{X_{ij}}{\sqrt{\sum_{i=1}^{p} X_{ij}^2}}\right]; i = 1, 2, \ldots \ldots \ldots, p; \quad j = 1, 2, \ldots \ldots, q \tag{4}$$

Step 3: Equation (5) represents the multiplication of the normalized matrix $[R]_{ij}$ with the weight found by the entropy method, resulting in the weighted normalized matrix $[D]_{ij}$.

$$[D]_{ij} = [R]_{ij} \times W_j \tag{5}$$

Step 4: Equations (6) and (7) represent the positive $[V^+]$ and negative $[V^-]$ ideal solutions that were determined to identify the ideal solution among all the parameters.

$$[V^+] = \left\{\left(\sum_i^{Max} \frac{V_{ij}}{j \in J}\right), \left(\sum_i^{Min} \frac{V_{ij}}{j \in J}\right), \; i = 1, 2, 3, \ldots \ldots \ldots \ldots, p\right\} \tag{6}$$
$$V^+ = V_1^+, V_2^+, V_3^+, \ldots \ldots \ldots \ldots, V_p^+$$

$$[V^-] = \left\{\left(\sum_i^{Min} \frac{V_{ij}}{j \in J}\right), \left(\sum_i^{Max} \frac{V_{ij}}{j \in J}\right), \; i = 1, 2, 3, \ldots \ldots \ldots \ldots, p\right\} \tag{7}$$
$$V^- = V_1^-, V_2^-, V_3^-, \ldots \ldots \ldots \ldots, V_p^-$$

Step 5: After the calculation of V^+ and V^-, the positive and negative separation matrixes (S_i^+ and S_i^-) are obtained according to Eq. (8) and (9), respectively.

$$S_i^+ = \left\{\sum_{J=1}^{M} (V_{ij} - V_j^+)^2\right\}^{0.5} \tag{8}$$

$$S_i^- = \left\{\sum_{J=1}^{M} (V_{ij} - V_j^-)^2\right\}^{0.5} \tag{9}$$

Step 6: The relative closeness coefficient (P_i) was prepared by Eq. (10) to identify the ideal solution according to TOPSIS analysis.

$$P_i = \frac{S_i^-}{S_i^+ + S_i^-} \tag{10}$$

Table 4 represents the compressive strength of geopolymer mortar at 7 and 28 days. The calculation was carried out by Eq. (3) to (10), and the relative closeness coefficient was determined as per Table 5. The relative closeness coefficient of Sample G was noted to be closer than that of other mortar fractions. Hence, the optimal ratios of s/b = 0.4 and SS/SH = 2.5 were optimized, respectively, according to the TOPSIS analysis.

Volume of coarse aggregate per unit volume of total aggregate

The volume of coarse aggregate has been taken as the value described in Table 10 of IS 10262:2019.[31] The coarse aggregate content has to be selected according to the type of fine aggregate.

Step 5: Aggregate

The absolute volume method has been used to determine the combined aggregate content.[31] V and SG are the volume and specific gravity of concrete, respectively. The total aggregate volume is denoted as V_{ta}, and the volume and specific gravity of GGBS are denoted as V_{GGBS} and SG_{GGBS}. Volume and specific gravity of NaOH and Na_2SiO_3 are denoted as V_{NH} and SG_{NH}, and V_{SS} and $SG_{SS,}$ respectively.

$$\text{Volume of concrete } (V) = V_{ta} + V_{NH} + V_{SS} + V_{GGBS} + V_{ea}$$

where

$$V_{NH} = \frac{W_{NH}}{SG_{NH}}; V_{SS} = \frac{W_{SS}}{SG_{SS}}; V_{GGBS} = \frac{W_{GGBS}}{SG_{GGBS}}$$

For 10 mm nominal-sized aggregates, 1% entrapped air is considered as per IS 10262:2019.[31] For 1 m^3 of concrete, the following calculation can be derived.

$$1 - 0.01 = V_{ta} + V_{NH} + V_{SS} + V_{GGBS} + V_{FA} + V_{SF} + V_{HRWRA} + V_{water}$$

$$0.99 = V_{ta} + V_{NH} + V_{SS} + V_{GGBS} + V_{FA} + V_{SF} + V_{HRWRA} + V_{water}$$

$$V_{ta} = 0.99 - (V_{NH} + V_{SS} + V_{GGBS} + V_{FA} + V_{SF} + V_{HRWRA} + V_{water})$$

$$V_{ta} = 0.99 - \left[\left\{\left(\frac{W_{GGBS}}{SG_{GGBS}}\right) + \left(\frac{W_{FA}}{SG_{FA}}\right) + \left(\frac{W_{SF}}{SG_{SF}}\right) + \left(\frac{W_{NH}}{SG_{NH}}\right) + \left(\frac{W_{SS}}{SG_{SS}}\right) + \left(\frac{W_w}{SG_w}\right) + \left(\frac{W_{HRWRA}}{SG_{HRWRA}}\right)\right\} \times \left\{\left(\frac{1}{1000}\right)\right\}\right]$$

Final mixture proportions of HSGPC

The mixture proportions of the HSGPC calculated by the aforementioned method are tabulated in Table 6.

Table 5—Relative closeness coefficient (P_i) from positive [S_i^+] and negative [S_i^-] ideal solutions

Sample	S_i^+	S_i^-	$S_i^+ + S_i^-$	P_i	Rank
A	0.103	0.015	0.118	0.127544	16
B	0.085	0.023	0.108	0.213132	15
C	0.087	0.030	0.117	0.257605	14
D	0.058	0.059	0.117	0.501315	12
E	0.049	0.073	0.121	0.598653	9
F	0.036	0.076	0.112	0.678368	5
G	0.019	0.098	0.117	0.835335	1
H	0.027	0.088	0.115	0.766434	2
I	0.046	0.077	0.124	0.625136	7
J	0.038	0.071	0.110	0.651032	6
K	0.026	0.081	0.107	0.755134	3
L	0.035	0.076	0.111	0.686851	4
M	0.050	0.070	0.120	0.584885	10
N	0.052	0.056	0.107	0.518196	11
O	0.055	0.053	0.107	0.490060	13
P	0.045	0.067	0.113	0.598827	8

EXPERIMENTAL METHODOLOGY

Preparation of HSGPC

The freshly mixed HSGPC was filled into the prescribed molds in different layers with 25 numbers of blows using a tamping rod by the guidelines provided in IS 3558-1983.[56] Following appropriate compaction procedures, a table vibrator was employed for 1.5 minutes to evacuate the air content presence in the freshly mixed concrete. A cube measuring 150 x 150 x 150 mm was used to assess the compressive strength of the concrete. All the specimens were stored in the laboratory following the casting process and maintained a consistent ambient temperature for 24 hours. After approximately 24 hours, the concrete specimens were removed from the molds and stored under ambient temperature until testing.

Fresh concrete test

The slump test was performed as per IS 1199-1959[57] to evaluate the workability of HSGPC. The freshly mixed concrete was filled in the slump cone apparatus in three different layers with 25 blows by a tamping rod on each layer. Afterward, the slump cone mold was slowly lifted, allowing the fresh mixture to fall downward. The difference in height between the settled concrete and the initial height of the slump cone indicated the slump value of the concrete in millimeters.

Hardened concrete tests

The compressive strength test was incorporated in accordance with IS 516-1959[58] by a 3000 kN compression testing machine with a 5.2 kN/s loading rate until the failure of the specimen. The average results of the three specimens were considered to evaluate the compressive strength.

Microstructural analysis

SEM/EDS—The granular particles were approximately 1 x 1 x 1 cm, and were extracted from the tested concrete samples at 28 days. The hydration stoppage method was employed to remove the capillary pore water. The dry concrete samples were given to analyze SEM images for the microstructure behavior of the HSGPC. The elemental structures of HSGPC samples were evaluated with EDS combined with SEM analysis. Concrete samples were extracted from the inner core of the tested cube and crushed into a fine powder, passing through a 75 μm sieve. The hydration stoppage method was employed to dry the powder sample. The INCA software detected EDS data from the concrete sample.

XRD-Rietveld analysis—The mineral compositions of the HSGPC samples were analyzed with an XRD device. Prepared powdered samples of 3 to 4 g were placed on the platform of the instrument for scanning at a rate of 0.02 degrees per second for 2θ of 5 to 65 degrees. The CuKa anode was used with the radiation of the XRD. To detect the presence of minerals in the tested concrete samples, Match! 3.0 software was employed.

The XRD-Rietveld analysis was carried out to investigate the quantitive analysis of the XRD spectrum. It overcomes various limitations associated with the conventional quantitive analysis of XRD spectra.[59,60] This approach demonstrates notable advantages in addressing quantitative challenges within complex multi-phase compounds.[61,62] The Rietveld method is a unique technique for analyzing samples, which involves determining crystal structure and comprehensively analyzing a powder diffraction pattern. Hence, the dependability of quantitative analysis is based on the authenticity of XRD data. If the mineral formation falls in the crystalline structure, it becomes possible to compute the theoretical intensity at every 2θ by employing the crystal structure parameters in conjunction with the peak shape parameters.[63]

Table 6—Mixture proportions of HSGPC

Ingredients	Quantities, kg/m^3			
	M70	M80	M90	M100
GGBS	402.00	460.00	495.00	535.00
FA	76.00	86.00	93.00	101.00
SF	25.00	29.00	31.00	34.00
NaOH	58.00	66.00	71.00	77.00
Na_2SiO_3	144.00	165.00	177.00	191.00
Fine aggregate	815.00	772.00	747.00	722.00
Coarse aggregate	973.00	955.00	941.00	923.00
Extra water	53.00	37.00	28.00	17.00
HRWRA	5.03	5.75	6.19	6.70

RESULTS AND DISCUSSION

A compressive strength test was carried out on the cube samples cast by the four mixture designs mentioned in Table 6. A concrete pan mixer was used for concrete casting work. After casting, the samples were cured at ambient temperature until the compressive strength test was carried out, after 24 hours, 7 days, and 28 days. From the standpoint of workability, sufficient workability was observed in all four mixture designs. At the same time, the compressive strength of all four trial batches offered above-par results.

Workability and compressive strength

The workability of the freshly mixed concrete was determined by the slump cone test, as per the guidelines mentioned in IS 1199-1959.[57] The workability was measured after properly mixing all the concrete ingredients and after a certain period. The findings revealed that the Grade M70 concrete exhibited higher flowability than Grades M80, M90, and M100. Additionally, when the slump cone was removed, the concrete slump collapsed. It was attributed to a higher *w*/*cm*, resulting in a higher alkaline solution than other concrete mixtures. Moreover, the inclusion of spherical fine aggregate particles played a role in enhancing the fluidity of the concrete mixture. The performance of higher-grade concrete, specifically M80, M90, and M100 (as shown in Fig. 3), noticed a significant flow drop as the *w*/*c* decreased and the binder content increased. The decrement in the workability is attributed to the presence of angular particles of GGBS, which enhance the internal shear forces. The incorporation of a plasticizer was found to enhance the longevity of flowability by condensing the binder particles.

The compressive strength of the concrete was conducted at 7 and 28 days, as shown in Fig. 3. At 7 days, the average

compressive strength values were recorded as 56.8, 68.1, 73.2, and 80.5 MPa. Furthermore, all concrete grades surpassed the target compressive strength at 28 days. It was noticed that as the concrete grade increased, the percentage enhancement in compressive strength also increased. The highest percentage increment of 77% was observed for Grade M100 concrete at 104.3 MPa. It was attributed to the combined effect of GGBS, FA, and SF enhancing the compressive strength of HSGPC. Including GGBS leads to various gels, such as calcium silicate hydrate (C-S-H) and N-A-S-H, which FA produces.

Moreover, it has been observed that the inclusion of C-S-H in the GPC results in enhanced mechanical strength.[46] An additional benefit of incorporating GGBS is hardening the freshly mixed concrete in the ambient atmosphere. The calcium present in GGBS exhibits a significant exothermic reaction upon contact with water molecules, facilitating the initiation of a polymerization process that would otherwise necessitate elevated temperatures. Furthermore, including SF as an additional binder enhances the particle packing in the concrete matrix at the microscale, primarily owing to its reduced particle size. Importantly, the smaller particles of SF can react at a faster rate with an alkaline solution, resulting in the formation of a fine gel. This gel contributes to developing a less porous hardened matrix, ultimately leading to improved compressive strength.

XRD-Rietveld analysis

The results of XRD spectrum patterns for the HSGPC samples are depicted in Fig. 4. The International Centre for Diffraction Data (ICDD) was used to detect all the minerals with the pair distribution functions (PDFs) from the XRD spectrum, such as quartz, ettringite, gypsum, calcite, zeolite, C-S-H, and C-A-S-H. Figure 4 shows that the highest peak intensity of the gypsum is between 25 and 30 degrees and 35 and 40 degrees, indicating the stipulated percentage of gypsum present in the concrete samples. The C-A-S-H gel is detected along with the gypsum intensity peak at 36 degrees. The multiple-peak intensity of quartz can be found at 21, 27, 39, 50, and 60 degrees. In addition, ettringite and C-S-H gel can be found as a noncrystalline structure between 20 and 30 degrees, which was attributed to the stipulated percentage of calcium in the chemical composition of GGBS. Previously published literature also claimed the structure of the C-S-H gel is noncrystalline in the given range. Moreover, the mineral identified as N-A-S-H (zeolite) can be found between 25 and 35 degrees, revealing the presence of the N-A-S-H gel.[6,64] Additionally, the minor peaks observed between 30 and 49 degrees specify the existence of C-S-H and C-A-S-H gels in HSGPC samples.

Table 7 represents the XRD-Rietveld analysis of the tested HSGPC concrete samples. Results indicate that the percentage of gypsum content decreases as the concrete grade increases. The percentage sharing of ettringite and calcite is approximately the same. It was attributed to the same percentage of binders contributing to all the concrete samples. Moreover, the percentages of the C-S-H, C-A-S-H, and N-A-S-H are significantly improved with the increase in concrete grade. It was ascribed to the percentage sharing of the binders and solutions significantly improving as the grade of concrete increased. Moreover, the enhancement in the compressive strength of the concrete mixture depends on the quantities of these gel formations.

SEM/EDS analysis

The SEM analysis of HSGPC concrete samples is illustrated in Fig. 5. A nonuniform, heterogeneous aluminosilicate gel matrix containing unreacted binder particles was observed during the microstructural observation of Grade M70 concrete. However, a few unreacted/partially reacted binder spheres remained somewhat detached from the aluminosilicate gel paste due to the coated plasticizer during mixing, and the same was observed during analysis.[65] Additionally, these unreacted binder spheres exhibit composite properties. The interface between these composites and the geopolymer matrix is a weak point, affecting the overall strength of GPC.[66] Figure 5(c) illustrates the M70 concrete sample, which appears to be weaker than the rest of the concrete samples. Additionally, both M70 (Fig. 5(c)) and M80 (Fig. 5(b)) GPC exhibited a few air voids. SEM analysis also revealed that the formatted gel diffused around unreacted binder particles and firmly attached them to the hardened matrix (Fig. 5(e)). Furthermore, the gel was found

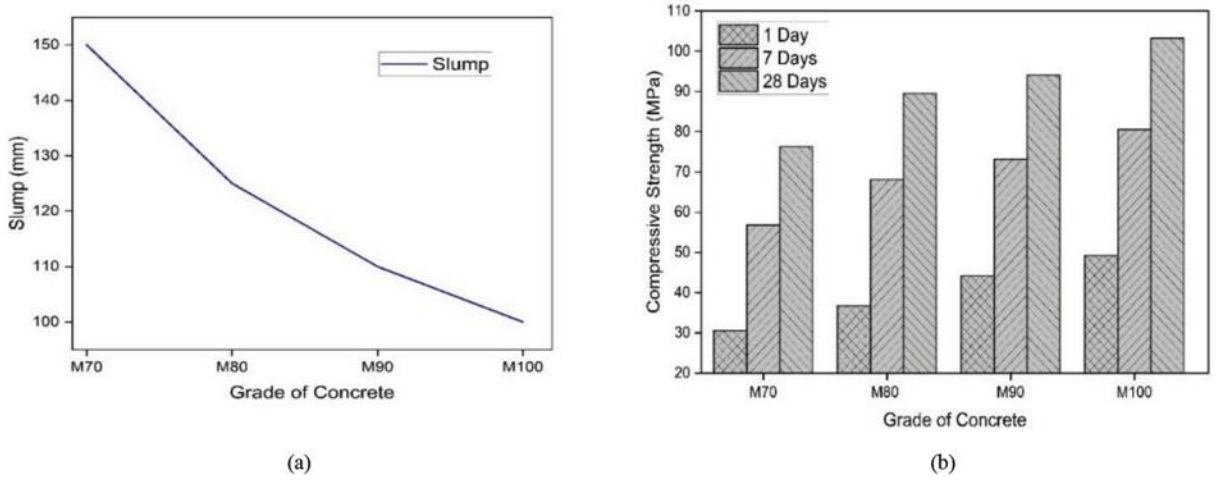

Fig. 3—Results of: (a) workability in terms of slump; and (b) compressive strength of HSGPC.

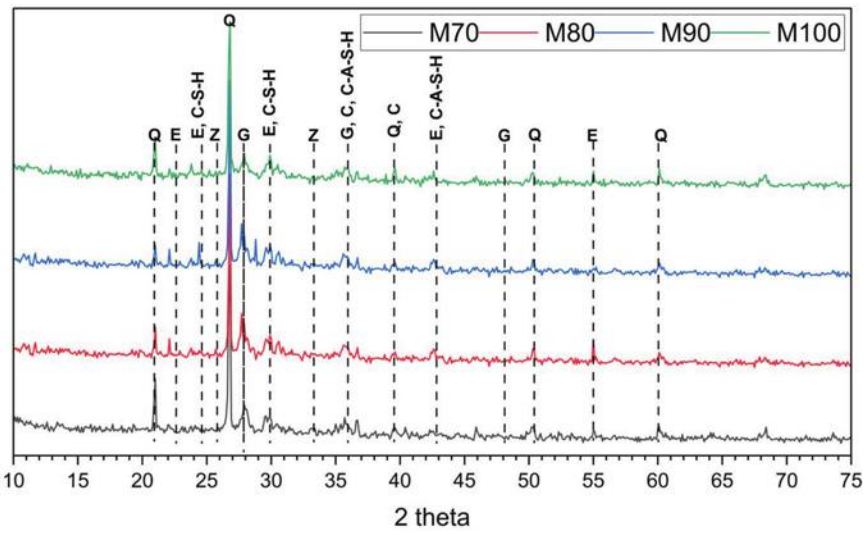

Fig. 4—XRD spectra of HSGPC. (Note: Q is quartz, E is ettringite, C-S-H is calcium silicate hydrate gel, G is gypsum, C-A-S-H is calcium aluminosilicate hydrate gel, Z is zeolite, and C is calcite.)

Table 7—XRD-Rietveld analysis for HSGPC

Mineral name	Source (PDF)	M70		M80		M90		M100	
		I/*Ic*	wt. %	*I*/*Ic*	wt. %	*I*/*Ic*	wt. %	*I*/*Ic*	wt. %
Quartz	01-079-1910	2.74	3.6	2.86	1.4	2.86	2.8	2.9	1.4
Ettringite	01-072-0646	1.54	24.5	1.54	27.3	1.54	25.1	1.56	22.2
Gypsum	01-074-1905	1.81	25.4	1.81	13.9	1.81	12.7	1.85	15.7
Calcite	01-083-1762	2.74	3.6	2.82	4.4	2.82	5	4.5	3.2
Sodium aluminosilicate hydrate (N-A-S-H, zeolite)	01-002-0417	2.42	11.2	0.8	10.9	0.8	12.1	11.3	16.1
Calcium silicate hydrate (C-S-H)	01-033-0306	0.81	3.5	0.82	7.5	1.81	11.2	2.1	18.8
Calcium aluminosilicate hydrate (C-A-S-H)	01-020-0452	0.56	28.2	0.56	34.6	1.41	31.1	1.56	22.6

Note: *I*/*Ic* is reference intensity ratio (*c* is corundum); M70 stops at 35th iteration: $R = 40.05\%$ ($P = 39$, $E = 20.57\%$, $R/E = 1.94$, $P = 34$, and EPS = 1.0); M80 stops at 29th iteration: $R = 42.97\%$ ($P = 39$, $E = 21.48\%$, $R/E = 2.00$, $P = 34$, and EPS = 1.0); M90 stops at 38th iteration: $R = 44.26\%$ ($P = 39$, $E = 21.89\%$, $R/E = 2.02$, $P = 34$, and EPS = 1.0); M100 stops at 27th iteration: $R = 48.88\%$ ($P = 39$, $E = 23.67\%$, $R/E = 2.07$, $P = 34$, and EPS = 1.0); *R* is reliability index; *P* is modification of intensity; *E* is extinction correction; EPS is empirical potential structure.

to fill the internal spaces, resulting in the production of a semi-homogeneous but highly compacted dense microstructure mostly noticed for GPC of Grades M90 (Fig. 5(e)) and M100 (Fig. 5(f)).

It was observed that as the concrete grade of HSGPC increases, the dissolution of Na and Ca also increases, as depicted in Fig. 6 and Table 8. According to previously published literature, the presence of a stipulated percentage of aluminum (Al), silica (Si), sodium (Na), and calcium (Ca) demonstrated the formation of hydrate and carbohydrate content in the geopolymerization process. It results in the formation of C-S-H, C-A-S-H, and N-A-S-H gels during the exothermic process.[6,67,68] The reduction in mechanical strength qualities associated with an increase in GPC might result from an increase in the number of soluble silicates in the mixture because excess silicate binder polymerization reduces the mechanical strength.[69]

Moreover, it was noted that as the grade of the HSGPC increases, the combined formation of Ca/Si, Ca/(Si + Al), and Na/(Si + Al) gels increases. Additionally, the Ca/Si and Ca/(Si + Al) ratios decreased while the Na/(Si + Al) ratio increased. It might reduce the development of C-S-H and C-A-S-H gel products, lowering the compressive strength. Calcium has limited solubility in alkaline solutions, precipitating as calcium hydroxide, which may have resulted in a drop in the Ca/Si and Ca/(Si + Al) ratios.[6,70]

CONCLUSIONS

In the present research work, a simplistic mixture design process is proposed. The consideration of the specific gravity of the ingredients for calculating the mixture proportions is the differentiating element from most of the published literature. The uniqueness of the methodology adopted for the high-strength geopolymer concrete (HSGPC) mixture design lies in its fusion with the guidelines provided by the Indian Standard IS 10262:2019. The developed mixture of HSGPC was experimentally assessed for workability, compressive strength, and microstructural properties. The following conclusions are drawn from the experimental and analytical studies.

- The optimal proportions of solution-binder (*s*/*b*) and sodium silicate-to-sodium hydroxide (*SS*/*SH*) ratios are 0.4 and 2.5, respectively. The optimization was based on compressive strength results, followed by the

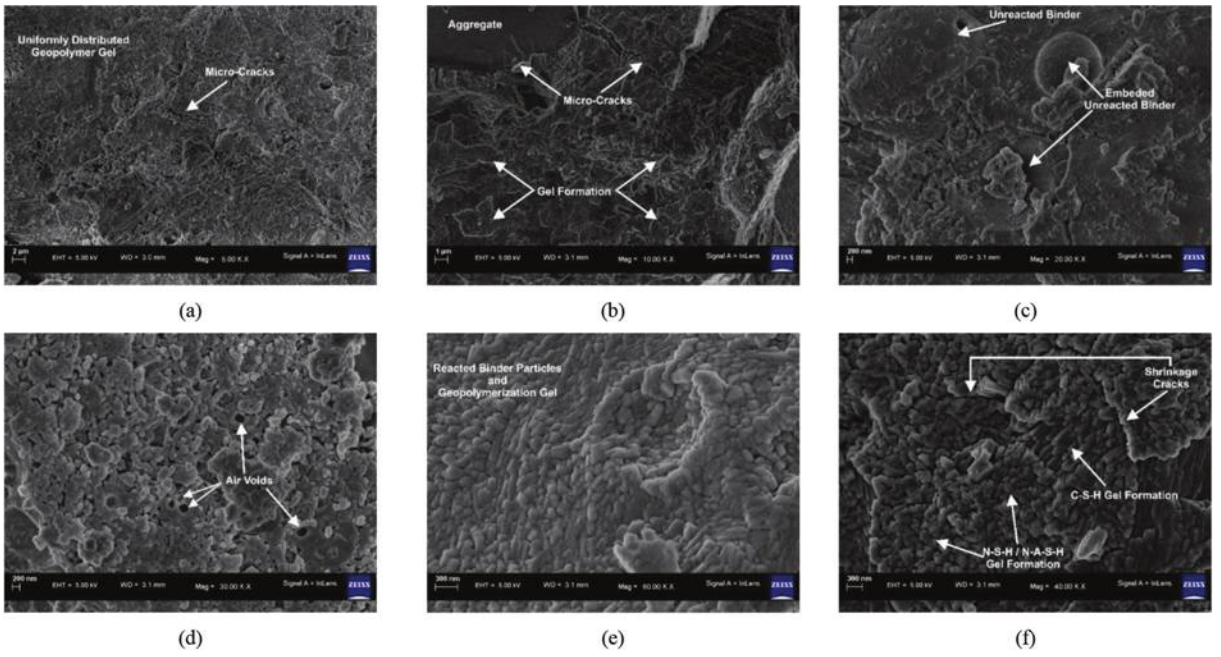

Fig. 5—SEM images of HSGPC.

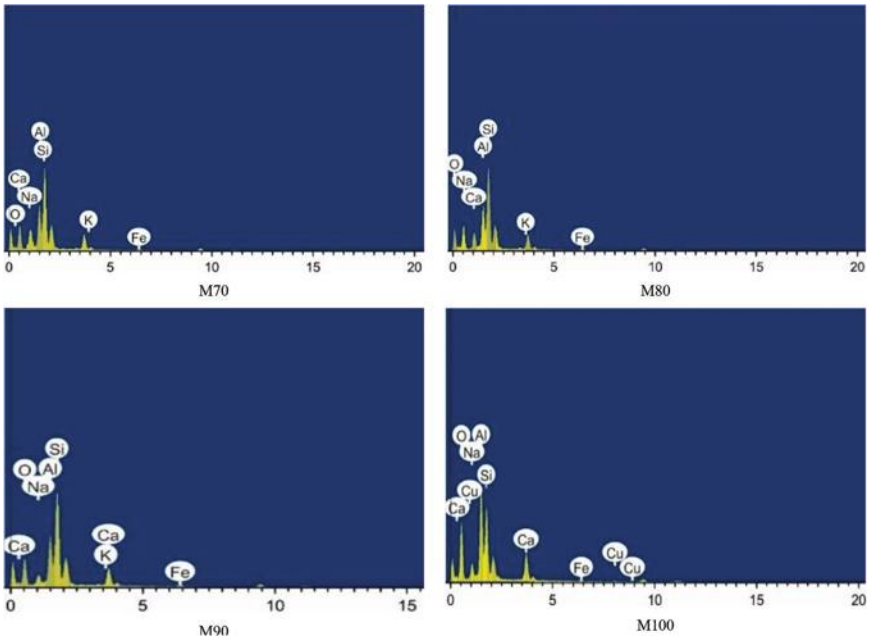

Fig. 6—Graphical representation of HSGPC by EDS technique.

Technique for Order of Preference by Similarity to Ideal Solution (TOPSIS) analysis.

- The promising workability and compressive strength were achieved using optimized *s*/*b* and *SS*/*SH* and channeling IS 10262:2019 for manufacturing HSGPC for the target strength-based method, representing its suitability for the cast-in-place work.
- The microstructural investigation revealed that due to the geopolymerization process, the dense microstructure is created as the grade of concrete increases. In addition, scanning electron microscopy (SEM)/energy-dispersive spectroscopy (EDS) and X-ray diffraction (XRD)-Rietveld analysis concluded that the enhancement of compressive strength could be correlated with the percentage share of each chemical composition determined by the XRD-Rietveld and EDS analyses of the HSGPC samples. It reveals that as the grade of the HSGPC increases, the combined effects of different gel formations, such as calcium silicate hydrate (C-S-H), calcium aluminosilicate hydrate (C-A-S-H), and sodium aluminosilicate hydrate (N-A-S-H), also increase in both analyses.

AUTHOR BIOS

Jagad Gaurav *is a Research Scholar in the Department of Civil Engineering at Sardar Vallabhbhai National Institute of Technology, Surat, Surat, Gujarat, India. He received his undergraduate degree from Shantilal Shah Engineering College, Bhavnagar, Gujarat, India, in 2014, and his postgraduate degree from Marwadi Education Foundation's Group of Institutions, Rajkot, Gujarat, India, in 2017. His research interests include concrete technology, structural design, repair and retrofitting, and special concrete.*

Table 8—Elemental compositions of HSGPC by EDS analysis

Elements	M70	M80	M90	M100
Al	18.450	19.270	19.800	20.540
Ca	13.390	9.560	14.770	15.120
Na	9.470	8.890	9.970	13.550
Si	51.480	50.250	52.470	53.960
[Ca/Si] × 100%	26.01	19.02	28.15	28.02
[Ca/(Si + Al)] × 100%	19.15	13.75	20.44	20.30
[Na/(Si + Al)] × 100%	13.54	12.79	13.80	18.19

Chetankumar Modhera *is a Professor (HAG) in the Department of Civil Engineering at Sardar Vallabhbhai National Institute of Technology, Surat, where he received his BE and ME in 1989 and 1997. He received his PhD from the Indian Institute of Technology Bombay, Mumbai, Maharashtra, India, in 2001. His research interests include concrete technology, special concrete, structural condition assessment, offshore structures design, and high-rise buildings.*

Dhaval Patel *is a Research Scholar in the Department of Civil Engineering at Sardar Vallabhbhai National Institute of Technology, Surat. He received his undergraduate degree from C. K. Pithawala College of Engineering and Technology, Surat, Gujarat, India, in 2013, and his postgraduate degree from Parul Institute of Technology, Waghodia, Vadodara, Gujarat, India, in 2015. His research interests include structural design, concrete technology, repair and retrofitting, and special concrete.*

REFERENCES

1. Khan, M. Z. N.; Shaikh, F. U. A.; Hao, Y.; and Hao, H., "Synthesis of High Strength Ambient Cured Geopolymer Composite by Using Low Calcium Fly Ash," *Construction and Building Materials*, V. 125, Oct. 2016, pp. 809-820. doi: 10.1016/j.conbuildmat.2016.08.097

2. Shehab, H. K.; Eisa, A. S.; and Wahba, A. M., "Mechanical Properties of Fly Ash Based Geopolymer Concrete with Full and Partial Cement Replacement," *Construction and Building Materials*, V. 126, Nov. 2016, pp. 560-565. doi: 10.1016/j.conbuildmat.2016.09.059

3. Farhan, N. A.; Sheikh, M. N.; and Hadi, M. N. S., "Investigation of Engineering Properties of Normal and High Strength Fly Ash Based Geopolymer and Alkali-Activated Slag Concrete Compared to Ordinary Portland Cement Concrete," *Construction and Building Materials*, V. 196, Jan. 2019, pp. 26-42. doi: 10.1016/j.conbuildmat.2018.11.083

4. Ryu, G. S.; Lee, Y. B.; Koh, K. T.; and Chung, Y. S., "The Mechanical Properties of Fly Ash-Based Geopolymer Concrete with Alkaline Activators," *Construction and Building Materials*, V. 47, Oct. 2013, 2013, pp. 409-418.

5. IS 17452:2020, "Use of Alkali Activated Concrete for Precast Products - Guidelines," Bureau of Indian Standards, New Delhi, India, 2020.

6. Reddy, M. S.; Dinakar, P.; and Rao, B. H., "Mix Design Development of Fly Ash and Ground Granulated Blast Furnace Slag Based Geopolymer Concrete," *Journal of Building Engineering*, V. 20, Nov. 2018, pp. 712-722. doi: 10.1016/j.jobe.2018.09.010

7. Allahverdi, A.; Shaverdi, B.; and Kani, E. N., "Influence of Sodium Oxide on Properties of Fresh and Hardened Paste of Alkali-Activated Blast-Furnace Slag," *International Journal of Civil Engineering*, V. 8, No. 4, Dec. 2010, pp. 304-314.

8. Garcia-Lodeiro, I.; Palomo, A.; and Fernández-Jiménez, A., "An Overview of the Chemistry of Alkali-Activated Cement-Based Binders," *Handbook of Alkali-Activated Cements, Mortars and Concretes*, F. Pacheco-Torgal, J. A. Labrincha, C. Leonelli, A. Palomo, and P. Chindaprasirt, eds., Woodhead Publishing Limited, Sawston, UK, 2015, pp. 19-47.

9. Reig, L.; Tashima, M. M.; Borrachero, M. V.; Monzó, J.; Cheeseman, C. R.; and Payá, J., "Properties and Microstructure of Alkali-Activated Red Clay Brick Waste," *Construction and Building Materials*, V. 43, June 2013, pp. 98-106. doi: 10.1016/j.conbuildmat.2013.01.031

10. Davidovits, J., *Geopolymer Chemistry and Applications*, Geopolymer Institute, Saint-Quentin, France, 2015.

11. Mahmoodi, O.; Siad, H.; Lachemi, M.; Dadsetan, S.; and Sahmaran, M., "Optimization of Brick Waste-Based Geopolymer Binders at Ambient Temperature and Pre-targeted Chemical Parameters," *Journal of Cleaner Production*, V. 268, Sept. 2020, Article No. 122285. doi: 10.1016/j.jclepro.2020.122285

12. Khalil, W. I.; Frayyeh, Q. J.; and Ahmed, M. F., "Evaluation of Sustainable Metakaolin-Geopolymer Concrete with Crushed Waste Clay Brick," *IOP Conference Series: Materials Science and Engineering*, V. 518, No. 2, 2019, Article No. 022053. doi: 10.1088/1757-899X/518/2/022053

13. Pouhet, R., "Formulation and Durability of Metakaolin-Based Geopolymers," PhD thesis, Paul Sabatier University – Toulouse III, Toulouse, France, 2015, 264 pp.

14. Fernández-Jiménez, A.; Palomo, A.; and Criado, M., "Microstructure Development of Alkali-Activated Fly Ash Cement: A Descriptive Model," *Cement and Concrete Research*, V. 35, No. 6, June 2005, pp. 1204-1209. doi: 10.1016/j.cemconres.2004.08.021

15. García-Lodeiro, I.; Fernández-Jiménez, A.; and Palomo, A., "Variation in Hybrid Cements over Time. Alkaline Activation of Fly Ash-Portland Cement Blends," *Cement and Concrete Research*, V. 52, Oct. 2013, pp. 112-122. doi: 10.1016/j.cemconres.2013.03.022

16. Somna, K.; Jaturapitakkul, C.; Kajitvichyanukul, P.; and Chindaprasirt, P., "NaOH-Activated Ground Fly Ash Geopolymer Cured at Ambient Temperature," *Fuel*, V. 90, No. 6, June 2011, pp. 2118-2124. doi: 10.1016/j.fuel.2011.01.018

17. Chen, Z.; Li, J.-S.; Zhan, B.-J.; Sharma, U.; and Poon, C. S., "Compressive Strength and Microstructural Properties of Dry-Mixed Geopolymer Pastes Synthesized from GGBS and Sewage Sludge Ash," *Construction and Building Materials*, V. 182, Sept. 2018, pp. 597-607. doi: 10.1016/j.conbuildmat.2018.06.159

18. Liu, Z.; Zhang, D.-W.; Li, L.; Wang, J.-X.; Shao, N.-N.; and Wang, D.-M., "Microstructure and Phase Evolution of Alkali-Activated Steel Slag during Early Age," *Construction and Building Materials*, V. 204, Apr. 2019, pp. 158-165. doi: 10.1016/j.conbuildmat.2019.01.213

19. Rakhimova, N. R., and Rakhimov, R. Z., "Alkali-Activated Cements and Mortars Based on Blast Furnace Slag and Red Clay Brick Waste," *Materials & Design*, V. 85, Nov. 2015, pp. 324-331. doi: 10.1016/j.matdes.2015.06.182

20. Vafaei, M., and Allahverdi, A., "High Strength Geopolymer Binder Based on Waste-Glass Powder," *Advanced Powder Technology*, V. 28, No. 1, Jan. 2017, pp. 215-222. doi: 10.1016/j.apt.2016.09.034

21. Xiao, R.; Polaczyk, P.; Zhang, M.; Jiang, X.; Zhang, Y.; Huang, B.; and Hu, W., "Evaluation of Glass Powder-Based Geopolymer Stabilized Road Bases Containing Recycled Waste Glass Aggregate," *Transportation Research Record: Journal of the Transportation Research Board*, V. 2674, No. 1, Jan. 2020, pp. 22-32. doi: 10.1177/0361198119898695

22. Salihoglu, N. K., and Salihoglu, G., "Marble Sludge Recycling by Using Geopolymerization Technology," *Journal of Hazardous, Toxic, and Radioactive Waste*, ASCE, V. 22, No. 4, Oct. 2018, p. 04018019. doi: 10.1061/(ASCE)HZ.2153-5515.0000415

23. Saloni; Parveen; and Pham, T. M., "Enhanced Properties of High-Silica Rice Husk Ash-Based Geopolymer Paste by Incorporating Basalt Fibers," *Construction and Building Materials*, V. 245, June 2020, Article No. 118422. doi: 10.1016/j.conbuildmat.2020.118422

24. Manjarrez, L.; Nikvar-Hassani, A.; Shadnia, R.; and Zhang, L., "Experimental Study of Geopolymer Binder Synthesized with Copper Mine Tailings and Low-Calcium Copper Slag," *Journal of Materials in Civil Engineering*, ASCE, V. 31, No. 8, Aug. 2019, p. 04019156. doi: 10.1061/(ASCE)MT.1943-5533.0002808

25. Xiao, R.; Ma, Y.; Jiang, X.; Zhang, M.; Zhang, Y.; Wang, Y.; Huang, B.; and He, Q., "Strength, Microstructure, Efflorescence Behavior and Environmental Impacts of Waste Glass Geopolymers Cured at Ambient Temperature," *Journal of Cleaner Production*, V. 252, Apr. 2020, Article No. 119610. doi: 10.1016/j.jclepro.2019.119610

26. IS 456:2000, "Plain and Reinforced Concrete—Code of Practice (Reaffirmed 2005)," Bureau of Indian Standards, New Delhi, India, 2000, 114 pp.

27. Ding, Y.; Dai, J.-G.; and Shi, C.-J., "Mechanical Properties of Alkali-Activated Concrete: A State-of-the-Art Review," *Construction and Building Materials*, V. 127, Nov. 2016, pp. 68-79. doi: 10.1016/j.conbuildmat.2016.09.121

28. Rafeet, A.; Vinai, R.; Soutsos, M.; and Sha, W., "Guidelines for Mix Proportioning of Fly Ash/GGBS Based Alkali Activated Concretes," *Construction and Building Materials*, V. 147, Aug. 2017, pp. 130-142. doi: 10.1016/j.conbuildmat.2017.04.036

29. Ferdous, W.; Manalo, A.; Khennane, A.; and Kayali, O., "Geopolymer Concrete-Filled Pultruded Composite Beams – *Concrete Mix Design and Application*," *Cement and Concrete Composites*, V. 58, Apr. 2015, pp. 1-13. doi: 10.1016/j.cemconcomp.2014.12.012

30. Amin, M.; Elsakhawy, Y.; Abu el-hassan, K.; and Abdelsalam, B. A., "Behavior Evaluation of Sustainable High Strength Geopolymer Concrete Based on Fly Ash, Metakaolin, and Slag," *Case Studies in Construction Materials*, V. 16, June 2022, Article No. e00976. doi: 10.1016/j.cscm.2022.e00976

31. IS 10262:2019, "Concrete Mix Proportioning—Guidelines," Bureau of Indian Standards, New Delhi, India, 2019, 44 pp.

32. Li, N.; Shi, C.; Zhang, Z.; Wang, H.; and Liu, Y., "A Review on Mixture Design Methods for Geopolymer Concrete," *Composites Part B: Engineering*, V. 178, Dec. 2019, Article No. 107490. doi: 10.1016/j.compositesb.2019.107490

33. Ng, T. S., and Foster, S. J., "Development of a Mix Design Methodology for High-Performance Geopolymer Mortars," *Structural Concrete*, V. 14, No. 2, June 2013, pp. 148-156. doi: 10.1002/suco.201200018

34. Ferdous, M. W.; Kayali, O.; and Khennane, A., "A Detailed Procedure of Mix Design for Fly Ash Based Geopolymer Concrete," *Proceedings of the Fourth Asia-Pacific Conference on FRP in Structures (APFIS 2013)*, Melbourne, VIC, Australia, Dec. 2013, 6 pp.

35. Montes, C.; Gomez, S. A.; Khadka, N.; and Allouche, E. N., "Statistical Software to Improve the Accuracy of Geopolymer Concrete Mix Design and Proportioning," *Proceedings*, 2013 World of Coal Ash (WOCA2013) Conference, Lexington, KY, Apr. 2013, 9 pp.

36. Patankar, S. V.; Ghugal, Y. M.; and Jamkar, S. S., "Mix Design of Fly Ash Based Geopolymer Concrete," *Advances in Structural Engineering: Materials, Volume Three*, V. Matsagar, ed., Springer India, New Delhi, India, 2015, pp. 1619-1634.

37. Pavithra, P.; Srinivasula Reddy, M.; Dinakar, P.; Hanumantha Rao, B.; Satpathy, B. K.; and Mohanty, A. N., "A Mix Design Procedure for Geopolymer Concrete with Fly Ash," *Journal of Cleaner Production*, V. 133, Oct. 2016, pp. 117-125. doi: 10.1016/j.jclepro.2016.05.041

38. Anuradha, R.; Sreevidya, V.; Venkatasubramani, R.; and Rangan, B. V., "Modified Guidelines for Geopolymer Concrete Mix Design Using Indian Standard," *Asian Journal of Civil Engineering*, V. 13, No. 3, 2012, pp. 353-364.

39. Lahoti, M.; Narang, P.; Tan, K. H.; and Yang, E.-H., "Mix Design Factors and Strength Prediction of Metakaolin-Based Geopolymer," *Ceramics International*, V. 43, No. 14, Oct. 2017, pp. 11433-11441. doi: 10.1016/j.ceramint.2017.06.006

40. Phoo-ngernkham, T.; Phiangphimai, C.; Damrongwiriyanupap, N.; Hanjitsuwan, S.; Thumrongvut, J.; Chindaprasirt, P., "A Mix Design Procedure for Alkali-Activated High-Calcium Fly Ash Concrete Cured at Ambient Temperature," *Advances in Materials Science and Engineering*, V. 2018, 2018, Article No. 2460403.

41. Serag Faried, A.; Sofi, W. H.; Taha, A.-Z.; El-Yamani, M. A.; and Tawfik, T. A., "Mix Design Proposed for Geopolymer Concrete Mixtures Based on Ground Granulated Blast Furnace Slag," *Australian Journal of Civil Engineering*, V. 18, No. 2, 2020, pp. 205-218. doi: 10.1080/14488353.2020.1761513

42. Luan, C.; Shi, X.; Zhang, K.; Utashev, N.; Yang, F.; Dai, J.; and Wang, Q., "A Mix Design Method of Fly Ash Geopolymer Concrete Based on Factors Analysis," *Construction and Building Materials*, V. 272, Feb. 2021, Article No. 121612.

43. Hadi, M. N. S.; Farhan, N. A.; and Sheikh, M. N., "Design of Geopolymer Concrete with GGBFS at Ambient Curing Condition Using Taguchi Method," *Construction and Building Materials*, V. 140, June 2017, pp. 424-431. doi: 10.1016/j.conbuildmat.2017.02.131

44. Bhogayata, A.; Dave, S. V.; and Arora, N. K., "Utilization of Expanded Clay Aggregates in Sustainable Lightweight Geopolymer Concrete," *Journal of Material Cycles and Waste Management*, V. 22, No. 6, Nov. 2020, pp. 1780-1792. doi: 10.1007/s10163-020-01066-7

45. Dave, S. V.; Bhogayata, A.; and Arora, N. K., "Mix Design Optimization for Fresh, Strength and Durability Properties of Ambient Cured Alkali Activated Composite by Taguchi Method," *Construction and Building Materials*, V. 284, May 2021, Article No. 122822. doi: 10.1016/j.conbuildmat.2021.122822

46. Dave, S. V., and Bhogayata, A., "The Strength Oriented Mix Design for Geopolymer Concrete Using Taguchi Method and Indian Concrete Mix Design Code," *Construction and Building Materials*, V. 262, Nov. 2020, Article No. 120853. doi: 10.1016/j.conbuildmat.2020.120853

47. Imtiaz, L.; Ur Rehman, S. K.; Memon, S. A.; Khan, M. K.; and Javed, M. F., "A Review of Recent Developments and Advances in Eco-Friendly Geopolymer Concrete," *Applied Sciences*, V. 10, No. 21, 2020, Article No. 7838. doi: 10.3390/app10217838

48. Xie, T.; Visintin, P.; Zhao, X.; and Gravina, R., "Mix Design and Mechanical Properties of Geopolymer and Alkali Activated Concrete: Review of the State-of-the-Art and the Development of a New Unified Approach," *Construction and Building Materials*, V. 256, Sept. 2020, Article No. 119380. doi: 10.1016/j.conbuildmat.2020.119380

49. ACI Committee 211, "Standard Practice for Selecting Proportions for Normal, Heavyweight, and Mass Concrete (ACI 211.1-91) (Reapproved 2009)," American Concrete Institute, Farmington Hills, MI, 1991, 38 pp.

50. Hardjito, D., and Rangan, B. V., "Development and Properties of Low-Calcium Fly Ash-Based Geopolymer Concrete," Research Report GC 1, Curtin University, Perth, WA, Australia, 2005, 103 pp.

51. Rangan, B. V., "Design and Manufacture of Flyash-Based Geopolymer Concrete," *Concrete in Australia*, V. 34, No. 2, 2008, pp. 37-43.

52. IS 383:2016, "Coarse and Fine Aggregate for Concrete—Specification," Bureau of Indian Standards, New Delhi, India, 2016, 21 pp.

53. Phoo-ngernkham, T.; Maegawa, A.; Mishima, N.; Hatanaka, S.; and Chindaprasirt, P., "Effects of Sodium Hydroxide and Sodium Silicate Solutions on Compressive and Shear Bond Strengths of FA-GBFS Geopolymer," *Construction and Building Materials*, V. 91, Aug. 2015, pp. 1-8. doi: 10.1016/j.conbuildmat.2015.05.001

54. IS 9103:1999, "Concrete Admixtures—Specification (Reaffirmed 2004)," Bureau of Indian Standards, New Delhi, India, 1999, 22 pp.

55. Rao, R. V., "Group Decision Making in the Manufacturing Environment," *Decision Making in the Manufacturing Environment: Using Graph Theory and Fuzzy Multiple Attribute Decision Making*, Springer, London, UK, 2007, pp. 341-346.

56. IS 3558-1983, "Code of Practice for Use of Immersion Vibrators for Consolidating Concrete (Reaffirmed 2004)," Bureau of Indian Standards, New Delhi, India, 1983, 22 pp.

57. IS 1199-1959, "Methods of Sampling and Analysis of Concrete (Reaffirmed 2004)," Bureau of Indian Standards, New Delhi, India, 1959, 49 pp.

58. IS 516-1959, "Method of Tests for Strength of Concrete (Reaffirmed 2004)," Bureau of Indian Standards, New Delhi, India, 1959, 30 pp.

59. Wang, Z.; Chen, Y.; Xu, L.; Zhu, Z.; Zhou, Y.; Pan, F.; and Wu, K., "Insight into the Local C-S-H Structure and Its Evolution Mechanism Controlled by Curing Regime and Ca/Si Ratio," *Construction and Building Materials*, V. 333, May 2022, Article No. 127388. doi: 10.1016/j.conbuildmat.2022.127388

60. Battocchio, F.; Monteiro, P. J. M.; and Wenk, H.-R., "Rietveld Refinement of the Structures of 1.0 C-S-H and 1.5 C-S-H," *Cement and Concrete Research*, V. 42, No. 11, Nov. 2012, pp. 1534-1548. doi: 10.1016/j.cemconres.2012.07.005

61. Renaudin, G.; Russias, J.; Leroux, F.; Frizon, F.; and Cau-dit-Coumes, C., "Structural Characterization of C-S-H and C-A-S-H Samples—Part I: Long-Range Order Investigated by Rietveld Analyses," *Journal of Solid State Chemistry*, V. 182, No. 12, Dec. 2009, pp. 3312-3319. doi: 10.1016/j.jssc.2009.09.026

62. Meral, C.; Benmore, C. J.; and Monteiro, P. J. M., "The Study of Disorder and Nanocrystallinity in C-S-H, Supplementary Cementitious Materials and Geopolymers Using Pair Distribution Function Analysis," *Cement and Concrete Research*, V. 41, No. 7, July 2011, pp. 696-710. doi: 10.1016/j.cemconres.2011.03.027

63. Wang, Y.; Huo, H.; Chen, B.; and Cui, Q., "Development and Optimization of Phosphogypsum-Based Geopolymer Cement," *Construction and Building Materials*, V. 369, Mar. 2023, Article No. 130577. doi: 10.1016/j.conbuildmat.2023.130577

64. García-Lodeiro, I.; Fernández-Jiménez, A.; Palomo, A.; and Macphee, D. E., "Effect of Calcium Additions on N–A–S–H Cementitious Gels," *Journal of the American Ceramic Society*, V. 93, No. 7, July 2010, pp. 1934-1940. doi: 10.1111/j.1551-2916.2010.03668.x

65. Lokuge, W.; Wilson, A.; Gunasekara, C.; Law, D. W.; and Setunge, S., "Design of Fly Ash Geopolymer Concrete Mix Proportions Using Multivariate Adaptive Regression Spline Model," *Construction and Building Materials*, V. 166, Mar. 2018, pp. 472-481. doi: 10.1016/j.conbuildmat.2018.01.175

66. Steveson, M., and Sagoe-Crentsil, K., "Relationships between Composition, Structure and Strength of Inorganic Polymers: Part 2 Fly Ash-Derived Inorganic Polymers," *Journal of Materials Science*, V. 40, No. 16, Aug. 2005, pp. 4247-4259. doi: 10.1007/s10853-005-2794-x

67. Deb, P. S.; Nath, P.; and Sarker, P. K., "The Effects of Ground Granulated Blast-Furnace Slag Blending with Fly Ash and Activator Content on the Workability and Strength Properties of Geopolymer Concrete Cured at Ambient Temperature," *Materials & Design*, V. 62, Oct. 2014, pp. 32-39. doi: 10.1016/j.matdes.2014.05.001

68. Jawahar, J. G., and Mounika, G., "Strength Properties of Fly Ash and GGBS Based Geo Polymer Concrete," *Asian Journal of Civil Engineering*, V. 17, No. 1, Feb. 2016, pp. 127-135.

69. Gao, K.; Lin, K.-L.; Wang, D.; Hwang, C.-L.; Shiu, H.-S.; Chang, Y.-M.; and Cheng, T.-W., "Effects SiO_2/Na_2O Molar Ratio on Mechanical Properties and the Microstructure of Nano-SiO_2 Metakaolin-Based Geopolymers," *Construction and Building Materials*, V. 53, Feb. 2014, pp. 503-510. doi: 10.1016/j.conbuildmat.2013.12.003

70. Hajimohammadi, A., and van Deventer, J. S. J., "Dissolution Behaviour of Source Materials for Synthesis of Geopolymer Binders: A Kinetic Approach," *International Journal of Mineral Processing*, V. 153, Aug. 2016, pp. 80-86. doi: 10.1016/j.minpro.2016.05.014

ACI MATERIALS JOURNAL TECHNICAL PAPER

Title No. 121-M07

Mechanical Responses of Polymer Concrete Submerged in Acidic Solution

by M. Bastami, M. Abbasnejadfard, M. Aslani, M. Abbasnejadfard, and R. Hayatiani

*Polymer concrete (PC) sewer pipelines are subjected to corrosive environments during their operation time. The aim of this study is to investigate the effect of sulfuric acid on the mechanical characteristics of PC. In this context, specimens were submerged in 5 and 15% sulfuric acid solutions (named SP5 and SP15, respectively) up to 180 days and then subjected to monotonic and cyclic compressive and tensile loadings. Results demonstrated that the specimens that were immersed in 15 vol% of sulfuric acid (MC15 and MT15) had the greatest losses in compressive and tensile strength, which were 33% and 21% (70 and 8 MPa), respectively, compared to the control specimens. Peak strain, compressive strength, and energy absporption capacity (*EA*) for MC15 are approximately 1.6, 2, and 1.7 times higher than corresponding values for normal concrete. Corroded PC specimens still have a substantially higher strength and energy absorption capacity than cement-based concrete. Based on the obtained results, stress-strain relationships were proposed for SP5 and SP15 in compression and tension.*

Keywords: acidic environment; constitutive equation; energy dissipation; monotonic and cyclic tests; unsaturated polyester polymer concrete (UPPC).

INTRODUCTION

Polymer concrete (PC) is a high-performance material that has a widespread application in the construction of sewer pipelines, precast members, and highway surfaces. It has a number of benefits over normal concrete (NC), including high mechanical strength, fast curing, low permeability, durability, and chemical attack resistance.[1-12] PC is a composite formed of fillers, catalysts, accelerators, fine and coarse aggregates, and resins as the binding agents. Various types of polymers have been used in the fabrication of PC, such as unsaturated polyester, epoxy, and acrylic.[1,9-11,13-15] Unsaturated polyester resin provides benefits in terms of short curing time, high strength, and comparatively low prices. Despite its benefits, PC has some disadvantages, one of which is its limited workability because of its high viscosity. Its workability can be improved by adding monomers such as methyl methacrylate.[16,17]

Several studies have been conducted to evaluate the mechanical characteristics of PC.[14,15,18-28] The results indicate that PC demonstrates better mechanical properties than ordinary cement-based concrete. However, the strength and durability of the PC may be affected by subjection to severe environments such as wastewater and acid rain. Several researches have been performed to study the effect of corrosive environments on the mechanical characteristics of different types of PC. Ribeiro et al.[29] stated that the bending strength and mass of epoxy PC are slightly decreased by immersion in sulfuric acid and chloride sodium solutions for various periods from 1 to 84 days. Gorninski et al.[22] examined the chemical resistance of polymeric mortar composites using isophthalic polyester and orthophthalic polyester. The compositions of orthophthalic polyester PC with the lowest concentrations of fly ash showed the lowest flexural resistance to chemical agents. Reis[5,21] evaluated the mechanical characteristics of epoxy PC subjected to eight different corrosive agents. The results showed that higher flexural and compressive strength reductions were observed in mortars submitted in formic acid, and they were 85% and 55%, respectively. Dębska and Lichołai[19] studied the effect of five different aggressive media on epoxy mortars modified with polyethylene terephthalate glycolyzates. It was reported that, unlike ordinary cement mortars, the mentioned composites showed excellent chemical corrosion resistance. Additionally, none of the specimens exhibited any penetration or cracking. Rahman et al.[30] assessed the loss in mass and compressive strength of the portland cement mortar, epoxy resin-based polymer cement mortar, and polymer mortar specimens after immersion in different corrosive agents. Results indicated that polymer mortar demonstrated the least decrease in compressive strength (28% after immersion in an acid solution for 200 days) and mass loss (7% for 200 days in sulfuric acid) compared to the two other mortars. The relative mass loss and compressive strength decreased as the epoxy content increased. Moodi et al.[31] evaluated the strength and durability of polymer and latex-modified concretes. Results demonstrated that in PC, a remarkable improvement was achieved by using 20% polyester resin, and no reduction was observed in flexural strength after 50 cycles of freezing and thawing, while it was decreased by approximately 20% in latex-modified mortar.[31] Ghassemi and Toufigh[32] investigated the environmental effects on the mechanical properties of epoxy polymer concrete (EPC) and ordinary cement-based concrete (OCC), which were exposed to four chemical solutions with pH values of 2.5, 7, and 12.5, and artificial seawater for 12 months. The acidic solution was the most destructive environment for OCC and PC, and high epoxy resin content demonstrated the best compressive strength after 1 year of immersion in the acidic solution, and it was reduced by 22%.

ACI Materials Journal, V. 121, No. 1, January 2024.

MS No. M-2022-321.R1, doi: 10.14359/51739202, received May 20, 2023, and reviewed under Institute publication policies.

Most of the previous studies were focused on the effects of corrosive environments on EPC, and minor studies have been conducted to investigate the mechanical properties of unsaturated polyester polymer concrete (UPPC). On the other hand, the existing studies on UPPC are limited to its compressive and flexural tests, while its other mechanical characteristics (especially direct tensile strength, energy absorption ratio, and stiffness degradation due to cyclic loading) were not investigated. Moreover, no stress-strain equation has been proposed for acid-immersed UPPC, neither for compression nor for tension. In this regard, the current study focuses on the impact of 5 and 15 vol% sulfuric acids on the compressive strength of UPPC for various periods of time. Then monotonic and cyclic tests were performed on UPPC specimens that were subjected to 5 and 15 vol% sulfuric acid for 180 days (in the following sections, these specimens are named SP5 and SP15, respectively). The results of SP5 and SP15 were compared with the results of control PC and cement-based concrete in terms of maximum tensile and compressive strength, elastic modulus, energy absorption ratio, stiffness degradation, and stress-strain curves. Also, based on the results of cyclic and monotonic compressive and tensile testing, stress-strain equations are proposed for UPPC materials that are submerged in sulfuric acid solution.

RESEARCH SIGNIFICANCE

As there have been few studies on the effects of corrosive environments on UPPC, the purpose of this research is to investigate the effect of acidic environments on the mechanical characteristics of UPPC. This study is distinctive as it conducted compressive and direct tensile testing on UPPC specimens that have been submerged in sulfuric acid while being subjected to monotonic and cyclic loadings. Moreover, novel compressive, tensile, unloading, and reloading constitutive equations are proposed for corrosive UPPC. The stress-strain equations presented in the current study provide the opportunity for numerical simulations of corroded UPPC in future investigations.

MATERIALS AND SPECIMEN PREPARATION

UPPC was produced using fine and coarse aggregates with maximum diameters of 4.75 and 9.5 mm, respectively. The fine and coarse aggregates comprise 14 and 60% of the total UPPC weight, respectively. The fineness modulus of the fine aggregate is 3.42. The grading of the aggregates used in this experiment is presented in Fig. A1 in the Appendix* and compared with the thresholds of ASTM C33[33] and DIN 1045-2[34] standards to ensure that the aggregates are well graded.

The resin used in this research was unsaturated orthophthalic polyester, the properties of which are presented in Table A1. To prepare UPPC, fine and coarse aggregates were heated up to 150°C to remove the moisture, and the dust was removed by a collector. Gravel, sand, calcium carbonate, and resin were added at 60, 14, 15.5, and 10.3% of total UPPC weight, respectively. At the end of the mixing process, methyl ethyl ketone peroxide as an initiator (0.16%) and cobalt octoate as an accelerator (0.04%) were automatically added to the mixture to activate the curing process. After the vibration and mixing processes, the fresh mixtures were placed into the molds. The specimens were removed from molds after 2 hours and cured at room temperature for 28 days. Table A2 summarizes the composition of the UPPC mixture. The mentioned mixture design has been used in the construction of PC pipes of sanitary sewage networks in cities or factories. The target design compressive strength of this concrete is based on the strength needed when the pipe is under significant jack pressure when using microtunneling construction methods; due to that, this mixture design is constant during pipe manufacturing.

An acidic solution was prepared by adding 5 and 15% of sulfuric acid (H_3SO_4) to distilled water. The pH values for 5 and 15% sulfuric acid solutions are 2 and 1.5, respectively. These values were constantly monitored and controlled. These percentages of sulfuric acid were considered as corrosive environments in accordance with ASTM C267-01[35] specifications and past studies, in which the concentration of sulfuric acid solutions in studies varied in the range of 5 to 15%.[20,29,30,36] Moreover, the pH level of the strongest acidic environment in the previous studies was approximately 2. The pH values for 5 and 15% sulfuric acid solutions are 2 and 1.5, respectively, and they provide a pH of less than 2, similar to the previous studies.[21,32] Different test specimens were immersed in the acidic solution at different time intervals, which are discussed in the following section.

EXPERIMENTAL INVESTIGATION

This study was conducted in three phases. First, the compressive strength of UPPC was studied by performing uniaxial compressive tests to investigate the effect of sulfuric acid during different immersion times. Then, monotonic and cyclic testing were performed for both compressive and tensile loadings, and the results of the average stress-strain curves were compared with control specimens. Finally, empirical relationships were proposed for envelope curves, monotonic curves, and unloading and reloading paths for tension and compression for SP5 and SP15 specimens.

Uniaxial compressive tests

Forty-five 100 x 100 x 100 mm UPPC cubic specimens were fabricated and cured for 28 days. Then they were exposed to 5 and 15% (UC5 and UC15) sulfuric acid solutions for 7, 28, 56, 84, and 180 days to study the effect of the immersion period with different acid concentrations on the compressive strength of UPPC according to the ASTM C267-01[35] specifications. In every test duration, three UC5 and three UC15 specimens were tested, and the average compressive strengths of UC5 and UC15 were compared to the average compressive strengths of three specimens cured at room temperature outside of the acid solution. The rate of loading was 400 N/s (refer to Fig. 1(a)).

*The Appendix is available at **www.concrete.org/publications** in PDF format, appended to the online version of the published paper. It is also available in hard copy from ACI headquarters for a fee equal to the cost of reproduction plus handling at the time of the request.

(a) specimens of uniaxial compressive testing

(b) Monotonic and cyclic compressive test setup

(c) Monotonic and cyclic tensile test setup

Fig. 1—Uniaxial compressive specimens, monotonic and cyclic compressive test setup, and tensile test setup.

Table 1—Number of tests and specimens

Tests	Environmental condition	Abbreviation	Number	Dimensions, mm	Curing time, days
Monotonic compressive	5% sulfuric acid	MC5	3	Ø60 x 120	180
	15% sulfuric acid	MC15	3		
	Control specimens	MC	3		
Cyclic compressive	5% sulfuric acid	CC5	3	Ø60 x 120	180
	15% sulfuric acid	CC15	3		
	Control specimens	CC	3		
Monotonic tensile	5% sulfuric acid	MT5	3	Dumbbell-shaped	180
	15% sulfuric acid	MT15	3		
	Control specimens	MT	3		
Cyclic tensile	5% sulfuric acid	CT5	3	Dumbbell-shaped	180
	15% sulfuric acid	CT15	3		
	Control specimens	CT	3		

Monotonic and cyclic compressive tests

Nine cylindrical specimens were used for the monotonic compressive tests, and the same number of specimens were considered for cyclic compressive tests. The dimensions of the specimens were Ø60 x 120 mm, and they were fabricated according to DIN 51290-3[37] specifications (Fig. 1(b)). More details about the number of specimens and their environmental conditions and curing time are presented in Table 1.

After 24 hours, all specimens were demolded and cured for 28 days before being exposed to the acidic solution for 180 days. Two vertical PFL-30 strain gauges were glued to the specimens to measure the average vertical deformation during the monotonic and cyclic loading (Fig. 1(b)). In the monotonic compressive tests, the rates of displacement loading were 0.02 mm/s. For the cyclic compressive test, the reloading and unloading rate was 5 kN/s, and the maximum acted force increased by 25 kN in each cycle.

Monotonic and cyclic tensile tests

Using nine dumbbell-shaped UPPC specimens, the effect of 5 and 15% sulfuric acid on the tensile strength of UPPC specimens was examined (Fig. 1(c) and Fig. A2), which were subjected to the direct monotonic tensile tests. The same number of specimens were implemented to perform the cyclic tensile tests. Table 1 provides more detailed information about the number of specimens, their environmental conditions, and curing time. Dumbbell-shaped specimens were fabricated and tested according to DIN 51290-3[37] specifications. Figure A2(a) displays the dimensions of the specimens. Two steel plates with threaded holes were placed on the top and bottom of specimens. Two eye bolts were fastened to the plates, and the specimens were connected to the universal tester by hinges. The hinges can reduce the eccentricity and prevent the transmission of bending moment. The universal tester stretched the bolts, and then the tensile load was acted on the specimens by the eye bolts (Fig. 1(c)). The tensile monotonic load rate was 0.01 mm/s, and two vertical strain gauges (PFL-60) were attached to the middle of the dumbbell-shaped specimens. The loading and unloading rate of cyclic tensile tests was 1 kN/s, and the amplitude of each cycle increased by 5 kN compared to the previous step. Both cyclic and monotonic tensile tests were carried out using a universal testing machine with a 600 kN

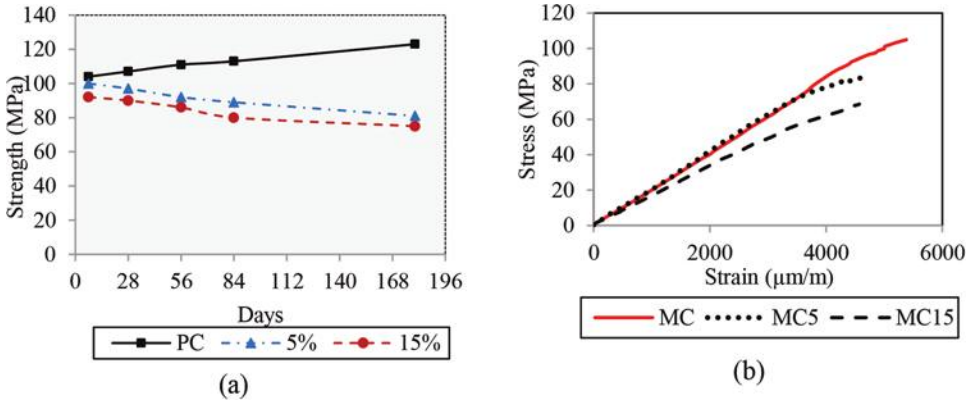

Fig. 2—(a) Uniaxial compressive strength-exposure time; and (b) average monotonic compressive stress-strain curves.

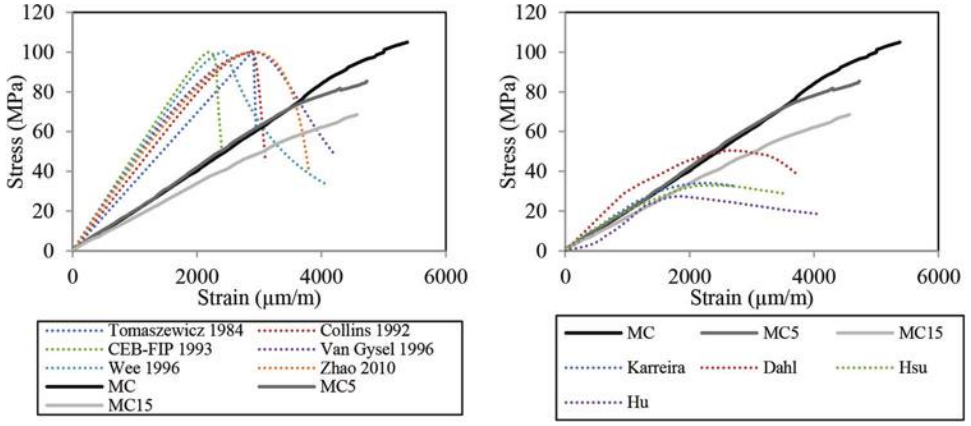

Fig. 3—Compressive stress-strain curves of: (a) NC versus UPPC; and (b) HSC versus UPPC.

loading capacity, and a data logger system was implemented to record the strain data (refer to Fig. 1(c)).

RESULTS AND DISCUSSION

Uniaxial compressive test results

Cubic UPPC specimens were immersed in 5 and 15% (UC5 and UC15) sulfuric acid solutions for 7, 28, 56, 84, and 180 days. The effect of the exposure period on the compressive strength of UPPC is demonstrated in Fig. 2(a). Results indicate that the average compressive strength of control specimens increases approximately 18% from 104 to 123 MPa during the 180 days of curing. Moreover, after 180 days of immersion, the compressive strengths of UC5 and UC15 are reduced by roughly 18% and 19%, respectively, compared to their initial strength. The average compressive strengths of UC5 and UC15 are reduced by 34% and 39% of the average compressive strength of control specimens, respectively. For a better understanding of the durability of UPPC in the acid environment, one ordinary cement-based concrete cube was also placed in 5% sulfuric acid solution to measure its compressive strength after immersion in sulfuric acid. But the cement-based concrete specimen was destroyed after 14 days. It was discovered that even though the UPPC specimens' compressive strength dropped to 75 MPa, UP5 and UP15 specimens demonstrated the perfect performance in terms of compressive strength in the corrosive environment in comparison to NC.

Monotonic compressive tests results

Three specimens were subjected to the 5% sulfuric acid (MC5), and three were immersed in 15% sulfuric acid solution (MC15) for 180 days. Their stress-strain curves under monotonic compressive loading and average curves are depicted in Fig. A3. The results were compared with the average monotonic compressive curves of control specimens (MC), which were cured for 180 days (Fig. 2(b)). The maximum average compressive stress of MC, MC5, and MC15 specimens were approximately 104, 84, and 70 MPa, respectively. This means that the monotonic compressive strength decreased up to 33% after being exposed to sulfuric acid. The average ultimate strain of the MC specimens was 5.4×10^{-3} mm/mm, while the average maximum strain of MC5 and MC15 reduced to 4.71×10^{-3} and 4.5×10^{-3} mm/mm, respectively (refer to Table A3). In all compressive tests, the specimens failed suddenly at the maximum stress, so it was impossible to depict the softening part of the monotonic stress-strain curves.

The results of the monotonic compressive tests of UPPC were compared with the results of previous compressive tests of NC[38-41] and high-strength concrete (HSC)[42-47] in Fig. 3 and 4. The average peak strains for MC, MC5, and MC15 were higher than 100%, 74%, and 66% of the average maximum strain of the mentioned HSC curves, respectively, whereas their maximum strength of HSC was 100 MPa. Also, the maximum strains of MC, MC5, and MC15 were observed to be 2.4, 2.11, and 2.05 times greater than the

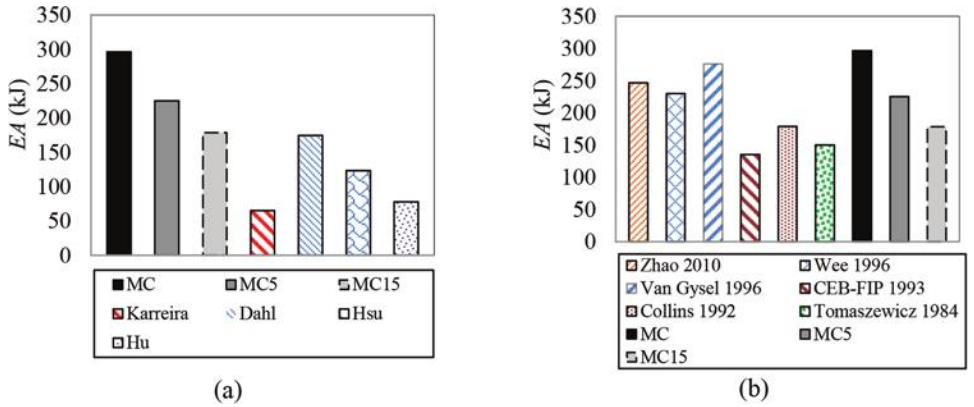

Fig. 4—Comparison of EA *of UPPC with results of previous studies: (a) NC; and (b) HSC.*

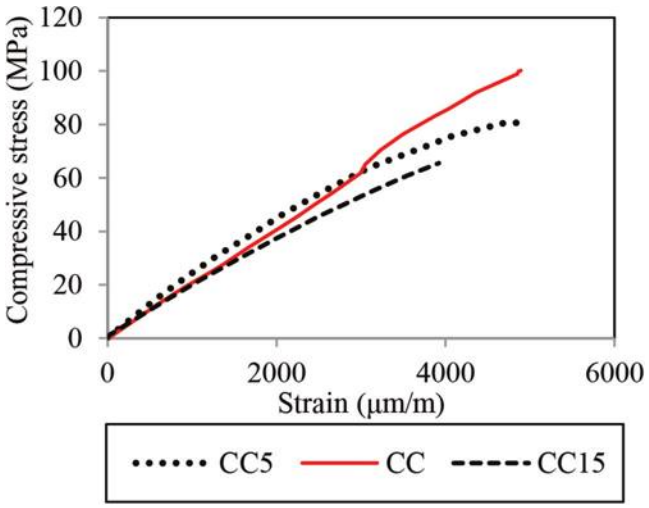

Fig. 5—Comparison of average envelope stress-strain curves of CC, CC5, and CC15.

average peak strain of the mentioned NC test results. The compressive strength of MC15 underwent a more significant decrease than other specimens. But the compressive strength of MC15 is still two times higher than the average NC compressive strength. The higher ultimate strain of UPPC indicates that it can bear more deformations than HSC and NC. Furthermore, compared to NC, it has a larger fracture energy because of its higher strength and ultimate strain.

The energy absorption capacity (*EA*), also known as the strain-energy density, is the amount of energy absorbed by the specimen per unit volume and is defined as the area under the stress-strain (σ-ε) curve up to failure strain[27,48] as

$$EA = \int \sigma \cdot d\varepsilon \tag{1}$$

The average *EA*s of the MC, MC5, and MC15 specimens were calculated and compared with those of NC and HSC in Fig. 4. The computed *EA*s for the MC, MC5, and MC15 specimens were 1.56, 1.18, and 0.96 times higher than the average *EA*s of the six HSC results, respectively. Therefore, although there were more decreases in maximum stress and strain of the MC15 specimens, they displayed approximately equal *EA* compared to the HSC. Also, *EA*s for the MC, MC5, and MC15 specimens were 3.11, 2.46, and 1.87 times higher than the average *EA*s of the four mentioned NC, respectively. Thus, the areas under the compressive stress-strain curve for the MC, MC5, and MC15 specimens are greater than those for NC, and more energy was absorbed by the UPPC elements.

The elastic modulus (*E*) was obtained analytically from the stress-strain curve according to ASTM C469-02[49] as

$$E = \frac{\sigma_2 - \sigma_1}{\varepsilon_2 - 0.005\%} \tag{2}$$

where σ_1 is the stress corresponding to the strain of 0.005%; σ_2 is the stress corresponding to 40% of the peak stress; and ε_2 is the strain at the stress level of σ_2. The average *E* obtained for UPPC was approximately 21,000 MPa for the average monotonic compressive results. The average elastic modulus of MC5 specimens was similar to the control specimens, while it was decreased to 18,000 MPa for MC15 specimens. The value for HSC, which has compressive strength equal to that of the UPPC employed in the current investigation (100 MPa), was 40,000 MPa. ACI 363R-10[50] proposed the following equation to calculate the elastic modulus of HSC based on compressive strength

$$E_c = 14{,}495 + 2176\,(f_c')^{0.5} \tag{3}$$

According to Eq. (3), the elastic modulus of UPPC cannot be estimated by the empirical equations provided by ACI 363R-10 for HSC, and comprehensive studies must be done to propose a realistic relationship between the compressive strength and elastic modulus of different types of PC.

Cyclic compressive test results

The stress-strain curves of cyclic compressive loading are presented in Fig. A4, and the average envelope curves of CC, CC5, and CC15 are calculated and compared in Fig. 5. The average maximum compressive strength for CC specimens is approximately 100.17 MPa, while exposure of the UPPC specimens to the acidic environments decreased the maximum strength of CC5 and CC15 to 80 and 65 MPa, respectively. The average and standard deviation of the maximum strength, maximum strain, and elastic modulus of cyclic compressive tests were obtained as demonstrated in Table A4. Moreover, the average envelope curves of cyclic compressive tests are compared with the average curves of

monotonic compressive tests for control specimens SP5 and SP15, as shown in Fig. A5. It is obvious that the monotonic loading curve is tracked with the envelope curve in all three conditions. Despite minor variations, the maximum strength at the peak point is nearly similar in the monotonic and cyclic loading conditions.

Because the UPPC specimens stay elastic and energy dissipation is not visible during the first cycles, the unloading path is almost asymptotic to the reloading path. Crack propagation and damage formation cause considerable degradation in stress and elastic stiffness in the final step of cyclic loading, and the unloading curves turn into concave paths. The reloading branch is a convex curve with a decreasing slope until it reaches zero stress. The accumulated residual axial strain of concrete after being unloaded (ε_{un}) to zero stress is referred to as the plastic strain ε_{pl}. The plastic strain increases by enhancement of the loading cycles. The reloading strain ε_{re} is related to the ε_{pl}, too. The relationship between ε_{un} and ε_{pl}, as well as the $\varepsilon_{pl} - \varepsilon_{re}$ function, are required to be determined to describe the unloading and reloading parts of cyclic loops. Thus, the best-fitted parabolic equations are defined to describe ε_{pl} as a function of ε_{un} as well as the relationship between ε_{pl} and ε_{re} by regression analysis on data obtained from cyclic compressive tests. The R^2 for $\varepsilon_{pl} - \varepsilon_{un}$ and $\varepsilon_{pl} - \varepsilon_{re}$ equations are more than 0.94, and they match the experimental results well, which can also be observed in Fig. A6.

In cyclic tests, the elastic stiffness degradation (*ESD*) was used to evaluate specimen damage. *ESD* (Eq. (4)) is the slope of a straight line drawn between the unloading and plastic strain points of each cycle, divided by the elastic modulus (E_0) of the envelope curve. The plastic strain point, according to this definition, is where the cyclic curve meets the strain axis after complete unloading.

$$ESD_i = \frac{E_{unl_i}}{E_0} \tag{4}$$

In Eq. (4), ESD_i is the elastic stiffness degradation in the i-th cycle; E_{unl_i} is the slope between the unloading point and plastic strain point of the i-th cycle, and is called the unloading modulus; and E_0 is the modulus of elasticity of undamaged material.

The results of average *ESD* for CC, CC5, and CC15 specimens are shown in Fig. 6. It can be seen that the rate of degradation is increased in CC5 and CC15 and is approximately 0.72 in their final cycles, while it is 0.81 for CC specimens. Moreover, a sharp drop in the stiffness of the CC15 specimen is observed in the final step of cyclic loading, while for CC and CC5 specimens, this reduction is smoother, which indicates that in CC15, microcracks fall into macrocracks more rapidly. The value of *ESD* for NC and steel fiber-reinforced concrete reached 20%, according to Xu et al.[51] This indicates that the crack propagation was negligible for UPPC prior to the last cycle, and the majority of damage occurred during the final cycle.

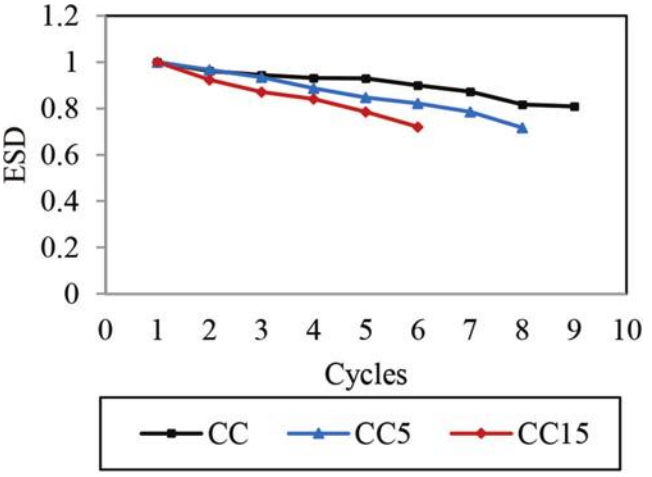

Fig. 6—Stiffness degradation ratio for cyclic loading.

Monotonic tensile test results

All the specimens presented in Table 1 for the monotonic tensile test (MT) were tested after 180 days, and MT5 and MT15 specimens were immersed in 5 and 15% sulfuric acid solutions, respectively. The average monotonic stress-strain curves are shown in Fig. 7(a). For control specimens, the average ultimate tensile strength and strain were 10.48 MPa and 484×10^{-6} mm/mm, respectively. The acid environment decreased the average monotonic strength of MT5 and MT15 by approximately 18% and 21%, respectively, compared to the MT specimens (refer to Table A5). Tensile test results for MT, MT5, and MT15 were compared with those for NC,[52-54] as shown in Fig. 7(b). It was observed that the maximum average stresses for MT, MT5, and MT15 were 3.5, 2.9, and 2.73 times the maximum average stresses of the three mentioned results for NC. Although M15 specimens were exposed to 15% sulfuric acid for 180 days, they had much higher tensile strength compared to the NC. This is considered an essential feature of PC that UPPC specimens can bear much more stress and provide more deformability than NC while they are in an acidic environment.

The *EA* parameters were also calculated for MT, MT5, and MT15, and they were compared with tensile test results for NC, as shown in Fig. 7(c). The *EA* parameters for MT, MT5, and MT15 were 2.9, 2.3, and 2.1 times higher than the average *EA* for NC. This result indicates that the UPPC was able to absorb more energy than NC during tension loading. The specimens submerged in sulfuric acid still absorbed a significant amount of energy due to their high tensile strength and failure strain rather than the NC, which allowed the UPPC components to withstand a significant amount of deformations without significant damage.

ACI 363R-10 suggested several equations that described the relationship between the tensile strength and compressive strength of HSC, and one of them is stated as Eq. (5). The average maximum compressive strengths of MC, MC5, and MC15 specimens were approximately 104, 84, and 70 MPa, respectively, and according to Eq. (5), their corresponding tensile strengths are 5.96, 5.2, and 4.65 MPa, respectively. Based on the results of teh current study, the maximum average tensile strengths of MT, MT5, and MT15 were approximately 10.48, 8.6, and 8.3 MPa, respectively.

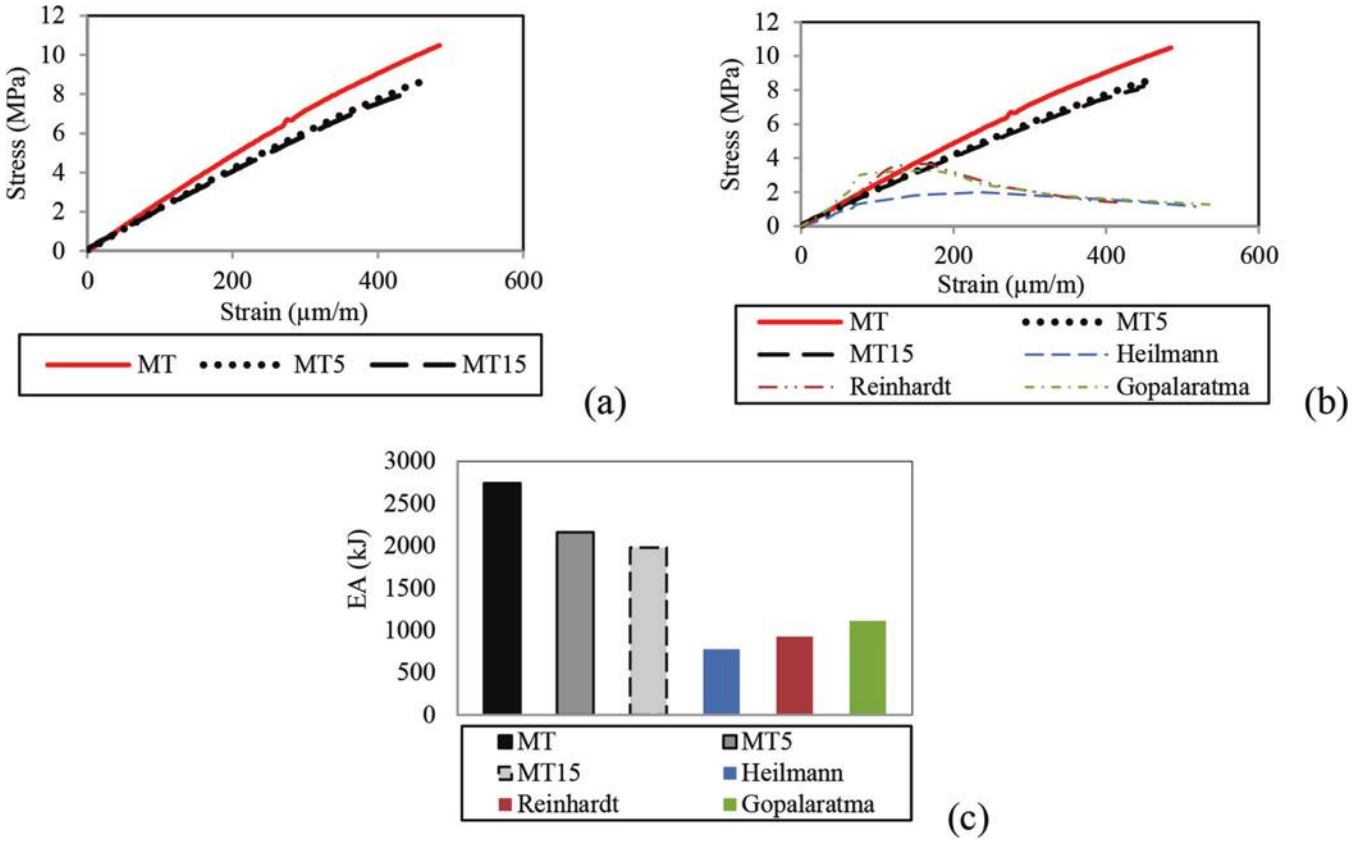

Fig. 7—Comparison of: (a) monotonic tensile test results; (b) tensile strengths of UPPC with NC; and (c) energy absorption capacity of UPPC and NC.

The results of the tests indicate that the ACI code recommendations for cement concrete are not applicable for PC, and it is necessary to construct appropriate relationships to describe the relationship between the tensile strength and compressive strength of UPPC more accurately in future studies.

$$f_t = 0.32 f_c'^{0.63} \quad (5)$$

Cyclic tensile test results

The test results of specimens subjected to cyclic tensile tests (as introduced in Table 1) are shown Fig. A7. The envelope curves were depicted for each cyclic response, and the average results of each environmental condition are shown in Fig 8. The average maximum tensile strength for CT specimens is approximately 10.8 MPa, while the average maximum strength of CT5 and CT15 diminished by 20% and 31%, respectively, due to the exposure of UPPC specimens to the acidic environment. The average and standard deviation of the maximum strength, maximum strain, and elastic modulus of cyclic tensile tests are obtained as demonstrated in Fig. A7.

The dumbbell-shaped specimens suddenly failed at the maximum load, and no significant cracking or crashing was detected during the test before the last phase. Moreover, results of *ESD* for CT, CT5, and CT15 specimens indicate that the slopes of unloading curves did not fluctuate during the loading and no significant degradation occurred during the cyclic tensile tests. Also, as the number of loading cycles

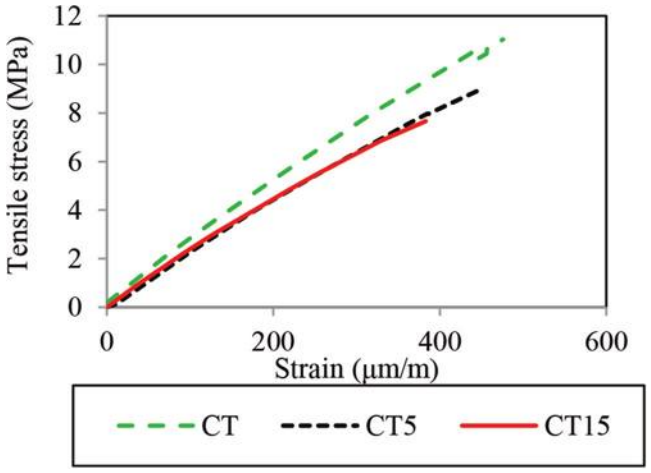

Fig. 8—Comparison of average envelope stress-strain curves of CT, CT5, and CT15.

increases, it can be seen that the unloading and reloading curves are linear and parallel. To characterize the unloading and reloading parts of cyclic loops, it is necessary to understand the relationship between the unloading strain ε_{un} and plastic strain ε_{pl}, as well as between plastic strain ε_{pl} and reloading strain ε_{re}. Thus, using data from cyclic tensile tests and regression analyses, linear equations for the unloading strain ε_{un} as a function of plastic strain ε_{pl}, and the relationship between plastic strain ε_{pl} and reloading strain ε_{re} are obtained. Results are displayed in Fig. A8.

Due to the perfect bonding between the resin matrix and aggregates, there was no detectable crack prior to the failing of specimens, and no wide hysteresis loops were recorded. The average envelope curves of CT, CT5, and CT15 specimens are compared with the average monotonic tensile curve for MT, MT5, and MT15 specimens in Fig. A9. It is clear that in all three cases, the stress-strain curves of the monotonic loading are similar to the envelope curves. Moreover, the maximum strength is nearly equal under the two loading conditions, despite minor variations, which are due to some inevitable test measurement errors and PC's heterogeneous structure.[51,55]

Constitutive equation

In this section of the study, stress-strain equations are proposed for monotonic and cyclic responses and unloading and reloading curves obtained from the compressive and tensile tests. As the monotonic and envelope curves are consistent with each other for both compression and tension loadings, the proposed relationships are based on the monotonic curves.

The main variables for all tests results are stress (σ), strain (ε), initial elastic modulus (E_0), and the secant elastic modulus of the maximum peak point (E_p). The proposed equations have been provided in dimensionless form, allowing them to be compared with the experimental results and those of other studies. In this regard, the stress and strain parameters were normalized as

$$s = \frac{\sigma}{\sigma_m}, e = \frac{\varepsilon}{\varepsilon_m} \tag{6}$$

where σ_m and ε_m are the maximum stress and strain, respectively.

For compressive loading, numerous studies have proposed constitutive relations for both NC[43,56-59] and HSC.[38,39,42,45,60-63] According to the monotonic compressive and tensile test results, the stress-strain relationships consist of one concave ascending part, which their elastic modulus (the slope of the curves) diminishes by increasing the strain. Thus, the proposed equation must be a function of E_0 and E_p. Moreover, it was discovered that the concave rising curve of the average monotonic and envelope curves could be described by a fractional function in which the stress ratio is dependent on the strain ratio ($s = f(e)$). According to the experimental data, the tangent modulus is the maximum at the beginning of the diagram, which decreases to zero at the maximum stress. This leads to considering the bell-shaped curve as the general shape of the stress-strain curve. The bell-shaped curve can be described according to Eq. (7)

$$e^B s + (C)s - (A)e = 0 \tag{7}$$

A, B, and C are constant coefficients given by boundary conditions. According to Fig. A10, the boundary conditions can be determined as the following relations

$$\begin{cases} s(1) = 1 \\ s(0) = 0 \end{cases} \quad \begin{cases} s'(0) = \dfrac{E_0}{E_p} = k \\ s'(1) = 0 \end{cases} \quad E_p = \frac{\sigma_{max}}{\varepsilon_{max}} \tag{8}$$

Because the diagram in Fig. A10 is shown as a stress-strain ratio, the derivative function generated from this diagram ($s'(e)$) displays the ratio of tangential elastic modulus to the secant elastic modulus of the maximum peak point ($E(e)/E_p$). Equation (9) is obtained by applying the mentioned boundary conditions to Eq. (7). As a result, the stress-strain function of PC in an acidic environment was characterized by using the mathematical relationships, taking into account the boundary conditions. Equation (10) was derived by using the similar methods that combined statistical methods with mathematical equations.[64]

$$s = \frac{k \times e}{(k-1) + (e)^k}; k = \frac{E_0}{E_0 - E_p} \tag{9}$$

$$s = \frac{(e)}{1 + (e)^{\left(\frac{E_p}{E_0}\right)} - (e)^{2\left(\frac{E_0}{E_p}\right)-1}} \tag{10}$$

The comparison between Eq. (9) and (10) and the experimental results is shown in Fig. 9. Moreover, the root-mean-square error (RMSE), correlation coefficient, and R^2 between the experimental stress-strain curves and empirical results (Eq. (9)) were calculated and compared in Table A7. To validate the accuracy of Eq. (9) and (10), the experimental stress-strain results of other studies conducted for PC were compared with Eq. (9) and (10).[2,24,65] Therefore, the obtained E_p and E_0 from their experimental tests were calculated and stress-strain curves were depicted according to Eq. (9) (refer to Fig. A11). It is clear that the proposed equations not only describe the compressive stress-strain equation of PC in an acidic environment in this study, but are also suitable for describing the compressive stress-strain of other PC materials with different strengths and elastic moduli.

The monotonic tensile curves for MT, MT5, and MT15 are the ascending curves with decreasing secant modulus similar to the compressive curves. Therefore, elastic modulus and secant modulus would be the main parameters for describing the stress-strain curves. Several studies have been conducted to express the tensile curves of NC.[52,53,66] The monotonic tensile curves are semi-linear curves whose slopes decrease with increasing strain. Therefore, it is assumed that a power function with a power value close to 1 can describe the monotonic tensile curves. Based on the elastic modulus and secant modulus of MT5 and MT15 and using statistical methods, Eq. (11) is proposed to describe the tensile responses of UPPC specimens immersed in an acidic environment.

$$s = (e)^{1/n}; n = \frac{E_0}{E_p} \tag{11}$$

In Fig. 10, the proposed stress-strain relationship is compared with the experimental results of the UPPC specimens. Moreover, the RMSE, correlation coefficient, and R^2 between the experimental stress-strain curves, and empirical results (Eq. (11)) were calculated and compared in Table A7. The predicted curves agreed well with the experimental data, indicating that the proposed constitutive relations presented in Eq. (11) can accurately describe the

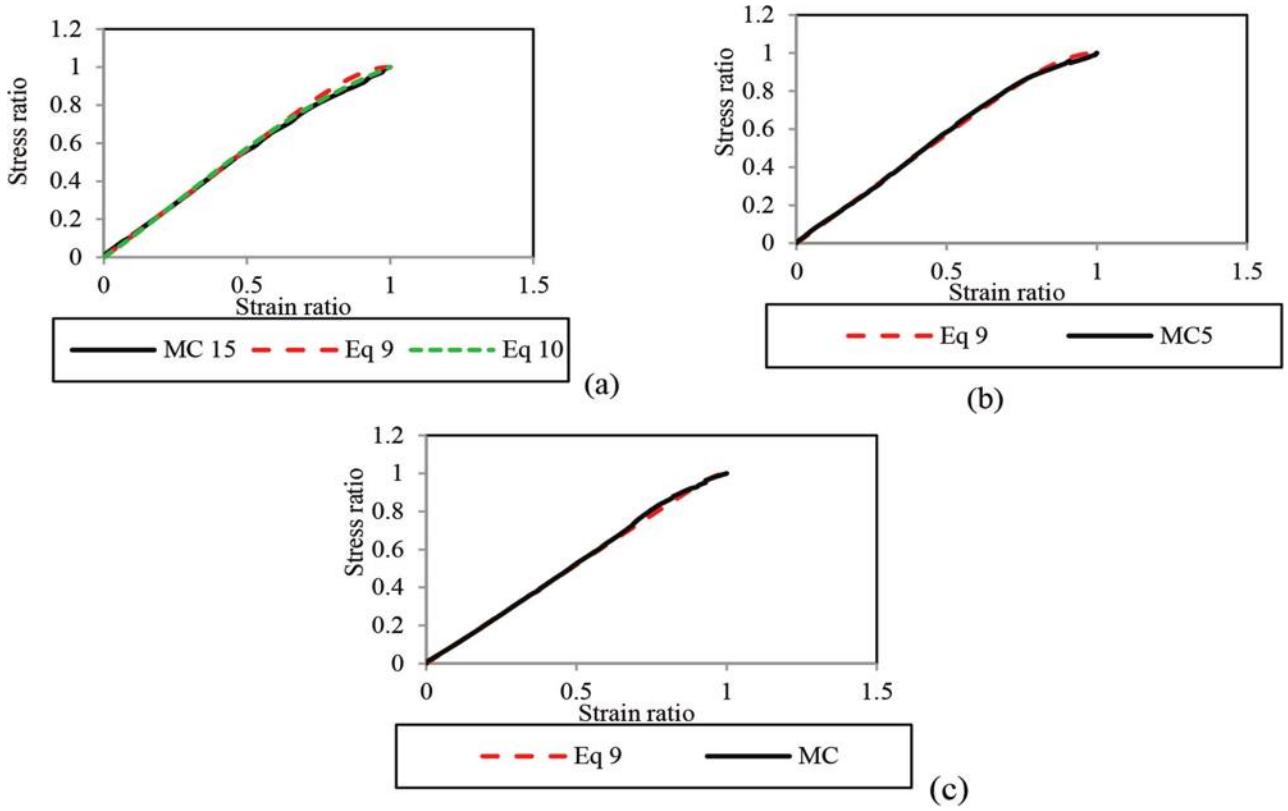

Fig. 9—Average monotonic compressive curve versus proposed equations: (a) MC15; (b) MC5; and (c) MC.

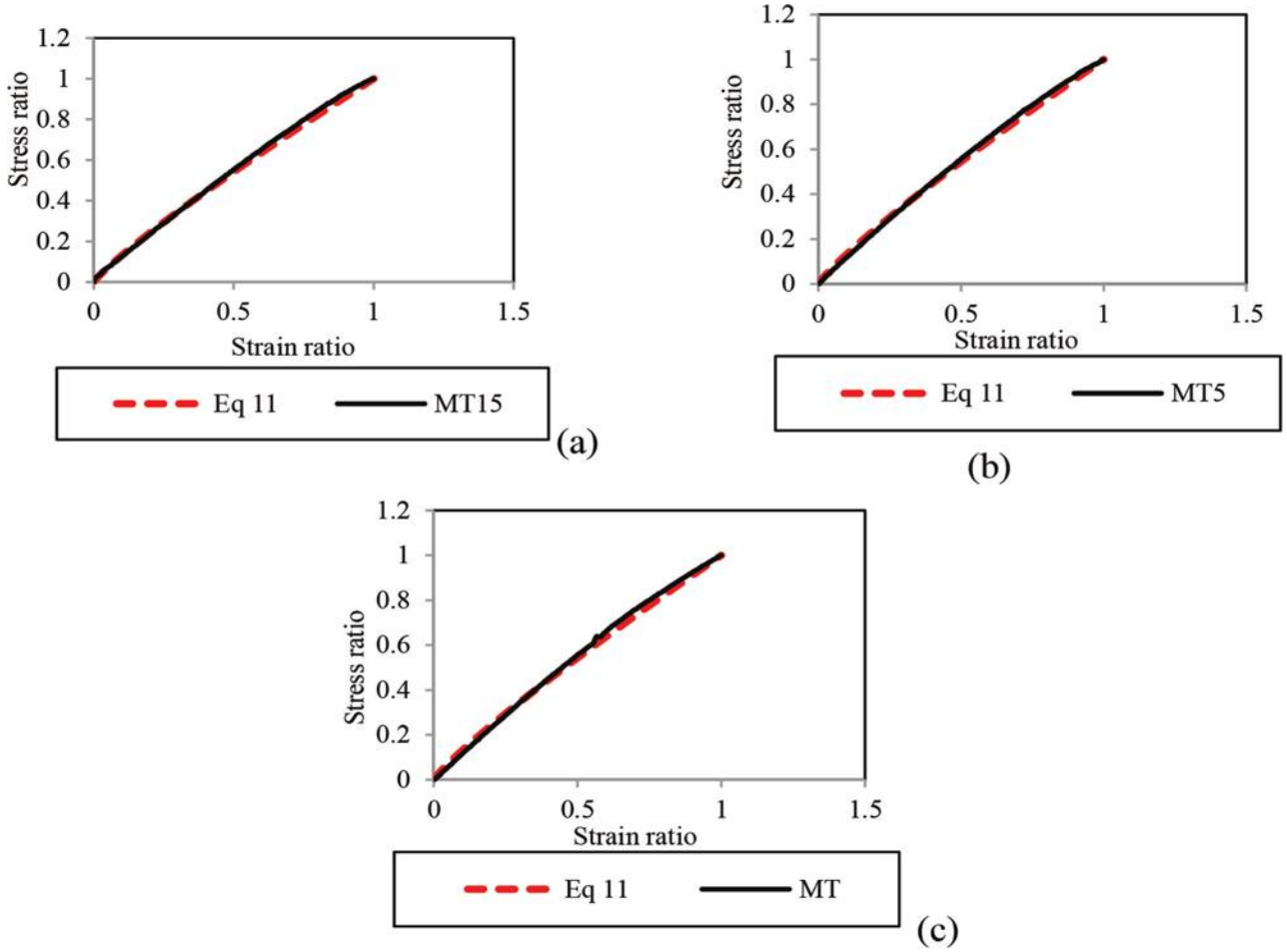

Fig. 10—Average monotonic tensile curve versus proposed equations: (a) MT15; (b) MT5; and (c) MT.

tensile behavior of UPPC specimens immersed in acidic environments.

To describe the stress-strain relationships of unloading and reloading parts of cyclic compressive curves for CC5 and CC15 tests, the previous proposed equations for unloading and reloading paths for cement-based concrete were studied.[67] It was noticed that the power-law equation is proper to describe unloading and reloading parts of the cyclic compressive curve, and unloading stress and strain, plastic strain reloading stress and strain, and elastic modulus are the main variables in defining these equations. By modifying the proposed equation by Bahn and Hsu[67] and using ε_{un}-ε_{pl} and ε_{pl}-ε_{re} relationships (as mentioned in Fig. A6), Eq. (12) and (13) are proposed

$$\sigma_c = \left(\sigma_p + (\sigma_{cu} - \sigma_p)\left(\frac{\varepsilon_c - \varepsilon_p}{\varepsilon_{cu} - \varepsilon_p}\right)^{E_0/E_p}\right) \quad (12)$$

$$\sigma_c = \left(\sigma_p + (\sigma_{re} - \sigma_p)\left(\frac{\varepsilon_c - \varepsilon_p}{\varepsilon_{re} - \varepsilon_p}\right)^{E_p/E_0}\right) \quad (13)$$

where ε_{cu} and σ_{cu} indicate the strain and stress at the starting point of unloading on the skeleton curve; ε_p and σ_p are the strain and stress of the end point of the unloading path; and ε_{re} and σ_{re} are the strain and stress at the final point of the reloading path on the skeleton curve. Figure A12 displays the comparison between the unloading curves of a CC15 test with Eq. (12), and Fig. A13 describes the reloading part of a CC5 test and obtained curve from Eq. (13). In these figures, the unloading and reloading curves are depicted separately for a test specimen. It is quite clear that Eq. (12) and (13) agreed well with the experimental results, and they are appropriate to describe the unloading and reloading paths.

For the cyclic tensile tests, the results of unloading and reloading curves for CT5 and CT15 demonstrate that the unloading and reloading path are linear. By using ε_{un}-ε_{pl} and ε_{pl}-ε_{re} relationships (as mentioned in Fig. A8), linear Eq. (14) and (15) are defined

$$\sigma_T = \left(\sigma_p + (\sigma_{un} - \sigma_p)\left(\frac{\varepsilon_T - \varepsilon_p}{\varepsilon_{un} - \varepsilon_p}\right)\right) \quad (14)$$

$$\sigma_T = \left(\sigma_p + (\sigma_{re} - \sigma_p)\left(\frac{\varepsilon_T - \varepsilon_p}{\varepsilon_{re} - \varepsilon_p}\right)\right) \quad (15)$$

The comparison between the empirical unloading and reloading equations with experimental tensile cyclic results, as demonstrated in Fig. A14 and A15, indicate that the proposed linear equations (Eq. (14) and (15)) are traced well in the test results, and they are appropriate to describe the cyclic response of UPPC in tension.

Failure mechanism

The combination of the unsaturated polyester resin with the peroxide formed a chemical bond consisting of many long-branched ring chains that developed during the curing time. These connected hexagonal nets of benzene rings encircle the aggregates and provide the firm connection between the sand and gravel. The fillers also filled the tiny gaps during the linkage of the aggregates. This branched chain that surrounds the aggregates is a hydrophobic gel, and it can hardly be dissolved by water solutions. Therefore, they protect the aggregates against the corrosive environment, and only the aggregates or fillers that are on the surface of the specimens may deteriorate in sulfuric acid. Thus, not only does unsaturated polyester resin provide the firm bonding between the aggregates, but it also acts as a protector and prevents corrosion of the aggregates in harsh environments. PC's performance is directly related to the resin content. Increasing the resin concentration in polymer concrete can lead to a strong anti-acidic behavior, making the PC specimens more resistant in acidic environments.[36]

After being exposed to sulfuric acid, the surface color of UPPC specimens changed to a pale gray. Due to the impermeable surface of the PC, no evident crack formed on the surface of the specimens during the immersion period. While the resin of the PC surface protects the specimens against the formation of porosity, shallow porous surfaces formed because of the damage to the aggregates on the surface of specimens. However, the depth of the acid penetration was limited to less than 1 cm (refer to Fig. 1 and A16).

Figure 11 demonstrates general failure mechanisms observed in different specimens. In both tensile and compressive tests, the failure plane occurred at both the resin matrix and aggregates due to the excellent bonding provided by the resin. The failure of all compressive specimens (except the specimens immersed in 15% sulfuric acid) occurred with sudden rupture and loud sound. In the case of the compressive tests of the specimens immersed in 15% sulfuric acid, spalling of the PC around the surfaces was observed before the complete failure of samples (refer to Fig. A17). Then the specimens collapsed slowly, without any significant sound. In all compressive specimens, the crack originated from the middle of the specimen and then developed to the top and bottom of the points where loading was applied. The failure planes were vertical, and their angles ranged between 90 and 60 degrees (Fig. 11, A17, and A18). The shear cones formed at the end of the loading.

In all tensile tests, the failure planes were horizontal, and they were perpendicular to the loading axes in the necking section of the specimens (Fig. 11 and A19). Due to the cohesion between the aggregate and resin and the high tensile strength of resin, breaking of coarse aggregates was detected in the failure plane.

Limitations of study and recommendations for future studies

There were a number of limitations in conducting this study. Due to the high price of cyclic tensile and compressive tests, which includes the cost of strain gauges, the cost of making specimens, and the cost of conducting tests, the number of tests performed was limited. Due to the limited capacity of the universal testing device (600 kN), the dimensions of the compressive test specimens were limited, while still having to satisfy the DIN 51290-3 standard requirements. It is proposed that the effect of different corrosive environments, including acidic, alkaline, and salty environments, on the strength of UPPC materials be investigated in

Fig. 11—Failure modes of: (a) cubic specimens in compression; (b) cylindrical specimens in compression; and (c) dumbbell-shaped specimens in tension.

further studies. It is also required to investigate the effect of various environmental conditions such as different temperature and pressure conditions and long-term loading on the strength of UPPC specimens.

CONCLUSIONS

This study aims to investigate the long-term effects of sulfuric acid environments on the durability and the mechanical properties of unsaturated polyester polymer concrete (UPPC). Therefore, specimens were fabricated and cured for 28 days, immersed in 5 and 15% sulfuric acid, and then monotonic and cyclic tests were done to depict the average tensile and compressive stress-strain curves for immersed polymer concrete (PC). The following conclusions can be drawn from the results of this investigation:

- The average compressive strength of control specimens increased approximately 18%, from 104 to 123 MPa, during the 180 days of curing, while the average compressive strength of UC5 and UC15 were reduced up to 34 and 39%. UC15 still demonstrated adequate strength compared to the normal concrete (NC) and high-strength concrete (HSC).
- The results of monotonic compressive tests demonstrated that the average maximum strength of UPPC decreased from 104 to 84 MPa and 70 MPa for MC5 and MC15 specimens, respectively. While MC15 demonstrated more strength and strain degradation, as expected, its peak strain, compressive strength, and energy absorption capacity (*EA*) are approximately 1.67, 2, and 1.7 times higher than NC.
- Elastic stiffness degradation was approximately 0.72 for both CC5 and CC15 in their final cycles, while it is 0.81 for CC specimens. The rate of elastic stiffness degradation (*ESD*) increased for CC15 compared to the CC and CC5 specimens. *ESD* is reported to be approximately 0.2 for cement-based concrete, and it demonstrates that the failure of the UPPC occurred abruptly during the final cycles of loading.
- The results of direct monotonic tensile tests showed that the acidic environment decreased the average monotonic strength of MT5 and MT15 by 18% and 21%, respectively, compared to the MT specimens. However, the maximum strength and *EA* of MT15 is approximately 2.73 and 2.1 times higher than that of NC, respectively. The UPPC was able to demonstrate better performance in the cases of absorbed energy and strength compared to the NC.

- Empirical equations were proposed to describe the average monotonic and envelope curves for SP5 and SP15 specimens and compared with the experimental stress-strain relationship. The proposed equation agreed well with the test results and the models are applicable for predicting the monotonic and cyclic behavior of UPPC in an acidic environment.
- Fracture of the gravels was observed in final failure modes, and the failure plane crossed throughout the coarse aggregates. In compressive tests, the failure plane was cone-shaped, while it was horizontal in tensile loading. The failure occurred with the sudden destruction of specimens with a load sound both in compressive and tensile tests, except in the compressive test of specimens that were immersed in 15% sulfuric acid for 180 days.
- Sulfuric acid altered the color of UPPC to pale gray. No apparent cracks formed in specimens due to the acidic environment, only some shallow holes formed on the surface of the UPPC specimens, and the acid solution permeated the specimens only less than 1 cm.

AUTHOR BIOS

Morteza Bastami *is an Associate Professor at the International Institute of Earthquake Engineering and Seismology (IIEES), Tehran, Iran. He received his PhD in earthquake engineering from Kobe University, Kobe, Japan, in 2007. His research interests include concrete technologies, structural engineering, and risk analysis.*

Mostafa Abbasnejadfard *is a PhD Candidate at IIEES. He received his MS from the University of Tabriz, Tabriz, Iran, in 2013. His research interests include polymer- and cement-based composite material and infrastructure assessment.*

Mohsen Aslani *is CEO of Louleh-Beton-Polymer Co., Tehran, Iran. He received his BS in mechanical engineering from Iran University of Science and Technology, Tehran, Iran, in 1988. His research interests include concrete technologies, polymer concrete, and concrete pipe construction.*

Morteza Abbasnejadfard *is a Research Associate at IIEES. He received his PhD in earthquake engineering from IIEES in 2020. His research interests include structural design, structure and infrastructure rehabilitation, and risk assessment.*

Rasool Hayatiani *is a Polymer Chemist who received his MS from the University of Isfahan, Isfahan, Iran, in 2014. His research interests include polymer composites and concrete pipe construction.*

REFERENCES

1. Zhang, H.; Zhang, G.; Han, F.; Zhang, Z.; and Lv, W., "A Lab Study to Develop a Bridge Deck Pavement Using Bisphenol a Unsaturated Polyester Resin Modified Asphalt Mixture," *Construction and Building Materials*, V. 159, No. 1, Jan. 2018, pp. 83-98. doi: 10.1016/j.conbuildmat.2017.10.126

2. Vipulanandan, C., and Paul, E., "Performance of Epoxy and Polyester Polymer Concrete," *ACI Materials Journal*, V. 87, No. 3, May-June 1990, pp. 241-251. doi: 10.14359/2187

3. Rebeiz, K. S.; Serhal, S. P.; and Craft, A. P., "Properties of Polymer Concrete Using Fly Ash," *Journal of Materials in Civil Engineering*, ASCE, V. 16, No. 1, 2004, pp. 15-19. doi: 10.1061/(ASCE)0899-1561(2004)16:1(15)

4. Jo, B. W.; Park, S. K.; and Park, J. C., "Mechanical Properties of Polymer Concrete Made with Recycled PET and Recycled Concrete Aggregates," *Construction and Building Materials*, V. 22, No. 12, Dec. 2008, pp. 2281-2291. doi: 10.1016/j.conbuildmat.2007.10.009

5. Reis, J. M. L., "Fracture Assessment of Polymer Concrete in Chemical Degradation Solutions," *Construction and Building Materials*, V. 24, No. 9, Sept. 2010, pp. 1708-1712. doi: 10.1016/j.conbuildmat.2010.02.020

6. Yang, Z.; Peng, H.; Wang, W.; and Liu, T., "Crystallization Behavior of Poly(ε-caprolactone)/Layered Double Hydroxide Nanocomposites," *Journal of Applied Polymer Science*, V. 116, No. 5, 2010, pp. 2658-2667. doi: 10.1002/app.31787

7. Reis, J. M. L., and Jurumenh, M. A. G., "Experimental Investigation on the Effects of Recycled Aggregate on Fracture Behavior of Polymer Concrete," *Materials Research*, V. 14, No. 3, 2011, pp. 326-330. doi: 10.1590/S1516-14392011005000060

8. Jamshidi, M., and Pourkhorshidi, A. R., "Modified Polyester Resins as an Effective Binder for Polymer Concretes," *Materials and Structures*, V. 45, No. 4, 2012, pp. 521-527. doi: 10.1617/s11527-011-9779-9

9. Elalaoui, O.; Ghorbel, E.; Mignot, V.; and Ben Ouezdou, M., "Mechanical and Physical Properties of Epoxy Polymer Concrete After Exposure to Temperatures Up to 250°C," *Construction and Building Materials*, V. 27, No. 1, 2012, pp. 415-424. doi: 10.1016/j.conbuildmat.2011.07.027

10. Agavriloaie, L.; Oprea, S.; Barbuta, M.; and Luca, F., "Characterisation of Polymer Concrete with Epoxy Polyurethane Acryl Matrix," *Construction and Building Materials*, V. 37, 2012, pp. 190-196. doi: 10.1016/j.conbuildmat.2012.07.037

11. Yeon, K. S.; Cha, J. Y.; Yeon, J. H.; and Seung, I. B., "Effects of TMPTMA and Silane on the Compressive Strength of Low-Temperature Cured Acrylic Polymer Concrete," *Journal of Applied Polymer Science*, V. 131, No. 20, 2014, pp. 1-8. doi: 10.1002/app.40939

12. Jin, N. J.; Yeon, J.; Seung, I.; and Yeon, K. S., "Effects of Curing Temperature and Hardener Type on the Mechanical Properties of Bisphenol F-Type Epoxy Resin Concrete," *Construction and Building Materials*, V. 156, 2017, pp. 933-943. doi: 10.1016/j.conbuildmat.2017.09.053

13. Hyun, S. H., and Yeon, J. H., "Strength Development Characteristics of UP-MMA Based Polymer Concrete with Different Curing Temperature," *Construction and Building Materials*, V. 37, 2012, pp. 387-397. doi: 10.1016/j.conbuildmat.2012.07.094

14. Lokuge, W., and Aravinthan, T., "Effect of Fly Ash on the Behaviour of Polymer Concrete with Different Types of Resin," *Materials and Design*, V. 51, 2013, pp. 175-181. doi: 10.1016/j.matdes.2013.03.078

15. Ferdous, W.; Manalo, A.; Aravinthan, T.; and Van Erp, G., "Properties of Epoxy Polymer Concrete Matrix: Effect of Resin-to-Filler Ratio and Determination of Optimal Mix for Composite Railway Sleepers," *Construction and Building Materials*, V. 124, 2016, pp. 287-300. doi: 10.1016/j.conbuildmat.2016.07.111

16. Kim, K.-K.; Urgessa, G. S.; and Yeon, J. H., "Analysis and Modeling of Uniaxial Compressive Creep of MMA-Modified Unsaturated Polyester Polymer Concrete," *Journal of Materials Research and Technology*, V. 9, No. 6, 2020, pp. 12773-12782. doi: 10.1016/j.jmrt.2020.09.039

17. Hashemi, M. J.; Jamshidi, M.; and Aghdam, J. H., "Investigating Fracture Mechanics and Flexural Properties of Unsaturated Polyester Polymer Concrete (UP-PC)," *Construction and Building Materials*, V. 163, 2018, pp. 767-775. doi: 10.1016/j.conbuildmat.2017.12.115

18. Kou, S. C., and Poon, C. S., "A Novel Polymer Concrete Made with Recycled Glass Aggregates, Fly Ash and Metakaolin," *Construction and Building Materials*, V. 41, 2013, pp. 146-151. doi: 10.1016/j.conbuildmat.2012.11.083

19. Dębska, B., and Lichołai, L., "A Study of the Effect of Corrosive Solutions on Selected Physical Properties of Modified Epoxy Mortars," *Construction and Building Materials*, V. 65, 2014, pp. 604-611. doi: 10.1016/j.conbuildmat.2014.05.038

20. Pacheco-Torgal, F., and Jalali, S., "Sulphuric Acid Resistance of Plain, Polymer Modified, and Fly Ash Cement Concretes," *Construction and Building Materials*, V. 23, No. 12, 2009, pp. 3485-3491. doi: 10.1016/j.conbuildmat.2009.08.001

21. Reis, J. M. L., "Mechanical Characterization of Polymer Mortars Exposed to Degradation Solutions," *Construction and Building Materials*, V. 23, No. 11, 2009, pp. 3328-3331. doi: 10.1016/j.conbuildmat.2009.06.047

22. Gorninski, J. P.; Dal Molin, D. C.; and Kazmierczak, C. S., "Comparative Assessment of Isophtalic and Orthophtalic Polyester Polymer Concrete: Different Costs, Similar Mechanical Properties and Durability," *Construction and Building Materials*, V. 21, No. 3, 2007, pp. 546-555. doi: 10.1016/j.conbuildmat.2005.09.003

23. Jung, K. C.; Roh, I. T.; and Chang, S. H., "Evaluation of Mechanical Properties of Polymer Concretes for the Rapid Repair of Runways," *Composites, Part B: Engineering*, V. 58, 2014, pp. 352-360. doi: 10.1016/j.compositesb.2013.10.076

24. Toufigh, V.; Hosseinali, M.; and Shirkhorshidi, S. M., "Experimental Study and Constitutive Modeling of Polymer Concrete's Behavior in Compression," *Construction and Building Materials*, V. 112, 2016, pp. 183-190. doi: 10.1016/j.conbuildmat.2016.02.100

25. Bulut, H. A., and Şahin, R., "A Study on Mechanical Properties of Polymer Concrete Containing Electronic Plastic Waste," *Composite Structures*, V. 178, 2017, pp. 50-62. doi: 10.1016/j.compstruct.2017.06.058

26. Hassani Niaki, M.; Fereidoon, A.; and Ghorbanzadeh Ahangari, M., "Mechanical Properties of Epoxy/Basalt Polymer Concrete: Experimental and Analytical Study," *Structural Concrete*, V. 19, No. 2, 2018, pp. 366-373. doi: 10.1002/suco.201700003

27. Heidarnezhad, F.; Jafari, K.; and Ozbakkaloglu, T., "Effect of Polymer Content and Temperature on Mechanical Properties of Lightweight Polymer Concrete," *Construction and Building Materials*, V. 260, 2020, p. 119853. doi: 10.1016/j.conbuildmat.2020.119853

28. Ferdous, W.; Manalo, A.; Wong, H. S.; Abousnina, R.; AlAjarmeh, O. S.; Zhuge, Y.; and Schubel, P., "Optimal Design for Epoxy Polymer Concrete Based on Mechanical Properties and Durability Aspects," *Construction and Building Materials*, V. 232, 2020, p. 117229. doi: 10.1016/j.conbuildmat.2019.117229

29. Ribeiro, M. C. S.; Tavares, C. M. L.; and Ferreira, A. J. M., "Chemical Resistance of Epoxy and Polyester Polymer Concrete to Acids and Salts," *Journal of Polymer Engineering*, V. 22, No. 1, 2002, pp. 27-44. doi: 10.1515/POLYENG.2002.22.1.27

30. Rahman, M. M.; Islam, M. A.; and Uddin, M. T., "Excellent Durability of Epoxy Modified Mortars in Corrosive Environments," *Journal of Polymer Engineering*, V. 36, No. 1, 2016, pp. 79-85. doi: 10.1515/polyeng-2015-0105

31. Moodi, F.; Kashi, A.; Ramezanianpour, A. A.; and Pourebrahimi, M., "Investigation on Mechanical and Durability Properties of Polymer and Latex-Modified Concretes," *Construction and Building Materials*, V. 191, 2018, pp. 145-154. doi: 10.1016/j.conbuildmat.2018.09.198

32. Ghassemi, P., and Toufigh, V., "Durability of Epoxy Polymer and Ordinary Cement Concrete in Aggressive Environments," *Construction and Building Materials*, V. 234, 2020, p. 117887. doi: 10.1016/j.conbuildmat.2019.117887

33. ASTM C33-03, "Standard Specifications for Concrete Aggregates," ASTM International, West Conshohocken, PA, 2003, 11 pp.

34. DIN 1045-2:2014, "Concrete and Reinforced Concrete, Design and Construction," Deutsches Institut für Normung, Berlin, Germany, 2014.

35. ASTM C267-01(2012), "Standard Test Methods for Chemical Resistance of Mortars, Grouts, and Monolithic Surfacings and Polymer Concretes," ASTM International, West Conshohocken, PA, 2001, 6 pp.

36. Nodehi, M., "Epoxy, Polyester and Vinyl Ester Based Polymer Concrete: A Review," *Innovative Infrastructure Solution*, V. 7, No. 1, 2022, p. 64 doi: 10.1007/s41062-021-00661-3

37. DIN 51290-3:1991, "Testing of Polymer Concretes (Reactive Resin Concretes) for Mechanical Engineering Purposes; Testing of Separately Manufactured Specimens," Deutsches Institut für Normung, Berlin, Germany, 1991.

38. Hsu, L. S., and Hsu, C. T. T., "Complete Stress-Strain Behaviour of High-Strength Concrete under Compression," *Magazine of Concrete Research*, V. 46, No. 169, 1994, pp. 301-312. doi: 10.1680/macr.1994.46.169.301

39. Carreira, D. J., and Chu, K. H., "Stress-Strain Relationship for Plain Concrete in Compression," *ACI Journal Proceedings*, V. 82, No. 6, Nov.-Dec. 1985, pp. 797-804. doi: 10.14359/10390

40. Dahl, K. K. B., "A Constitutive Model for Normal and High Strength Concrete," Afdelingen for Bærende Konstruktioner, Dankmarks Tekniske Højskole, 1992.

41. Hu, X.; Lu, Q.; Xu, Z.; Zhang, W.; and Cheng, S., "Compressive Stress-Strain Relation of Recycled Aggregate Concrete under Cyclic Loading," *Construction and Building Materials*, V. 193, 2018, pp. 72-83. doi: 10.1016/j.conbuildmat.2018.10.137

42. Tomaszewicz, A., "Betongens Arbeidsdiagram," SINTEF Report No. STF 65A84065, Trondheim, Norway, 1984.

43. Collins, M. P.; Mitchell, D.; and Macgregor, J. G., "Structural Design Considerations for High Strength Concrete," *Concrete International*, V. 15, No. 5, May 1993, pp. 27-34.

44. *fib*, "CEB-FIP Model Code 1990," International Federation for Structural Concrete, Lausanne, Switzerland, 1993, 460 pp.

45. Van Gysel, A., and Taerwe, L., "Analytical Formulation of the Complete Stress-Strain Curve for High Strength Concrete," *Materials and Structures*, V. 29, No. 9, 1996, pp. 529-533. doi: 10.1007/BF02485952

46. Wee, T. H.; Chin, M. S.; and Mansur, M. A., "Stress-Strain Relationship of High-Strength Concrete in Compression," *Journal of Materials in Civil Engineering*, ASCE, V. 8, No. 2, 1996, pp. 70-76. doi: 10.1061/(ASCE)0899-1561(1996)8:2(70)

47. Lu, Z.-H., and Zhao, Y.-G., "Empirical Stress-Strain Model for Unconfined High-Strength Concrete Under Uniaxial Compression," *Journal of Materials in Civil Engineering*, ASCE, V. 22, No. 11, 2010, pp. 1181-1186. doi: 10.1061/(ASCE)MT.1943-5533.0000095

48. Farnam, Y.; Moosavi, M.; Shekarchi, M.; Babanajad, S. K.; and Bagherzadeh, A., "Behaviour of Slurry Infiltrated Fibre Concrete (SIFCON) Under Triaxial Compression," *Cement and Concrete Research*, V. 40, No. 11, 2010, pp. 1571-1581. doi: 10.1016/j.cemconres.2010.06.009

49. ASTM C469-02, "Standard Test Method for Static Modulus of Elasticity and Poisson's Ratio of Concrete in Compression," ASTM International, West Conshohocken, PA, 2002.

50. ACI Committee 363, "Report on High-Strength Concrete (ACI PRC-363-10)," American Concrete Institute, Farmington Hills, MI, 2010, 65 pp.

51. Xu, L.; Li, B.; Ding, X.; Chi, Y.; Li, C.; Huang, B.; and Shi, Y., "Experimental Investigation on Damage Behavior of Polypropylene Fiber Reinforced Concrete under Compression," *International Journal of Concrete Structures and Materials*, V. 12, No. 1, 2018, p. 68. doi: 10.1186/s40069-018-0302-3

52. Yankelevsky, D. Y., and Reinhardt, H. W., "Response of Plain Concrete to Cyclic Tension," *ACI Materials Journal*, V. 84, No. 5, Sept.-Oct. 1987, pp. 365-373.

53. Gopalaratnam, V. S., and Shah, S. P., "Softening Response of Plain Concrete in Direct Tension," *ACI Journal Proceedings*, V. 82, No. 3, May-June 1985, pp. 310-323. doi: 10.14359/10338

54. Heilmann, H. G.; Hilsdorf, H.; and Finsterwalder, K., "Strength and Deformation of Concrete under Tensile Stress," *Bulletin*, 1969, 94 pp.

55. Li, P.; Sui, L.; Xing, F.; and Zhou, Y., "Static and Cyclic Response of Low-Strength Recycled Aggregate Concrete Strengthened Using Fiber-Reinforced Polymer," *Composites, Part B: Engineering*, V. 160, 2019, pp. 37-49. doi: 10.1016/j.compositesb.2018.10.002

56. Ramesh, K.; Seshu, D. R.; and Prabhakar, M., "Constitutive Behaviour of Confined Fibre Reinforced Concrete under Axial Compression," *Cement and Concrete Composites*, V. 25, No. 3, 2003, pp. 343-350. doi: 10.1016/S0958-9465(02)00051-3

57. Tasnimi, A. A., "Mathematical Model for Complete Stress-Strain Curve Prediction of Normal, Light-Weight and High-Strength Concretes," *Magazine of Concrete Research*, V. 56, No. 1, 2004, pp. 23-34. doi: 10.1680/macr.2004.56.1.23

58. Belén, G. F.; Fernando, M. A.; Diego, C. L.; and Sindy, S. P., "Stress-Strain Relationship in Axial Compression for Concrete Using Recycled Saturated Coarse Aggregate," *Construction and Building Materials*, V. 25, No. 5, 2011, pp. 2335-2342. doi: 10.1016/j.conbuildmat.2010.11.031

59. Wang, W.; Zhao, L.; Liu, Y.; and Li, Z., "Mechanical Properties and Stress-Strain Relationship in Axial Compression for Concrete with Added Glazed Hollow Beads and Construction Waste," *Construction and Building Materials*, V. 71, 2014, pp. 425-434. doi: 10.1016/j.conbuildmat.2014.05.005

60. Popovics S., "A Numerical Approach to the Complete Stress-Strain Curve of Concrete," *Cement and Concrete Research*, V. 3, No. 5, Sept. 1973, pp. 583-599.

61. Wang, P. T.; Shah, S. P.; and Naaman, A. E., "Stress-Strain Curves of Normal and Lightweight Concrete in Compression," *ACI Journal Proceedings*, V. 75, No. 11, Nov. 1978, pp. 603-611. doi: 10.14359/10973

62. Bastami, M., and Aslani, F., "Preloaded High-Temperature Constitutive Models and Relationships for Concrete," *Scientia Iranica*, V. 17, No. 1, Feb. 2010, pp. 11-25.

63. Aslani, F., and Samali, B., "Constitutive Relationships for Self-Compacting Concrete at Elevated Temperatures," *Materials and Structures*, V. 48, 2015, pp. 337-356. doi: 10.1617/s11527-013-0187-1

64. Abbasnejadfard, M.; Bastami, M.; and Hashemi, S. A., "Experimental Investigation on the Stress-Strain Behavior of Unsaturated Polyester Polymer Concrete Subjected to Monotonic and Cyclic Loadings," *Journal of Building Engineering*, V. 48, 2022, p. 103966. doi: 10.1016/j.jobe.2021.103966

65. Chen, D.; Liu, F.; Yang, F.; Jing, L.; Feng, W.; Lv, J.; and Luo, Q., "Dynamic Compressive and Splitting Tensile Response of Unsaturated Polyester Polymer Concrete Material at Different Curing Ages," *Construction and Building Materials*, V. 177, 2018, pp. 477-498. doi: 10.1016/j.conbuildmat.2018.05.058

66. Sima, J. F.; Roca, P.; and Molins, C., "Cyclic Constitutive Model for Concrete," *Engineering Structures*, V. 30, No. 3, 2008, pp. 695-706. doi: 10.1016/j.engstruct.2007.05.005

67. Bahn, B. Y., and Hsu, C.-T. T., "Stress-Strain Behavior of Concrete Under Cyclic Loading," *ACI Materials Journal*, V. 95, No. 2, Mar.-Apr. 1998, pp. 178-193.

JOIN AN ACI Chapter!

The American Concrete Institute has Chapters and Student Chapters located throughout the world. Participation in a local chapter can be extremely rewarding in terms of gaining greater technical knowledge and networking with leaders in the concrete community.

Because chapters are distinct and independent legal entities, membership includes both ACI members and non-ACI members and is made up of a diverse blend of architects, engineers, consultants, contractors, educators, material suppliers, equipment suppliers, owners, and students—basically anyone interested in concrete. Many active ACI members initially became involved in ACI through their local chapter. In addition to technical programs and publications, many chapters sponsor ACI Certification programs, ACI educational seminars, project award recognition programs, and social events with the goal of advancing concrete knowledge.

Check out the Chapters Special Section from the November 2020 *Concrete International*: www.concrete.org/publications/concreteinternational.aspx

---

Student Chapters

Join or form an ACI Student Chapter to maximize your influence, knowledge sharing, and camaraderie! ACI has 240+ student chapters located throughout the world, each providing opportunities for students to:

- Connect with their peers and participate in concrete-related activities such as: student competitions, ACI Conventions, ACI Certification Programs, ACI Educational Seminars, local chapter meetings, social events, and community service projects;
- Network with members of local chapters, many of whom have been in the industry for decades and can help to develop professional relationships and offer career advice;
- Win recognition for their universities through the University Award; and
- Learn about the many scholarships and fellowships offered by the ACI Foundation and by ACI's local chapters.

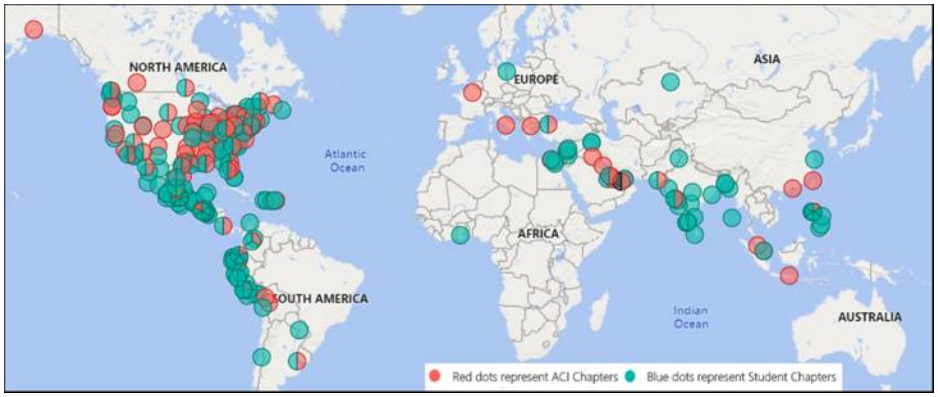

ACI MATERIALS JOURNAL TECHNICAL PAPER

Title No. 121-M08

Flexural Residual Strength of Lightweight Concrete Reinforced with Micro-Steel Fibers

by Hak-Young Kim, Keun-Hyeok Yang, Hye-Jin Lee, Seung-Jun Kwon, and Xiao-Yong Wang

The objective of the present study is to assess the flexural residual strengths of lightweight aggregate concrete (LWAC) reinforced with micro-steel fibers. Further, the material class of such concrete was examined through comparison with the fiber-reinforced concrete classification specified in the provisions of fib *2010. Fourteen beam specimens were classified into L (21 MPa [3.05 ksi]) and H (40 MPa [5.80 ksi]) groups according to the design compressive strength of LWAC. The volume fraction of micro-steel fibers varied from 0 to 1.5% at a spacing of 0.25% in each beam group. From the beam test results under the three-point loading condition, flexural stress-crack mouth opening displacement (CMOD) curves were measured and then discussed as a function of the fiber reinforcing index (β_f). The flexural residual strengths corresponding to four different CMOD values (0.5, 1.5, 2.5, and 3.5 mm [0.02, 0.06, 0.1, and 0.14 in.]) were compared with previous empirical equations and* fib *2010 classification. The various analyses of the measured results indicate that β_f can be regarded as a critical factor in directly determining the magnitude of flexural residual strengths and assessing material classification. The proposed refined equations improve the accuracy in predicting the flexural residual strengths of concrete beams with different densities and reinforced with different types of steel fibers. Consequently, micro-steel fibers are a promising partial replacement for conventional steel reinforcing bars to enhance the ductility of LWAC elements.*

Keywords: crack mouth opening displacement (CMOD); fiber reinforcing index; lightweight aggregate concrete (LWAC); residual strength.

INTRODUCTION

With the global movement toward sustainable activities in the concrete industry, artificial lightweight aggregates (LWAs) have continued to gain interest since the 2000s to manage the conservation of natural resources and depletion of natural aggregates. Although artificial LWAs are recognized as a sustainable construction material, they typically exhibit lower strength and stiffness than conventional natural aggregates.[1-3] Because of the inferior properties of LWAs, lightweight aggregate concrete (LWAC) exhibits lower crack and tensile resistances and more brittle failure than normalweight concrete (NWC) at the same compressive strength.[4,5] Moreover, the crack propagations in LWAC typically penetrate aggregate particles, significantly reducing the aggregate interlock resistance along the crack planes.[6] Thus, different crack opening displacement and fracture responses between LWAC and NWC are expected at the same compressive strength.

The use of fibers is widely known[7-10] as one of the most effective approaches to improve the crack resistance, tensile strength, and ductility of concrete. Steel fibers have been widely applied to structural and nonstructural elements because they have superior reinforcing effects and excellent interaction with the cement matrix. They also exhibit stability with nonmetallic (synthetic and natural) fibers despite the several disadvantages of synthetic fibers (for example, poor dispersion in concrete and loss of workability of fresh concrete) compared with natural fibers.[7,11] Thus, several studies[10-18] have been conducted to examine the effect of steel fibers on enhancing the crack resistance and ductility of LWAC. However, the efficiency of steel fiber reinforcement was mostly verified in NWC. From a comprehensive review of previous studies on fiber-reinforced LWAC, Hassanpour et al.[11] pointed out that the use of steel fibers in single or hybrid forms is a reliable solution to resolve the high brittleness and low mechanical properties of LWAC. Balendran et al.[12] revealed that the effect of steel fibers on the increase in flexural strength and toughness index was more notable for LWAC than for NWC at the same compressive strength. The ductility of fiber-reinforced LWAC is mostly assessed by the flexural toughness index calculated in the load-deflection curve of beams in accordance with ASTM C1018-97.[19] However, the RILEM standard[20] and *fib* 2010 model[21] specify that flexural residual tensile strength must be used to evaluate the gradual loss of strength and minimum post-cracking performance of steel fiber-reinforced concrete (SFRC). The evaluation determines whether steel fibers can be used as a substitute for conventional reinforcement at the ultimate limit state. Because the flexural residual strength is determined from the tensile stress-crack mouth opening displacement (CMOD) curve measured in the beams subjected to three-point bending, the approach for estimating the relationship between the flexural toughness index and flexural residual tensile strength of SFRC remains vague. Moreover, further test data must be compiled to examine the effect of steel fibers on the flexural residual strength of LWAC. This is because the crack resistance of SFRC depends on several factors. These include the cement matrix characteristics, interfacial strength between the cement matrix and aggregates, and aggregate strength. Numerous fiber parameters such as dimension, shape, elastic modulus, tensile strength, bonding and chemical compatibility with the cement matrix, and fiber dosage also influence the SFRC crack resistance.

ACI Materials Journal, V. 121, No. 1, January 2024.
MS No. M-2023-001.R1, doi: 10.14359/51739203, received August 2, 2023, and reviewed under Institute publication policies.

Table 1—Details of test specimens and summary of test results

No.	Group	Specimen	Details of micro-steel fiber					f_c', MPa	ρ_c, kg/m^3	f_L, MPa	$f_L/\sqrt{f_c'}$	f_r, MPa	$f_r/\sqrt{f_c'}$	$f_{r,1}$, MPa	$f_{r,2}$, MPa	$f_{r,3}$, MPa	$f_{r,4}$, MPa	$f_{r,3}/f_{r,1}$
			Type	V_f, %	L_f, mm	S_f	β_f											
1	L	L-0	None	—	—	—	—	20.9	1212	1.32	—	1.32	0.29	—	—	—	—	—
2		L-0.25	Hooked-end	0.25	30	100	1.08	21.1	1228	1.44	0.31	3.08	0.67	2.32	2.93	2.93	2.61	1.26
3		L-0.5		0.5	30	100	2.01	24.4	1254	1.30	0.26	3.35	0.68	2.47	3.18	3.13	3.03	1.27
4		L-0.75		0.75	30	100	3.02	24.3	1268	1.96	0.40	4.94	1.00	4.59	4.72	4.28	3.81	0.93
5		L-1.0	Hooked-end + straight	0.75+0.25	30+13	100+65	3.58	25.6	1288	1.71	0.34	5.31	1.05	4.38	5.16	4.69	4.08	1.07
6		L-1.25		0.75+0.5	30+13	100+65	4.32	24.4	1315	1.79	0.54	6.42	1.30	6.14	5.95	5.39	4.72	0.88
7		L-1.5		0.75+0.75	30+13	100+65	4.87	25.5	1332	2	0.26	7.80	1.54	7.06	7.67	7.32	6.41	1.04
8	H	H-0	None	—	—	—	—	45.2	1468	1.59	—	1.59	0.24	—	—	—	—	—
9		H-0.25	Hooked-end	0.25	30	100	0.73	46.8	1481	1.84	0.23	5.31	0.78	3.10	4.25	3.82	3.51	1.23
10		H-0.5		0.5	30	100	1.41	49.7	1515	1.99	0.34	6.23	0.88	3.92	4.76	4.78	4.42	1.22
11		H-0.75		0.75	30	100	2.06	52.5	1540	2.35	0.27	6.12	0.84	4.96	5.99	5.75	5.30	1.16
12		H-1.0	Hooked-end + straight	0.75+0.25	30+13	100+65	2.43	55.7	1593	3.07	0.41	8.71	1.17	7.89	8.50	7.26	5.92	0.92
13		H-1.25		0.75+0.5	30+13	100+65	2.86	55.9	1591	3.10	0.54	9.02	1.21	8.80	8.71	8.00	6.62	0.91
14		H-1.5		0.75+0.75	30+13	100+65	3.16	60.4	1645	3.17	0.41	9.63	1.24	8.40	9.30	9.42	8.98	1.12

Note: V_f, L_f, S_f, and β_f are volume fraction, length, aspect ratio and reinforcing index of fibers, respectively; f_c', ρ_c, f_L, and f_r are measured compressive strength, density, limit strength of proportionality, and flexural strength, respectively, of concrete; and $f_{r,i}$ (i = 1, 2, 3, and 4) is flexural residual strength measured in flexural tensile stress-CMOD curve. 1 kg/m^3 = 0.062 lb/ft^3; 1 mm = 0.039 in.; 1 MPa = 145 psi.

The present study aims to assess the flexural residual tensile strengths of high-strength LWAC reinforced with copper-coated micro-steel fibers. The main test parameters were the compressive strength of concrete and volume fraction of the fibers. Three-point bending tests of beams were conducted in accordance with RILEM recommendations. The residual strengths corresponding to four different CMOD values (0.5, 1.5, 2.5, and 3.5 mm [0.02, 0.06, 0.1, and 0.14 in.]) were determined and compared with the results of empirical prediction equations,[22-24] which were formulated from regression analysis using the test data compiled from steel fiber-reinforced NWC beam specimens. In addition, refined equations were proposed to assess the flexural residual strengths of concrete beams rationally, considering different beam densities and various types of steel fiber reinforcements. The measured flexural residual strengths were analyzed as a function of fiber reinforcing index to assess the class and hardening/softening responses of fiber-reinforced concrete (FRC) beams directly in accordance with the material classification specified in *fib* 2010.[21]

RESEARCH SIGNIFICANCE

While the flexural ductility of FRC has been mostly examined by using toughness indexes obtained from the load-deflection curves of beams, very few investigations are available to understand the flexural residual strength and crack opening resistance of fiber-reinforced LWAC. The present study provides valuable data on the flexural tensile stress-CMOD relationship of high-strength LWAC reinforced with micro-steel fibers at different volume fractions. The effect of concrete unit weight on the flexural residual strengths is assessed from the comparisons with previous prediction equations formulated through the regression analysis using test data compiled from NWC beams reinforced with the conventional macro-steel fibers and FRC material classification specified in *fib* 2010. This study found that the micro-steel fibers are more effective in enhancing the flexural residual strengths of LWAC than the conventional macro-steel fibers. Overall, the present discussion indicated that the micro-steel fibers are promising as a partial replacement of the conventional steel reinforcing bars for enhancing the ductility of concrete elements.

EXPERIMENTAL DETAILS

Specimens

Twelve LWAC mixtures reinforced with copper-coated micro-steel fibers were prepared, as listed in Table 1. Two unreinforced LWAC mixtures were also prepared as control specimens. The concrete mixtures were classified into L-group and H-group according to their design compressive strengths—that is, 21 and 40 MPa (3.05 and 5.80 ksi), respectively. For each group, the volume fraction (V_f) of steel fibers varied from 0 to 1.5% at an interval of 0.25%. Hooked-end steel fibers were primarily added to the LWAC mixtures designed at a V_f value not exceeding 0.75%. In contrast, in the other mixtures, 0.75% hooked-end fibers and 0.25 to 0.75% straight fibers with no additional treatment were used to minimize the rapid workability loss of concrete due to the clumping of undispersed fibers. The specimens are identified by referring to the test parameters. Thus, the first letter and second figure indicate the group and volume fraction of fibers, respectively. For example, L-0.25 indicates an LWAC mixture with a design compressive strength of 21 MPa (3.05 ksi) and reinforced with 0.25% V_f micro-steel fibers.

Table 2—Properties of micro-steel fibers

Type	Physical properties				Mechanical properties			Dimensions and shapes
	ρ_f, g/cm^3	L_f, mm	d_f, mm	S_f	F_f, MPa	E_f, MPa	τ, MPa	
Hooked-end	7.85	30	0.3	100	2650	206,000	18.7	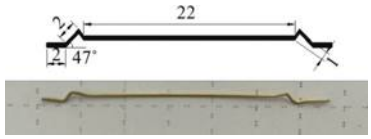
Straight		13	0.2	65			8.6	

Note: ρ_c, d_f, F_f, E_f, and τ are density, diameter, tensile strength, elastic modulus, and bond stress of fibers, respectively. 1 g/cm^3 = 62.43 lb/ft^3; 1 mm = 0.039 in.; 1 MPa = 145 psi.

Table 3—Physical properties of artificial lightweight aggregates

Classification		Maximum size, mm	Bulk density, kg/m^3	Specific gravity, kg/m^3	Water absorption, %	Fineness modulus
Coarse aggregate	Expanded clay granule	8	420	780	20.0	7.21
		13	880	1750	12.2	7.40
Fine aggregate	Expanded glass particle	1.0	340	820	21.2	1.65
	Expanded clay granule	4.75	770	1550	15.5	3.04

Note: 1 kg/m^3 = 0.0624 lb/ft^3; 1 mm = 0.039 in.

Lee et al.[25] introduced a fiber reinforcing index (β_f) to consider the effect of numerous fiber parameters comprehensively. These parameters include the dimension, shape, dosage, and bonding capacity as well as the chemical compatibility with the cement matrix with respect to the toughness and tensile resistance of concrete, as identified in the following

$$\beta_f = \sum_{i=1}^{n} g_i V_{f,i} S_{f,i}^{0.1} \sqrt{\tau_i / f_c'} \quad (1)$$

where i is the type of fiber used in each concrete mixture; g and S_f are the snubbing factor and aspect ratio of discontinuous fibers, respectively; τ is the interfacial bond strength of the fiber with the cement matrix; and f_c' is the compressive strength of concrete. The g value of the micro-steel fibers differs from that of the macro-steel fibers because of the interlocking friction between the discontinuous fibers and aggregates or cement matrix. However, no investigations assessing the dispersion and orientation of micro-steel fibers within cement matrixes with different workability have been found. Thus, this study assumes that the g value is 2.9 for all types of steel fibers according to the micromechanical models of Li et al.[26] From the properties of the micro-steel fibers summarized in Table 2, the β_f values determined for the L-group and H-group specimens are 1.08 to 4.87 and 0.73 to 3.16, respectively.

Materials

The copper-coated steel wires were cold-worked into straight or hooked-end fibers. The nominal diameter and length of the hooked-end fibers were 0.3 and 30 mm (0.012 and 1.18 in.), respectively, resulting in an aspect ratio of 100; the corresponding dimensions of the straight fibers were 0.2 and 13 mm (0.0079 and 0.51 in.), respectively, yielding an aspect ratio of 65. Note that fibers with a diameter not exceeding 0.3 mm (0.012 in.) are commonly classified as microfibers. From the results of the direct pullout tests of the fibers, the calculated bond strengths of the hooked-end and straight fibers within the cement matrix were 18.7 and 8.6 MPa (2.71 and 1.25 ksi), respectively.

Ordinary portland cement (OPC) conforming to ASTM C150/C150M Type I[27] was used as a main cementitious material for all the concrete mixtures. The artificially expanded clay granules satisfying the requirements for structural LWAs specified in ASTM C330/C330M[28] were used for lightweight coarse and fine aggregates, as summarized in Table 3. Coarse particles with a maximum size (d_a) of 8 mm (0.31 in.) and bulk density of 420 kg/m^3 (26.22 lb/ft^3) were used in the L-group mixtures, whereas coarse particles with d_a = 13 mm (0.51 in.) and bulk density of 880 kg/m^3 (54.92 lb/ft^3) were used for the H-group specimens. In addition, expanded glass particles with d_a = 1.0 mm (0.039 in.) were incorporated into lightweight fine aggregates to achieve the standard grading curves specified in ASTM C33/C33M.[29]

The LWA features a spherical shape with a slightly smooth surface texture. The artificial expansion of wet molded clay at a temperature of approximately 1300°C (2372°F) allowed the formation of porous core structures (Fig. 1(a) to (c)), causing high water absorption as well as low strength and stiffness. The expanded glass particles exhibited more-porous structures than the lightweight fine granules (Fig. 1(d)). Thus, the specific gravity of the expanded glass particles was approximately 47% lower than that of the

(a) Expanded clay granule for fine aggregate

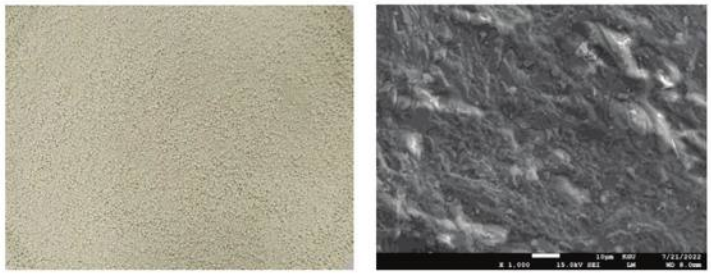

(b) Expanded glass particle

(c) Expanded clay granule for coarse aggregate (bulk density: 420 kg/m^3 [26.22 lb/ft^3])

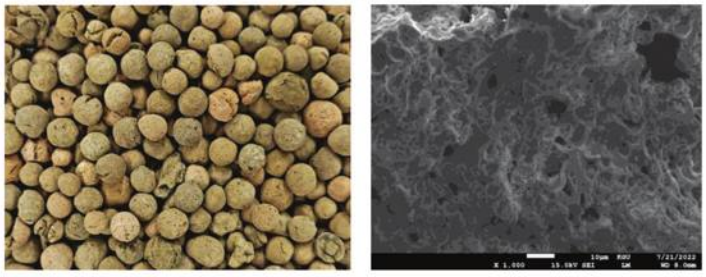

(d) Expanded clay granule for coarse aggregate (bulk density: 880 kg/m^3 [54.94 lb/ft^3])

Fig. 1—Shape and SEM images of LWAs.

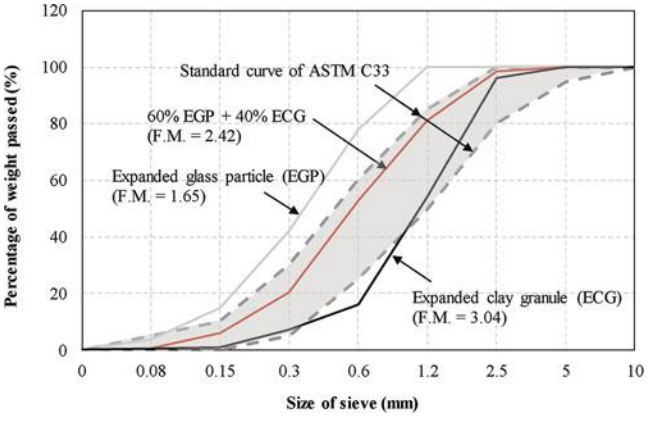

Fig. 2—Particle distribution curves of lightweight fine aggregates. (Note: 1 mm = 0.039 in.)

lightweight fine granules. The particle distribution of the lightweight fine aggregates used is plotted in Fig. 2. The standard grading curves recommended in ASTM C33 are also presented in the same figure. The lightweight fine granules exhibited discontinuous grading with no particle interference because the particles less than 1.25 mm (0.05 in.) in size were virtually undetected. This is because the expanded glass particles were incorporated into lightweight fine granules with a volumetric ratio of 60% with respect to the total volume of fine aggregates to achieve continuous grading.

Casting, curing, and testing

All the aggregates were thoroughly watered to simulate a damp state and subsequently air-dried for another 24 hours in an outdoor shade to achieve a saturated surface-dry state. The moisture content in the aggregates was measured prior

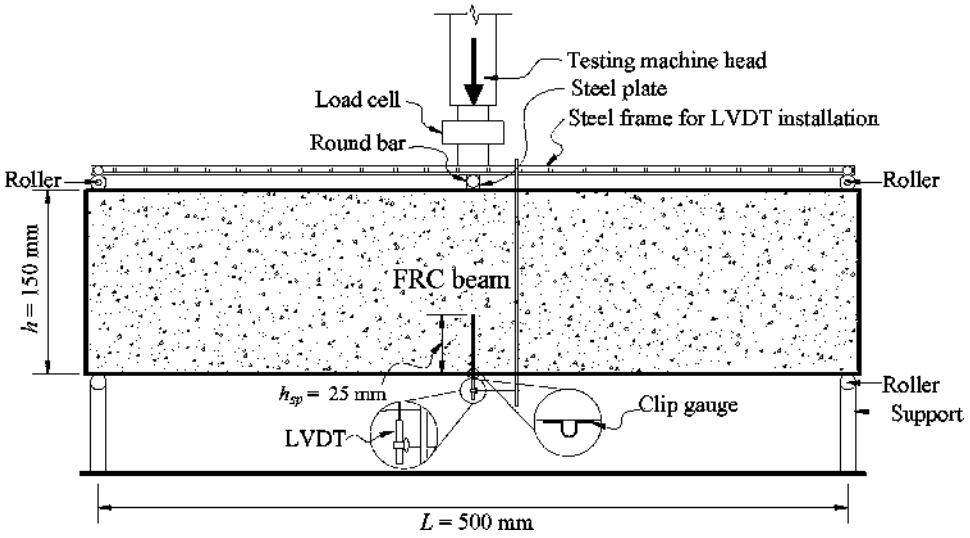

Fig. 3—Three-point bending tests for flexural stress-CMOD curve. (Note: 1 mm = 0.039 in.)

to mixing and subsequently taken into account to compensate for the net unit water content of each mixture proportion to avoid the segregation or excessive bleeding of fresh concrete. The aggregates were mixed with OPC in a 0.35 m^3 (12.36 ft^3) capacity mixer pan for 1 minute and then wet-mixed for another minute.

The initial slump and air content of fresh concrete were recorded in accordance with the testing procedures specified in ASTM C143/C143M[30] and ASTM C231,[31] respectively. Cylindrical specimens with a diameter and height of 100 and 200 mm (3.94 and 7.87 in.), respectively, were cast to measure the compressive strength and density of concrete. Beam specimens with a square section of 150 mm (5.91 in.) on each side and a length of 550 mm (21.65 in.) were also prepared to measure the flexural stress-CMOD curve. All specimens were cured at room temperature until they were tested at a specified age. The specimens were demolded at an age of 2 days after casting.

The compressive strength and density of air-dried concrete were recorded at the age of 28 days in accordance with the ASTM C39/39M[32] and C138/C138M[33] procedures, respectively. The flexural stress-CMOD curves of beams are obtained from the three-point bending tests according to RILEM TC 162-TDF,[20] as presented in Fig. 3. The beam specimens were notched at midspan by wet sawing, producing a single notch 5 mm (0.20 in.) wide and 25 mm (0.98 in.) deep, 3 days before conducting the bending tests. The beam specimens were simply supported by the steel rollers installed at a center-to-center distance of 500 mm (19.69 in.). Both end supports allow horizontal movements, minimizing any restraining forces due to the friction between the steel roller and specimens. Loading was applied at a displacement rate of 0.2 mm/min (0.0078 in./min). The applied load was recorded using a load cell fixed to the head of the testing machine. The deflection at midspan was measured using two 5 mm (0.20 in.) capacity linear variable differential transducers (LVDTs). The notch-opening mouth displacement was recorded using a 5 mm (0.20 in.) capacity clip gauge. Instead of using the overall section depth (h), the flexural stress was calculated from the moment at midspan using the h_{sp} measured from the tip of the notch to the top surface of the section. To classify the post-cracking strength of FRC, the *fib* 2010 model[21] considers the flexural residual strength values based on the assumption of linear-elastic behavior. For serviceability specifications and ultimate conditions, CMOD values of 0.5, 1.5, 2.5, and 3.5 mm (0.02, 0.06, 0.1, and 0.14 in.) were selected from the model, thereby identifying the corresponding flexural residual strengths of $f_{r,1}$, $f_{r,2}$, $f_{r,3}$, and $f_{r,4}$, respectively.

TEST RESULTS AND DISCUSSION

Crack propagation and failure characteristics

The typical crack propagation and failure characteristics of beams L-0.5, L-1.0, H-0.5, and H-1.0 at ultimate failure are shown in Fig. 4. The first flexural crack generally occurred at the tip of the notch and rapidly propagated toward the extreme layer in compression. Additional flexural or diagonal cracks were not observed in all the beams until their ultimate failure. Thus, all the beams were primarily governed by the flexural crack that occurred at the tip of the notch, exhibiting no crack distribution, regardless of the volume of steel fibers added to the present beams. The flexural cracks mostly passed through the lightweight coarse aggregate particles, thereby forming a relatively smooth failure plane. This indicates that the crack propagation in LWAC is more dependent on the strength of lightweight aggregates than that of the cement matrix. The effect of fiber content on crack penetration through the aggregate particles is negligible because the bridging action of fibers typically begins with the development of cracks. The figure also reveals the satisfactory distribution of steel fibers in the beams. No undispersed clumping of fibers was observed along the failure plane, even for specimens with V_f values exceeding 1.0%. With the increase in CMOD, the steel fibers gradually fractured or were pulled out from the cement matrix. Thus, no bridging action of steel fibers was expected across the crack at the ultimate failure of the beams.

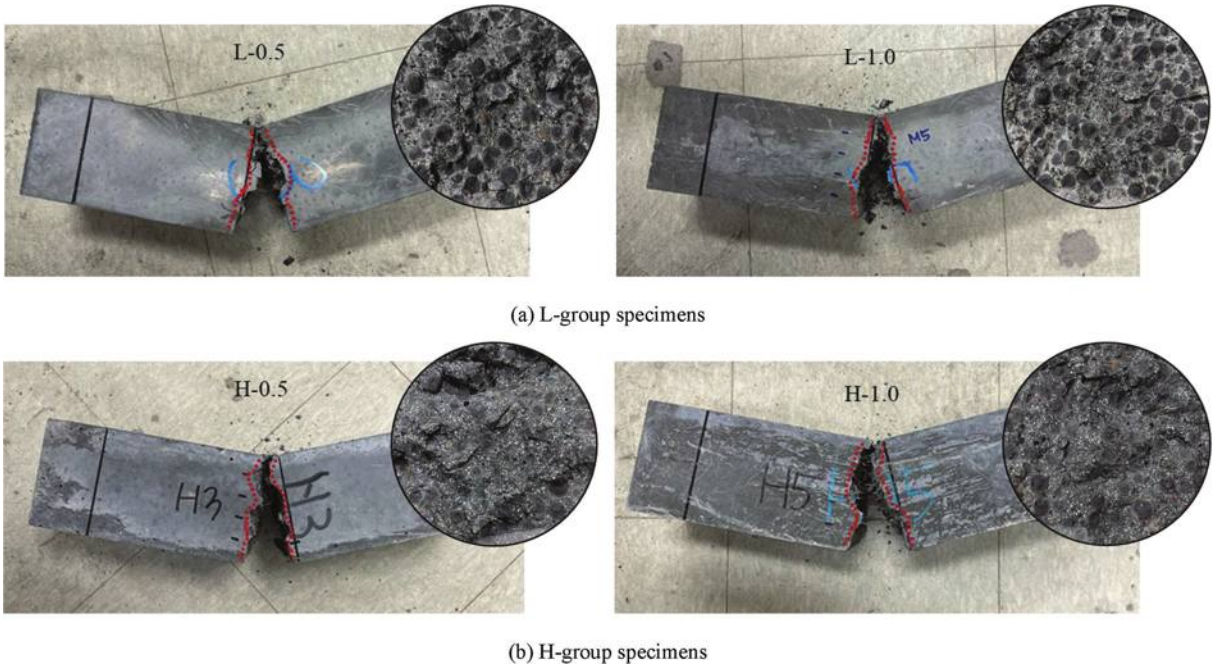

Fig. 4—Crack propagation around aggregate particles at failure plane.

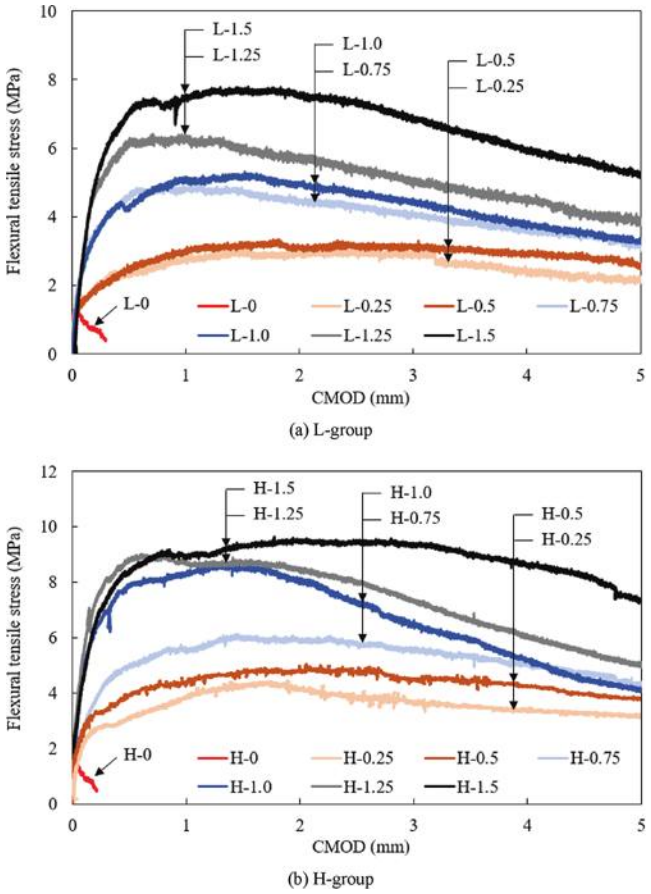

Fig. 5—Flexural tensile stress-CMOD relationship of beams. (Note: 1 MPa = 145 psi; 1 mm = 0.039 in.)

Flexural tensile stress-CMOD curve

The flexural tensile stress-CMOD curves derived for each beam specimen are shown in Fig. 5. Table 1 also summarizes the test results, including the limit strength (f_L) of proportionality, flexural strength (f_r), and flexural residual strengths ($f_{r,i}$). The value of f_L was determined based on a CMOD value of 0.05 mm (0.002 in.) in accordance with EN 14651.[34] Because all the FRC beams reached their f_r value after CMOD exceeded 0.05 mm (0.002 in.), the flexural stress corresponding to the CMOD value of 0.05 mm (0.002 in.) was selected as f_L for such beams. All fiber-reinforced beams exhibited satisfactory CMOD performance, which is typically observed among fiber-reinforced NWC beams.[22] No crack opening displacement was observed until the first flexural crack occurred; thereafter, the CMOD increased rapidly. Fiber-reinforced LWAC beams exhibited very different propagation of CMOD from the counterpart unreinforced beams. The unreinforced beams immediately failed with the occurrence of the flexural crack at the tip of the notch. Hence, CMOD was measured with very small propagation for the unreinforced specimens, indicating that no flexural residual strengths could be calculated for such beams. Meanwhile, all the reinforced beams exhibited a hardening response after the occurrence of the flexural crack. No pulling out of fibers was observed for all the beams until the CMOD value reached 1.5 to 2.0 mm (0.06 to 0.08 in.). The f_L and f_r values obtained for the H-group beams were higher than those for the L-group beams because the increase in f_c' commonly led to the improvement of tensile resistance. Meanwhile, lower $f_L/\sqrt{f_c'}$ values are obtained for H-group beams with $V_f \leq 0.75\%$, beyond which an inverse trend was observed, when compared with L-group beams. The normalized flexural strength ($f_r/\sqrt{f_c'}$) increased with V_f varying from 0.29 to 1.54 for the L-group beams and from 0.24 to 1.24 for the H-group beams. The flexural strength recommended by ACI 318-19[35] is $0.465\sqrt{f_c'}$ for fiber-less LWAC. The flexural strengths of the unreinforced LWAC beams are lower than those predicted by the ACI 318-19 equation. This might be attributed to the fact that the stress concentration around the notch that previously formed at the critical section induced

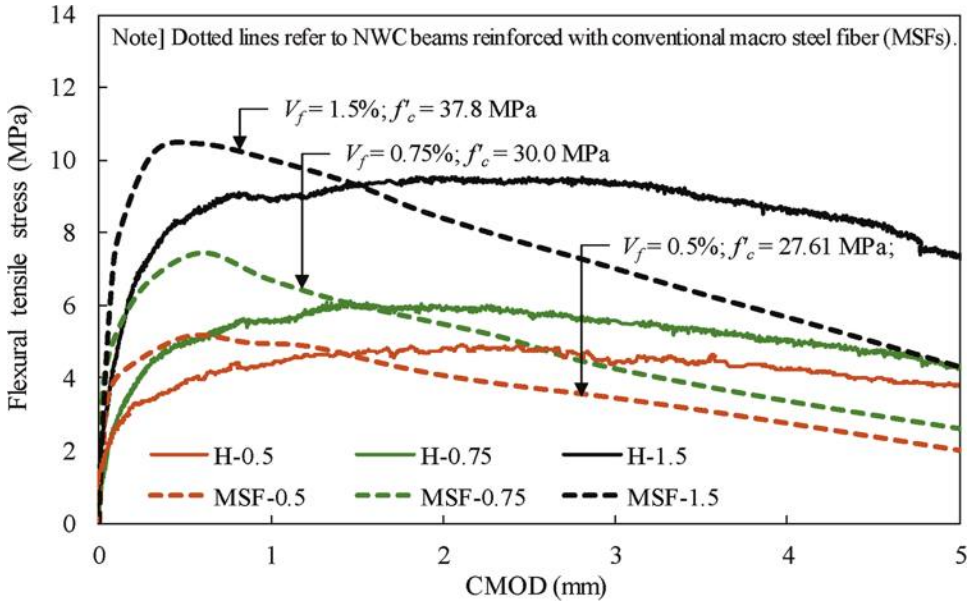

Fig. 6—Comparisons of flexural tensile stress-CMOD relationship between present LWAC beams and previous NWC beams reinforced with conventional macro-steel fibers. (Note: 1 MPa = 145 psi; 1 mm = 0.039 in.)

early crack formation at the tip of the notch, thus reducing the flexural strength of the beams.

The addition of micro-steel fibers significantly increased the f_L and f_r values of the beams. The increase rates obtained for beams L-0.25 and H-0.25 were 131% and 225%, respectively, compared with the $f_r/\sqrt{f'_c}$ value for unreinforced beams. In addition, all the beams reinforced with micro-steel fibers exhibited a typical hardening response after reaching f_L; they exhibited a gradual increase in flexural stress with CMOD. The effect of steel fiber content on the flexural tensile stress-CMOD curves was minimal up to V_f = 0.5%. The beams with V_f = 0.5% exhibited flexural tensile stress-CMOD curves that are considerably similar to those with V_f = 0.25%; this tendency was not significantly affected by f'_c. Additionally, beam specimens with $V_f \geq$ 1.0% mostly exhibited a gradual decrease in flexural stress when the CMOD values exceeded 1 to 1.5 mm (0.039 to 0.06 in.). Nevertheless, a hardening response was observed beyond the CMOD value corresponding to the proportionality limit. However, beam H-1.5 displayed a more ductile response than the other beams with $V_f \geq$ 1.0%. The micro-steel fibers under extremely high flexural tensile stress could be fractured or pulled out from the crack plane. Thus, a gradual decrease in flexural stress occurred with the increase in the CMOD of beams with $V_f \geq$ 1.0%. This resulted in lower flexural residual strengths in beams where the CMOD value was 3.5 mm (0.14 in.) than in beams whose CMOD was 1.5 mm (0.06 in.).

The present flexural tensile stress-CMOD curves are compared with the curves compiled from the previous NWC beams[36] reinforced with conventional macro-steel fibers that are 35 mm (1.38 in.) in length and with hooked ends (Fig. 6). The effect of the type of steel fibers on the slope at the ascending branch of the curves up to f_L is insignificant. As a result, considerably similar f_L values are obtained in both the NWC and LWAC beams at the same V_f. The previous NWC beams displayed a hardening response beyond the CMOD value of up to 0.6 to 0.9 mm (0.024 to 0.035 in.), corresponding to f_L. They also exhibited a higher f_r value than the present LWAC beams at the same V_f. Meanwhile, a more distinct gradual decrease in flexural stresses was observed after the peak stress of the previous NWC beams. This differs from the plastic flow tendency observed among the LWAC beams. This implies that micro-steel fibers are more favorable than conventional macro-steel fibers in restraining the crack opening because the former has better dispersion in the cement matrix than the latter. Consequently, higher residual strength values—that is, $f_{r,2}$, $f_{r,3}$, and $f_{r,4}$—are expected for the micro-SFRC than for the macro-SFRC at the same V_f.

Flexural residual strengths

Table 1 summarizes the measured values in each beam specimen. The values of $f_{r,i}$ increased in proportion to β_f. All beams yielded by approaching the values of $f_{r,2}$ and $f_{r,3}$ regardless of β_f, indicating that these values are higher than those of $f_{r,1}$ and $f_{r,4}$. For the beams with β_f less than 2.0 ($V_f \leq$ 0.5% for the L-group and $V_f \leq$ 0.75% for the H-group), the obtained $f_{r,1}$ values were lower than the other identified residual strengths of the beams with β_f exceeding 2.0; $f_{r,4}$ was lower than $f_{r,1}$. The H-group beams commonly exhibited higher $f_{r,i}$ values than the L-group beams with the same V_f because of the increase in flexural strength with f'_c. Additionally, the $f_{r,4}$ values in all the fiber-reinforced beams exceeded 1 MPa (0.145 ksi), and $f_{r,1}$ exceeded 1.5 MPa (0.218 ksi). Thus, the minimum V_f of micro-steel fibers must be limited to 0.25% for LWAC with the design compressive strength not exceeding 40 MPa (5.80 ksi) to achieve the minimum residual strengths recommended in RILEM TC 162-TDF.[20]

Each flexural residual strength ($f_{r,i}$) normalized by f_L as a function of β_f is presented in Fig. 7. All the fiber-reinforced beams yielded $f_{r,i}$ values higher than f_L values because a rapid drop in flexural stress was not observed even after the peak stress was attained. The values of $f_{r,i}/f_L$ tended to increase with β_f, although beams H-1.0 and H-1.25 exhibited

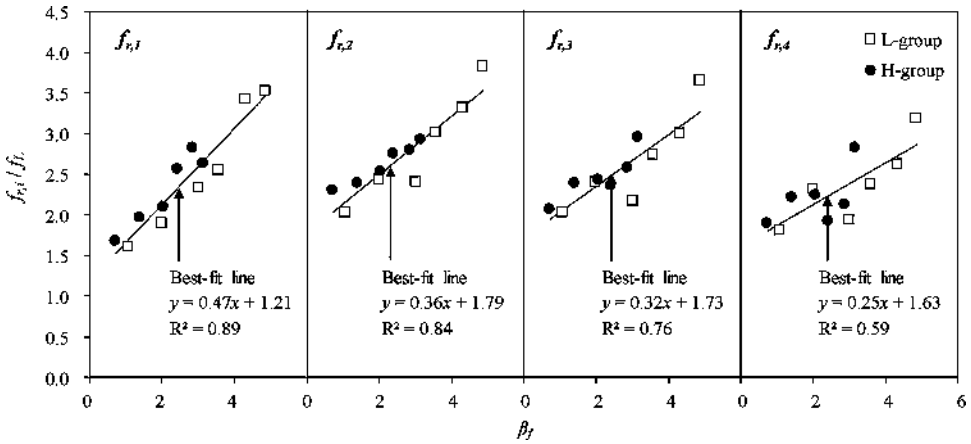

Fig. 7—Normalized flexural residual strengths as function of β_f.

Table 4—Summary of previous equations for flexural residual strengths

Researcher	Equations	Schematic generalization of flexural stress-CMOD relationships of FRC
Venkateshwaran et al.[22]	$f_{r,i} = (1 + L_f/100)^{0.5}\{A_1(f_c')^{0.5} + B_1(V_f S_f) + C_1 N^2\}$ For i = 1, 2, 3, and 4, A_1 = 0.32, 0.353, 0.3, and 0.284; B_1 = 6.214, 7.337, 7.629, and 7.018; C_1 = 0.034, 0.3, 0.373, and 0.343, respectively.	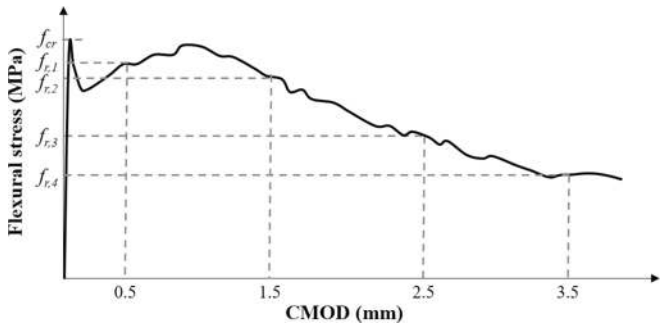
Carrillo et al.[23]	$f_{r,i} = \frac{1}{A_2}(V_f S_f + N^3) \cdot \sqrt{F_f f_c'}$ For i = 1, 2, 3, and 4, A_2 = 2000, 1800, 1900, and 2100, respectively.	
Gondokusumo et al.[24]	$f_{r,i} = (f_c')^{A_3}(V_f S_f)^{B_3}\{0.4 + (0.6\rho_c/2200)\}^{C_3}$ For i = 1, 2, 3, and 4, A_3 = 0.6, 0.645, 0.636, and 0.613; B_3 = 0.558, 0.507, 0.507, and 0.492; C_3 = 4.78, 5.944, 5.944, and 6.185, respectively.	

*For present fiber-reinforced beams, f_L was determined at CMOD value of 0.05 mm (0.002 in.) in accordance with EN 14651.

Note: N is number of hooked ends in steel fiber.

lower $f_{r,4}/f_L$ values than beam H-0.75 because of the gradual decrease in flexural stress after reaching the peak. Consequently, β_f can be considered a critical factor in determining the magnitude of the flexural residual strengths of FRC beams, as presented in the best-fit line of the test data shown in Fig. 7.

COMPARISONS WITH PREDICTION MODELS

Venkateshwaran et al.[22] and Carrillo et al.[23] proposed empirical equations derived by regression analysis using test data mainly obtained from NWC beams reinforced with conventional macro-steel fibers. Gondokusumo et al.[24] also proposed empirical equations introducing the reduction factor to account for the reduced tensile resistance of LWAC. Table 4 summarizes these equations for directly determining $f_{r,i}$. The ratios (γ_s) of predicted flexural residual strengths to experimental results with respect to the variation of β_f are shown in Fig. 8. The mean ($\gamma_{s,m}$) and standard deviation ($\gamma_{s,s}$) of the ratios are also given in the figure. The empirical equations derived by Venkateshwaran et al. exhibited a relatively large scatter in predicting the $f_{r,i}$ values of the present beams. An overestimation of the strengths is obtained for beams with $\beta_f \leq 3.6$; this overestimation is independent of f_c'. The $\gamma_{s,m}$ values determined from the equation of Venkateshwaran et al. are 1.30, 1.33, 1.37, and 1.43 for $f_{r,1}$, $f_{r,2}$, $f_{r,3}$, and $f_{r,4}$, respectively; the corresponding values of $\gamma_{s,s}$ are 0.43, 0.37, 0.38, and 0.36, respectively. The predictions obtained using the equation from Carrillo et al. are similar to those estimated using the equation of Venkateshwaran et al. because both equations have been formulated using virtually the same data sets. The $\gamma_{s,m}$ values determined using the equation from Carrillo et al. are 1.19, 1.14, 1.13, and 1.16 for $f_{r,1}$, $f_{r,2}$, $f_{r,3}$, and $f_{r,4}$, respectively; the corresponding values of $\gamma_{s,s}$ are 0.40, 0.33, 0.32, and 0.30, respectively. Although the equation from Carrillo et al. yields lower $\gamma_{s,m}$ values than those computed by the equation from Venkateshwaran et al., a wide scatter is still observed. The equation from Gondokusumo et al. considerably underestimated $f_{r,i}$, although a reduction factor for LWAC was introduced. The underestimation is more notable for the L-group beams than for the H-group beams. The values of $\gamma_{s,m}$ determined by the equation from Gondokusumo et al. are 0.42, 0.34, 0.34, and 0.34 for $f_{r,1}$, $f_{r,2}$, $f_{r,3}$, and $f_{r,4}$, respectively; the corresponding values of $\gamma_{s,s}$ are 0.16, 0.13, 0.13, and 0.13, respectively.

Proposed refined equations

Previous empirical equations commonly considered the volume fraction and aspect ratio of fibers, number of hooked ends in the fibers, and compressive strength of concrete in formulating $f_{r,i}$ (Table 1). In addition, the equations are inconsistent in assessing the $f_{r,i}$ values of LWAC beams reinforced with micro-steel fibers. This study implemented

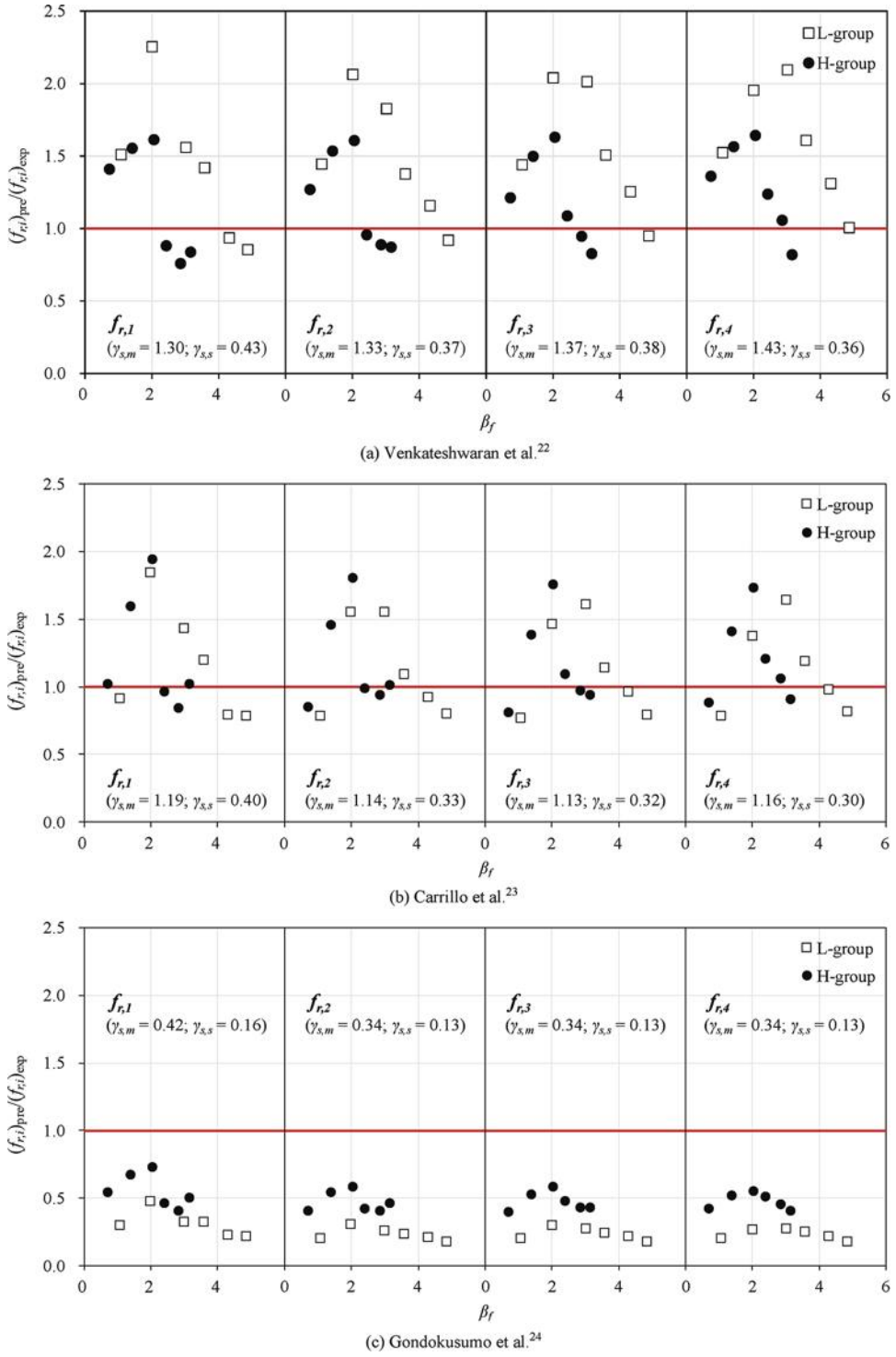

Fig. 8—Comparisons between experimental flexural residual strengths and predictions.

nonlinear regression analysis using the test data, database established by Carrillo et al., and test data used by Gondokusumo et al. The main parameter ranges in the data sets using the present regression analysis are as follows. For f_c', ρ_c, V_f, β_f, and S_f, the ranges are 21.3 to 89.7 MPa (3.09 to 13.01 ksi), 1398 to 2397 kg/m^3 (87.27 to 149.64 lb/ft^3), 0.24 to 1.5%, 0.38 to 4.40, and 44 to 100, respectively. The present study considers f_c', β_f, ρ_c, and the type of steel fiber as the primary influencing factors in establishing the fundamental model for $f_{r,i}$. Each parameter was combined and tuned repeatedly through trial and error using a statistical program until a relatively high correlation coefficient (R^2) was obtained. Based on the regression analysis, $f_{r,i}$ can be expressed in the following form (Fig. 9)

$$f_{r,i} = f_c'^{0.75}\left[a_1 \ln\left\{\left(\frac{\rho_c}{\rho_0}\right)^{1.2}\beta_f^{1.8}\right\} + b_1\right] \quad (2)$$

for i = 1, 2, 3, and 4, a_1 = 0.114, 0.118, 0.105, and 0.093, respectively; and b_1 = 0.22, 0.25, 0.24, and 0.22, respectively; where ρ_0 = 2300 kg/m^3 (143.58 lb/ft^3) is the reference value for concrete density. In comparing the test data, the

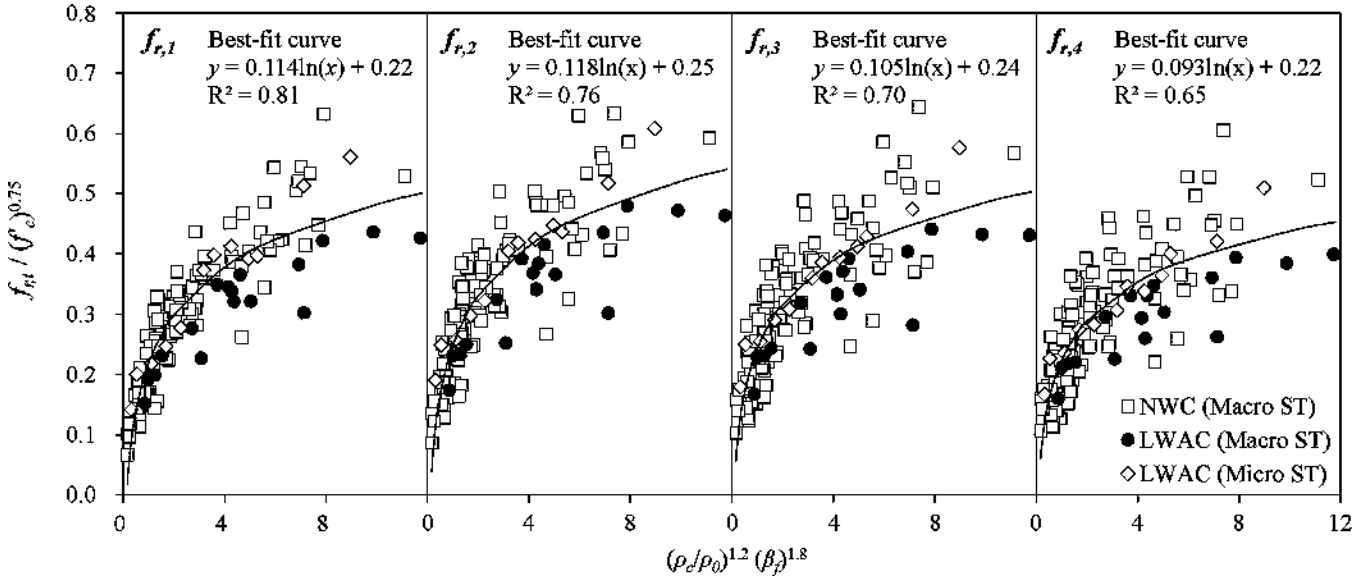

Fig. 9—Refined models for flexural residual strengths.

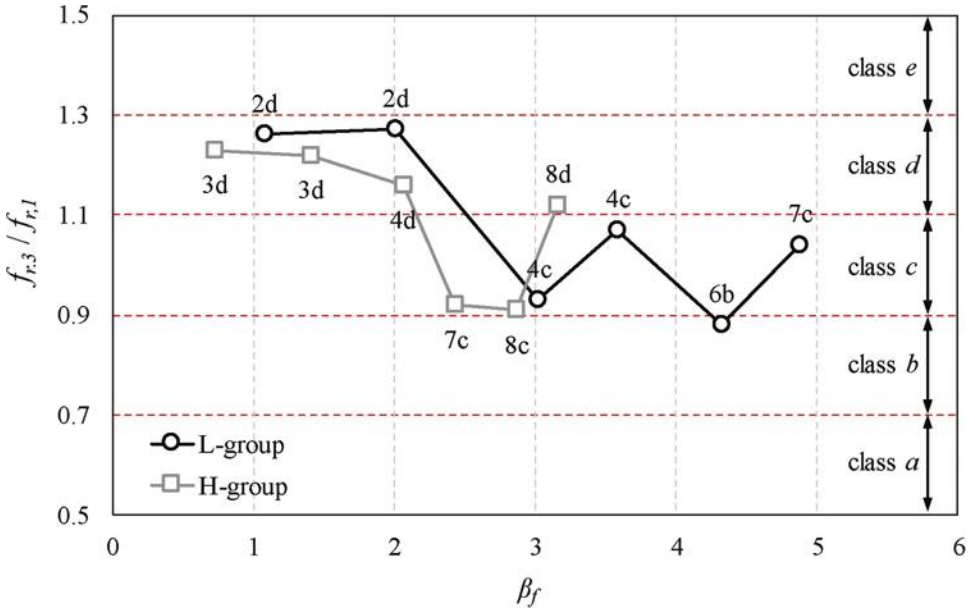

Fig. 10—Classification of measured flexural residual strengths in accordance with fib *2010.*

proposed refined equations yield $\gamma_{s,m}$ values of 1.03, 1.02, 1.01, and 1.01 as well as $\gamma_{s,s}$ values of 0.33, 0.25, 0.24, and 0.25 for $f_{r,1}$, $f_{r,2}$, $f_{r,3}$, and $f_{r,4}$, respectively. Hence, the refined equation permits a simpler application and higher accuracy in predicting the flexural residual strengths of concrete beams with different densities and reinforced with different types of steel fibers.

DESIGN CLASSIFICATION OF *fib* 2010

For the structural application of FRC, *fib* 2010[21] categorizes the flexural residual strength of FRC beams obtained by three-point loading into five classes. It considers the ratios of the characteristic $f_{r,1}$ values (representing serviceability) to the characteristic $f_{r,3}$ values (representing the ultimate condition). The FRC beams tested are classified using the measured flexural residual strengths in accordance with *fib* 2010 (Fig. 10). In the same figure, the $f_{r,1}$ value is written in front of the class name of each beam specimen. The beam specimens can be classified as a function of β_f. The beams with β_f not exceeding 2.0 ($V_f \leq 0.75\%$ for the present beams) commonly belong to class *d* and exhibit $f_{r,1}$ values less than 5 MPa (0.73 ksi); the other beams mainly belong to class *c*. For the beams in class *c*, $f_{r,1}$ varies from 4.4 to 7.0 MPa (0.64 to 1.02 ksi) for the L-group and from 7.9 to 8.8 MPa (1.14 to 1.28 ksi) for the H-group. This indicates that higher steel fiber contents can yield higher $f_{r,1}$ values, which may result in lower $f_{r,3}/f_{r,1}$ values. The foregoing may be attributed to the fact that steel fibers with high flexural stresses across the crack plane tend to fracture and pullout, resulting in a decrease in the transferring stresses caused by the bridging effect of fibers. Additionally, slightly higher $f_{r,3}/f_{r,1}$ values are typically obtained for the L-group beams than for the H-group beams at the same β_f level. This implies that the decrease in flexural stress after reaching the peak strength

tends to be more distinct with the increase in f_c' at the same β_f level.

As recommended by *fib* 2010, conventional reinforcing bars can be fully or partially replaced by fiber reinforcement at the ultimate limit state if $f_{r,1}/f_L > 0.4$ and $f_{r,3}/f_{r,1} > 0.5$. As indicated in Fig. 10, $f_{r,3}/f_{r,1}$ values exceeding 0.9 are obtained for all the fiber-reinforced beams. Moreover, $f_{r,1}/f_L$ values are in ranges 1.61 to 3.53 and 1.69 to 2.65 for the L-group and H-group beams, respectively. This leads to the conclusion that micro-steel fibers are a potential partial replacement for conventional steel reinforcing bars for enhancing the ductility of concrete elements regardless of the type of concrete.

CONCLUSIONS

The present study examined the flexural residual strengths of lightweight aggregate concrete (LWAC) beams reinforced with micro-steel fibers. The experimental flexural strengths were also compared with the predictions of previous design equations and material classifications specified in *fib* 2010 for fiber-reinforced concrete (FRC). Fourteen beam specimens were classified according to the compressive strength (f_c') of concrete: L-groups (design strength: 21 MPa [3.05 ksi]) and H-groups (design strength: 40 MPa [5.80 ksi]). The volume fraction (V_f) of micro-steel fibers varied from 0 to 1.5% in each beam group. The flexural residual strengths were identified as $f_{r,1}$, $f_{r,2}$, $f_{r,3}$, and $f_{r,1}$ with respect to the crack mouth opening displacement (CMOD) values of 0.5, 1.5, 2.5, and 3.5 mm (0.02, 0.06, 0.1, and 0.14 in.), respectively; then, they were discussed as a function of the fiber reinforcing index (β_f).

On the other hand, further explorations are required for reliable application of fiber-reinforced LWAC with different classes of toughness: 1) the determination of the optimal volume fraction of micro-steel fibers for LWAC with different compressive strengths and toughness capacities; 2) the effect of other types of fibers combined with micro-steel fibers on the flexural stress-CMOD relationship; 3) the effect of micro-steel fibers on the inelastic response of LWAC with different compressive strengths; 4) numerical modeling and analysis to simulate and predict the response of LWAC elements with micro-steel fibers under various loading conditions; 5) various design equations for mechanical properties of LWAC reinforced with different types and volume fractions of fibers; and 6) assessment of the environmental impact of using micro-steel fibers in LWAC and comparisons with conventional reinforcing steel bars and other reinforcing materials.

Based on the experimental program and relevant comparisons, the following conclusions are drawn:

1. All the beams are primarily governed by the flexural crack that occurs at the tip of the notch and passes through the lightweight aggregate particles.

2. The effect of steel fiber content on the flexural tensile stress-CMOD curves is minimal up to $V_f = 0.5\%$, showing a typical hardening response.

3. The effect of the type of steel fibers on the slope at the ascending branch of the curves up to f_L is insignificant. However, a more distinct gradual decrease in flexural stress is observed after reaching the peak stress of the previous normalweight concrete (NWC) beams reinforced using conventional macro-steel fibers. Hence, higher residual strengths of $f_{r,2}$, $f_{r,3}$, and $f_{r,4}$ are expected for micro-steel-FRC (SFRC) than for macro-SFRC at the same V_f.

4. All fiber-reinforced beams possess $f_{r,4}$ and $f_{r,1}$ values exceeding 1 and 1.5 MPa (0.145 and 0.218 ksi), respectively. Thus, the minimum V_f of micro-steel fibers must be limited to 0.25% to achieve the minimum residual strengths recommended in RILEM TC 162-TDF.

5. The empirical equations derived by Venkateshwaran et al. and Carrillo et al. tend to overestimate the $f_{r,i}$ value of the LWAC beams reinforced with micro-steel fibers. The equation by Gondokusumo et al. considerably underestimates $f_{r,i}$. These equations exhibit a relatively large inaccuracy in predicting $f_{r,i}$ of LWAC beams reinforced with micro-steel fibers.

6. The refined equations proposed as functions of f_c', β_f, and ρ_c reasonably assess the flexural residual strengths of concrete beams with different densities and reinforced with different types of steel fibers.

7. The comparison of results with the *fib* 2010 recommendations indicates that micro-steel fibers are a promising partial replacement for conventional steel reinforcing bars for enhancing the ductility of concrete elements regardless of the type of concrete.

AUTHOR BIOS

Hak-Young Kim *is a Vice-President, Korea Disaster Prevention Safety Technology Co., Ltd, South Korea. He received his BS, MS, and PhD in architectural engineering from Dankook University, Seoul, South Korea, in 2004, 2009, and 2015. His research interests include the development of design models of sustainable concrete using various recycling materials.*

ACI member **Keun-Hyeok Yang** *is a Professor at Kyonggi University, Suwon, South Korea. He received his BS, MS, and PhD in architectural engineering from Chung-Ang University, Seoul, South Korea, in 1995, 1999, and 2002. His research interests include the development of sustainable concrete materials and structural technology.*

Hye-Jin Lee *is a Doctoral Student at Kyonggi University, where she received her MS in architectural engineering in 2018. Her research interests include examining the mechanical properties of lightweight aggregate concrete.*

ACI member **Seung-Jun Kwon** *is a Professor at Hannam University, Daejeon, South Korea. His research interests include modeling of microstructures and deterioration analysis in cement composites using neural network algorithms, and strengthening techniques for concrete structures.*

ACI member **Xiao-Yong Wang** *is a Professor in the Department of Architectural Engineering at Kangwon National University, Chuncheon, South Korea. His research interests include modeling the performance of structural concrete, technology to improve the performance of concrete, and the structural performance of steel-concrete composite structures.*

ACKNOWLEDGMENTS

This work was supported by a grant from the Korea Agency for Infrastructure Technology Advancement (KAIA) funded by the Ministry of Land, Infrastructure and Transport (Grant 22NANO-C156177-03) and from the National Research Foundation of Korea (NRF) funded by the Korea government (MSIT) (No. NRF-2018R1A5A1025137).

NOTATION

d_a = maximum size of aggregates
d_f = diameter of fibers
E_f = elastic modulus of fibers
F_f = tensile strength of fibers

f_c' = measured compressive strength of concrete
f_L = limit strength of proportionality under flexure
f_r = flexural strength of concrete
$f_{r,i}$ = (i = 1, 2, 3, and 4) flexural residual strength
g = snubbing factor of discontinuous fibers
h = overall section depth
h_{sp} = depth measured from tip of notch to top surface of section
i = type of fiber used in concrete
L_f = length of fibers
S_f = aspect ratio of fibers
V_f = volume fraction of fibers
β_f = fiber reinforcing index
γ_s = ratios of predicted flexural residual strengths to experimental results
$\gamma_{s,m}$ = mean of γ_s
$\gamma_{s,s}$ = standard deviation of γ_s
ρ_0 = reference value for concrete density (=2300 kg/m^3 [143.58 lb/ft^3])
ρ_c = density of concrete
ρ_f = density of fibers
τ = interfacial bond strength of fiber with cement matrix

REFERENCES

1. ACI Committee 211, "Standard Practice for Selecting Proportions for Structural Lightweight Concrete (ACI 211.2-98)," American Concrete Institute, Farmington Hills, MI, 1998, 18 pp.

2. ACI Committee 213, "Guide for Structural Lightweight-Aggregate Concrete (ACI 213R-03)," American Concrete Institute, Farmington Hills, MI, 2003, 38 pp.

3. Gesoğlu, M.; Güneyisi, E.; Özturan, T.; Öz, H. O.; and Asaad, D. S., "Self-Consolidating Characteristics of Concrete Composites Including Rounded Fine and Coarse Fly Ash Lightweight Aggregates," *Composites Part B: Engineering*, V. 60, 2014, pp. 757-763. doi: 10.1016/j.compositesb.2014.01.008

4. Neville, A. M., *Properties of Concrete*, fifth edition, Pearson Education Limited, Harlow, UK, 2018.

5. Lee, K. H.; Yang, K. H.; Mun, J. H.; and Kwon, S. J., "Mechanical Properties of Concrete Made from Different Expanded Lightweight Aggregates," *ACI Materials Journal*, V. 116, No. 2, Mar. 2019, pp. 9-19. doi: 10.14359/51712265

6. Sim, J. I.; Yang, K. H.; Lee, E. T.; and Yi, S. T., "Effect of Aggregate and Specimen Sizes on Lightweight Concrete Fracture Energy," *Journal of Materials in Civil Engineering*, ASCE, V. 26, No. 5, 2014, pp. 845-854. doi: 10.1061/(ASCE)MT.1943-5533.0000884

7. Xie, C.; Cao, M.; Khan, M.; Yin, H.; and Guan, J., "Review on Different Testing Methods and Factors Affecting Fracture Properties of Fiber Reinforced Cementitious Composites," *Construction and Building Materials*, V. 273, 2021, pp. 1-27. doi: 10.1016/j.conbuildmat.2020.121766

8. Fu, C.; Ye, H.; Wang, K.; Zhu, K.; and He, C., "Evolution of Mechanical Properties of Steel Fiber-Reinforced Rubberized Concrete (FR-RC)," *Composites Part B: Engineering*, V. 160, 2019, pp. 158-166. doi: 10.1016/j.compositesb.2018.10.045

9. Lantsoght, E. O. L., "How Do Steel Fibers Improve the Shear Capacity of Reinforced Concrete Beams Without Stirrups?" *Composites Part B: Engineering*, V. 175, 2019, p. 107079. doi: 10.1016/j.compositesb.2019.107079

10. Chen, B., and Liu, J. Y., "Contribution of Hybrid Fibers on the Properties of the High-Strength Lightweight Concrete Having Good Workability," *Cement and Concrete Research*, V. 35, No. 5, 2005, pp. 913-917. doi: 10.1016/j.cemconres.2004.07.035

11. Hassanpour, M.; Shafigh, P.; and Mahmud, H. B., "Lightweight Aggregate Concrete Fiber Reinforcement—A Review," *Construction and Building Materials*, V. 37, 2012, pp. 452-461. doi: 10.1016/j.conbuildmat.2012.07.071

12. Balendran, R. V.; Zhou, F. P.; Nadeem, A.; and Leung, A. Y. T., "Influence of Steel Fibres on Strength and Ductility of Normal and Lightweight High Strength Concrete," *Building and Environment*, V. 37, No. 12, 2002, pp. 1361-1367. doi: 10.1016/S0360-1323(01)00109-3

13. Liu, X.; Wu, T.; and Liu, Y., "Stress–Strain Relationship for Plain and Fibre-Reinforced Lightweight Aggregate Concrete," *Construction and Building Materials*, V. 225, 2019, pp. 256-272. doi: 10.1016/j.conbuildmat.2019.07.135

14. Okeh, C. A. O.; Begg, D. W.; Barnett, S. J.; and Nanos, N., "Behaviour of Hybrid Steel Fibre Reinforced Self Compacting Concrete Using Innovative Hooked-End Steel Fibres Under Tensile Stress," *Construction and Building Materials*, V. 202, 2019, pp. 753-761. doi: 10.1016/j.conbuildmat.2018.12.067

15. Ye, Y.; Liu, J.; Zhang, Z.; Wang, Z.; and Peng, Q., "Experimental Study of High-Strength Steel Fiber Lightweight Aggregate Concrete on Mechanical Properties and Toughness Index," *Advances in Materials Science and Engineering*, V. 2020, 2020, pp. 1-10. doi: 10.1155/2020/5915034

16. Li, J. J.; Wan, C. J.; Niu, J. G.; Wu, L. F.; and Wu, Y. C., "Investigation on Flexural Toughness Evaluation Method of Steel Fiber Reinforced Lightweight Aggregate Concrete," *Construction and Building Materials*, V. 131, 2017, pp. 449-458. doi: 10.1016/j.conbuildmat.2016.11.101

17. Nahhab, A. H., and Ketab, A. K., "Influence of Content and Maximum Size of Light Expanded Clay Aggregate on the Fresh, Strength, and Durability Properties of Self-Compacting Lightweight Concrete Reinforced with Micro Steel Fibers," *Construction and Building Materials*, V. 233, 2020, pp. 1-14. doi: 10.1016/j.conbuildmat.2019.117922

18. Turk, K.; Bassurucu, M.; and Bitkin, R. E., "Workability, Strength, and Flexural Toughness Properties of Hybrid Steel Fiber Reinforced SCC with High-Volume Fiber," *Construction and Building Materials*, V. 266, 2021, pp. 1-13. doi: 10.1016/j.conbuildmat.2020.120944

19. ASTM C1018-97, "Standard Test Method for Flexural Toughness and First-Crack Strength of Fiber-Reinforced Concrete (Using Beam With Third-Point Loading) (Withdrawn 2006)," ASTM International, West Conshohocken, PA, 1997.

20. RILEM TC 162-TDF, "Test and Design Methods for Steel Fiber Reinforced Concrete Final Recommendation," *Materials and Structures*, V. 36, No. 262, 2003, pp. 560-567. doi: 10.1617/14007

21. *fib*, "*fib* Model Code for Concrete Structures 2010," International Federation for Structural Concrete, Lausanne, Switzerland, 2013, 434 pp.

22. Venkateshwaran, A.; Tan, K. H.; and Li, Y., "Residual Flexural Strengths of Steel Fiber Reinforced Concrete with Multiple Hooked-End Fibers," *Structural Concrete*, V. 19, No. 2, 2018, pp. 352-365. doi: 10.1002/suco.201700030

23. Carrillo, J.; Vargas, J. D.; and Alcocer, S. M., "Model for Estimating the Flexural Performance of Concrete Reinforced with Hooked End Steel Fibers Using Three-Point Bending Tests," *Structural Concrete*, V. 22, No. 3, 2021, pp. 1760-1783. doi: 10.1002/suco.202000432

24. Gondokusumo, G. S.; Venkateshwaran, A.; Tan, K. H.; and Liew, J. Y. R., "Unified Equations to Predict Residual Flexural Tensile Strength of Lightweight Steel Fiber-Reinforced Concrete," *Structural Concrete*, V. 22, No. 4, 2021, pp. 2202-2222. doi: 10.1002/suco.202100172

25. Lee, H. J.; Kim, H. Y.; and Yang, K. H., "Toughness Evaluation Model of Steel Fiber-Reinforced Lightweight Aggregate Concrete," *Journal of the Korean Recycled Construction Resources*, V. 17, No. 6, 2022, pp. 215-216.

26. Li, V.; Mihashi, H.; Wu, H. C.; and Alwan, J., "Micromechanical Models of Mechanical Response of PFRCC High Performance Fiber Reinforced Cementitious Composites," *RILEM Proceedings*, V. 3, 1996, pp. 43-100.

27. ASTM C150/C150M-22, "Standard Specification for Portland Cement," ASTM International, West Conshohocken, PA, 2022, 9 pp.

28. ASTM C330/C330M-14, "Standard Specification for Lightweight Aggregates for Structural Concrete," ASTM International, West Conshohocken, PA, 2014, 4 pp.

29. ASTM C33/C33M-18, "Standard Specification for Concrete Aggregates," ASTM International, West Conshohocken, PA, 2018, 8 pp.

30. ASTM C143/C143M-15, "Standard Test Method for Slump of Hydraulic-Cement Concrete," ASTM International, West Conshohocken, PA, 2015, 4 pp.

31. ASTM C231/C231M-10, "Standard Test Method for Air Content of Freshly Mixed Concrete by the Pressure Method," ASTM International, West Conshohocken, PA, 2010, 10 PP.

32. ASTM C39/C39M-21, "Standard Test Method for Compressive Strength of Cylindrical Concrete Specimens," ASTM International, West Conshohocken, PA, 2021, 8 pp.

33. ASTM C138/C138M-23, "Standard Test Method for Density (Unit Weight), Yield, and Air Content (Gravimetric) of Concrete," ASTM International, West Conshohocken, PA, 2023, 6 pp.

34. EN 14651:2005, "Test Method for Metallic Fibered Concrete-Measuring the Flexural Tensile Strength (Limit of Proportionality (LOP), Residual)," European Committee for Standardization, Brussels, Belgium, 2005.

35. ACI Committee 318, "Building Code Requirements for Structural Concrete (ACI 318-19) and Commentary (ACI 318R-19) (Reapproved 2022)," American Concrete Institute, Farmington Hills, MI, 2019, 624 pp.

36. Christidis, K. I.; Badogiannis, E. G.; and Mintzoli, C., "Flexural Behaviour of Pumice Lightweight Concrete Reinforced with End-Hooked Steel Fibres," *Structures*, V. 33, 2021, pp. 3835-3847. doi: 10.1016/j.istruc.2021.06.090

ACI MATERIALS JOURNAL TECHNICAL PAPER

Title No. 121-M09

Evaluation of AASHTO T 397: Standard Method of Test for Uniaxial Tensile Response of Ultra-High-Performance Concrete

by Sahith Gali and Sri Sritharan

Ultra-high-performance concrete (UHPC) is a cementitious concrete material known for its sustained post-cracking tensile performance. Various specimen geometries and different test approaches have been used to establish the tensile characteristics of UHPC. Intending to standardize a direct tension test method, this paper independently evaluates a procedure developed by the Federal Highway Administration (FHWA), which has been adopted into AASHTO T 397. To verify the reliability and repeatability of the test method, 216 tensile specimens were cast from three different UHPC types with fiber-volume fractions of 1, 2, and 3% and tested at six laboratories. The measured responses were characterized for different phases of the tensile behavior and analyzed to understand the scatter in the test data. It was found that testing can be executed with a 60 to 70% success rate with carefully prepared samples and some modifications to the proposed test method. The test results show an increase in both the tensile strength and multicracking phase with an increase in fiber-volume fraction, but the crack straining phase depends primarily on the type of UHPC. Using the test data, average and characteristic tensile responses were established, which are intended, respectively, for analysis and design purposes.

Keywords: AASHTO T 397; direct tensile test; fiber volume; multicracking; tensile behavior; ultra-high-performance concrete (UHPC).

INTRODUCTION

Ultra-high-performance concrete (UHPC) is a concrete material comprising purposefully graded fine particles and includes fibers in the composition. UHPC is a cementitious composite that can attain high strength, desired durability, ductility, and toughness.[1-5] The addition of fibers provides tensile ductility and improved fracture energy to UHPC.[6-11] Determining the material's mechanical properties is fundamental for designing and analyzing structural members with that material. Previous studies show that UHPC exhibits better mechanical characteristics than conventional and fiber-reinforced concretes.[1,2,12,13] The tensile characteristic of UHPC is an essential but challenging property to determine and quantify in the laboratory, as with any cementitious material.

According to Wille et al.,[14] the tensile response of UHPC can be divided into three phases: elastic, strain hardening, and crack-based softening. Simple tests such as bending and wedge splitting require high computational work to back-calculate the tensile response and identify these three phases.[11,15-17] In contrast, direct tensile tests without much computational effort can provide the tensile response comprising of elastic, strain-hardening, and softening phases.

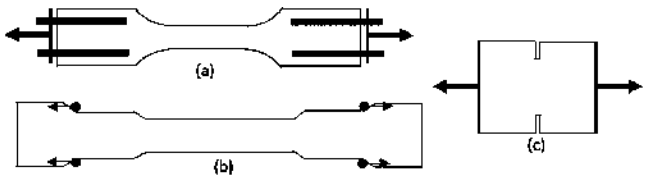

Fig. 1—Schematic view of direct tensile test setups of: (a) dog-bone unit with fixed ends[27]; (b) dog-bone unit with pinned ends[8]; and (c) notched specimens with glued ends.[20]

However, direct tensile tests are difficult to perform as the crack formation unevenly distributes stresses across the test sample's cross section, producing an unstable response. Several aspects affect the direct tensile tests, and important factors include specimen shape and boundary conditions of the specimen at the gripping.[14,18] From the literature, specimen shapes used for direct tensile tests can be classified into dog-bone shapes, notched prisms, and unnotched prisms.

Unnotched tests allow capturing the initial elastic response and strain-hardening response, but they are highly sensitive to the support conditions.[19] In comparison, notched tests capture softening responses and do not allow the development of multiple cracking.[20] In the past, a variety of dog-bone specimens were tested to capture the tensile response[8,19-26] (examples are shown in Fig. 1(a) and (b)). Furthermore, a test developed by the Federal Highway Administration (FHWA)[6] also successfully captured the response, which uses prisms with a 2 x 2 in. (50.8 x 50.8 mm) cross section with enhanced end regions by attaching thin aluminum plates. The ease of preparation of samples due to the square cross section along the length makes this test method appealing. Another important aspect of direct tensile testing is the type of boundary condition used. Different gripping systems have been used, including fixed-end[27] (shown in Fig. 1(a)), pinned-end[8] (shown in Fig. 1(b)), and glued-end systems[14,20,28] (shown in Fig. 1(c)). Pinned-end systems allow for easy specimen alignment and uniform stress before cracking but do not allow even crack opening due to the possible rotation at the end after the initial cracking, resulting in inaccurate post-cracking behavior.[8,21] Glued-end systems with the specimen's top and bottom ends glued onto

ACI Materials Journal, V. 121, No. 1, January 2024.
MS No. M-2023-010.R2, doi: 10.14359/51739204, received July 31, 2023, and reviewed under Institute publication policies.

the loading frame frequently have local stress development at the adhered surfaces, resulting in a nonuniform transfer of stresses leading to premature failure.[19,20,23,24] Fixed-end gripping systems prevent the rotation and avoid the development of local stresses but cannot avert possible accidental eccentricity in the system starting from the initial phase of testing.[4,24-26] However, the fixed-end gripping system provides accurate average post-cracking behavior, which is an essential part of the tensile response of UHPC.

The cracking of the specimens and the associated resistance due to fibers bridging the cracks form the basis for the post-cracking tensile response of UHPC. Previously, studies successfully used several optical techniques to investigate the formation and propagation of the cracks and study the influence of fibers in fiber-reinforced concrete and UHPC specimens.[27,29-31] An optical measurement system is one of the optical techniques previously used for this investigation.[27,32] This system tracks the movement of light-emitting diodes (LEDs) attached to the surface of the specimen, providing valuable information about the behavior of the cracked UHPC test units.

RESEARCH SIGNIFICANCE

Despite a wide variety of tests, specimen geometries, and test approaches used, no standard direct tension test method has been established that defines the specimen geometry, support conditions, and a standard analysis to characterize the tensile behavior of UHPC. The main objective of the study reported herein is to independently evaluate the reliability and repeatability of a tensile test method developed by FHWA,[5] which has been adopted into AASHTO T 397.[33]

AASHTO T 397 TENSILE TEST METHOD

This direct tensile test method uses a 2 x 2 x 17 in. (50.8 x 50.8 x 431.8 mm) UHPC specimen, four tapered aluminum plates per specimen, and a set of four linear variable displacement transducers (LVDTs). Aluminum plates are tapered to allow the transition of tensile stresses into the gauged region to force the crack formation in this region. Once the test specimen is cast and cured, plates are attached on both sides at each end using a thin layer of high-strength, high-stiffness epoxy.

The tensile testing machine should have wide enough grips to accommodate the specimens with a 2.4 x 2 in. (60.96 x 50.8 mm) cross section. Specimens are gripped with sufficient pressure to avoid slippage within the grip during the test. Wedge- and flat-grip test setups are two gripping systems suggested for this test procedure. A grip pressure of 5.8 ksi (40 MPa) was initially suggested for side-loading hydraulic wedge grips. Flat grips are manually pressed onto the test specimen through torquing of bolts (a detailed description is reported in AASHTO T 397[33]). A schematic representation of the tension test setup is shown in Fig. 2(a) and (b). Displacements of the test specimen with the application of tensile loads are captured using the LVDT setup. The testing protocol suggests the application of an initial axial compression load under displacement control until the stress in the cross section reaches 1 ksi (7 MPa), which is to verify accurate application of the load and capture of the data. Then, the tensile load is applied in displacement control such that the specimen is subjected to a stress of 1.5 ± 0.5 ksi/min (10 ± 3 MPa/min) in the elastic phase of the testing, and once the required displacement rate is set, the test will continue at that rate until the end. A displacement rate of approximately 0.006 in./min (0.15 mm/min) was found reasonable to generate the required stress rate.[33] The test may be completed once the load is decreased to less than 50% of the peak load.

An expected uniaxial tensile response of UHPC[33] is shown in Fig. 2(c), which includes multiple phases. The elastic phase initiates from the start of the loading until the intersection of a strain offset (0.02% offset) to the initial elastic stress-strain response and the captured stress-strain response in the inelastic region corresponding to the first cracking strain ($\epsilon_{t,cr}$) of the UHPC matrix. The multi-cracking phase starts at the onset of the first cracking of the UHPC matrix, followed by continuous cracking within the gauged region. In this phase, specimens carry near-constant or increasing stress without any cracks widening, with fibers bridging the cracks until peak stress is reached. During the crack straining

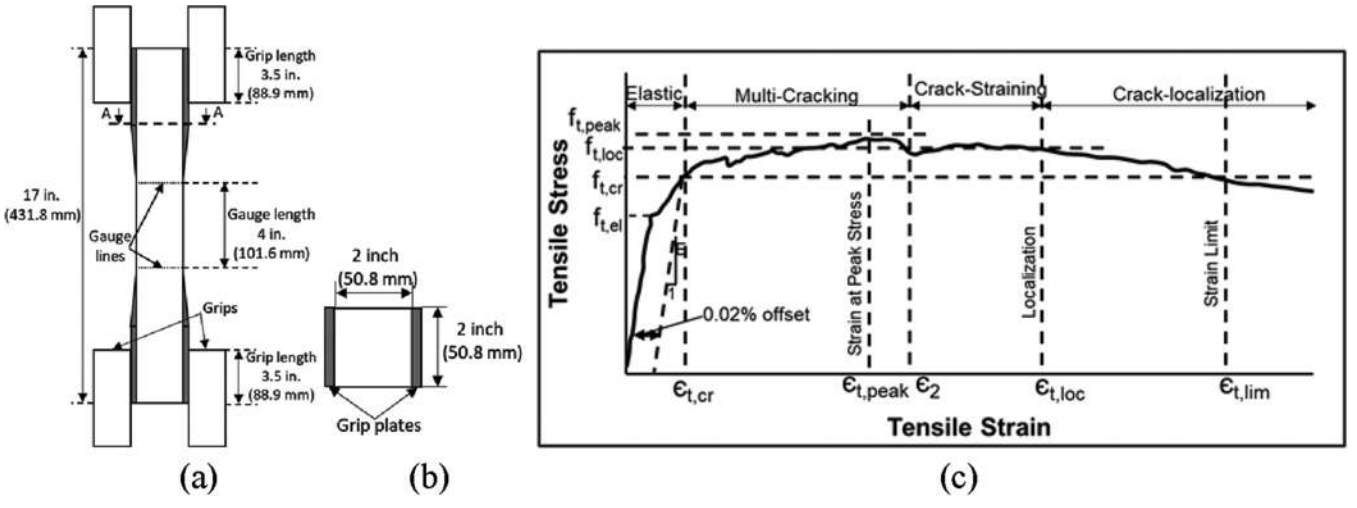

Fig. 2—Schematic representation of AASHTO T 397: (a) tension test setup; (b) specimen cross section (A-A); and (c) expected tensile stress-strain response of UHPC specimen.[33]

phase, the crack opening is observed, and this phase depends on the fiber elastic straining and fiber-matrix interface debonding. This phase ends when the capacity of strain hardening is reached (until localization strain $\epsilon_{t,loc}$). In the next phase, softening develops due to the continued widening of an individual crack. During this phase, fibers experience multiple failure modes[34] (that is, fracture, debonding, and pullout) at the crack in this localization phase.

MATERIALS AND METHODS

To evaluate the AASHTO T 397 test method, commercially available UHPC from three different suppliers in the United States, identified as UHPC A, UHPC B, and UHPC C, were chosen. The fiber-volume fraction is an additional variable included in the evaluation. High-strength straight steel-wire fibers with a length of 0.5 in. (12.7 mm) and diameter of 0.008 in. (0.203 mm), as typically used, were incorporated in all three UHPCs. However, three different fiber-volume fractions—3%, 1%, and 2%—were used with UHPC A, UHPC B, and UHPC C test samples, respectively. A total of 216 tension samples with dimensions of 17 in. (431.8 mm) long and 2 x 2 in. (50.8 x 50.8 mm) square cross sections were cast from three UHPC types, as detailed in Table 1. For each UHPC type, three batches of 24 tensile samples, 12 cubes (2 in. [50.8 mm]), and 12 cylinders (3 x 6 in. [76.2 x 152.4 mm]) were cast, yielding 72 tension test samples.

All samples were cast, and aluminum plates were affixed by the authors at Iowa State University (ISU), but they were tested in batches at six different laboratories to evaluate the repeatability and reliability of the test method. This paper identifies testing laboratories as TL1 through TL6. Each laboratory was asked to test three sets containing 10 specimens from UHPC A, UHPC B, and UHPC C. Two additional specimens per UHPC type were also made available for each laboratory to conduct trial tests and make them familiar with the testing procedure. Individual UHPC specimens made from UHPC A, UHPC B, and UHPC C were identified as A#, B#, and C# (# is range from 11 to 82), respectively. The specimens cast from the same batches were tested simultaneously at two different laboratories when possible.

Compressive tests

Compressive strengths of UHPC were obtained by testing 2 in. (50.8 mm) cubes and 3 x 6 in. (76.2 x 152.4 mm) cylinders at the age of 14, 28, 60, and 72 days at ISU. Twelve cubes and 12 cylinders were cast with each set of tensile samples; of these, three cubes and three cylinders were tested at each respective age. All the cubes and cylinders were tested according to ASTM C109/C109M-20b[35] and ASTM C1856/C1856M-17,[36] respectively.

Table 1—Summary of UHPC specimens produced

Specimen type	Dimensions, in. (mm)	Number of specimens		
		UHPC A	UHPC B	UHPC C
Tensile	17 x 2 x 2 (431.8 x 50.8 x 50.8)	72	72	72
Cylinders	3 (diameter) x 6 (76.2 x 152.4)	36	36	36
Cubes	2 x 2 x 2 (50.8 x 50.8 x 50.8)	36	36	36

Direct tensile testing

All the specimens were cured at ambient temperature for at least 60 days. Close to the shipping date, all the specimens were taken out from curing and were prepared for testing. Specimen preparation is one of the initial aspects of the AASHTO T 397 tensile test procedure. The plate face and specimen face were roughened with a sanding belt, a thin layer of epoxy was applied on both faces, and the plates were then affixed to the specimen using C-clamps. The finished and test-ready specimen is shown in Fig. 3(a).

Elongation in the specimen was measured on all four sides using an LVDT setup. This extensometer setup was mounted along the sample's gauge lines (shown in Fig. 2(a)) on the tension specimen. The specimen was centered within the extensometer setup, as shown in Fig. 3(b).

The prepared test specimen and the extensometer setup were aligned vertically between the testing machine's wedge grips. Five of the six laboratories chosen for testing used conventional hydraulic wedge grips, and a new type of flat-plate gripping system was used for the tests at TL6. The specimen was gripped along the grip lengths as seen in Fig. 3(c) with a gripping pressure in the range of 2.17 to 3.62 ksi (15 to 25 MPa), which is lower than recommended for side-loading hydraulic wedge grips. A reduced gripping pressure was justified to minimize a localized tension failure developing adjacent to the aluminum plates, as observed during the trial tests by ISU and two other testing laboratories. The lower gripping pressure was sufficient to prevent slippage of the test unit at the grips.

The full tensile test setup with hydraulic wedge grips is shown in Fig. 3(c). As part of investigating the reliability of the direct tension test method, specimens were tested using different machines to check the dependency of the machine type on the test outcome. This effort included laboratories with machine types (MTS and Suzhou) and different load capacities (200, 110, and 22 kip [890, 489, and 98 kN]). The experimental data from the LVDTs, axial load, and

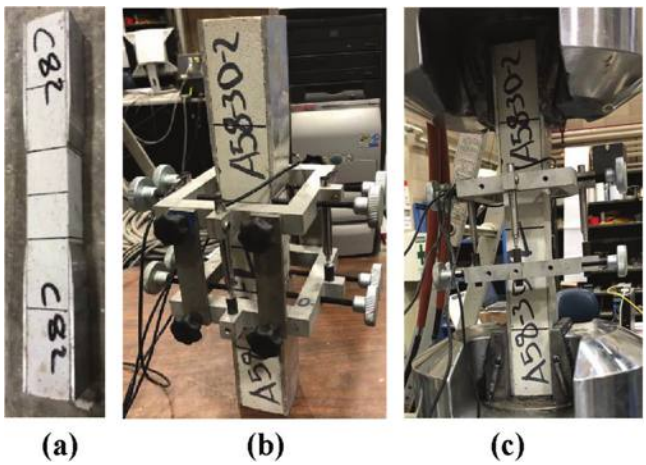

Fig. 3—(a) Test-ready specimen; (b) specimen with LVDT extensometer; and (c) setup in uniaxial test machine.

machine crosshead displacement were collected using an external data acquisition system. Specimens were tested at a displacement rate of 0.006 in./min (0.15 mm/min) in labs TL1 through TL5, and a displacement rate of 0.02 in./min (0.51 mm/min) was used in TL6, which corresponded to a loading rate of 1.3 ksi/min (9 MPa/min), which is within the loading protocol as per AASHTO T 397.[33]

EXPERIMENTAL RESULTS

Experimental test results of the specimens tested under compression and tension are reported and discussed in this section.

Compression test results

Compression test results from the cube and cylinder testing, along with the conversion factors (CFs), are reported in Table 2. The CF was obtained by dividing the 3 in. (76.2 mm) cylinder compressive strength by the corresponding 2 in. (50.8 mm) cube compressive strength. Failure in all the specimens due to compression is by split cracking and minor spalling of UHPC. Typical explosive failures that occur with high-strength concretes were not witnessed due to the presence of fibers. Variation in compressive strengths obtained from cubes and cylinders as a function of age is shown in Fig. 4(a). At least 80% of the maximum strength was attained within 14 days from casting for all mixtures. After 28 days, the increase in strength was not substantial compared to the early-age strength increase. Change in strength is reduced with the age of UHPC.

The influence of fiber volume on compressive strengths was not significant because the test program used different UHPC types with varying fiber volumes. However, the relation between cube and cylinder compressive strengths was examined as a function of fiber volume and age. The variation in compressive strengths with varying fiber volume at 28 days is shown in Fig. 4(b). Compressive strengths obtained from cubes are comparable to cylinders for UHPC A and UHPC C mixtures. In contrast, compressive strengths from cylinders are higher for specimens with lower fiber volume—that is, UHPC B.

It was interesting to note that the CF remained consistent for each UHPC regardless of age. Consequently, the CF in obtaining 3 in. (76.2 mm) cylinder strength from 2 in. (50.8 mm) cube strength varied from one UHPC to another. In contrast, Graybeal,[37] from his set of tests, proposed a CF of 0.96. All the CFs are reported in Table 3. Changes in CFs can be attributed to the use of different UHPCs. The packing density of concrete varies with UHPC types, leading to strength variation in smaller-volume cubes than cylinders.

Table 2—Mean compressive strengths obtained from three UHPC mixtures and conversion factors (CF is cylinder strength/cube strength)

Age		14 days	28 days	60 days	72 days
		f_c ± standard deviation, ksi (MPa)	f_c ± standard deviation, ksi (MPa)	f_c ± standard deviation, ksi (MPa)	f_c ± standard deviation, ksi (MPa)
UHPC B	Cube	16.37 ± 0.78 (112.9 ± 5.4)	17.55 ± 0.51 (121 ± 3.5)	18.26 ± 0.77 (125.9 ± 5.3)	18.44 ± 0.65 (127.1 ± 4.5)
	Cylinder	18.12 ± 0.72 (124.9 ± 5)	19.9 ± 0.52 (137.2 ± 4)	21.02 ± 0.63 (144.9 ± 4.3)	21.31 ± 0.64 (146.9 ± 4.4)
	CF	1.11	1.13	1.15	1.16
UHPC C	Cube	17.57 ± 0.67 (121.1 ± 4.6)	18.04 ± 0.52 (124.4 ± 3.6)	18.44 ± 0.66 (127.1 ± 4.5)	18.47 ± 0.61 (127.3 ± 4.2)
	Cylinder	17.74 ± 0.86 (122.3 ± 5.9)	18.67 ± 0.49 (128.7 ± 3.4)	19.16 ± 0.6 (132.1 ± 4.1)	19.38 ± 0.72 (133.6 ± 4.96)
	CF	1.01	1.03	1.04	1.05
UHPC A	Cube	17.4 ±1.2 (119.9 ± 8.3)	19.3 ± 0.78 (133 ± 5.4)	19.67 ± 0.81 (135.6 ± 5.6)	20.08 ± 1.05 (138.4 ± 7.2)
	Cylinder	17.8 ± 0.68 (122.7 ± 4.7)	19.23 ± 0.81 (132.6 ± 5.6)	19.69 ± 1.07 (135.7 ± 7.4)	19.86 ± 1.04 (136.9 ± 7.17)
	CF	1.02	0.99	1	0.98

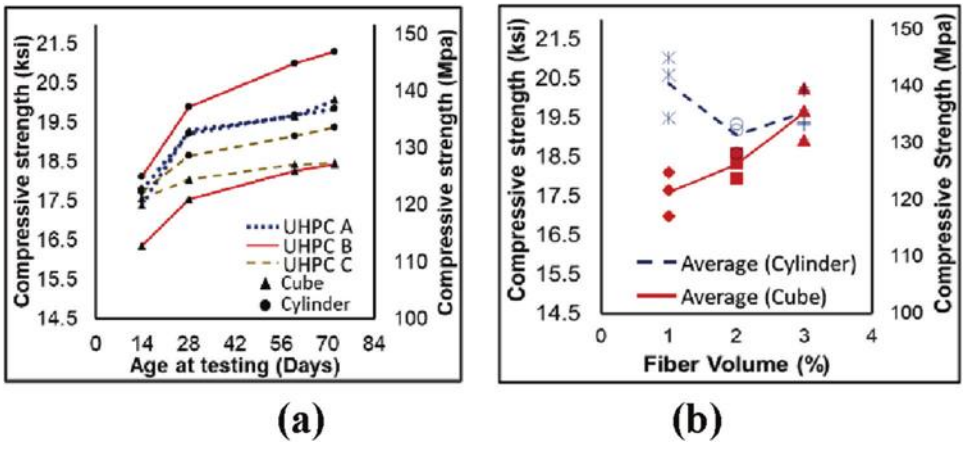

Fig. 4—(a) Average compressive strengths; and (b) compressive strengths of specimens with fiber volume (28-day strengths).

Tension test results

Tensile test data from different laboratories were obtained and analyzed and are presented in this section. The quality of data depends on whether the localized cracks develop within or outside the gauged region. When a crack localizes in a test within the gauged region, the test satisfactorily captures the full response of the test specimen. For successful tests, different phases of the tensile response including elastic, multi-cracking, crack straining, and crack localization were identified.

Any test response that showed strength below 70% of the average strength obtained from the same UHPC batch was considered unsuccessful, as this could be due to poor fiber distribution and/or specimen imperfection, forcing the crack to develop earlier than typical specimens. The testing was carried out successfully by the laboratory staff or students with minimal instructions at each laboratory. Laboratories TL1 and TL2 used 200 kip (890 kN) capacity uniaxial machines, and laboratories TL3, TL4, and TL5 used 110 kip (489 kN) capacity uniaxial machines to test the tensile specimens. All these laboratories used a hydraulic wedge gripping system for the tests. TL6 used a low-capacity 22 kip (98 kN) test machine with manual flat grips. Laboratories with high-capacity machines (that is, 200 kip [890 kN] capacity) appear to show a relatively lower success rate when testing lower-strength tension specimens (that is, UHPC B). The use of lower-capacity machines (110 and 22 kip [489 and 98 kN]) with adjusted grip pressures produced a close to 70% success rate for the proposed test procedure. Both the gripping systems, hydraulic wedge grips (used in TL3, TL4, and TL5), and manual flat grips (used in TL6) showed similar success rates. Table 4 summarizes the success rate of tested specimens for each test lab.

Typical tensile responses—This section discusses the types of tensile responses and failures obtained for the test samples. Figure 5 shows three different responses along with the corresponding failed units. In Fig. 5(a), the failure of the specimen was initiated by debonding of the plates with the application of relatively high gripping pressure and the development of localized cracks occurring close to the gripping region. This unfavorable response could also be due to a possible defect in specimen preparation. In such cases, the responses of the specimens are not useful beyond the formation of the first crack. The response in Fig. 5(c) has a useful response until the end of the multi-cracking phase. This specimen failed due to crack localization occurring just outside the gauged region (shown in Fig. 5(d)). LVDTs capture the response only between the gauged zone, and if the crack is localized outside the gauged region, the complete response would not be captured. These responses are good until the onset of localized crack. The measured peak strengths from these types of specimen failures can be used to get the tensile capacity of the specimens. The response shown in Fig. 5(e) is similar to the ideal response shown in Fig. 2(c), in which all the phases are captured. For this specimen, the crack was localized within the gauged region (shown in Fig. 5(f)), producing a successful test. All the successful tests reported in Table 4 have similar responses.

Tensile response characterization—As denoted in Fig. 5 and 6, the multi-cracking phase starts at strain $\epsilon_{t,cr}$. Figure 5 depicts the responses of UHPC A, while Fig. 6(a) and (b) represent UHPC B and UHPC C samples. Strain ϵ_2 marks the end of a multi-cracking phase and the start of the crack straining phase, whereas strain $\epsilon_{t,loc}$ marks the end of the crack straining phase and the onset of crack localization. $\epsilon_{m\text{-}cr}$ represents the multi-cracking strain, and $\epsilon_{cr\text{-}st}$ is the crack straining value. Both tensile strength and $\epsilon_{m\text{-}cr}$ increase with fiber-volume fraction due to an increase in resistance from a larger number of fibers crossing the localized crack. A smaller crack straining phase was identified for UHPC C (2% fibers) responses than the responses obtained for UHPC A (3% fibers) and UHPC B (1% fibers) samples. The crack straining phase appears to depend on the fiber-matrix interaction, which varies with the type of UHPC used, irrespective of fiber volumes.

Effect of fiber volume—Typical stress-strain responses of the UHPC specimens at different fiber-volume fractions are shown in Fig. 7(a), and the corresponding responses up to 0.005 strain are shown in Fig. 7(b). All the specimens have an elastic phase until the first cracking load, followed by the expected multiple cracking, crack straining, and crack localization phases. Furthermore, a linear increase in tensile strength with an increase in fiber-volume fraction is seen in Fig. 8. A percentage increase in strengths with an increase in fiber volume is shown in Table 5. A higher number of microcracks were identified at a higher volume fraction

Table 3—Conversion factors to obtain compressive strength of cylinders from compressive strength of cubes

	Fiber volume, %	CF
UHPC B	1	1.14
UHPC C	2	1.03
UHPC A	3	1
Graybeal[37]	2	0.96

Table 4—Success rates of testing procedure across different labs

Specimens	Total samples tested (No. of samples failed within gauge)						Success rate, %
	Lab 1, 200 kip (890 kN) machine	Lab 2, 200 kip (890 kN) machine	Lab 3, 110 kip (489 kN) machine	Lab 4, 110 kip (489 kN) machine	Lab 5, 110 kip (489 kN) machine	Lab 6, 22 kip (98 kN) machine	
UHPC A	10 (5)	10 (3)	10 (7)	10 (8)	10 (6)	10 (7)	60
UHPC B	10 (2)	10 (2)	10 (8)	10 (6)	10 (7)	10 (6)	52
UHPC C	10 (4)	10 (5)	10 (7)	10 (6)	10 (9)	10 (8)	65
Success rate, %	36.6	33.3	73.3	66.6	73.3	70	59

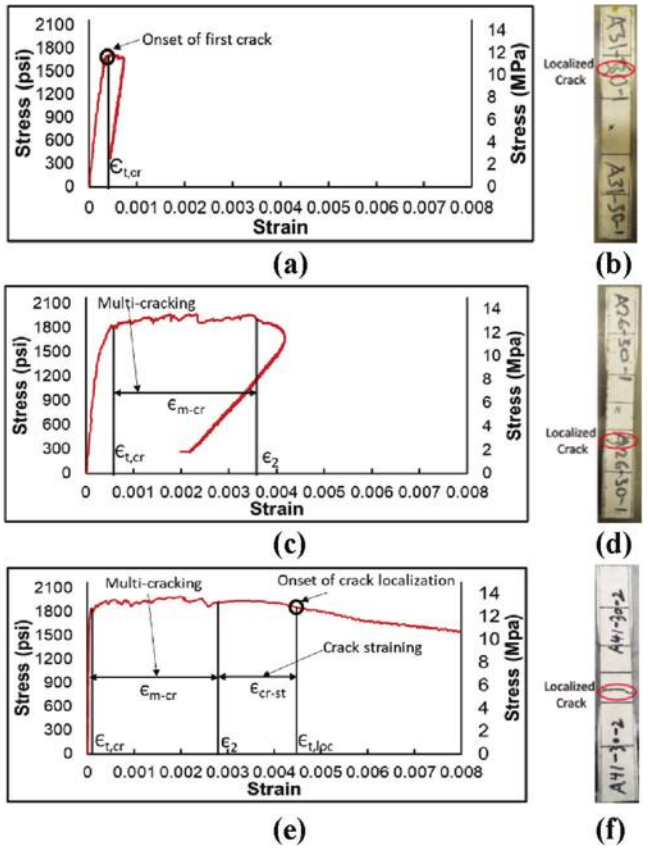

Fig. 5—(a, b) Stress-strain response of Specimen A31 with failure due to debonding of plates and picture of the failed specimen; (c, d) stress-strain response of Specimen A26 with crack localized outside gauged region and picture of failed specimen; and (e, f) stress-strain response of Specimen A41 with crack localized within gauged region and picture of failed specimen.

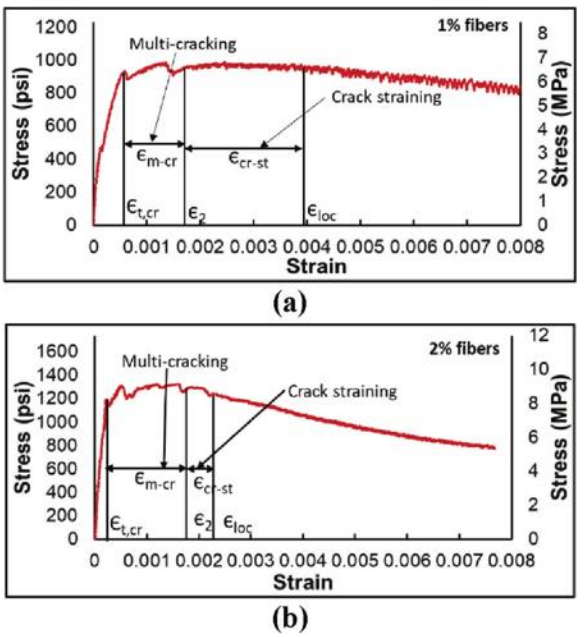

Fig. 6—Stress-strain response of one UHPC specimen from set of: (a) UHPC B; and (b) UHPC C.

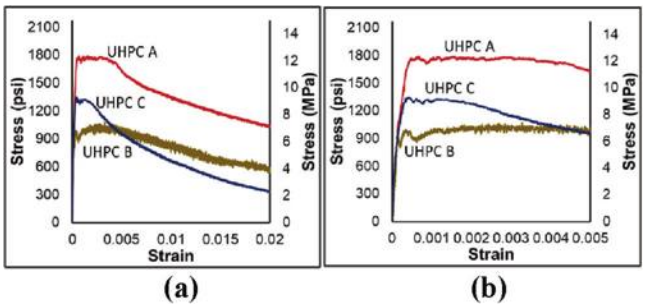

Fig. 7—(a) Stress-strain response of UHPC at different fiber volumes; and (b) initial stress-strain response up to strain of 0.005.

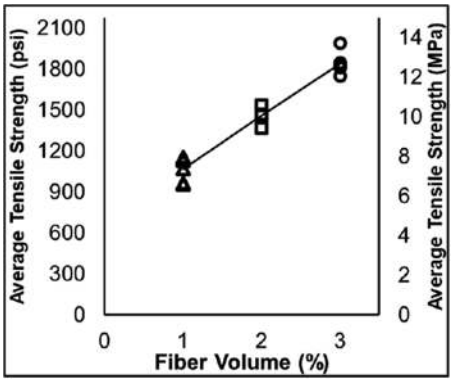

Fig. 8—Average tensile strengths at different fiber-volume fractions.

of fibers. The test results show that the testing procedure captured satisfactory tensile responses using varied fiber-volume fractions.

To confirm the fiber representation, a randomly chosen tension sample from each UHPC was cut at or adjacent to the localized crack and smoothened (refer to Fig. 9), and the number of fibers at the section was quantified. Fibers were counted by a combination of visual inspection and image processing software. The number of fibers across UHPC A, UHPC B, and UHPC C specimens were found to be 1453, 485, and 846, respectively, representing 464 fibers per 1% fiber volume on average. Fiber quantities in UHPC A and UHPC B specimens were closer to or higher than the average fiber count. In contrast, fiber quantity in the UHPC C specimen was somewhat lower than the average value. The effect on fiber distribution and the small crack straining phase may also be attributed to the presence of small aggregates in the UHPC C specimen (Fig. 6(b)).

The average representative strain values from the successful tests at three fiber volumes are shown in Table 6. An increase in $\epsilon_{m\text{-}cr}$ with fiber volume is consistent across all the labs. The change in $\epsilon_{cr\text{-}st}$ is consistent across all the labs and depends on the UHPC type.

Variation within lab—This section examines the variation of stress-strain responses reported by the same laboratory. As previously noted, three sets of specimens at three different fiber-volume fractions from three different laboratories are reported. Stress-strain responses of all the 10 samples from UHPC A, UHPC B, and UHPC C sets that were tested at TL1, TL3, and TL4 are shown in Fig. 10(a), (c), and (e), and

Table 5—Average maximum tensile stress at different fiber-volume fractions

Fiber volume, %	Average maximum tensile stress, psi (MPa) [% increase in strength compared to 1% fiber specimens]					
	Lab 1	Lab 2	Lab 3	Lab 4	Lab 5	Lab 6
1	1130.3, 7.79	970.6, 6.69	987.2, 6.8	1108.3, 7.64	1146.11, 7.9	1085.8, 7.5
2	1537.2 (10.6) [36]	1366.4 (9.4) [40.8]	1457.5 (10.1) [47.6]	1468.8 (10.1) [32.5]	1463.8 (10.1) [27.7]	1443.1 (9.9) [32.9]
3	1988.6 (13.7) [76]	1843.2 (12.7) [89.9]	1830.8 (12.6) [85.4]	1811.6 (12.5) [63.5]	1829.1 (12.6) [59.6]	1817.3 (12.5) [67.4]

Table 6—Average representative strains at different fiber-volume fractions

Fiber volume, %	$\epsilon_{t,cr}$ (standard deviation)	ϵ_2 (standard deviation)	$\epsilon_{m\text{-}cr}$ (standard deviation)	$\epsilon_{t,loc}$ (standard deviation)	$\epsilon_{cr\text{-}st}$ (standard deviation)
3	0.0004 (0.002)	0.00294 (0.0008)	0.00258 (0.0007)	0.00431 (0.001)	0.00137 (0.0005)
2	0.00038 (0.00019)	0.00216 (0.00072)	0.00178 (0.00067)	0.00291 (0.00082)	0.00075 (0.00026)
1	0.00048 (0.00032)	0.00206 (0.00058)	0.00158 (0.00043)	0.00397 (0.00094)	0.00191 (0.000564)

corresponding specimens with localized cracks are shown in Fig. 10(b), (d), and (f), respectively. Considering the five tests from the UHPC A set (A12, A17, A18, A20, and A21) in TL1 that were successful, though the first cracking stress is similar, there were big load variations after the first cracking stress during the multi-cracking phase in A17, A18, and A21. These variations can be attributed to the sensitivity of the high-capacity (200 kip [890 kN]) machine used. Similar tensile strengths and responses from the specimens within the lab were observed in TL3 and TL4. Slight variations in these responses were due to each specimen's fiber distribution. Refer to Appendix A* for the remaining responses from all the labs. Using this test procedure, repeatable tensile responses (successful tests) from the same set of samples were obtained.

Variation across labs—In this section, variation of tensile stress-strain responses of successful tests across different laboratories was examined. Each lab captured typical stress-strain responses for several samples, although variations across the labs were observed. The responses of specimens tested at different laboratories are shown in Fig. 11. Similar shaded plots in Fig. 11 represent specimen responses from the same UHPC batch. The variations in the responses within the same lab can be attributed to the fiber distribution in each specimen. Issues with the data acquisition frequency and sensitivity of a high-capacity test machine in lab TL1 resulted in large load drops and noise in the responses. Similar load drops were not observed in TL2 that tested specimens from the same UHPC batches and used identical capacity machines. Tests from these two labs showed a lower success rate than other labs. Two specimen responses of the UHPC A set showed a higher capacity and faster drop in load compared to other responses influencing the load drop in the average response, resulting in a smaller multi-cracking phase compared to the UHPC A set from TL4. Because of this, average responses obtained by averaging the data from all the specimens cannot be taken directly in the analysis, and a different approach is required to obtain a true average response. The approach to getting the average response was detailed in the previous research[5] and discussed later in this

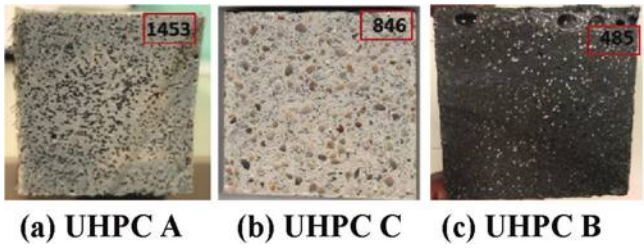

Fig. 9—Examination of fiber distribution.

paper. Responses from labs TL5 and TL6 were similar, and slight variations that were observed could be due to the type of machines and the gripping system used. Specimen A79 from the lab TL6 was cracked within the gauge length but has shown a strength (1080 psi [7.4 MPa]) below 30% of the average strength (1780 psi [12.3 MPa]) from the remaining specimens of the same lab. This specimen response was treated as an unsuccessful test.

The average tensile responses across all the laboratories at each fiber-volume fraction are shown in Fig. 12. All responses from each fiber-volume fraction can be seen to lie within the sum and difference of the total average response and 1.5 times the standard deviation—similar to the test responses obtained from previous studies by FHWA.[6] This shows that the test results from the tensile test procedure are fairly accurate between the laboratories and are consistent at different fiber-volume fractions.

Quantifying UHPC tension characteristics—Tensile responses of all the specimens from each set across all labs are shown, along with average response and two theoretical responses in Fig. 13. Similar to the concept proposed by Graybeal and Baby,[5] the generated responses for each set of specimens include average and characteristic responses. The average response is appropriate when predicting the response of UHPC members, while the characteristic response is meant for use in design conservatively. Both responses include an initial elastic-plastic region followed by a softening to a strain of 0.01. For the average response, the elastic part was obtained using the average modulus of elasticity, and the stress plateau is from the average cracking strength of that specimen set. The average cracking strength is the average of stresses corresponding to the strains 0.002, 0.0017, and 0.0015 for UHPC A, UHPC C, and UHPC B, respectively, which are always within the multi-cracking phase in all the

*The Appendix is available at **www.concrete.org/publications** in PDF format, appended to the online version of the published paper. It is also available in hard copy from ACI headquarters for a fee equal to the cost of reproduction plus handling at the time of the request.

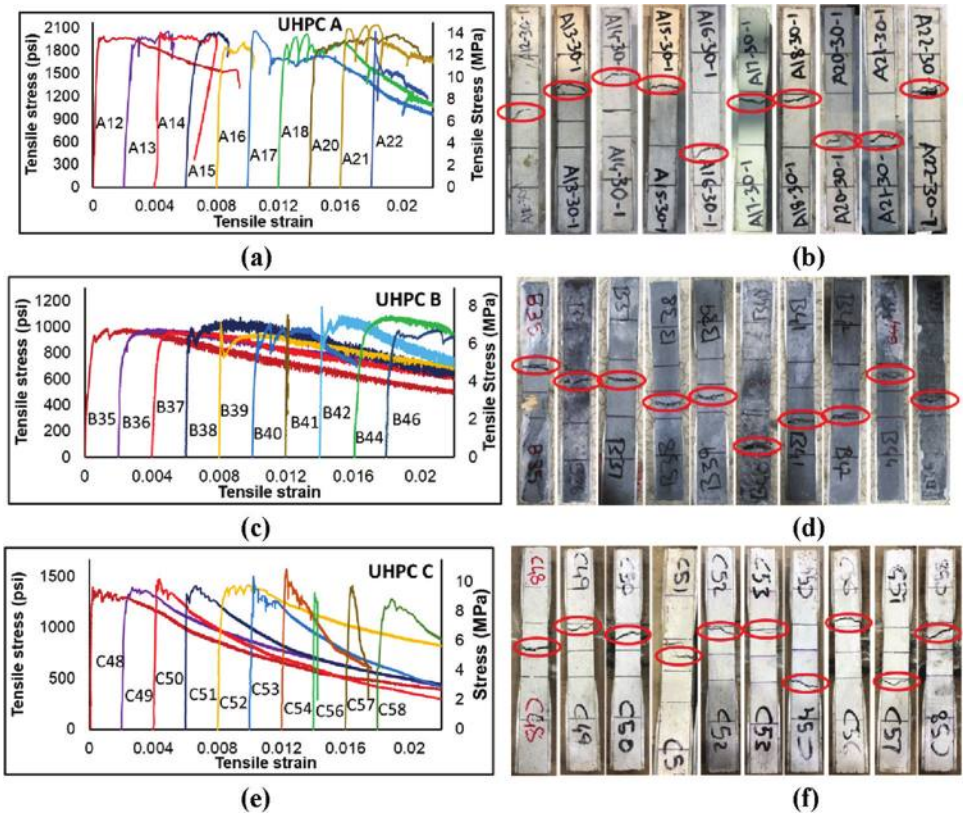

Fig. 10—Uniaxial tensile responses and failed specimens of: (a, b) UHPC A specimens from TL1; (c, d) UHPC B specimens from TL3; and (e, f) UHPC C specimens from TL4.

specimens and depend on the fiber volumes. The softening portion of the response was determined by fitting a polynomial equation to the obtained average response up to a strain of 0.01. For the characteristic response, average values were lowered by a value of t-student coefficient times the standard deviation.[6] Required coefficients depend on the number of successful tests available for each set of specimens. Characteristic response provides a response above which 95% of the responses of the test units from that set should fall. Average and characteristic responses provide designers with critical information in developing UHPC structural design specifications.

Based on the responses obtained from tensile testing of UHPC specimens, equations to establish average and characteristic responses were developed. The initial three points of the average and characteristic responses comprising the elastic-plastic part of the response were obtained, as described in the previous section. The stress at the strain of 0.01 is also the average value from all the responses at that strain.

Equations (1) and (2) provide the crack localization portion joining the third and fourth points for the average and characteristic responses

$$f_{loc,i} = f_t \exp[0.16(f_t - f_{t1})(\epsilon_t - \epsilon_{xi})] \quad (1)$$

$$f_{locc,i} = f_{tc} \exp[0.16(f_t - f_{t1})(\epsilon_{tc} - \epsilon_{xci})] \quad (2)$$

where $f_{loc,i}$ is the localized crack stress at a strain of ϵ_{xi} ($\epsilon_{xi} > \epsilon_t$); f_t is the average tensile strength; f_{t1} is the average stress at the strain of 0.01; ϵ_t is the average strain at the initiation of crack localization; $f_{locc,i}$ is the localized crack stress at a strain of ϵ_{xci} ($\epsilon_{xci} > \epsilon_{tc}$); f_{tc} is the characteristic tensile strength = f_t-(aS); ϵ_{tc} is the average characteristic strain at the initiation of crack localization = ϵ_t–(aS); a is the t-student coefficient; and S is standard deviation.

The equations developed provided satisfactory compliance with the obtained responses from different specimens. A comparison is shown in Fig. 14.

The design and characteristic responses may be established for any UHPC with a suitable volume of fibers using the approach described previously. However, the key values needed to establish the average and characteristic responses should be obtained from a sufficient set of successful tests. As per the study, the minimum number of successful tests should be in the range of 15 to 20.

DISCUSSION

Identifying the labs capable of conducting these tests was challenging because of the large grip sizes required to accommodate specimens of a width of 2.4 in. (60.96 mm). Through investigation, it was discovered early that the proposed grip pressures were higher, and the lower grip pressures recommended in this paper were sufficient not to allow any slip during the tests. There was also an indication that machine capacity matters from the test results obtained with different-capacity machines. The study did not investigate the care needed to cast and prepare samples.

Different phases in the tensile behavior: elastic, multi-cracking, crack-straining, and crack localization, can be

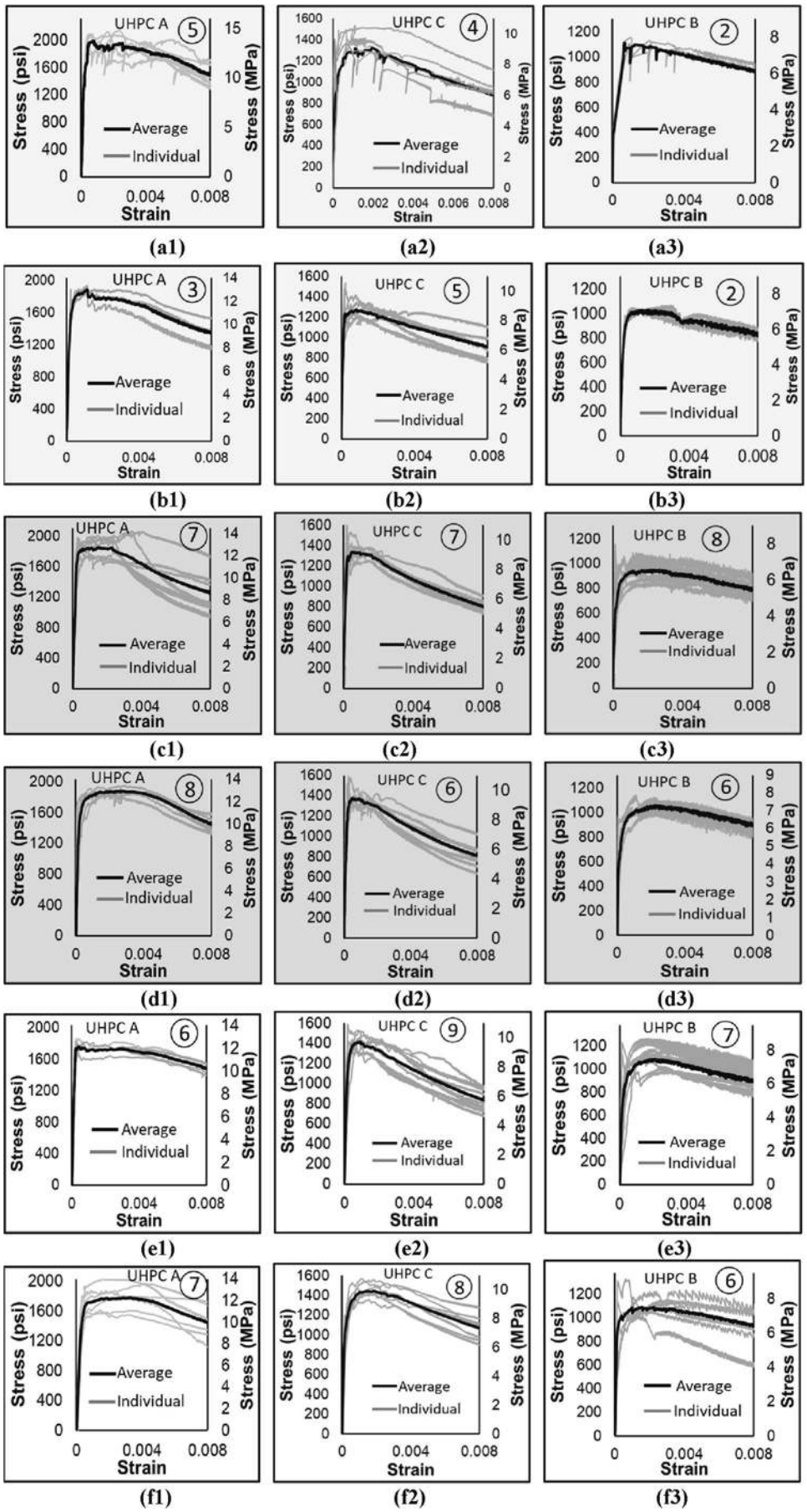

Fig. 11—Tensile stress-strain responses of successful tests from labs: (a1) to (a3) TL1; (b1) to (b3) TL2; (c1) to (c3) TL3; (d1) to (d3) TL4; (e1) to (e3) TL5; and (f1) to (f3) TL6. (Number of successful tests is shown on top right of each plot.)

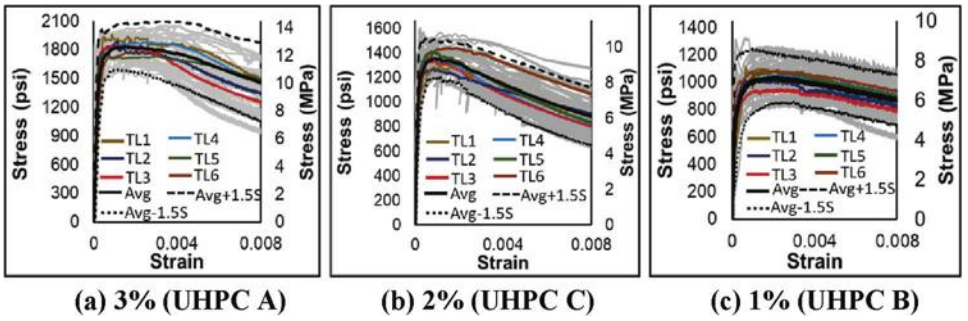

Fig. 12—Tensile stress-strain responses of specimens with different fiber volumes.

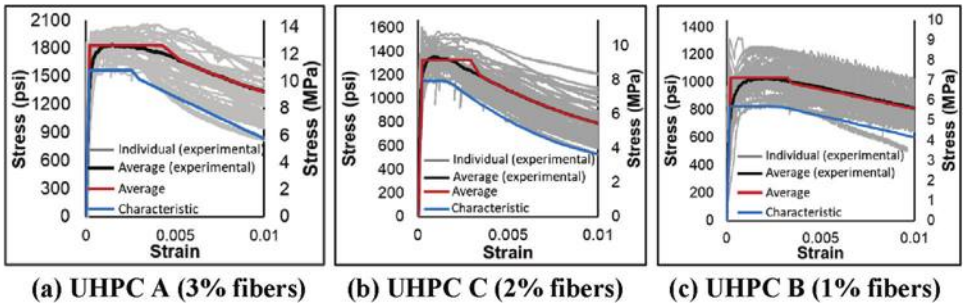

Fig. 13—Stress-strain response of UHPC specimens showing design curves from each set.

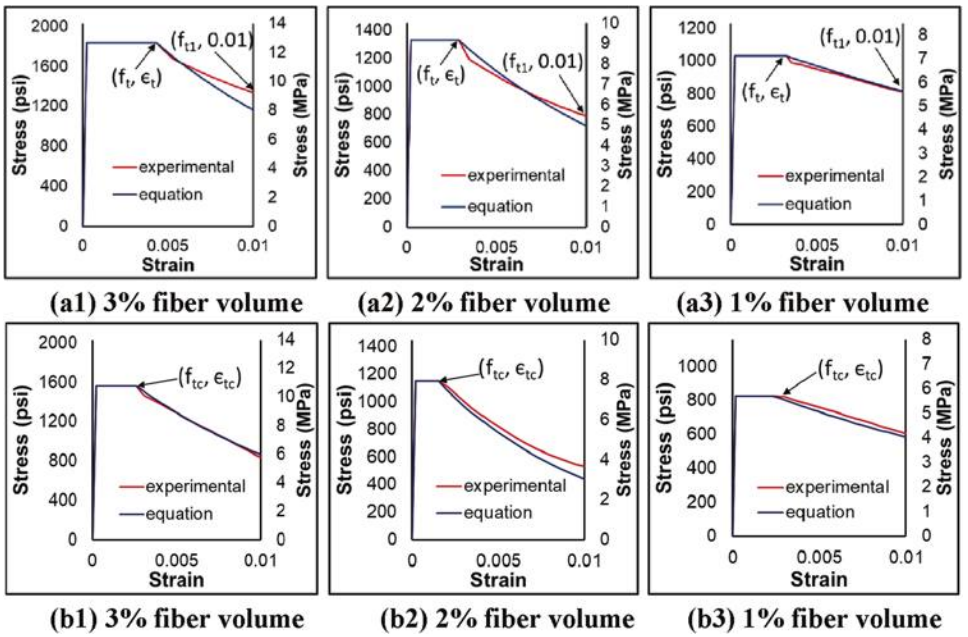

Fig. 14—Comparison of specimen responses with different fiber volumes from empirical equations and: (a1, a2, a3) average responses; and (b1, b2, b3) characteristic responses.

captured from successful tests. The phases of the tension responses were identified by visual inspection, and testing of an additional specimen (of the UHPC A set) was conducted by incorporating a non-contact optical method with LEDs. This system was used to capture the crack formation and propagation with more detailed information. The specimen was identified as UHPC A1, and LEDs were attached to the specimen at 1 in. (25.4 mm) intervals along two vertical lines that were 0.5 in. (12.7 mm) on either side of the centerline on the front face, as shown in Fig. 15(a). LEDs on the left of the centerline were identified as L_1, L_2,..., L_5, and LEDs on the right were identified as R_1, R_2,…., R_5. The strains between a pair of LEDs were determined as $L_{1\text{-}2}$ from LEDs L_1 and L_2 and $R_{1\text{-}2}$ from LEDs R_1 and R_2…and so on, with respect to their initial position. A high-definition camera that tracks kinetic and kinematic motion in real time was used to track the movement of all LEDs during testing. Data received from this measurement technique was used to capture the variation in microcracking along the length and onset of local crack information more precisely. Three LVDTs and the reference points were hot glued to the specimen at the gauge lines on the remaining three sides of the specimen, as shown in Fig. 15(b). Strains from the LVDT data were calculated as displacements measured divided by their gauge length of

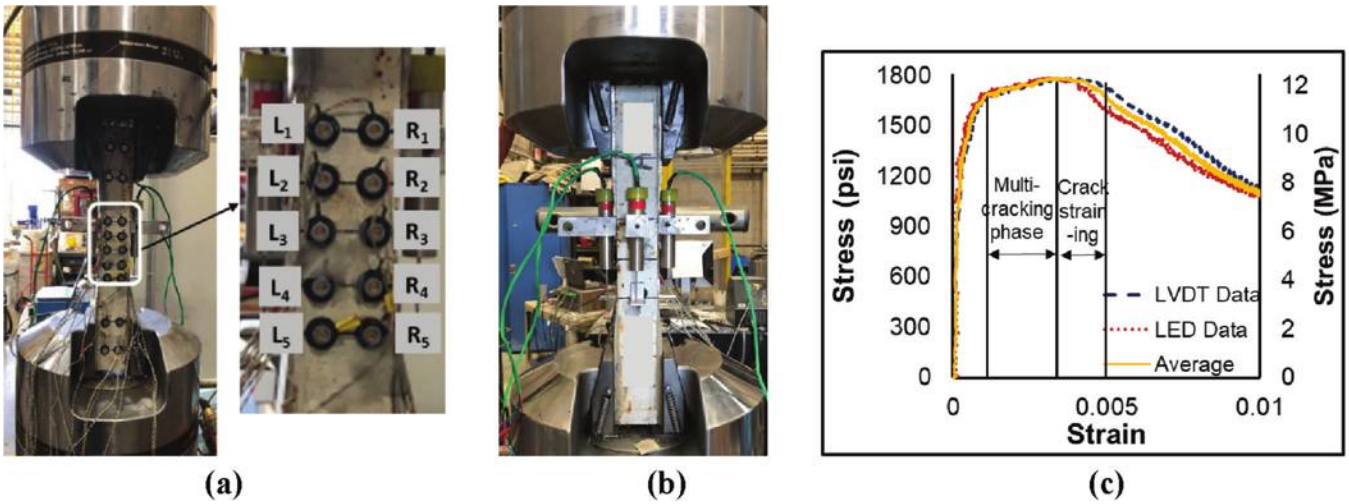

Fig. 15—Photographs of test setup showing: (a) front side of specimen with LEDs; (b) back side of specimens with LVDTs; and (c) LVDT and LED stress-strain responses of UHPC A1.

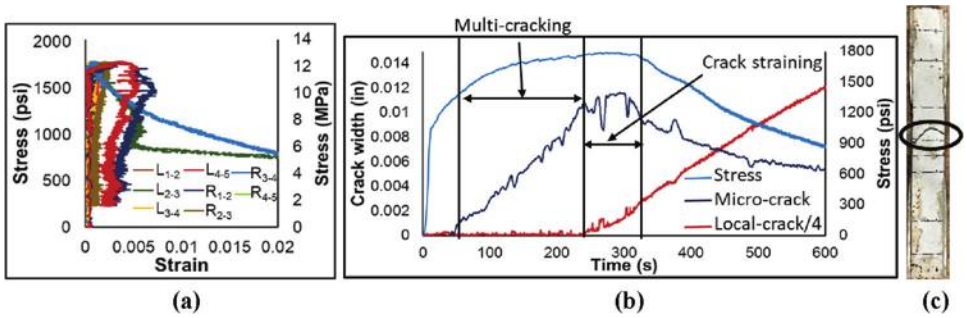

Fig. 16—UHPC A1 specimen: (a) LED strains at 1 in. (25.4 mm) intervals with stress; (b) load, accumulated microcrack width, and local crack width variation with time; and (c) failed specimen.

4 in. (101.6 mm). Tensile stress-strain response, including the different phases, obtained for the specimen from LED and LVDT data is shown in Fig. 15(c). To further analyze the response, LED data were examined.

Testing of the specimen UHPC A1 was considered successful as the localized crack was formed within the gauged region (Fig. 16(c)). LED strains at 1 in. (25.4 mm) intervals with the application of load are shown in Fig. 16(a). Variations in these strains along the specimens are attributed to the formation and propagation of microcracks. In this specimen, the local crack was observed to be developed between LED pairs L_2-R_2 and L_3-R_3. The microcrack strain was taken as an average of strains L_{1-2}, L_{3-4}, L_{4-5}, R_{1-2}, R_{3-4}, and R_{4-5}. Using this strain, the total accumulated microcrack width along the gauge length was calculated as the average micro strain multiplied by the gauge length. The total deformation of the specimen within the gauged region was calculated by averaging the displacements measured between LED pairs L_1, L_5, and R_1, R_5. Local crack width was calculated by subtracting the accumulated microcrack widths from the total deformation.

The tensile load data and variation of local and microcrack widths with the time of the UHPC A1 specimen are shown in Fig. 16(b). For the UHPC A1 specimen, the start of the multi-cracking phase observed in the load response coincides with the initiation of accumulated microcrack width measured from LED data. A continuous increase in microcrack widths was observed during this response phase. Initiation of local crack and stabilization of microcracking (accumulated) attributed to the crack straining phase. This phase follows with a drop in microcracking (accumulated) width and a continuous increase in local crack width, coinciding with a drop in the load resembling crack localization. This method identifies different phases of the tensile response from the microcrack and local crack developments and matches the phases characterized by visual inspection of the load response.

CONCLUSIONS

This paper evaluated the reliability and repeatability of a direct tensile test procedure developed by the Federal Highway Administration (FHWA) which has been adopted by the American Association of State Highway and Transportation Officials (AASHTO). For this evaluation, three sets of tensile specimens manufactured from three different ultra-high-performance concretes (UHPCs) and varying steel-fiber volumes (that is, 1, 2, and 3%) were tested at six laboratories. All test samples were prepared by the authors of this paper. The tests were deemed successful when specimens developed localized cracks within the gauged region. The compressive strengths of the UHPCs were also evaluated. The conclusions drawn from the study are presented as follows.

1. The influence of fiber volume on UHPC compressive strengths was not significant. Conversion factors (CFs) to obtain 3 in. (76.2 mm) cylinder compressive strengths from 2 in. (50.8 mm) cube compressive strengths were independent of the age of the concrete but varied among different UHPCs and different fiber volumes in the range of 0.98 to 1.16. With carefully prepared test specimens, the AASHTO T 397 test method developed by the FHWA can be used for establishing the direct tension response of UHPC with steel fibers in the 1 to 3% range with a success rate of 60 to 70%.

2. The boundaries of different phases of UHPC tension response were satisfactorily identified through visual observations of the measured responses. It is shown that the localized crack begins to develop at the onset of the crack straining phase.

3. When the sample size of the successful tests exceeds 30, the test method captured the multiple phases of the UHPC tensile response within 1.5 times the standard deviation.

4. The tensile strength of UHPC is directly proportional to the fiber volume. As the fiber volume was increased, the multi-cracking phase was also extended regardless of the UHPC used.

5. The crack straining phase was found to depend on the UHPC type and not on fiber volume.

6. The average and characteristic responses of UHPC tensile behavior can be established using the equations presented in this paper with minimum successful tests of 15.

RECOMMENDATIONS

Based on the experimental investigation presented herein, presented as follows are recommendations to increase the chances of conducting successful direct tension tests described in AASHTO T 397.

1. Higher-capacity uniaxial machines often resulted in a lower success rate, presumably due to the strength of specimens being small. The use of test machines with a capacity not exceeding 110 kip (489 kN) is recommended.

2. Securing aluminum plates to the ends of the specimens is a critical step for producing successful tests. Roughening and applying epoxy on both the plate and specimen surfaces is suggested to adequately secure the plates to the test specimens.

3. The originally proposed gripping pressure of 5.8 ksi (40 MPa) was found to be unnecessarily high, resulting in crack development near the ends of the grips. A reduced gripping pressure of 2.17 to 3.62 ksi (15 to 24.9 MPa) (depending on machine capability) is recommended. Even a lower gripping pressure may be appropriate, as long as the test can be conducted without experiencing any slippage of the specimens.

4. Use of C-clamps across the tapered portions of the aluminum plates help minimize crack development outside the gauged region, increasing the test success rate.

5. With the aforementioned recommendations, a test success rate of 50% may be assumed in deciding the number of test samples. Conservatively, testing a minimum of six specimens is recommended to achieve a minimum of three successful tests.

AUTHOR BIOS

ACI member **Sahith Gali** *is a Postdoctoral Research Associate in the Civil Construction and Environmental Engineering Department at Iowa State University, Ames, IA. He received his PhD from the Indian Institute of Technology Hyderabad, Telangana, India. He is a member of ACI Committee 239, Ultra-High-Performance Concrete, and ACI Subcommittees 239-C, Structural Design on UHPC, and 239-D, Materials & Methods of Construction with UHPC. His research interests include the behavior of ultra-high-performance concrete, fiber-reinforced concrete, and advanced cement-based materials.*

Sri Sritharan, *FACI, is the Anson Marston Distinguished Professor in the Department of Civil, Construction, and Environmental Engineering and Assistant Dean in the College of Engineering at Iowa State University. He is a past Chair and current member of ACI Committee 341, Performance-Based Seismic Design of Concrete Bridges; and a member of Joint ACI-ASCE Committee 447, Finite Element Analysis of Reinforced Concrete Structures. His research interests include the design of concrete structures, ultra-high-performance concrete, and earthquake engineering.*

ACKNOWLEDGMENTS

The study presented in this paper was undertaken as part of Pool Fund Project TPF-5(366), for which the Iowa Department of Transportation (DOT) serves as the lead agency. Other DOTs participating in this study include California, Connecticut, Georgia, New York, and Washington. A. Abu-Hawash and K. Clute of Iowa DOT serve, respectively, as the Chair of the Technical Advisory Committee and Research Manager of this project. Besides Iowa State University, testing of the ultra-high-performance concretes (UHPCs) was conducted at the following institutions: the University of Alabama, North Carolina State University, the University of Florida, and the University of Houston. The authors would like to thank the faculty members, technicians, and students at these institutions for their effort and feedback. The authors would also like to acknowledge all the material suppliers who have donated the UHPCs for the study.

REFERENCES

1. Naaman, A. E., and Reinhardt, H. W., "Characterization of High-Performance Fiber-Reinforced Cement Composites—HPFRCC," *High-Performance Fiber-Reinforced Cement Composites*, V. 2, A. E. Naaman and H. W. Reinhardt, eds., E&FN Spon, London, UK, 1996, pp. 1-24.

2. Graybeal, B. A., "Practical Means for Determination of the Tensile Behavior of Ultra-High-Performance Concrete," *Journal of ASTM International*, V. 3, No. 8, Sept. 2006.

3. Graybeal, B. A., "Ultra-High-Performance Concrete," FHWA-HRT-11-038, U.S. Department of Transportation, Federal Highway Administration, Washington, DC, Mar. 2011.

4. Graybeal, B. A., and Baby, F., "Development of Direct Tension Test Method for Ultra-High-Performance Fiber-Reinforced Concrete," *ACI Materials Journal*, V. 110, No. 2, Mar.-Apr. 2013, pp. 177-186.

5. Graybeal, B. A., and Baby, F., "Tension Testing of Ultra-High- Performance Concrete," FHWA-HRT-1-053, U.S. Department of Transportation, Federal Highway Administration, Washington, DC, Feb. 2019.

6. Gopalaratnam, V. S.; Shah, S. P.; Batson, G.; Criswell, M.; Ramakishnan, V.; and Wecharatana, M., "Fracture Toughness of Fiber Reinforced Concrete," *ACI Materials Journal*, V. 88, No. 4, July-Aug. 1991, pp. 339-353.

7. Armelin, H. S., and Banthia, N., "Predicting the Flexural Postcracking Performance of Steel Fiber Reinforced Concrete from the Pullout of Single Fibers," *ACI Materials Journal*, V. 94, No. 1, Jan.-Feb. 1997, pp. 18-31.

8. Wille, K.; Kim, D. J.; and Naaman, A. E., "Strain-Hardening UHP-FRC with Low Fiber Contents," *Materials and Structures*, V. 44, No. 3, 2011, pp. 583-598. doi: 10.1617/s11527-010-9650-4

9. Voit, K., and Kirnbauer, J., "Tensile Characteristics and Fracture Energy of Fiber Reinforced and Non-Reinforced Ultra-High-Performance Concrete (UHPC)," *International Journal of Fracture*, V. 188, No. 2, 2014, pp. 147-157. doi: 10.1007/s10704-014-9951-7

10. Gali, S., and Subramaniam, K. V., "Evaluation of Crack Propagation and Post-Cracking Hinge-Type Behavior in the Flexural Response of Steel Fiber Reinforced Concrete," *International Journal of Concrete Structures and Materials*, V. 11, No. 2, 2017, pp. 365-375. doi: 10.1007/s40069-017-0197-4

11. Gali, S., and Subramaniam, K. V., "Multi-Linear Stress-Crack Separation Relationship for Steel Fiber Reinforced Concrete: Analytical Framework and Experimental Evaluation," *Theoretical and Applied Fracture Mechanics*, V. 93, Feb. 2018, pp. 33-43. doi: 10.1016/j.tafmec.2017.06.018

12. Sritharan, S.; Bristow, B.; and Perry, V., "Characterizing an Ultra-High-Performance Material for Bridge Applications under Extreme

Loads," *Proceedings of the 3rd International Symposium on High Performance Concrete*, Orlando, FL, Oct. 2003.

13. Sritharan, S., "Design of UHPC Structural Members: Lessons Learned and ASTM Test Requirements," *Advances in Civil Engineering Materials*, V. 4, No. 2, 2015, pp. 113-131. doi: 10.1520/ACEM20140042

14. Wille, K.; El-Tawil, S.; and Naaman, A. E., "Properties of Strain Hardening Ultra-High-Performance Fiber Reinforced Concrete (UHP-FRC) under Direct Tensile Loading," *Cement and Concrete Composites*, V. 48, Apr. 2014, pp. 53-66. doi: 10.1016/j.cemconcomp.2013.12.015

15. Olesen, J. F., "Fictitious Crack Propagation in Fiber-Reinforced Concrete Beams," *Journal of Engineering Mechanics*, ASCE, V. 127, No. 3, 2001, pp. 272-280. doi: 10.1061/(ASCE)0733-9399(2001)127:3(272)

16. Vandewalle, L.; Nemegeer, D.; Balazs, L.; Barr, B.; and Barros, J., "RILEM TC 162-TDF: Test and Design Methods for Steel Fibre Reinforced Concrete'-σ-ε-Design Method—Final Recommendation," *Materials and Structures*, V. 36, No. 262, 2003, pp. 560-567. doi: 10.1617/14007

17. Baby, F.; Graybeal, B. A.; Marchand, P.; and Toutlemonde, F., "UHPC Tensile Behavior Characterization: Inverse Analysis of Four-Point Bending Test Results," *Materials and Structures*, V. 46, No. 8, 2013, pp. 1337-1354. doi: 10.1617/s11527-012-9977-0

18. Zhou, Z., and Qiao, P., "Direct Tension Test for Characterization of Tensile Behavior of Ultra-High-Performance Concrete," *Journal of Testing and Evaluation*, V. 48, No. 4, July-Aug. 2020, pp. 2730-2749.

19. Roth, M. J.; Eamon, C. D.; Slawson, T. R.; Tonyan, T. D.; and Dubey, A., "Ultra-High-Strength, Glass Fiber-Reinforced Concrete: Mechanical Behavior and Numerical Modeling," *ACI Materials Journal*, V. 107, No. 2, Mar.-Apr. 2010, pp. 185-194.

20. Zhang, J.; Stang, H.; and Li, V. C., "Experimental Study on Crack Bridging in FRC under Uniaxial Fatigue Tension," *Journal of Materials in Civil Engineering*, ASCE, V. 12, No. 1, 2000, pp. 66-73. doi: 10.1061/(ASCE)0899-1561(2000)12:1(66)

21. Sujivorakul, C., "Development of High-Performance Fiber-Reinforced Cement Composites Using Twisted Polygonal Steel Fibers," PhD dissertation, University of Michigan, Ann Arbor, MI, 2002.

22. Rossi, P., "High-Performance Multimodal Fiber-Reinforced Cement Composites (HPMFRCC): The LCPC Experience," *ACI Materials Journal*, V. 94, No. 6, Jan.-Feb. 1997, pp. 478-483.

23. Cunha, V. M.; Barros, J. A.; and Sena-Cruz, J. M., "An Integrated Approach for Modelling the Tensile Behaviour of Steel Fibre Reinforced Self-Compacting Concrete," *Cement and Concrete Research*, V. 41, No. 1, 2011, pp. 64-76. doi: 10.1016/j.cemconres.2010.09.007

24. Kamal, A.; Kunieda, M.; Ueda, N.; and Nakamura, H., "Evaluation of Crack Opening Performance of a Repair Material with Strain Hardening Behavior," *Cement and Concrete Composites*, V. 30, No. 10, 2008, pp. 863-871. doi: 10.1016/j.cemconcomp.2008.08.003

25. Jun, P., and Mechtcherine, V., "Behaviour of Strain-Hardening Cement-Based Composites (SHCC) under Monotonic and Cyclic Tensile Loading: Part 1—Experimental Investigations," *Cement and Concrete Composites*, V. 32, No. 10, 2010, pp. 801-809. doi: 10.1016/j.cemconcomp.2010.07.019

26. Park, S. H.; Kim, D. J.; Ryu, G. S.; and Koh, K. T., "Tensile Behavior of Ultra-High-Performance Hybrid Fiber-Reinforced Concrete," *Cement and Concrete Composites*, V. 34, No. 2, 2012, pp. 172-184. doi: 10.1016/j.cemconcomp.2011.09.009

27. Levandowski, C. J., "Investigating Micro-Crack and Local Crack Formation and Propagation in Ultra-High-Performance Concrete (UHPC)," PhD dissertation, Iowa State University, Ames, IA, 2018.

28. Dobrusky, S., and Bernardi, S., "Uni-Axial Tensile Tests for UHPCFRC," UHPC 2017, RILEM International Conference on Ultra-High-Performance Fiber-Reinforced Concrete, Montpellier, France, Sept. 2017, pp. 165-174.

29. Carloni, C., and Subramaniam, K. V., "Direct Determination of Cohesive Stress Transfer during Debonding of FRP from Concrete," *Composite Structures*, V. 93, No. 1, 2010, pp. 184-192. doi: 10.1016/j.compstruct.2010.05.024

30. Gali, S., and Subramaniam, K. V., "Investigation of the Dilatant Behavior of Cracks in the Shear Response of Steel Fiber Reinforced Concrete Beams," *Engineering Structures*, V. 152, Dec. 2017, pp. 832-842. doi: 10.1016/j.engstruct.2017.09.050

31. Shen, X., and Brühwiler, E., "Influence of Local Fiber Distribution on Tensile Behavior of Strain Hardening UHPC Using NDT and DIC," *Cement and Concrete Research*, V. 132, June 2020, p. 106042. doi: 10.1016/j.cemconres.2020.106042

32. Hou, T. C., and Lynch, J. P., "Electrical Impedance Tomographic Methods for Sensing Strain Fields and Crack Damage in Cementitious Structures," *Journal of Intelligent Material Systems and Structures*, V. 20, No. 11, 2009, pp. 1363-1379. doi: 10.1177/1045389X08096052

33. AASHTO T 397, "Standard Method of Test for Uniaxial Tensile Response of Ultra-High-Performance Concrete," American Association of State Highway and Transportation Officials, Washington, DC, 2022.

34. Sritharan, S., "Design of UHPC Structural Members: Lessons Learned and ASTM Test Requirements," *Advances in Civil Engineering Materials*, V. 4, No. 2, 2015, pp. 113-131. doi: 10.1520/ACEM20140042

35. ASTM C109/C109M-20b, "Standard Test Method for Compressive Strength of Hydraulic Cement Mortars (Using 2-in. or 50-mm Cube Specimens)," ASTM International, West Conshohocken, PA, 2020.

36. ASTM C1856/C1856M-17, "Standard Practice for Fabricating and Testing Specimens of Ultra-High-Performance Concrete," ASTM International, West Conshohocken, PA, 2017.

37. Graybeal, B. A., "Compression Testing of Ultra-High-Performance Concrete," *Advances in Civil Engineering Materials*, V. 4, No. 2, July 2015, pp. 102-112.

CALL FOR ACTION

ACI Invites You To...

Share your expertise

Do you have EXPERTISE in any of these areas?

- BIM
- Chimneys
- Circular Concrete Structures Prestressed by Wrapping with Wire and Strand
- Circular Concrete Structures Prestressed with Circumferential Tendons
- Concrete Properties
- Demolition
- Deterioration of Concrete in Hydraulic Structures
- Electronic Data Exchange
- Insulating Concrete Forms, Design, and Construction
- Nuclear Reactors, Concrete Components
- Pedestal Water Towers
- Pipe, Cast-in-Place
- Strengthening of Concrete Members
- Sustainability

Then become a REVIEWER for the *ACI Structural Journal* or the *ACI Materials Journal*.

Become a Reviewer for the ACI Journals

How to become a Reviewer:

1. Go to: **http://mc.manuscriptcentral.com/aci**;
2. Click on "Create Account" in the upper right-hand corner; and
3. Enter your E-mail/Name, Address, User ID and Password, and Area(s) of Expertise.

Update your Manuscript Central user account information

Did you know that the database for MANUSCRIPT CENTRAL, our manuscript submission program, is separate from the ACI membership database?

How to update your user account:

1. Go to **http://mc.manuscriptcentral.com/aci**;
2. Log in with your current User ID & Password; and
3. Update your E-mail/Name, Address, User ID and Password, and Area(s) of Expertise.

QUESTIONS?

E-mail any questions to Journals.Manuscripts@concrete.org.

American Concrete Institute

Always advancing

ACI MATERIALS JOURNAL TECHNICAL PAPER

Title No. 121-M10

Comparison and Critical Review of Durability Design in Design Codes

by Diala Basim Al-Haddad, Gul Ahmed Jokhio, and Abid Abu-Tair

Several incidents of early deterioration of structures have been reported in literature; such incidents have a negative impact. Insufficiencies in the durability design may result from a possible absence of explicit guidelines in design codes and standards that establish a standardized language for building design, construction, and operation. Most design codes and standards, while providing a robust framework for structural capacity and serviceability, do not address durability design to a desirable degree. This study examines and critically reviews the durability design in three international codes: the American, British, and Eurocodes. The study revealed that the European and British standards have comparatively more precise and comprehensive durability provisions, whereas the American code has a larger scope for development. The study introduces a proposal for the improvement of durability design provisions in codes to provide beneficial examples that can assist in the update of upcoming editions of these codes.

Keywords: ACI 318 Code; durability provisions; durability requirements; exposure conditions; international design codes.

INTRODUCTION

Durability refers to the ability of a structure to perform as per the designed features during its lifetime in a specific environment. Durability issues in reinforced concrete (RC) construction are a worldwide concern because they harm economic progress, natural resources, and human safety (Beushausen et al. 2021). As a result, efforts have been carried out in most design codes and standards to include requirements for providing robust and durable RC structures.

The ACI 318 Code is the most widely used and adopted code for the design of concrete structures (Hooton 2019). It specifies requirements for safe, serviceable, and cost-effective constructions (Suprenant 2019). However, as concluded in this study, the code's durability design provisions for concrete structures are not comprehensive or well understood. This study aims to assess durability design provisions and compare the ACI 318 Code with other international design codes and standards to recognize their strategy and implementation of durability design and lead to establishing proposals and recommendations to contribute to the successful international practice of the American code.

RESEARCH SIGNIFICANCE

This study examines the areas that need to be improved in the ACI Code and other international design codes through a critical review of the durability provisions of these documents. It proposes additional durability-related terminology and additional detailed exposure conditions to mitigate misinterpretation and ensure correct input for the designation of durability requirement values and service life modeling to achieve adequate and comprehensive durability design rather than structural design. The outcomes of this study can benefit and help improve the code if implemented.

DURABILITY PROVISIONS DEVELOPMENT IN INTERNATIONAL DESIGN CODES AND STANDARDS

Durability development in ACI 318 Code

Since its original publication in 1910, the ACI 318 Code has evolved tremendously (Ghosh 2016a). Design criteria and constraints on concrete strength and durability in the code are constantly evaluated and revised. Yehia et al. (2013) summarized the change in the code during the period 1999 to 2011 and showed the criteria of newer codes are generally more conservative than those of previous codes. Although the 2011 Code (ACI Committee 318 2011) covers additional exposure circumstances than the 1999 code, there are no notable differences between the two versions. Adding to that, since 1989, durability requirements have been included in addition to desired compressive strength when proportioning concrete mixtures. In 2008, an addendum was introduced that allowed the ASTM C1012 specification to evaluate the sulfate resistance of concrete mixtures using different cementitious materials listed in Table 4.3.1 (ACI Committee 318 2008), which defines the maximum expansion due to sulfate exposure if different cementitious materials specified in the code are employed.

Following that, ACI 318-11 went into further changes seen in ACI 318-14. Ghosh (2016b) highlights the significant changes between these two consecutive published codes as follows:

1. Table 4.2.1 of ACI 318-11—Exposure Categories and Classes is changed to Table 19.3.1.1. This table has undergone a lot of revisions: The "Severity" column was removed from the table; the exposure classes F1, F2, and F3 conditions were modified; "Limited exposure to water" replaced "occasional exposure to moisture; "Frequent exposure to water" substituted "continuous contact with moisture"; and Exposure Classes P0 and P1 (P for Permeability) were renamed W0 and W1 (W for Water Contact).

ACI Materials Journal, V. 121, No. 1, January 2024.
MS No. M-2023-204.R1, doi: 10.14359/51739154, received August 25, 2023, and reviewed under Institute publication policies.

2. Table 4.3.1 of ACI 318-11—Concrete Requirements by Exposure Class is changed to Table 19.3.2.1 as follows: For Exposure Classes F1 and F3, the maximum water-cementitious materials ratio (*w*/*cm*) and the minimum compressive strength criteria changed. The cementitious material types that are authorized in concrete assigned to Exposure Classes S1, S2, and S3 were altered.

3. New commentary for Section 19.3.3.2 specifies that the air content standards of ACI 318 apply to new concrete samples taken at the point of discharge from a mixer or a transportation unit when it arrives on site. If the licensed design expert specifies that a different location is accepted, the construction documents must include the necessary provisions.

The technical work for ACI 318-19 was completed by ACI Committee 318 (2019). The pervasive use of color to highlight distinct areas of the document and improve the readability of figures is one of the most noticeable changes to the Code and Commentary. Moehle (2019), the Chair of the ACI Committee 318 during the 2019 Code cycle, summarizes the provisions modified by including regulations for the use of shotcrete in addition to including new rules to prevent alkali-silica reaction (ASR). When this type of exposure is discovered, the licensed design professional (LDP) is responsible for investigating the best course of action for aggregates that are vulnerable to ASR. The Code prohibits the use of aggregate that is prone to alkali-carbonate reaction.

In 2022, ACI Committee 318 voted to maintain ACI 318-19. The references in both the Code (mentioned in Chapter 3) and the Commentary (listed after the Appendixes) were examined and updated as part of the reapproval process; the document has been renamed ACI 318-19(22). Technical changes are not permitted when a document is reapproved. As a result, any reference modifications that would have resulted in a technical change have been postponed until the next scheduled Code revision in 2025. ACI 318-19 and ACI 318-19(22) are identical requirements, except for reference alterations.

Durability development in British standards

The British Standard BS 8500-1 outlines concrete specifications and provides direction to designers (BSI 8500-1:2015+A2:2019 2019). It details the concrete quality that should be specified for various exposure classes, as well as the expected working life and minimum cover to normal reinforcement. It also covers materials, testing methods, and procedures that are not covered by BS EN 206.

As BS 8500-1 clarified, the primary goal of the amendment is to broaden the scope of cementitious materials covered. Natural pozzolana, natural calcined pozzolana, high-reactivity natural calcined pozzolana as an addition, portland pozzolana and pozzolanic cements, and a range of ternary cements with up to 20% limestone fines are now available. In addition, the choice to employ durability modeling or an equal durability process has been explained.

Durability specifications have a prescriptive approach. Kessy et al. (2015) stated that among the five options provided for the specifier for specifying concrete mixtures in BS 8500-1, the first two and last categories are referred to as performance approaches, but closer inspection reveals that they are prescriptive with maximum water-cement ratio (*w*/*c*), minimum cement content, and strength class requirements. They also discussed that BS 8500-1 allows for multiple binder types to be used depending on the exposure class. The maximum *w*/*c* and minimum cement content have been adjusted to suit the planned service life of 50 and 100 years, respectively, Tables A.4 and A.5 of BS 8500-1 contain cover depth criteria for several degradation methods, which are not included in EN 206-1. Nonetheless, the defined metrics (other than the cover) cannot be quantified and so cannot be considered performance-based in the strictest sense.

Durability development in Eurocode

The Eurocodes are aimed at developing and operating the internal market for building products and engineering services by resolving discrepancies that restrict their free movement within the Community (European Commission 2016). They are now in the maintenance and evolution stages to keep up with the range of new technologies, materials, and societal needs.

EN 206-1 has seen very few changes since its initial publication in 2000, with most updates consisting of language corrections, clarifications, and updated references to new European standards. Kansara (2012) concluded that the European code requires that structural protection must be determined by considering the structure's intended use, design working life, maintenance program, and actions, as well as the potential significance of direct and indirect actions, environmental conditions, and consequential effects (for example, deformations due to creep and shrinkage). Steel reinforcement corrosion protection is thought to be dependent on the density, quality, and thickness of the concrete cover, as well as cracking. The maximum *w*/*c* and minimum cement content are controlled, and the cover density and quality may be tied to a minimum concrete strength class.

A new durability design idea, analogous to the concept of strength classes, has been proposed to overcome the discrepancies of the present European prescriptive method by Von Greve-Dierfeld and Gehlen (2016a,b,c), who introduced and built on a system of exposure materials resistance classes for durability design. Design charts showing values for the minimal concrete cover as a function of material resistance and exposure class are produced using a partial safety factor format.

In the next version of EN 1992-1, the idea of exposure resistance classes (ERCs) is introduced. Performance verification in the future is expected to be based on either deemed-to-satisfy criteria, as it is today, or performance testing and the ERC idea. Geiker et al. (2021) stated that the proposed ERC approach will promote transparency in concrete performance classification and facilitate the unification of concrete standards across Europe.

INVESTIGATION FINDINGS FOR ACI 318 DURABILITY DESIGN PROVISIONS SHORTCOMINGS

The study identified several areas where the ACI 318 Code needs to be improved—either important durability components need to be included or expansion to the current provision to cover other critical durability issues, as follows:

1. Durability-related terminology; several definitions need to be added, and the existing definitions should be harmonized among other ACI publications. For example, in ACI 318-19(22), ACI 350-20, and ACI 201.1R-08, the term "service life" is not defined yet referenced in the comments. In contrast, the ACI 365.1R and ACI 562 definition is provided.

2. The limited criteria for exposure conditions should be extended to incorporate more categories and classes.

3. In contrast to the examined documents, the ACI 318 Code does not specify service life classifications.

4. The ACI 318-19(22) Code does not refer to durability planning, and the code does not address any requirement for future maintenance or repair of structures.

5. The code does not address the project's key stakeholders' contribution to the durability design, unlike the British and Eurocode.

6. There is no guidance for complex, specialized structures, or service environments with a mix of chemical and mechanical demands.

7. The Code has no provisions for particularly severe exposures, such as chemical contact, high temperatures, temporary freezing and thawing during construction, abrasive conditions, or any unique durability issues relevant to the structure.

8. The Code does not address aesthetics such as the final surface finish, this should be specified in the project documents.

9. The ACI 318 approach to durability is limited to prescriptive criteria for concrete materials and concrete cover based on environmental exposure conditions. Minimal provisions allowed for a performance approach for types and quantities of supplementary cementitious material (SCM) to resist sulfate attack.

10. ACI 318-19(22) allows for the use of stainless steel and other corrosive resistance reinforcement, however, no guidance for the cases where they should be employed.

11. ASR and carbonation are very detrimental factors for concrete structures, yet ASR is mentioned minimally and carbonation is not considered in the ACI 318 Code.

12. The Code relates the minimum compressive strength amount with the durability requirements. These are not necessarily related elements.

13. Freezing and thawing and sulfate attack provisions are fragmented and dispersed throughout the code.

14. The corrosion resistance of the reinforcement does not align with the ACI 318 durability standards for a specific concrete cover.

COMPARISON AND CRITICAL REVIEW FOR DURABILITY PROVISIONS IN INTERNATIONAL DESIGN CODES AND STANDARDS

Exposure conditions

As exposure classes are the first step in the durability design process and service life modeling, they should be clear, simple, comprehensive, and easy to interpret. The exposure conditions examined in this study are established to develop a prescriptive durability design approach rather than performance-based methods. Even though some of the Eurocode and British standard exposure classes might be indirectly applicable to performance-based approaches for today's modern structures, these approaches need more detailed input; thereby, they should be improved and combined with supplementary guidelines for a detailed and accurate assigning of exposure conditions.

Figure 1 illustrates the overall classification of exposure conditions in the international design codes; ACI 318-19(22) is the least comprehensive and limited in providing examples of different environmental conditions.

Freezing and thawing (F&T) is the first exposure category mentioned in the ACI 318 code. It is one of the most typical physical deteriorations of concrete in cold conditions, which causes major damage and cracks in concrete structures (Fig. 2). Even though the F&T exposure condition is comprehensive in the ACI 318, BS 8500-1, and EC2 design codes (refer to Table 1), clarification of specific terms

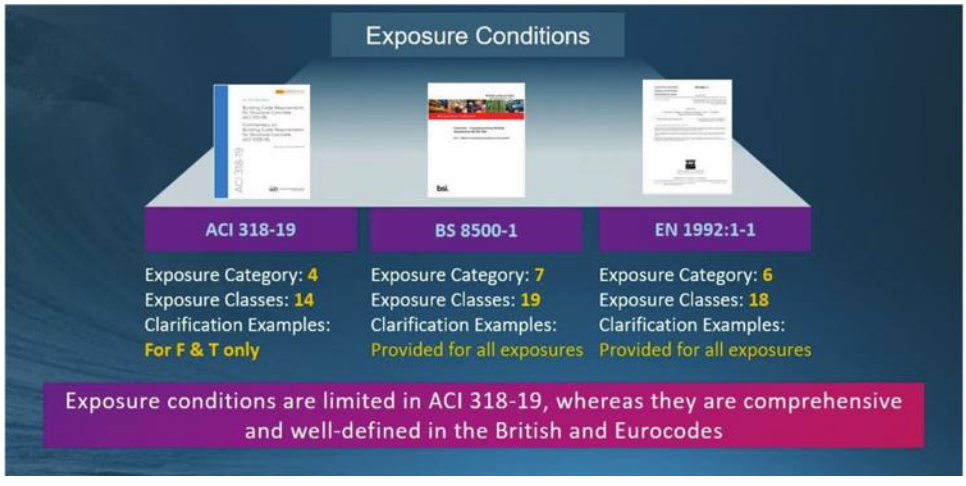

Fig. 1—Comparison of exposure categories and classes in international codes and standards.

Fig. 2—Buildings damaged due to F&T effect (Paul 2014).

Table 1—F&T exposure conditions comparison in studied codes

ACI 318-19(22)		BS 8500-1		EN 1992-1-1	
Class/design	Description of environment	Class/design	Description of environment	Class/design	Description of environment
F0	Concrete not exposed to F&T cycles	XF1	Moderate water saturation without a deicing agent	XF1	Moderate water saturation without a deicing agent
F1	Concrete exposed to F&T cycles with limited exposure to water	XF2	Moderate water saturation with deicing agent	XF2	Moderate water saturation with deicing agent
F2	Concrete exposed to F&T cycles with frequent exposure to water	XF3	High water saturation without deicing agent	XF3	High water saturation without deicing agent
F3	Concrete exposed to F&T cycles with frequent exposure to water and deicing chemicals	XF4	High water saturation with a deicing agent or seawater	XF4	High water saturation with a deicing agent or seawater

is required. According to ACI 318-19(22), limited exposure to water falls under the F1 category. However, it can be challenging to determine whether this limited exposure causes water saturation; hence, designers consider F2 exposure as a safe option. This issue should be addressed to avoid such confusion, and a testing method or modeling should be provided. In EC2 and BS 8500-1, classes need to clarify the definition of "moderate" for XF1 and XF2, as some countries considered it as lower than the critical degree of saturation and adopted the XD3 exposure class. A clear criterion should be provided to avoid confusion among countries adopting this standard.

The second exposure category in the American code is sulfate attack. It is a decomposition mechanism in which sulfate ions attack the elements of cement paste and result in cracking, spalling, and expansion of concrete (Fig. 3). In ACI 318-19(22) and Eurocode, multiple factors need to be considered for the exposure to sulfates. This includes: 1) adding the source of sulfates due to industrial and/or agricultural effects; 2) considering the frequency of water exposure (static or dynamic), as this affects the chemical reaction and ion diffusion and physical attack due to salt crystallization; 3) specifying the type of cation associated with sulfates as these have different rates, mechanisms, and effects on concrete deterioration. In ascending order, the deteriorating effect of the cations is calcium, sodium/potassium, and magnesium; and 4) the combined effect of chloride and sulfates, studies showed that chloride will limit sulfate ingress (Al-Haddad et al. 2023). The British standard considered all the aforementioned factors for the durability design against sulfate attack. Refer to Table 2 for a comparison of sulfate attack exposure classes in the codes.

Water exposure is the third exposure category that is mentioned in the American code but not in EC2 and British standards. The critical impact of water is the alkali-silica reaction. This phenomenon, which is mostly seen in pavements, bridges, walls, dams and hydraulic structures, barriers, and nuclear/power plant structures, is very detrimental to structures (Fig. 4). The studied codes did not mention the exposure category for this environmental condition apart from the requirement of moisture, this could be explained by the factors that need to combine to begin the reaction, alkali is mostly from the materials making up the concrete whereas moisture is from the environment. Thereby, the Eurocode related it as a cause of the chemical

attack, whereas the British standard assigned the responsibility of avoiding it to the supplier.

The fourth and last exposure category mentioned in ACI 318-19(22) is reinforcement corrosion. In contrast with the EC2 and BS which are well-defined, the American standard is very simple and does not do justice to informed durability design as it does not cover all the possible factors that induce corrosion (Table 3). This approach does not cover corrosion due to carbonation or chloride from different sources, or by water and other factors such as F&T. Additionally, steel corrosion might be a secondary deterioration after cracks or spalling resulting from other durability limiting factors such as sulfate attack and F&T. Moreover, chloride sources might come from the concrete constituents that have to be controlled. All these mentioned factors must be accounted for to avoid steel corrosion and provide a durable design.

Eurocode and the British standard begin with categorizing corrosion of steel reinforcement into no corrosion category, X0. The British code is detailed about that, whereas EC2 can expand its application on reinforced structures not only indoor but also outdoor structures in arid dry areas.

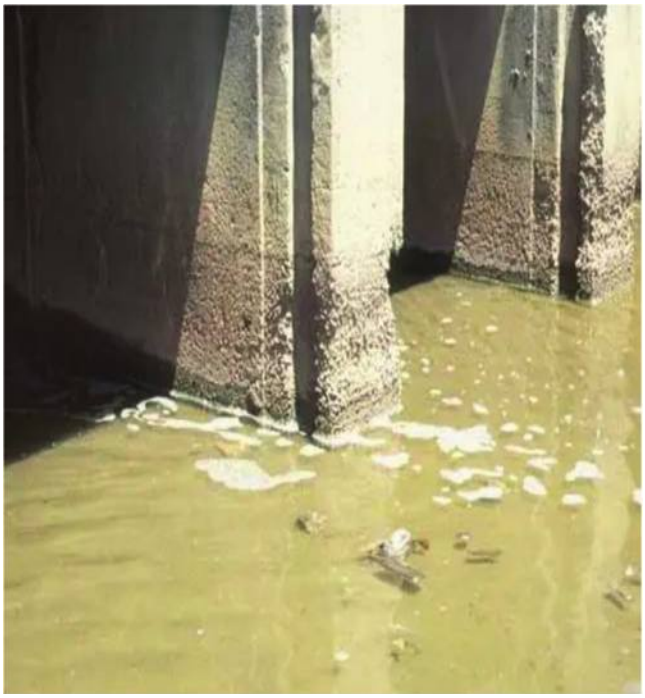

Fig. 3—Structure affected by sulfate attack (Suryakanta 2015).

Exposure class XC1 includes two scenarios that relate to the carbonation mechanism and corrosion induced by carbonation. XC1 (wet) exposures can be neglected and XC1 (dry) is the same as X0 conditions; thereby, this category needs to be revised as it has no relevant function to be applied.

Despite the adequate details for XC classes in EC2 and BS 8500-1, another exposure class should be added to include areas with high CO_2 concentrations such as tunnels, car parking, and industrial areas. This will assist designers in including the CO_2 levels with the relative humidity amounts in their design for durability.

Another exposure category related to corrosion is the case when it is induced by chlorides from sources other than seawater, including deicing water, chloride in swimming pools, and industrial water, and for cyclic wet and dry. The latter case designated by XD3 needs to be handled carefully by the design practitioner as it is hard to quantify, particularly for nonstandard situations. Moreover, a consideration for the note from the revision of the Norwegian Annex to EN 206-1 recommends that exposure to XD3 in interior parking garages may be more severe than exposure to XD3 on a highway structure (SIST-TP CEN/TR 15868 2018,). This is because of the action of salt slurry precipitation accompanied by wetting and drying on the slab surfaces of indoor parking garages, as well as the resulting increase in surface salt concentrations over time. This effect requires further analysis and quantification before it can be considered in the establishment of revised deicing salt exposure classifications.

Fig. 4—Du Vallon-Charest highway interchange viaduct, Québec, QC, Canada, was recently demolished because of alkali-silica reaction (Fernandes and Broekmans 2013).

Table 2—Sulfate attack exposure conditions comparison in studied codes

ACI 318-19(22)		BS 8500-1		EN 1992-1-1	
Exposure category	Class/design	Exposure category	Class/design	Exposure category	Class/design
Water-soluble sulfate SO_4, in soil % by mass (S classes)	S0, S1, S2, S3	Chemical attack by aggressive ground (XA classes)	XA1, XA2, XA3	Chemical attack by aggressive ground (XA classes)	XA1, XA2, XA3
Dissolved sulfate SO_4 dissolved in water, ppm (S classes)	S0, S1, S2, S3	Chemical attack from seawater (XAS class)	XAS		

Table 3—Reinforcement corrosion exposure conditions comparison in studied codes

ACI 318-19(22)		BS 8500-1		EN 1992-1-1	
Exposure category	Class/design	Exposure category	Class/design	Exposure category	Class/design
Corrosion (C classes)	C0, C1, C2	No risk of corrosion or attack	X0	No risk of corrosion or attack	X0
		Corrosion induced by carbonation (XC classes)	XC1, XC2, XC3, and XC4 (XC3/4)	Corrosion induced by carbonation (XC classes)	XC1, XC2, XC3, XC4
		Corrosion induced by chlorides other than from seawater (XD classes)	XD1, XD2, XD	Corrosion induced by chlorides other than from seawater (XD classes)	XD1, XD2, XD
		Corrosion induced by chlorides from seawater (XS classes)	XS1, XS2, XS3	Corrosion induced by chlorides from seawater (XS classes)	XS1, XS2, XS3

For structures exposed to marine environments, corrosion might be initiated from the presence of chlorides either dissolved in water or airborne. Chen and Leung (2015) explained that the passive coating on the steel surface is damaged when corrosion-inducing substances (such as chlorides) reach a threshold concentration on the steel surface and reinforcement corrosion begins, such as the corrosion in the Cape Town bridge (Fig. 5).

The exposure class for chloride ingress is XS1; particularly more details should be given to the term "airborne" as there are multiple factors that affect such ingress. This includes the distance of the structure from the sea, ambient relative humidity, topographical situations, and wind features such as its speed, direction, frequency, and the formation of fog and mist. Considering the South African experience, they recognized that within 30 km from the sea and a combination of sufficient relative humidity and onshore wind, chloride ingress was initiated, contrasting other countries that have less chloride ingress due to low humidity.

Although corrosion induced by carbonation is widely variable, the American standard did not include it as an exposure condition. This limited concern might be related to the higher cover depth assigned by ACI 318 than the other studies ones, or due to the use of SCM or limestone additions to cement. This justification can be reasonable if the code is locally used; however, the ACI 318 code is widely used around the world and should include such exposures that are critical to the service life of structures.

Other critical factors that are not mentioned in the American, British, and Eurocode are the effect of strong and dangerous chemicals, temperature, solar radiation, and biological agents. Other exposures that can be considered nonstandard include global warming, running water exposure, and seasonal changes in humidity. The studied codes and standards are globally used; therefore, comprehensive, clear, reasonably detailed exposure categories should be provided based on experiences, studies, and approaches for each one so that the code practitioners can choose the proper first input to the durability design and exposure class, and provide safe and economic structural design.

Requirements for concrete durability in international codes and standards

Durability requirements in the studied codes are based on the limitation of fluid penetration by limiting the maximum *w*/*c* together with the employment of SCM. Because verifying *w*/*c* value on-site using test methods is challenging and can not be accurate, the codes relate this value to the strength of concrete as it is easier to test. Relating durability to a minimum required value of strength of concrete condition needs to be revised, as the durability of concrete does not necessarily depend on strength; a concrete mixture with 50 MPa strength does not indicate more durability than 35 MPa strength. It may be advisable to forego the additional unwanted strength of 15 MPa in favor of enhanced durability obtained by using SCM.

Moreover, ACI 318-19(22) needs to revise its requirement about the air-entrained limit to resist F&T. It recommends that if the member is not critically saturated, proper spacing of entrained air bubbles is not necessary; nevertheless, it is not always easy to guarantee that all concrete constructions will not become critically saturated. Thereby, air entrainment should always be applied as it is inexpensive insurance.

The British standard has detailed clear limits for durability requirements for exposure conditions. However, for *w*/*c* values assigned for F&T exposure, despite the use of SCMs that can provide a ratio as low as 0.35, the *w*/*c* values in BS 8500-1 are higher compared to ACI 318-19(22); the standard states that it will not always be achievable throughout the United Kingdom. Precast, pre-tensioned concrete units with a strength class of C40/50 or higher and cement having less than 25% fly ash or 46% slag cement have proven to be durable.

For sulfate attack requirements in ACI 318-19(22), the code offers performance options for the type and quantity of cementitious materials that will enhance the use of high-end proven methods to produce durable concrete. On the other hand, the code limits the maximum value of *w*/*c* up to 0.5, which does not reflect the benefit gained from using SCMs. It would be better if the code permitted higher *w*/*c* values for S1 and S2, which would result in more economical and workable concrete. Comparing the requirements in the American code given for exposure classes S2 and S3 option1, for the latter class, the code permits the use of SCM.

Fig. 5—Corrosion-induced damage on Cape Town concrete bridge exposed to airborne chlorides (Alexander and Beushausen 2019).

Nonetheless, the effect of these materials is not reflected in *w*/*c* and compressive strength. The expected outcome from adding SCM is to achieve lower *w*/*c*, which is not the case herein. A revision or at least an explanation should be provided to clarify this concern.

The ACI 318 Code related the concrete cover requirements to the type of reinforcement and casting method. There are other factors that the code should include for providing quality and economical concrete cover. The reinforcement's corrosion resistance for a particular concrete cover does not meet the ACI 318 durability standards. Exposure conditions must be unified and clearer for the certified engineer between Chapters 19 and 20. The Code did not relate reinforcement details with the concrete cover, and there are multiple chapters in the code that detail the requirements for different types of materials, but there are no cross references that a credentialed design professional might use to see them as a system.

The code recommends higher cover values for severe exposure conditions or fire. Yet this will increase the distance for the hazardous materials to reach the steel, reinforcement will be less effective, and cracking risk due to tensile stresses, temperature, and shrinkage will increase.

More factors affect concrete permeability that ACI 318-19(22) and BS 8500-1 do not mention and must be included, such as cement properties—for the same *w*/*c*, coarse cement particles will produce more porosity in the cement paste. Curing of concrete also has a vital role in the total porosity; a proper curing—preferably wet curing rather than steam curing—will contribute to reducing the pores.

DISCUSSION

Building codes evolve with time and technological advancements; to achieve long-term performance and sustainable structures, the three factors of strength, serviceability, and durability should be successfully harmonized and integrated (Fig. 6).

The study showed that the design codes share some similarities and variations; this is acceptable due to differences in their emphasis areas, application areas, and the type of document itself. However, some areas need to be improved, and specifications are dominantly prescriptive, with a mixture of other performance specifications. BS 8500-1 is the most

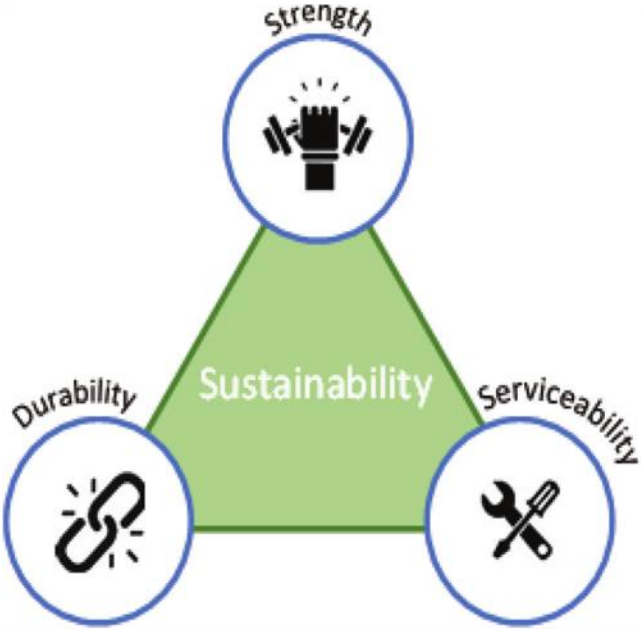

Fig. 6—Successful harmonization of strength, serviceability, and durability design must be considered in structural design process to achieve sustainable design.

detailed and comprehensive of these codes and standards, followed by EC2 and, finally, ACI 318-19(22).

For exposure conditions, ACI 318-19(22) should be comprehensive as it does not contain all elements that induce sulfate attack and steel corrosion, leaving the design practitioner with the struggle to decide which requirements to assign for exposures that are not listed in the code. For the British and Eurocode, while they provide detailed exposure conditions, some exposure classes need to be more precise, such as XC1, XD3, and XS1, as addressed in the previous critical review.

The three studied codes require and relate a minimum value for concrete strength for the durability requirements; nevertheless, strength and durability are not necessarily related, so this requirement should be modified. The other requirements for *w*/*c*, air-entrained, minimum cement content, and SCM are acceptable; nevertheless, due to the variety of available materials, geographical restrictions, available resources, and technology, no unified values can be assigned for all codes. These codes, however, may allow for further performance standards in addition to prescriptive specifications (hybrid approach); this approach will optimize the best approaches to achieving durable concrete.

Based on the comparison results and the critical review, additional exposure categories and classes can be added to the currently provided exposure categories in the ACI 318 code; for F&T, F3 classes can be subdivided into F3a and F3b to address the surface final finish of the structural members. For steel corrosion, additional detailed categories that include carbonation-induced corrosion and chloride-induced carbonation from sources of seawater and other than seawater can be included. The following tables (Tables 4 to 7) depict a proposal for the exposure categories and classes that can be adopted in the coming development of the ACI 318 Code.

Table 4—Proposed exposure classes for carbonation-induced corrosion

Exposure class	Severity	Condition	Example
C-C1	Low	Wet, rarely dry	Reinforced and prestressed concrete surfaces permanently submerged in non-aggressive water/permanently in contact with soil not containing chloride.
C-C2	Moderate	Moderate humidity	External reinforced and prestressed concrete surfaces sheltered from or exposed to direct rain.
C-C3	Major	Cyclic wet and dry	Reinforced and prestressed concrete surfaces subject to high humidity, repeated wetting, and drying.
C-C4	Severe	High concentration	Reinforced and prestressed concrete surfaces inside tunnels, car parking, and industrial areas

Table 5—Proposed exposure classes for chloride-induced corrosion apart from seawater

Exposure class	Severity	Condition	Example
C-D1	Low	Moderate humidity	Concrete surfaces exposed to airborne chlorides. Reinforced and prestressed concrete wall and structure supports more than 10 m horizontally from carriageway. Bridge deck soffits more than 5 m vertically above carriageway.
C-D2	Moderate	Wet, rarely dry	Parts of structures exposed to occasional or slight chloride conditions. Reinforced and prestressed concrete surfaces immersed in water containing chlorides. Buried highway structures more than 1 m below adjacent carriageway.
C-D3	Major	Cyclic wet and dry	Reinforced and prestressed concrete walls and structural supports within 10 m of carriageway. Bridge parapet edge beams. Buried highway structures less than 1 m below carriageway level. Reinforced pavements and car park slabs.
C-D4	Severe	Cyclic wet and dry	Reinforced and prestressed concrete slabs inside parking garages.

Table 6—Proposed exposure classes for chloride-induced corrosion from seawater

Exposure class	Severity	Condition	Example
C-S1a*	To be locally specified	Exposed to airborne salt but not in direct contact with the seawater	External reinforced and prestressed concrete surfaces in coastal areas.
C-S1b*	To be locally specified	Exposed to airborne salt but not in direct contact with the seawater	External reinforced and prestressed concrete surfaces in coastal areas.
C-S2	Moderate	Permanently submerged	Reinforced and prestressed concrete surfaces completely submerged or remaining saturated—for example, concrete below the mid-tide level
C-S3	Severe	Tidal, splash, and spray zones	Reinforced and prestressed concrete surfaces in the upper tidal zones and the splash and spray zone, including exposed soffits above seawater

*CS1a and CS1b are assigned based on distance of structure from sea; ambient relative humidity; topographical situations; wind features such as speed, direction, and frequency; and formation of salt-laden fog and mist.

The simplest enhancement that can be accomplished to the ACI 318 Code and also among other ACI documents is standardizing durability and service life prediction terminologies and concepts, using Table 8 as a starting point. This helps with communication outside the institute, a greater understanding of concepts within ACI, and harmonizing ACI's knowledge base and avoiding misinterpretation of these durability-related terms.

FURTHER RESEARCH

To enable the proposed exposure classes to be used in the durability design process, further research for comprehensive testing and/or modeling is required to designate the durability design requirements such as *w*/*c*, strength, and concrete cover.

Further research into a method of testing or modeling for the degree of water saturation in structural members to assign appropriate exposure classes F1 and F2.

CONCLUSIONS

Overall, the authors can conclude that the durability design requirements and recommendations in the ACI 318-19(22) design code are not comprehensive and do not encompass extended situations, such as the exposure conditions which did not address several critical exposure classes. The code provisions are fragmented among the code chapters as found for steel reinforcement corrosion. The code's durability provisions are too simple and insufficient to provide a new structure design that can withstand the aggressive environment for the desired long lifespan. This is a major concern for code practitioners—when compared to other

Table 7—Proposed exposure classes for F&T

Exposure class	Severity	Condition	Example
F1	Low	Concrete is exposed to F&T conditions, but very low probability of concrete being near saturation at the time of exposure	Vertical surfaces above level of snow accumulation or horizontal elevated floors in areas protected from direct exposure to moisture.
F2	Moderate	Concrete exposed to F&T conditions, with high probability of concrete being near saturation at time of exposure, but no deicing chemical exposure	Vertical surfaces above level of snow accumulation or horizontal elevated floors in areas protected from direct exposure to moisture.
F3	Major	Concrete exposed to F&T conditions, with high probability of concrete being near saturation at time of exposure, with deicing chemical exposure	Vertical surfaces below level of snow accumulation; with sufficient moisture exposure to allow concrete to be near saturation before freezing; retaining walls with one side exposed to moisture; and slabs-on-ground that are not protected
F4a	Severe	Concrete exposed to F&T conditions as well as deicing chemicals—hand-finished surfaces	Vertical surfaces that may have deicing-chemical-contaminated snow piled against them; sidewalks or pavements that receive deicing chemicals; and concrete that receives frequent exposure to seawater as well as F&T conditions.
F4b	Severe	Concrete exposed to F&T conditions as well as deicing chemicals on machine-finished surfaces	Vertical surfaces that may have deicing-chemical-contaminated snow piled against them; sidewalks or pavements that receive deicing chemicals; and concrete that receives frequent exposure to seawater as well as F&T conditions.

Table 8—Summary of relevant durability design and service life terms

Term	Definition	Reference document
Alkali content of concrete	Value calculated from mixture proportions and determined alkali contents of each of the constituents and used for verifying that the alkali content of concrete does not exceed the specified limit	BS 8500-1
Cement or combination content	Mass of cement or combination contained in a cubic meter of fresh, fully compacted concrete, expressed in kg/m^3	BS 8500-1
Combination	Restricted range of portland cement and additions which, having been combined in the concrete mixer, count fully towards the cement content and *w*/*c* in concrete	BS 8500-1
Design service (or working) life	(Design working life)—Assumed period for which a structure or part of it is to be used for its intended purpose with anticipated maintenance but without major repair necessary	EC2
Hydraulic gradient	The difference in the hydrostatic head of water on opposite sides of a concrete element, in meters, divided by the section thickness, in meters	BS 8500-1
Licensed design professional	By the statutory requirements of professional licensing laws of the state or jurisdiction in which the project is to be constructed, and who is in responsible charge of the structural design	ACI 318
Limit state	A state beyond which a structure or component no longer satisfies the design performance requirements states beyond which the structure no longer fulfills the relevant design criteria	EC2
Maintenance	Set of activities performed during the working life of the structure to enable it to fulfill the requirements for reliability combination of all technical and associated administrative actions during a component's service life (to retain it in a state in which it can perform its required functions)	EC2
Minimum cover	Depth of cover to reinforcement assumed for durability design	BS 8500-1
Reliability	The ability of a structure or a structural member to fulfill the specified requirements, including the design working life, for which it has been designed. Reliability is usually expressed in probabilistic terms	EC2
Repair	Activities performed to preserve or to restore the function of a structure that falls outside the definition of maintenance	EC2
Resistance	The capacity of a member or component, or a cross section of a member or component of a structure, to withstand actions without mechanical failure—for example, bending resistance, buckling resistance, tension resistance	EC2
Serviceability	Serviceability refers to the ability of the structural system or structural member to provide appropriate performance and functionality under the actions affecting the system. Serviceability requirements address issues such as deflections and cracking, among others	ACI 318 Commentary
Serviceability limit states	States that correspond to conditions beyond which specified service requirements for a structure or structural member are no longer met	EC2
Ultimate limit state	State associated with collapse or with other similar forms of structural failure	EC2

international codes, the code does not provide appropriate direction for durable structural design.

The Eurocode and British standard BS 8500-1 durability design provisions are well-defined and comprehensive; however, some areas need to be quantified and clarified and other areas need to be extended as discussed, particularly, in exposure category classifications.

Performance-based specifications should be included in all the reviewed design codes and a hybrid design approach (performance and prescriptive) should be enabled to benefit from the advantages of durability design.

AUTHOR BIOS

Diala Basim Al-Haddad *is a PMP-Certified Structural Civil Engineer. She received her BS from Jordan University of Science and Technology, Irbid, Jordan, and her MS from the British University in Dubai, Dubai, UAE. She is a member of the Society of Engineers, UAE, and Jordan Engineers Association. Her research interests include structural analysis and design, and the durability and rehabilitation of reinforced concrete structures.*

Gul Ahmed Jokhio *is an Associate Professor in structural engineering at the Faculty of Engineering and IT, British University in Dubai. He received his MSc and BE from NED University of Engineering and Technology, Karachi, Pakistan, in 1999 and 2002, respectively, and his PhD in civil engineering from Imperial College London, London, UK, in 2012. His research interests include structural analysis and design, and sustainable construction materials.*

Abid Abu-Tair *is a Professor of structural engineering at the Faculty of Engineering and IT at the British University in Dubai. He received his BE and PhD in structural engineering from Queen Mary College, London, UK, and his MSc in structural engineering from Imperial College London. His research interests include structural performance sustainability and asset management focusing on the durability of concrete structures.*

REFERENCES

ACI Committee 201, 2008, "Guide for Conducting a Visual Inspection of Concrete in Service (ACI PRC-201.1-08)," American Concrete Institute, Farmington Hills, MI, 16 pp.

ACI Committee 318, 2008, "Building Code Requirements for Structural Concrete (ACI 318-08) and Commentary (ACI 318R-08)," American Concrete Institute, Farmington Hills, MI, 473 pp.

ACI Committee 318, 2011, "Building Code Requirements for Structural Concrete (ACI 318-11) and Commentary (ACI 318R-11)," American Concrete Institute, Farmington Hills, MI, 503 pp.

ACI Committee 318, 2019, "Building Code Requirements for Structural Concrete (ACI 318-19) and Commentary (ACI 318R-19) (Reapproved 2022)," American Concrete Institute, Farmington Hills, MI, 624 pp.

ACI Committee 350, 2021, "Code Requirements for Environmental Engineering Concrete Structures (ACI 350-20) and Commentary (ACI 350R-20)," American Concrete Institute, Farmington Hills, MI, 544 pp.

Al-Haddad, D. B.; Jokhio, G. A.; and Tair, A. A., 2023, "Overview of Concrete Deterioration Due to Sulphate Attack and Comparison of Its Requirements in International Codes," BUiD Doctoral Research Conference 2022, Lecture Notes in Civil Engineering, K. Al Marri, F. Mir, S. David, and A. Aljuboori, eds., V. 320, Springer, Cham. doi: 10.1007/978-3-031-27462-6_19

Alexander, M., and Beushausen, H., 2019, "Durability, Service Life Prediction, and Modeling for Reinforced Concrete Structures – Review and Critique," *Cement and Concrete Research*, V. 122, pp. 17-29.

Beushausen, H.; Ndawula, J.; Helland, S.; Papworth, F.; and Linger, L., 2021, "Developments in Defining Exposure Classes for Durability Design and Specification," *Structural Concrete*, V. 22, No. 5, pp. 2539-2555. doi: 10.1002/suco.202000792

BS 8500-1:2015+A2:2019, 2019, "Concrete. Complementary British Standard to BS EN 206 - Method of Specifying and Guidance for the Specifier," British Standards Institution, London, UK.

Chen, E., and Leung, C. K. Y., 2015, "Finite Element Modeling of Concrete Cover Cracking Due to Non-Uniform Steel Corrosion," *Engineering Fracture Mechanics*, V. 134, pp. 61-78. doi: 10.1016/j.engfracmech.2014.12.011

EN 206-1, 2000, "Concrete - Part 1: Specification, performance, Production and Conformity," European Committee for Standardization, Brussels, Belgium.

EN 1992-1-1, 2004, "Eurocode 2: Design of Concrete Structures - Part 1-1: General Rules and Rules for Buildings," European Committee for Standardization, Brussels, Belgium.

Fernandes, I., and Broekmans, M. A. T. M., 2013, "Alkali-Silica Reactions: An Overview. Part I," *Metallography, Microstructure, and Analysis*, V. 2, No. 4, pp. 257-267. doi: 10.1007/s13632-013-0085-5

Geiker, M. R.; Hendriks, M. A. N.; and Elsener, B., 2023, "Durability-Based Design: The European Perspective," *Sustainable and Resilient Infrastructure*, V. 8, No. 2, pp. 169-184.

Ghosh, S. K., 2016a, "Significant Changes from 2011 to the 2014 Edition of ACI 318," *PCI Journal*, V. 61, No. 2, pp. 56-80. doi: 10.15554/pcij.03012016.56.80

Ghosh, S. K., 2016b, "Significant Changes between ACI 318-11 and ACI 318-14," *Structure Magazine*, pp. 25-28.

Hooton, R. D., 2019, "Future Directions for Design, Specification, Testing, and Construction of Durable Concrete Structures," *Cement and Concrete Research*, V. 124, Aug., p. 105827.

Kansara, K. D., 2012, "Durability Perspective in Codes of Practice for Design of Reinforced Concrete Structures," *The Structural Engineers Forum of India (SEFI)*, V. 11, p. 1-11

Kessy, J. G.; Alexander, M. G.; and Beushausen, H., 2015, "Concrete Durability Standards: International Trends and the South African Context. Journal of the South African Institution of Civil Engineering," *South African Institute of Civil Engineers*, V. 57, No. 1, pp. 47-58. doi: 10.17159/2309-8775/2015/v57n1a

Moehle, J. P., 2019, "Key Changes in the 2019 Edition of the ACI Building Code (ACI 318-19)," *Concrete International*, V. 41, No. 8, Aug., pp. 21-27.

Paul, A., 2014, "Freeze-Thaw Damage of Concrete - Effects & Preventive Measures," CivilDigital.com, https://civildigital.com/freeze-thaw-damage-concrete-effects-preventive-measures/. (last accessed Dec. 18, 2023)

SIST-TP CEN/TR 15868, 2018, "Survey on Provisions Valid in the Place of Use Used in Conjunction with the European Concrete Standard and Developing Practice," European Committee for Standardization, Brussels, Belgium.

Suprenant, B. A., 2019, "ACI Reference Specifications," *Concrete International*, V. 41, No. 10, Oct., pp. 42-48.

Suryakanta, 2015, "How to Protect Concrete from Sulphate Attack?" CivilBlog.Org, https://civilblog.org/2015/02/27/how-to-protect-concrete-from-sulphate-attack/#. (last accessed Dec. 18, 2023)

Von Greve-Dierfeld, S., and Gehlen, C., 2016a, "Performance-Based Durability Design, Carbonation, Part 3: PSF Approach and a Proposal for the Revision of Deemed-To-Satisfy Rules," *Structural Concrete*, V. 17, No. 5, pp. 718-728. doi: 10.1002/suco.201600085

Von Greve-Dierfeld, S., and Gehlen, C., 2016b, "Performance-Based Durability Design, Carbonation Part 2 – Classification of Concrete," *Structural Concrete*, V. 17, No. 4, pp. 523-532. doi: 10.1002/suco.201600067

Von Greve-Dierfeld, S., and Gehlen, C., 2016c, "Performance-Based Durability Design, Carbonation Part 1 – Benchmarking of European Present Design Rules," *Structural Concrete*, V. 17, No. 3, pp. 309-328. doi: 10.1002/suco.201600066

Yehia, S. A.; Mohamed, O. H.; Elamin, O. A.; Maroua, A.; Abu-Zidan, Y. F.; and Arabemirates, U., 2013, "Impact of Changes in ACI 318 Building Code: Changes in Durability and Structural Design Requirements," *Proceedings of the Seventh International Conference on Concrete under Severe Conditions – Environment and Loading*, RILEM Publications SARL, pp. 485-491.

ACI MATERIALS JOURNAL

The American Concrete Institute (ACI) is a leading authority and resource worldwide for the development and distribution of consensus-based standards and technical resources, educational programs, and certifications for individuals and organizations involved in concrete design, construction, and materials, who share a commitment to pursuing the best use of concrete.

Individuals interested in the activities of ACI are encouraged to explore the ACI website for membership opportunities, committee activities, and a wide variety of concrete resources. As a volunteer member-driven organization, ACI invites partnerships and welcomes all concrete professionals who wish to be part of a respected, connected, social group that provides an opportunity for professional growth, networking, and enjoyment.

American Concrete Institute